Evaluating the Interfacial Mechanics of Distributed Strain Sensors Mounted to GFRP Reinforcing Bars

By

Mina Javankhoshraftar

A thesis submitted to the University of Ottawa
in the fulfilment of the thesis requirement
for the degree of Master of Applied Science
in Civil Engineering

Department of Civil Engineering
University of Ottawa
Ottawa, Canada

June 2025

Abstract

In-service reinforced concrete (RC) structures in harsh environments face significant challenges such as corrosion and cracking, which undermine their durability and resilience. To address these issues and reduce maintenance costs, a novel solution is proposed that integrates glass fibre reinforced polymer (GFRP) reinforcing bars with distributed fibre optic sensors (DFOS). This multifunctional system incorporates continuous structural health monitoring (SHM) capabilities into the electromagnetically neutral, high-strength, and lightweight properties of GFRP bars, while protecting sensors from cracking and fracture within the concrete matrix.

Emerging sensing systems, such as optical frequency domain reflectometry (OFDR), offer sub-millimetre resolution in distributed strain measurements over long distances. This enables precise detection of strain peaks associated with concrete cracks at various locations along the RC structure throughout its service life.

Despite considerable prior research and development, the strain transfer efficiency and monitoring stability of OFDR-based DFOS bonded to GFRP bars under various stress conditions had not been thoroughly investigated. To fill this gap, this study examined the performance of DFOS in capturing tensile strain in GFRP bars under cyclic and sustained loading. Experimental testing and numerical analysis were conducted to identify key influencing factors and define limits for efficient and stable monitoring. Strain profiles from multiple test specimens were then analyzed using a developed closed-form model that accounts for elasto-plastic strain transfer from the host material to the sensor through the adhesive interface.

The experimental results demonstrated that OFDR-based DFOS reliably captured strain profiles along GFRP bars under varying loading conditions, including within the GFRP bar's

serviceability limits and up to strain levels approaching 1.3%. Beyond this threshold, sustained high-stress exposure triggered plastic response in the adhesive interface, leading to gradual bondline degradation, permanent interfacial slip, and progressive strain reading anomalies (SRAs), observed by loss of accuracy in strain values measured along the DFOS-bonded length as it degraded over time.

The numerical analysis closely aligned with experimental data, effectively capturing strain transfer behaviour during bond damage progression. This provides a practical framework for evaluating the quality of dynamic host–sensor interaction and potential monitoring efficiency loss under severe mechanical loading during service.

Overall, the findings establish effective monitoring ranges and emphasize the importance of better understanding the strain transfer mechanisms of bonded DFOS systems, identified as a primary source of measurement error, for enabling reliable long-term strain monitoring in demanding environments.

Acknowledgments

First and foremost, I would like to express my deepest gratitude to my esteemed supervisor, Dr. Martin Noël, whose exceptional expertise, guidance, and unwavering support have been instrumental throughout my research at the University of Ottawa. Dr. Noël's insightful feedback, constant encouragement, and dedication to my academic and personal growth have profoundly shaped this work. I feel incredibly fortunate to have had the opportunity to learn from him in terms of academic knowledge and personal development.

I am also deeply grateful to my respected co-supervisor, Dr. Liam Butler from York University, for his invaluable guidance and steadfast support. His mentorship has been essential to the success of this research, and I am sincerely thankful for his contributions to my academic journey.

I sincerely thank my committee members, Dr. Miroslava Kavgic from the University of Ottawa and Dr. Bora Pulatsu from Carleton University, for their invaluable guidance and feedback, which were crucial to the successful completion of this research.

My heartfelt appreciation goes to my colleague, Osama Barakat from York University, for his continuous support and collaboration during this research. Working together has been an enriching experience, and I greatly value the shared knowledge and ideas that have contributed to the progress of this project.

I would like to extend my sincere gratitude to IC-IMPACTS for their essential funding, which has been instrumental in advancing this research. Their continued support has been pivotal in the successful completion of this thesis.

My sincere thanks also go to our Indian collaborators, Dr. Durai Prabhakaran and Faizan Habib from IIT Jammu, for their valuable contributions throughout this study. Frequent interactions, idea exchanges, and the sharing of valuable insights throughout regular discussions have significantly enriched the quality and depth of this work.

I would also like to convey my sincere appreciation to the Structures Laboratory in the Department of Civil Engineering at the University of Ottawa for providing the resources and facilities necessary to conduct this research. I am equally grateful to Dr. Muslim Majeed and Dr. Jamal for their collaboration and support during this project.

My gratitude extends to my university batchmates, Issa Fowai, Mohammed Skalli, Rahul Singh, and Abdulla Zahmak, for their unwavering support and assistance, whether through insightful discussions or hands-on help, throughout this journey.

Finally, I express my most profound appreciation to my family, friends, and all those who have supported and guided me throughout this endeavour. Their encouragement and friendship have been an immense source of strength, particularly during the more challenging moments.

This work is dedicated to my parents, Hossein and Maryam, my sister, Mahya, and my supervisors, Dr. Martin Noël and Dr. Liam Butler. Their unwavering belief in my abilities, continuous encouragement, and steadfast support have been the foundation of my academic journey and the driving force behind my perseverance throughout this research.

Table of Contents

List of Figures

List of Tables

List of Abbreviations

BCs	Boundary conditions
BOTDA	Brillouin optical time domain analyzers
BOTDR	Brillouin optical time domain reflectometers
CN	Cyanoacrylate
CZM	Cohesive zone model
DFOS	Distributed fibre optic sensors
EP	Two-part epoxy
EX	Extensometer
FBG	Fibre Bragg grating
FEM	Finite element method
FOS	Fibre optic sensors
FPI	Fabry-Perot interferometer
FRP	Fibre reinforced polymer
GFRP	Glass fibre reinforced polymer
ODiSI	Optical distributed sensor interrogators
OFDR	Optical frequency domain reflectometry
PI	Polyimide
PVC	Polyvinyl chloride
RC	Reinforced concrete
SC	Sand-coated finishing
SERR	Strain energy release rate
SHM	Structural health monitoring
SMF	Single-mode fibre
SP	Spiral finishing
SRAs	Strain reading anomalies
STE	Strain transfer efficiency

List of Notations

Geometric and Spatial Notations

x	Axial distance
r	Radial distance
r_j	Radial distance of the DFOS jacket
r_c	Radial distance of the DFOS core optical fibre
$\boldsymbol{x}$	Relocated position of a layer in the deformed configuration
$\overline{\boldsymbol{x}}$	Relocated position of the adhesive bonding layer in the deformed configuration
S	Shared interface
S_0	Initial surface of the adhesive particle
$\bar{S}$	Adhesive interface occupying a region in the deformed configuration
Ω_h	Defined configuration of the host (substrate) body
Ω_a	Defined configuration of the adhesive bonding layer body
Ω_j	Defined configuration of the DFOS jacket body
$2L$	DFOS bonded length, spanning the segment $-L \leq x \leq L$
L_{eff}	Effective sensing length ($\varepsilon_{DFOS} \geq 0.95\varepsilon_{host}$)
L_{low}	Low-sensing segments ($\varepsilon_{DFOS} \leq 0.95\varepsilon_{host}$)
t_a	Adhesive bonding layer's thickness

Material and Mechanical Properties

K_e	Elastic interfacial stiffness
E	Elastic (Young) modulus
E_a	Elastic (Young) modulus of the adhesive bonding layer
E_j	Elastic (Young) modulus of the DFOS jacket
E_c	Elastic (Young) modulus of the DFOS core optical fibre
G	Shear modulus
G_a	Shear modulus of the adhesive bonding layer

G_j Shear modulus of the DFOS jacket

G_c Shear modulus of the DFOS core optical fibre

ν Poisson ratio

ν_a Adhesive's Poisson ratio

ν_j DFOS jacket's Poisson ratio

α_e^{Δ} Adhesive's elastic displacement transfer ratio

σ Normal stress

σ_h Normal stress in the host (to-be-monitored substrate)

σ_j Normal stress in the DFOS jacket

σ_c Normal stress in the DFOS core optical fibre

τ Shear stress

$\overline{\tau_a}$ Effective shear stress across the shared adhesive interface

τ_j Shear stress across the DFOS jacket

τ_c Shear stress across the DFOS core optical fibre

Strain and Displacement Notations

ε Strain

$\overline{\varepsilon_{EX}}$ Experimental simultaneous EX average strain reading

u Axial displacement

u_h Axial displacement of the host material

u_j Axial displacement of the DFOS jacket

$Z(x)$ Strain transfer coefficient at point x

$Z_{ex}(x)$ Experimental strain transfer coefficient at point x

$Z_e(x)$ Elastic strain transfer coefficient at point x

$Z_p(x,t)$ Perturbed (i.e., plastic/inelastic) strain transfer coefficient at point x

$Z_{th}(x)$ Theoretical strain transfer coefficient at point x

$\boldsymbol{\delta}$ Relative displacement between the adherends across the cohesive adhesive surface

$\bar{\delta}$ Relative axial displacement between the adherends across the adhesive surface

$\bar{\delta}^e$ Relative elastic, axial displacement between the adherends across the surface

$\hat{\delta}$ Incremental relative displacement at the damage tip

Time and Damage Notations

t Time

$q(t)$ Time-dependent damage spatial decay

$L_d(t)$ Damage length

$\dot{K}_{II}$ Stress intensity factor

$\dot{G}_{II}$ Energy release rate

Chapter 1

Introduction

1.1. Background and Problem Statement

Damage in structural components generally refers to any changes in their material and geometric properties that adversely affect their performance. The use of sensors to detect damage in civil engineering structures is often referred to as structural health monitoring (SHM) (Farrar and Worden 2007). SHM systems continuously assess a structure's mechanical properties through the measurement of various damage indicators, enabling the early detection of structural issues, preventing failures, minimizing maintenance costs, and extending the longevity of structures.

Monitoring critical structural damage indicators, such as stiffness variations, crack growth, and changes in environmental or chemical conditions like temperature, humidity, corrosion rate, and pH, is essential for the SHM of reinforced concrete (RC) structures, as extreme values of these parameters can significantly compromise structural integrity and lead to failure (Brownjohn 2007; Fendzi et al. 2016; Sampaio and Maia 2009). Cracks, in particular, are among the most common signs of distress in RC members that can potentially indicate a decrease in the structure's load capacity, stiffness, and durability. Cracks develop for a wide range of reasons, including shrinkage, overloading, temperature variations, and unforeseen events. This issue highlights the importance of SHM of structures for continuous crack assessment of RC members over a period of time (Wang et al. 2001; Abdel-Jaber and Glisic 2016; Zhang et al. 2024a).

In recent years, integrated sensing technologies with permanent installation and the capability of continuously monitoring structural health with remote real-time data have demonstrated effective adaptability to civil engineering structures. Among different types of crack monitoring sensors, fibre optic sensors (FOS), which can steadily monitor strain along RC members and provide strain

peaks corresponding to crack locations, represent one of the most rapidly expanding sensing approaches (Rodríguez et al. 2015; Wang et al. 2019; Berrocal et al. 2021).

FOS are characterized by their high sensitivity and accuracy, small size, durability, and corrosion resistance. The small core optical fibres, through which transmitted light passes and backscatters due to changes in signal intensity caused by variations in strain or temperature within the host material, are typically protected by cladding and one or more outer coatings. These fibres can be integrated internally or mounted on the surface of host materials, e.g. structural members, to monitor strain distribution by analyzing changes in the characteristics of backscattered light. This analysis helps detect shifts in structural parameters and assess crack formation and progression based on strain peaks, enabling timely protective or retrofitting measures to extend the lifespan of the structure (Lopez-Higuera et al. 2011; Zhang et al. 2024b).

Various industries have adopted different types of discrete/localized and distributed FOS technologies. Among the earliest proposed sensing principles, Fibre Bragg Grating (FBG) and Fabry-Perot interferometer (FPI) have been extensively explored across diverse structural materials and attachment methods, making them widely used for local or quasi-distributed optical sensing. However, these FOS systems typically offer discrete measurements, which limits their ability to capture detailed strain variations, locate damage precisely, and assess structural performance between sensing points (Sun et al. 2019; Li et al. 2022).

Compared to conventional FOS systems, distributed fibre optic sensors (DFOS) interrogator technologies that leverage the scattering properties of telecommunication-grade optical fibres with high spatial resolution offer superior performance by treating the optical fibre as a continuous sensor along RC members to visualize strain distribution. This allows for the effective capture of most strain peaks induced by concrete cracks at various locations within the host material under different loading conditions (Gowshikan et al. 2023). DFOS sensing principles are mainly

categorized into Brillouin-backscatter domain and Rayleigh-backscatter domain analysis.

Brillouin-backscatter domain analysis enables long-distance monitoring (kilometres) with lower spatial resolution and larger gauge lengths (tens of millimetres), making it suitable for broad-area coverage where high accuracy is less critical. In contrast, Rayleigh-backscatter analysis provides much higher resolution (down to ~0.63 *mm*) and accuracy over shorter distances (tens of metres), making it ideal for detailed positioning. These distinctions help engineers select the most appropriate DFOS method for specific SHM applications (Sun et al. 2024). For crack detection in RC structures, Rayleigh analysis is generally preferred due to its superior sensitivity to fine strain changes and microstructural damage, which Brillouin systems may not resolve. Optical distributed sensor interrogators (ODiSI), which use optical frequency domain reflectometry (OFDR), rely on Rayleigh scattering, caused by microscopic variations in the fibre's refractive index, to capture distributed strain and temperature profiles (Bassil et al. 2018; Lu et al. 2023).

Despite advancements in signal interrogation technologies and enhanced data logging capacity across both metric and time scales, the accuracy and sustainability of DFOS measurements ultimately rely on the fundamental physical principles that govern the multilayer sensing mechanism. This multilayer mechanism is primarily defined by the integrated sensor configuration, consisting of a central optical fibre sensing core encased in protective buffer coatings (jackets), and the method of deployment within or on the host material, which may introduce additional interfacial and interlaminar interactions. The protective coatings are commonly designed to prevent fracture of the bare core fibre in the service environment, while ensuring optimal adhesion to the host material being monitored (Li et al. 2003).

The strain transfer between the host material and the optical fibre, influenced by differences in stiffness and geometry of intermediate layers along the radial direction, therefore exists and plays a crucial role in the sensing fibre's ability to track strain variations in the host material accurately.

Strain in the host material is transmitted to the core optical fibre, where shear stresses along the interfaces between the bonding agent and the DFOS jacket layers influence the fibre's response, providing a scaled representation of the actual strain (Chapeleau and Bassil 2021). This phenomenon is commonly referred to as shear lag. Therefore, to enhance the efficacy of DFOS monitoring and extend their applications in smart RC structures, there is a need to broaden the exploration of DFOS interfacial interactions and strain transfer mechanics through diverse host materials and loading methods (Yan et al. 2022).

The application of DFOS in SHM of civil infrastructures has faced challenges that limit its widespread adoption. These challenges stem from the delicate nature of optical fibre cables, their complex strain transfer mechanisms, and the novelty of distributed optical sensing technologies, requiring specialized expertise in both installation and data interpretation. To overcome these barriers, numerous experimental and theoretical studies have been conducted, many focused on enhancing the long-term viability of DFOS for monitoring RC structures.

A particularly innovative approach involves embedding optical fibre sensor cables within the RC members at the construction stage. This technique, which involves either embedding the sensing fibres within the reinforcing bars (where feasible, as detailed in the following discussion) or attaching them externally to the bars' surfaces, has proven crucial in enhancing both the durability of the sensing units and the long-term quality and reliability of the obtained data. While the risk of damage to the optical fibres increases during concrete casting, especially in surface-bonded DFOS applications, this approach, by embedding the optical fibres within the concrete matrix for the structure's entire service life, protects the fibres from damage caused by concrete fractures and environmental factors at various stages of concrete performance. This protection enhances data collection reliability by ensuring the long-term stability and accuracy of DFOS measurements, thereby strengthening the ability of DFOS to deliver robust, continuous monitoring of RC structures (Bado et al. 2020; Bado and Casas 2021).

Similar to efforts aimed at enhancing the durability of infrastructure through SHM, fibre reinforced polymer (FRP) bars are increasingly recognized as a superior alternative to traditional steel reinforcement, particularly in environments prone to corrosion and for cost-effective reasons. FRP composites offer notable advantages, including exceptional corrosion resistance, high strength-to-weight and stiffness-to-weight ratios, and reduced long-term maintenance costs. These properties make FRP bars highly effective in extending the longevity of RC structures (AlNajmi and Abed 2020). Additionally, by highlighting their durability and resistance to environmental degradation, FRP bars can further provide robust protection for integrated optical fibres in DFOS-instrumented reinforcement due to minimized risk of deterioration in the host material. In this context, another key benefit of FRP bars is the feasible option to internally embed optical fibres within the host material, an approach that is particularly effective for composite materials like FRP and not viable with traditional steel reinforcement (Tang and Wu 2016)

The internal integration of optical fibres within the host material involves embedding them, whether coated or uncoated, into the composite matrix during the manufacturing process. In the case of FRP rods, this integration typically occurs during the pultrusion process, a widely used method for manufacturing FRP materials. The pultrusion process involves pulling continuous reinforcing fibres, such as glass or carbon, through a resin bath before passing them through a heated die, where the resin-saturated fibres are shaped into their final rod form. At the entrance of the die, the optical fibre embedment stage can be strategically introduced, allowing the fibre optic sensor cables to be incorporated alongside the structural fibres within the composite matrix. This can ensure proper alignment, protection, and seamless integration into the final product (Kalamkarov et al. 1999; Wang et al. 2009; Vemuganti et al. 2020).

To enhance the long-term performance of RC infrastructure in harsh Canadian environments, glass fibre reinforced polymer (GFRP) bars are increasingly adopted as an alternative to corrosion-susceptible steel reinforcement in construction applications. GFRP bars offer improved durability,

a high strength-to-weight ratio, and enhanced cost-efficiency, while also contributing to a reduced carbon footprint compared to other FRP composites.

Despite their advantages, these composites exhibit a relatively low elastic modulus, resulting in significantly higher strains than steel under similar stress levels. This, in turn, leads to wider cracks and greater deflections in GFRP-RC members during service conditions. Therefore, the high strength of GFRP reinforcement is generally not fully utilized in field applications, and serviceability conditions tend to govern the design of GFRP-RC members. Furthermore, elevated temperatures can cause the resin to decompose or soften, thereby reducing the mechanical properties of GFRP bars and potentially compromising their structural integrity. Sufficient concrete cover is crucial to protect them in fire exposure situations (Benmokrane et al. 2004; Qureshi 2022; Sbahieh et al. 2023; Gouda et al. 2023).

While GFRP reinforcing bars may exhibit limitations in fire resistance and ductility when compared to steel, their corrosion-resistant durability plays a critical role in maintaining both RC members and integrated optical fibre sensors, whether embedded internally within the GFRP core during pultrusion or bonded externally to the bar's surface. The unique combination of the aforementioned properties makes GFRP bars ideal for developing multifunctional composites, either through self-sensing capabilities via embedded optical fibres or by instrumenting them with surface-bonded DFOS, thus enhancing SHM management and advancing smart infrastructure.

The development of self-sensing reinforcing FRP bars with internal sensor embedment has evolved mainly across localized optical interrogating techniques, such as FBG and FPI. In contrast, the instrumentation of reinforcing bars with surface-bonded DFOS, particularly those monitored by OFDR-based interrogators, has recently garnered increased attention as a more practical SHM solution due to its ease of implementation and additional advantages (Falcetelli et al. 2020). The surface-bonded technique can surpass internal embedment by enabling the instrumentation of the

entire reinforcement cage with a single, continuous sensor cable. This method can effectively simplify installation, reduce system complexity, and ensure uniform strain measurement for quasi-real-time SHM, while eliminating the need for multiple data acquisition channels.

Given that current research predominantly focuses on using steel bars as the substrate for strain and crack monitoring with surface-bonded DFOS, the effectiveness of OFDR-based DFOS bonded to the surface of GFRP reinforcing bars remains underexplored. The field implementation of these multifunctional composites is still in its early stages of development. It lacks the necessary 'instrumental maturity,' a term that refers to the current limitations of integrated sensing technologies, which numerous studies and projects within the research focus are actively working to overcome (Bado and Casas 2021). In particular, a notable knowledge gap remains concerning strain transfer and monitoring capability under a wide range of strain levels and loading conditions.

Furthermore, numerous studies on the application of DFOS in civil engineering emphasize the need for a more comprehensive understanding of the strain transmission behaviour and the long-term monitoring stability of the multi-layered sensing systems involved. In this study, the term "sensing system" is used to describe the layered configuration comprising the host material, intermediate layers, including protective coatings and bonding agents (e.g., adhesives), and core optical fibre. Few studies have investigated this topic, and those available have mainly focused on monitoring the host GFRP under monotonic increasing loads, which may not reflect worst-case, long-term scenarios involving dynamic and sustained stresses.

On the other hand, in the context of surface-bonded DFOS, inelastic shear deformations of the adhesive and potential degradation of interfacial efficiency at the sensor–host interface have not been sufficiently explored. This issue is particularly relevant when instrumenting GFRP reinforcing bars, which exhibit substantial strain variation under load due to their unique stiffness properties. A comprehensive analysis of dynamic interfacial interactions and DFOS strain transfer

mechanics, accounting for these factors, is insufficiently addressed in the existing literature. Moreover, GFRP bars possess distinctive properties and surface features that impact interfacial adhesion of DFOS and influence interfacial strain transition behaviour and sensor readings.

This study aims to bridge the knowledge gap through a comprehensive experimental and numerical investigation of DFOS performance when adhesively bonded to unidirectional GFRP reinforcing bars under various loading conditions, thereby advancing SHM for RC structures.

1.2. Objectives and Scope of Research

This research comprises a unified experimental and analytical analysis to develop a deeper understanding of OFDR-based DFOS-bonded GFRP reinforcing bars, contributing to new applications in smart, sustainable GFRP-RC infrastructure with improved environmental resistance and effective crack and strain monitoring during service life.

The experimental program involved a series of uniaxial tension tests on fabricated DFOS GFRP bar specimens, each incorporating a uniquely designed sensing system. Key parameters, including bar size, bar surface characteristics, sensor installation method, DFOS coating and adhesive types, as well as loading conditions and histories, were systematically varied to assess long-term performance in distributed strain measurements under diverse conditions. The analytical program involved the numerical implementation of a closed-form analytical model developed in this study to simulate strain transfer mechanics across both elastic and plastic response regimes of the adhesively bonded sensor–host interface, thereby enabling the identification of bondline degradation and interfacial failure modes under severe loading conditions.

In this study, interfacial failure is defined as a permanent change in the adhesive bond interface response due to loading exceeding its yield (or critical bond) strength, resulting in progressive loss of interfacial cohesion along the DFOS bonded length. Although strain transfer to the optical fibre

may still occur, the accuracy of DFOS strain measurements is significantly compromised.

The scope of the research, briefly, was to fulfill the following objectives:

1) Examine the monitoring efficacy of OFDR-based DFOS bonded to the surface of GFRP bars by focusing on the impact of different DFOS deployment layouts and evaluating signal integrity, fidelity, and strain transfer efficiency and consistency under varying uniaxial tension stress levels, conditions, and histories in laboratory settings

2) Develop a refined closed-form analytical model of elasto-plastic strain transfer, particularly through the adhesive bondline, to predict and verify distributed strain data monitored by surface-bonded DFOS, establishing a framework for numerical analysis of dynamic reliability assessment of DFOS measurements and providing a foundation for future modifications, guidelines, and recommendations for DFOS on GFRP bars

Ultimately, the goal was to identify and generalize key opportunities and challenges in the performance of DFOS-bonded GFRP bar systems for strain monitoring. Opportunities include defining the potential range for stable and effective data logging without triggering sensor–host interfacial degradation. Challenges include shear lag effects that impact measurement accuracy, degradation of the adhesive bondline, and signal loss under elevated strain conditions, all of which may compromise the system's long-term effectiveness.

1.3. Thesis Organization

This thesis comprises six chapters, beginning with an introduction to the research topic, its objectives, and the key factors driving the research. Chapter two provides a literature review on the developments, applications, techniques, and mechanics of DFOS in SHM projects, focusing on the uses inside RC members attached and integrated into reinforcing bars. Chapter three describes the experimental program, including uniaxial tension test specimens, procedures, and

instrumentation, as well as the theoretical methodology for studying DFOS strain transfer mechanics. The outcomes of the laboratory tests are covered in chapter four, and chapter five focuses on the parametric analyses and quantitative correlations of experimental and numerical results, including the implication of the refined strain transfer model on strain data obtained from different test DFOS GFRP bar samples. The final chapter summarizes the main results, compares the observations of different investigated parameters, and provides conclusions and recommendations for future research and implementations.

Chapter 2

Literature Review

2.1. General

This chapter presents a comprehensive review of state-of-the-art DFOS technologies used as integrated SHM units, focusing on a range of theoretical, experimental, and field studies in civil engineering. It examines DFOS applications for strain and crack monitoring, sensor strain transfer mechanics, and common attachment techniques, with particular emphasis on recent innovations in integrating DFOS to reinforcing bars. The chapter also reviews FRP composite materials as highly suitable hosts for embedding FOS, especially in the reinforcement and strengthening of concrete structures monitored using these sensors. By analyzing installation techniques, mechanical and sensing principles, and host packaging materials used in DFOS-based SHM projects, the chapter highlights key advancements, current challenges, and future considerations for deploying DFOS within reinforcing bars in RC members for strain and crack monitoring.

2.2. SHM and DFOS

2.2.1. SHM Sensors Development

SHM has become crucial due to the aging infrastructure, particularly bridges designed for 50–80–year design lives, which are now facing heightened risks. Environmental impacts, such as pollution, natural hazards, and increased structural demands, like heavier traffic loads, push structures beyond their originally intended design parameters. SHM enables engineers to understand how structures behave under various conditions, including seismic activities, as well as monitor structural and environmental changes (Pellegrino et al. 2022).

Conducting a complete SHM project for RC structures involves several steps, from initial planning and instrumentation to data collection for detection, localization, quantification, and final

evaluation of damage. Monitoring parameters, encompassing defects, cracks, deformations, displacements, stresses, strains, loads, pressure, pH, humidity, chemical penetrations, and temperature variations, accelerates identifying and assessing damage intensity and causes. Specifying desired key monitoring parameters, measurement accuracy and resolution, and instrument protection and maintenance requirements is necessary to select the appropriate testing methods for assessing and detecting existing potential issues (Taheri 2019).

A wide range of physical effects is considered in assessing potential damage in RC structures. Instrumentation in civil engineering refers to the deployment of various measurement devices within or on a structure to collect data on different physical parameters, permanently or periodically, for function monitoring applications. SHM systems are crucial for assessing the structural performance of an RC member, providing real-time data on its physical and mechanical properties. Using data-driven or model-based techniques, they analyze damage indicators, quantifiable metrics that help evaluate specific damage characteristics (Azimi et al. 2020).

In the historical context, SHM methods have traditionally been categorised into two distinct groups: destructive and non-destructive. However, many traditional manual methods are costly and labour-intensive, lacking the capability for continuous health monitoring. This limitation has driven the integration of smart sensors. Continuous monitoring of RC member attributes is instrumental in estimating degradation rates and assessing structural functionality in real time. With advances in sensor technology, communication and conversion components, signal and data processing units, and AI-driven systems, modern SHM has evolved into a more sophisticated and automated approach, moving beyond manual inspections. This multidisciplinary framework enables instant and predictive damage assessment, supporting maintenance strategies based on loads, conditions, and defects, and enables data-driven evaluations of structural function and strength in compliance with safety standards and regulations (Kralovec and Schagerl 2020; Hassani and Dackermann 2023; Altabey et al. 2023).

These innovative integrated sensing technologies have transformed instrumentation in civil engineering by combining advanced sensors, data acquisition systems, and analytical tools into a unified framework. This transformation has enhanced SHM management by enabling engineers and researchers to better assess the performance of concrete infrastructure. In recent years, several integrated sensing technologies have been employed and refined to achieve more accurate data and reliable health assessments, supported by advances in technologies such as piezoelectric sensors, strain gauges, wireless sensor networks (WSN), and optical fibre sensors (Lynch 2006; Tomlinson and Bullough 1998; Zhang et al. 2021a).

Piezoelectricity, pioneered by the Curie Brothers in the early 1880s, has found diverse applications (Curie, J. and Curie, P. 1880). These sensors convert mechanical stress into electrical signals, enabling the detection of vibrations, pressure, and structural changes within concrete members (Dumoulin et al. 2014). Piezoelectric sensing technology offers high sensitivity and versatility across various applications, particularly SHM and dynamic response analysis.

However, it has material-related limitations. Ceramics like Lead Zirconate Titanate (PZT) are stable and efficient but raise environmental concerns due to their lead content. Barium Titanate (BaTiO3) shows good piezoelectric properties but is temperature-sensitive and less efficient. Additionally, design flaws like water solubility in certain crystals and temperature sensitivity can cause inaccuracies in structural condition indicators. Addressing these challenges is crucial for enhancing piezoelectric sensing technology (Aksel and Jones 2010; Ihn and Chang 2004).

Strain gauge sensors are ever-present in conventional civil engineering sensing systems, providing precise measurements of material strain. These sensors are favoured for their cost-effectiveness and ease of installation and benefit from a wealth of knowledge accumulated over time for interpreting strain data. Strain gauges offer precise, point-specific measurements, making them ideal for monitoring critical locations with expected high deformation or stress concentrations.

Nonetheless, their limitation to localized measurements can leave gaps in data, potentially missing important strain variations or structural issues between the measured points. Additionally, scalability is challenging for large-scale monitoring, as each strain gauge requires separate wiring to a data acquisition system, resulting in complex wiring and data management (Choi et al. 2008).

WSNs comprise interconnected nodes and platforms strategically positioned throughout a structure. These sensors collect continuous real-time data on various parameters, including temperature, humidity, strain, and corrosion. Upon integration with structural components, each node provides local information, while the system's interconnected nature allows it to cover a large area and assess the health status of the entire structure. These sensors feature advanced capabilities, including the ability to recharge using inductive power transfer modules wirelessly. This is made possible by integrating an ultra-low power configuration, ensuring consistent and efficient data collection and analysis without compromising the energy needs of the sensor nodes. Nevertheless, the placement of discrete sensors limits the spatial resolution of measurements, and there are challenges related to energy consumption, battery replacement, susceptibility to environmental factors, cost, communication delays, node failures, and data loss issues (Gallucci et al. 2017).

Point-based fibre optic sensors (FOS), such as fibre Bragg grating (FBG) sensors, are widely used in SHM for measuring strain, stress, temperature, and pressure at specific locations along an optical fibre. With diameters under 2 *mm*, optical fibres can be embedded in areas inaccessible to conventional sensors like strain gauges or thermocouples, detecting physical changes through intensity modulation or optical interference. FBG sensors operate via periodic refractive index variations over short segments (typically ~10 *mm*), creating Bragg reflectors that return specific wavelengths. Multiple reflectors can be multiplexed along a single fibre, enabling quasi-distributed sensing (Seo et al. 2020). However, covering large areas or long structures with FBGs requires multiple units, increasing installation complexity and leaving data gaps between sensing points.

To overcome these limitations, distributed fibre optic sensors (DFOS) were developed to provide continuous, high-resolution measurements along the entire fibre length. DFOS surpasses traditional point-based sensors, including FBGs, strain gauges, and LVDTs, by offering wider coverage, simplified installation, and lower maintenance requirements (Davis et al. 2017). These advantages make DFOS particularly suited for large-scale SHM. However, fully realising their potential, especially for detecting narrow, localized cracks, requires addressing current technical limitations to ensure accurate capture of detailed strain variations at fine spatial resolutions.

2.2.2. DFOS Applications

The introduction of optical fibre technology in the 1970s represented a significant leap forward in global communications. The innovation of low-attenuation optical fibres enabled high-bandwidth and long-distance communications, leading to extensive global deployment by 2000. This advancement paved the way for developing fibre-based optical processing devices, enhancing processing quality by minimizing insertion losses (Hill et al. 1978). Optical fibres have extended their utility well beyond telecommunications, emerging as key components in a wide array of distributed sensing applications, most notably in aeronautics, aerospace, civil engineering, biology, and environmental monitoring.

A market survey, reported by the Photonic Sensor Consortium and published by Information Gatekeepers, provides a comprehensive overview of the growth of the DFOS technologies market. Drawing on a market chart spanning the past two decades, the report illustrates a significant increase in the FOS technologies market, particularly in Rayleigh-backscattering domain-based sensing technology. The market investment was estimated to be over USD 1.3 billion in 2023, as depicted in **Figure 2-1** (Information Gatekeepers 2019). This market growth trend reflects the increasing application and effectiveness of DFOS technology across various industry sectors, including civil engineering and infrastructure for SHM to ensure optimal structural performance.

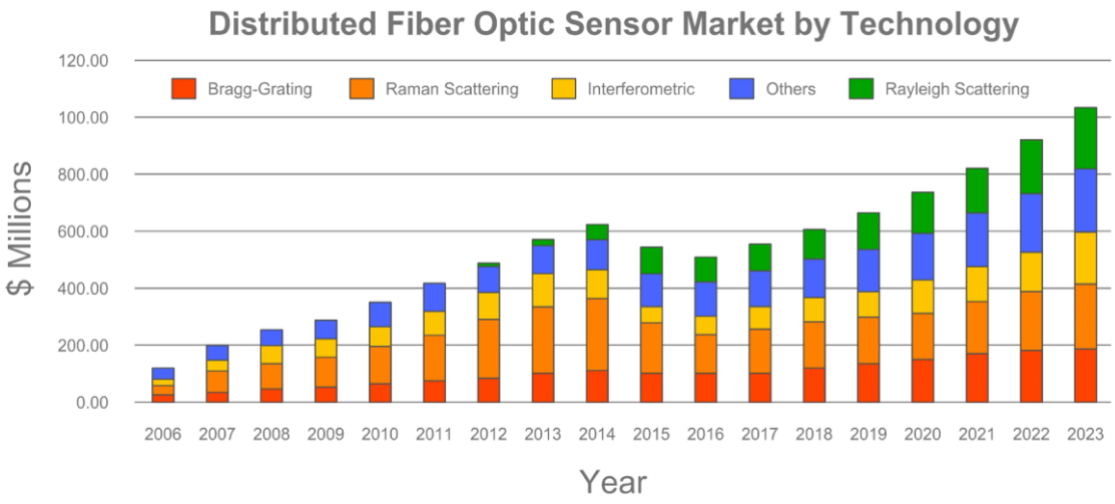

Figure 2-1. Growth of the DFOS technological market reported by the Photonic Sensor Consortium (Information Gatekeepers 2019)

In today's infrastructure, integrating sensing systems to enhance repair plans by enabling more precise maintenance through permanent SHM is essential. FOS offer beneficial performances in SHM applications, characterized by their compact dimensions, lightweight nature, lack of reliance on remote electrical power, immunity to electromagnetic interference, non-conductive properties, and capacity to withstand high temperatures.

An optical fibre is a cylindrical structure composed of three layers, typically made from glass to guide light. The inner core fibre, the main sensing component with a specific refractive index, is surrounded by a cladding layer with a lower refractive index and is commonly protected by outer jackets for durability and flexibility in various applications. The jacket can be made from materials such as Polyvinyl chloride (PVC), polyimide (PI), polyethylene, or a steel wire-reinforced ribbon strain cable featuring dual steel wires.

Optical fibres, categorized as multi-mode or single-mode, can function as multiple sensors at scattering points, responding to strain or temperature changes by transmitting a coherent signal and analyzing the backscattered light, which contains information about the core fibre's internal characteristics, as shown in **Figure 2-2** (Bao and Chen 2012).

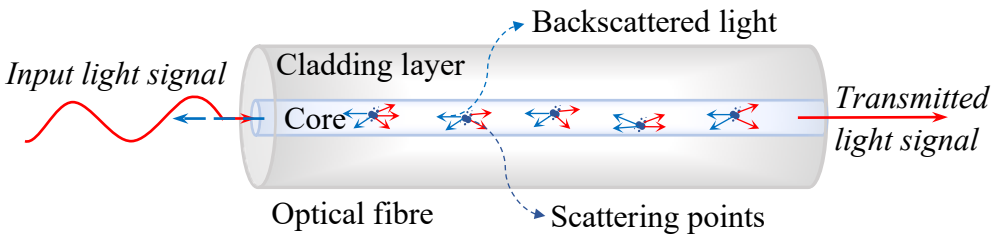

Figure 2-2. Schematic of light scattering in an optical fibre, adapted from Bao and Chen (2012)

Distributed optical sensing technologies generate strain and temperature measurements by performing an operation between the reference state, where the optical fibre remains in its baseline condition constantly with no distribution, and the perturbed state, where strain or temperature variation is applied to the fibre and alterations in the backscattering refractive index along the fibre is caused to find a spectral shift or time delay in the correlation peaks. The deployment of DFOS in various field and experimental settings has demonstrated the technology's efficacy in delivering real-time and continuous SHM through high-resolution strain and temperature monitoring, achieved by multiplexing numerous sensors along structural members (Ding et al. 2018).

The Luzzone Dam SHM Project is a notable example of Brillouin backscattering domain-based DFOS technology, where sensing cables were installed in a serpentine pattern during concrete pouring for temperature monitoring, demonstrating the feasibility of acquiring numerous measurement points using relatively simple sensors. The Bitumen Joint Monitoring Project exemplifies remote pre-warning SHM with DFOS, monitoring average strain near joints of the 40-year-old Plavinu dam. Similarly, the Italy Gas Pipeline Monitoring Project confirmed DFOS effectiveness for monthly strain and temperature monitoring along a 500-metre section of a 35-year-old buried gas pipeline, providing deformation data and simulating gas leakage with a spatial resolution of 1.5 metres after two years (Inaudi and Glisic 2005).

DFOS sensing technologies have also been widely applied in bridge SHM. The SHM of Nine Wells Bridge in Cambridge, UK, is a notable project that demonstrates the successful

implementation of Brillouin backscattering domain-based DFOS monitoring. The project involves instrumentation of six concrete beams of the bridge with SHM units to observe the long-term structural behaviour by detecting mechanical strains and temperature-induced strains. The project's findings indicated that the measured creep and shrinkage-induced strains closely aligned with two different analytical models (Webb et al. 2017).

The Sarajevo Bridge Monitoring Project in Barcelona, Spain, serves as another successful application of the DFOS system, effectively tracking the stresses induced in prestressed concrete box girder beams during deck enlargement activities. Observations revealed that excessive stresses were not transferred to the concrete during construction (Barrias et al. 2018a).

In addition, a DFOS system using Brillouin backscattering domain analysis was chosen for the crack visualization of the Götaälv bridge in Gothenburg, Sweden, after finding several cracks in the steel girders from 2007 to 2009, followed by a one-year trial period. The bridge spans 1000 metres and comprises a concrete slab supported by nine steel girders resting on over 50 columns. Consequently, a distributed sensing technology was required to cover the entire bridge length, enabling the detection of cracks at any location (Barrias et al. 2016).

A comprehensive study by de Battista et al. (2017) on the SHM of the Principal Tower in London, UK, utilized long-term Brillouin backscattering domain-based DFOS fixed to the reinforcing bars of its columns and core walls before concrete pouring. The primary objective was to assess the collective structural shortening from superimposed load, creep, and shrinkage during construction. The DFOS enabled continuous distributed measurements of axial deformation throughout the process, providing invaluable insights for structural appraisal and essential guidance for installing finishes and partitions on lower floors.

A recent paper by Zhang et al. (2024c) presents a comprehensive review of DFOS for monitoring underground tunnel infrastructure deformation, demonstrating their advantage over conventional

methods with cost-effective, high-density monitoring. They guide the selection of optimal configurations, including sensor types and interrogator systems, and note that signal loss and fibre installation quality are assessed based on attenuation and bending. The study highlights the importance of fibre protection and repairability, emphasizing that DFOS cables embedded in concrete during construction, like those attached to reinforcement cages, are more vulnerable to damage and more challenging to replace than those installed post-construction.

2.2.3. DFOS Strain and Crack Monitoring Techniques

The promise of multiplexing schemes among optical fibre cables has become a pivotal technology in strain and crack monitoring, providing continuous, high-resolution data over extensive lengths of structures and allowing for detailed and comprehensive structural assessments. These multiplexing arrangements include the division of optical wavelength, frequency, travel time, and spatial or coherence-domain multiplexing. Often used in combination, these methods extend point-based sensors on a fibre-optic network, enhancing measurement capabilities while reducing costs.

Advancements in optoelectronics and fibre-optic communications have driven down the cost of optical components, enabling the widespread use of long-length fibres in remote and distributed sensing applications. Modern DFOS systems utilise optical scattering phenomena, namely Rayleigh, Brillouin, and Raman scattering, to detect local external perturbations such as temperature and strain. These systems operate by analysing changes in the amplitude, frequency, polarization, or phase of the backscattered light.

Light scattering in optical fibres is a random statistical process that occurs in all directions. In DFOS scattering domains, the terms “pump” and “probe” beams refer to two types of continuous waves (CW) used to induce and measure scattering effects within the fibre, respectively. Both beams propagate bidirectionally through the sensing fibre and are reflected at the far end, enabling precise detection and analysis of strain or temperature variations (Bao and Chen 2011, 2012).

The frequency spectrum of scattered light includes Rayleigh, Brillouin, and Raman scattering, as shown in **Figure 2-3**. Rayleigh scattering, marked by a central peak at the incident light frequency, arises from non-propagating material-density fluctuations and causes spectral broadening without a central frequency shift, making it an elastic scattering process. Brillouin scattering, located adjacent to the Rayleigh peak, is caused by light interacting with propagating acoustic phonons, while Raman scattering results from light scattering off molecular vibrations or optically generated phonons and is used exclusively as a temperature transducer (Fernandez et al. 2005).

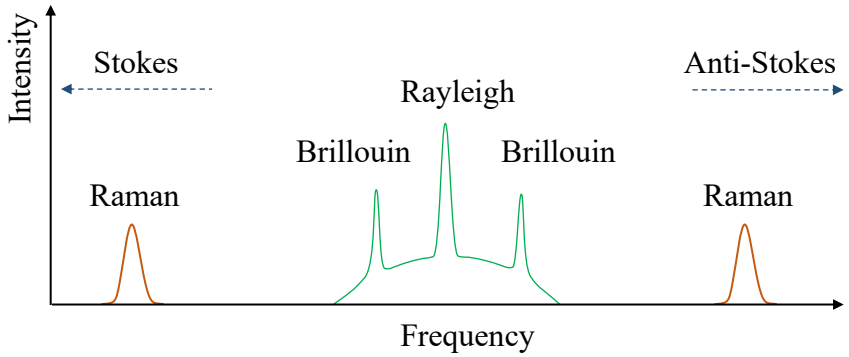

Figure 2-3. Rayleigh, Brillouin, and Raman scattering, adapted from Lu et al. (2019)

Both Brillouin and Raman scattering are inelastic due to the frequency shift between the incident and scattered light. Scattering that shifts to lower frequencies than the incoming photons is known as the Stokes component, and scattering that shifts to higher frequencies is the anti-Stokes component. These scattering mechanisms provide the basis for DFOS technologies, enabling detailed measurements of temperature and strain along the optical fibre (Bao and Chen 2012; Lu et al. 2019). For strain monitoring aims, the precision of measuring Brillouin frequency shifts remains limited. This constrains the spatial resolution of Brillouin scattering domain to a minimum of around one metre and limits the maximum contribution of the sensor system.

Rayleigh backscattering offers high spatial resolution in measurements due to its intrinsic reliance on the naturally occurring scattering of light along the fibre, unlike Brillouin scattering, which

requires a broader interaction region to analyze frequency shifts associated with acoustic phonons, leading to lower spatial resolution (Alasia et al. 2005; Niklès et al. 1996; Zeringue et al. 2012). Rayleigh scattering occurs when light encounters particles significantly smaller than its wavelength, such as atoms or molecules in a homogeneous medium. This phenomenon arises from impurities present in the core fibre, combined with density and compositional inconsistencies embedded in the fibre's structure during fabrication. These irregularities persist as the temperature cools from the glass softening point to room temperature and cannot be eliminated, despite the use of advanced manufacturing techniques. Consequently, Rayleigh scattering persists with the lowest loss level of approximately 0.2 *dB/km* in single-mode fibres (SMF) (Li 2017).

The inherent Rayleigh scattering in standard single-mode fibres, originally designed for fibre optic communications, is highly beneficial for optical fibre sensing, acting as a tracer to transmit measured information. Strain or temperature changes alter the optical path between tracers due to physical elongation, thermal expansion, and photo-elastic effects, causing a relative wavelength shift. Similar to FBG sensing, this enables precise detection of strain and temperature variations. Since Rayleigh scattering takes place in the backward direction within the fibre, it is feasible to conduct detection in the backward mode, which is crucial in the context of optical fibre sensing. Nowadays, DFOS interrogators provide direct calculation of spectral shift, $\Delta\upsilon$, through $\Delta\upsilon/\upsilon = K_T\Delta T + K_\varepsilon\varepsilon$, where K_T and K_ε are the temperature and strain calibration constants.

Early DFOS systems primarily used optical time domain reflectometry (OTDR) in Rayleigh-based interrogators, relying on return time at the fibre input. This laid the groundwork for advancements despite the low spatial resolution (about one metre) provided by a short, high-power laser pulse. Subsequent innovations, such as optical frequency domain reflectometry (OFDR), improved the sensitivity, spatial resolution, and range of DFOS systems.

In OFDR sensing systems, a tunable wave light source produces narrow linewidth light with swept

wavelengths. This light is divided by directional couplers into a pump optical beam and a probe beam, corresponding to the signal travelling through the fibre under test (FUT). The probe beam interacts with the medium, and the backscattered light from this interaction then interferes with the reference beam. A photodetector captures the resulting interference pattern, also known as a beat signal. As the laser wavelength or frequency (υ) is swept, the photodetector records the variations in optical intensity by measuring the detected optical intensity of the backscattered light at different frequencies along the fibre through a fast Fourier transform (FFT) algorithm as a function of time.

OFDR can precisely locate and quantify changes in the scattering pattern induced by the perturbation and translate them into strain and temperature measurements using proper calibration coefficients. The FFT algorithm efficiently computes the discrete Fourier transform (DFT) and its inverse, the most widely used transform in digital signal processing. The DFT maps $x(t)$-series into the frequency domains, $X(\upsilon)$. The result of the FFT is a complex number that provides both amplitude and phase information for each frequency component. The intensity of frequency components in the original time series can be determined by analyzing the magnitude of these complex numbers. The magnitude of the FFT output (optical intensity) is typically plotted against frequency to show the frequency spectrum of the optical intensity signal, as shown in **Figure 2-4**.

The spatial resolution of OFDR sensing technology depends on the laser's optical frequency sweep range and the precision of the FFT. OFDR technology measures temperature change in the absence of strain using $\Delta T = -(\bar{\lambda}/cK_T)\Delta\upsilon$, where $\bar{\lambda}$ is the centre wavelength of the scan, and similarly, strain in the absence of a temperature change using $\varepsilon = -(\bar{\lambda}/cK_\varepsilon)\Delta\upsilon$ (Froggatt and Moore 1998; Rao et al. 2010; Palmieri 2013; Li 2017).

A novel approach involves utilizing DFOS not merely as conduits for data transmission but as sensors capable of capturing information. This concept transforms the optical fibre into a highly sensitive device with numerous measurement points, enabling the acquisition of data along its

length to detect, locate, and quantify damage in monitored structures with high precision and efficiency. The post-processing of strain profiles of RC members extracted from DFOS is crucial for effective crack visualization and quantification. This process involves several key steps, starting with the initial filtering and smoothing of raw data to eliminate noise and enhance signal clarity. Cracks cause local strain peaks and redistribution in the DFOS strain curve, as illustrated in **Figure 2-5**. Hence, strain anomalies indicative of potential cracks can be identified and isolated. Advanced analytical techniques are then employed to map these anomalies, allowing for precise localization and characterization of cracks. The final step involves quantifying the extent and severity of the identified cracks, providing valuable insights into structural health and integrity.

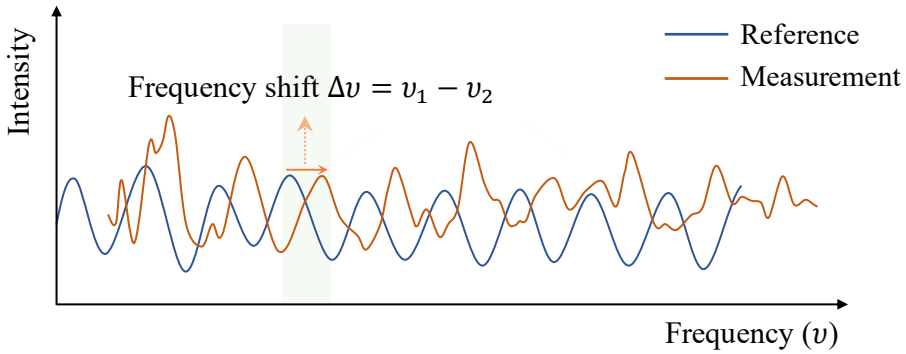

Figure 2-4. OFDR principle for strain measurement, adapted from Palmieri (2013)

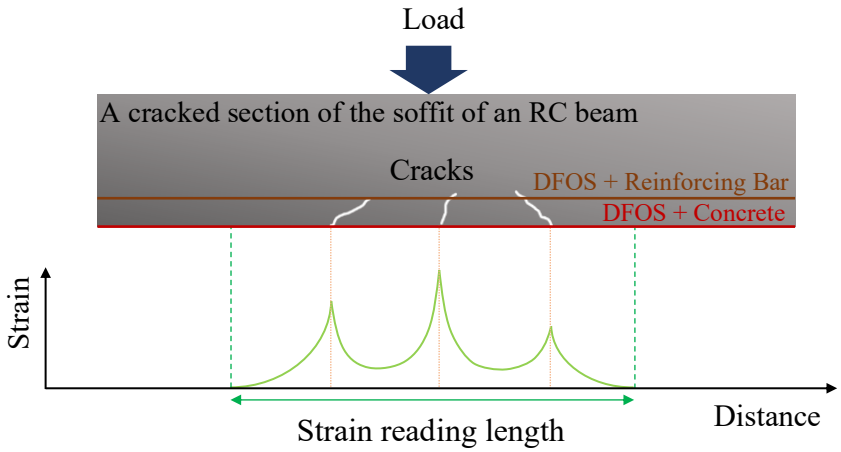

Figure 2-5. Theoretical schematic of DFOS-based crack monitoring in RC beams, adapted from Tan et al. (2021a)

Enhancing the spatial resolution in DFOS enables the measurement of strain over smaller optical fibre segments. This capability is crucial for accurately assessing strain distribution, particularly in the vicinity of cracks where strain can exhibit rapid changes over short distances. A low spatial resolution results in the averaging of strain over a larger segment, potentially overlooking strain variations. Thus, an inaccurate portrayal of strain distribution may occur, as abrupt changes related to crack formation could be obscured or left undetected. For example, a substantial local strain variation caused by a crack might not be distinctly identifiable by a low-resolution sensor, given its tendency to average strain over a wider area, potentially encompassing regions devoid of strain changes. In contrast, a finer spatial resolution, such as the 0.63 *mm* achieved through Rayleigh domain-based technologies, enables more detailed measurements. This heightened resolution facilitates the precise capture of sharp strain gradients around cracks, thereby offering a more accurate assessment of the presence, dimensions, and progression of cracks (Tan et al. 2021a).

When DFOS are directly bonded to a concrete surface, the optical fibre cable must accommodate local interfacial slip and outer layer deformation, typically of lower stiffness, to prevent fibre rupture and maintain compatibility with crack-induced displacement over a span of several centimetres. In such cases, DFOS registers a sharp strain peak at the crack but does not reflect the actual concrete surface strain nearby, which drops to zero. Conversely, when DFOS is attached to internal reinforcement, peak strain values align with changes in the host material's tensile stress. As cracks form, concrete loses its ability to carry tensile stress, reducing the cracked section's moment of inertia and increasing local strain in the reinforcement. This localized strain rise enables DFOS to identify crack locations and estimate crack widths through the strain distribution along the transfer length, as shown in **Figure 2-5** (Berrocal et al. 2021a; b).

A study presented by Brault et al. (2019) investigates the efficacy of DFOS for in-situ crack monitoring of RC elements under load testing during the construction of the Rideau Centre Expansion in Ottawa, Ontario, Canada. By utilizing DFOS and linear potentiometers to monitor

two beams and a drop panel subjected to loads from six scissor lifts (average weight of 12.9 kN each), the research demonstrated the precision and utility of DFOS in capturing strain measurements with an accuracy of approximately 1 $\mu\varepsilon$. The ability of DFOS to detect both positive and negative bending strains allowed for detailed analysis of the elements' inflection points, providing valuable insights into support conditions and moment transfer dynamics. Crack quantification using the DFOS strain curve of reinforcing bars was the subject of an experimental investigation by Brault and Hoult (2019) involving nine DFOS steel-RC beam tests. The study presented a viable approach for measuring tension stiffening and reinforcement strains at all crack locations, while also comparing different crack width estimation methods. By plotting reinforcement strains at crack sites against crack widths, the researchers were able to demonstrate a strong correlation between a theoretical model for crack size and experimental data.

2.2.4. DFOS Strain Transfer Mechanics

While DFOS data logging capabilities have improved significantly, the effectiveness and durability of sensing units depend on the inherent physical properties of their multilayer sensing structures. Bare optical fibres need a softer protective coating that can withstand compaction pressure during DFOS implementation and the service life monitoring of structural components. Interpreting strain measurements from buffered optical fibres is then complex, as the core fibre is typically coated with protective jackets and embedded or bonded to a host material. The interaction between these layered materials significantly influences strain transfer, with differences in their stiffness and geometry across applications make understanding strain transfer essential for accurate measurements in SHM (Alexander et al. 2012; Wang et al. 2019).

Shear-lag theory was initially developed to describe stress transfer in composite materials, such as between fibres and matrices in fibre reinforced composites (Cox 1952). Its principles have been adapted to study strain transfer in optical fibre sensors. The theory models the strain transfer from

a deforming substrate to the embedded or bonded optical fibre via only interfacial shear stresses. A paper by Claus et al. (1989) provides a summary of research that had been done on FOS strain transfer mechanics over the past 10 years before 1989 and concludes with an examination of the lifecycle behaviour of embedded optical fibres, emphasizing how the coating on the fibres plays a crucial role in the efficiency of the strain transfer process.

Since the early days of fibre optic sensing, when FBG sensors embedded in composites were prevalent, numerous studies have investigated different host materials, configurations, and loading methods. These efforts focused on understanding interfacial interactions and strain transfer mechanics within FOS systems, aiming to optimize intermediate layers for more accurate strain transfer to the core fibre. For instance, Pak (1991) investigated strain transfer efficiency in optical fibres embedded within a host matrix, noting that due to stiffness mismatches and shear stresses, the strain transferred to the fibre may differ from the host material's strain. The study found that optimal strain transfer occurs when the coating's shear modulus matches the geometric mean of the fibre and matrix shear moduli.

LeBlanc et al. (1996) studied how strain gradients, typically found in non-uniform strain environments or near cracks, affect the reflected spectra of FBG sensors, reporting measurement resolution of 0.8 *mm* for a 5-*mm* grating. They found that such gradients cause spectral broadening or splitting, since various parts of the grating reflect light at different Bragg wavelengths. These phenomena must be accounted for to avoid misinterpretation of strain transfer data. Around the same time, Ansari and Libo (1998) introduced a shear lag parameter to improve the interpretation of actual host strains captured by FOS. Their model, evaluated on sensors bonded parallel to the strain direction, includes the mechanical and geometrical effects of the intermediate layers.

LeBlanc (1999) contributed analytical and numerical models to describe strain transfer mechanics and interfacial failure in single-ended FOS setups, which were experimentally verified using FBG

and Fabry–Perot interferometer (FPI) interrogators. Further developments came from Li et al. (2002), who proposed a more realistic strain transfer formulation for interferometric FOS embedded in concrete mortar by incorporating elasto-plastic properties of the soft coating around the glass core, especially relevant under large deformations from concrete cracking.

Continuing this line of research, Li (2006) derived an analytical model to calculate average strain transfer rates in FOS embedded within a host and middle layer, introducing the concept of a critical adherence length. Later, Li et al. (2009a) provided a framework to predict strain transfer for embedded FBG sensors and showed that fibre midpoint strain measurements may not represent host strain unless a minimum bond length is met. More recently, Wang and Xiang (2016) developed numerical models for Brillouin optical time domain analyzer (BOTDA) systems, focusing on fibres embedded in asphalt. They used Goodman's hypothesis to incorporate the viscoelastic behaviour of host and protective materials, aiming to reduce strain transfer errors in three-layer systems. The model also explored the influence of cracks and sensing length on strain transfer behaviour and was validated under lab conditions across varying temperatures.

While much of the research on strain transfer in optical fibre systems has focused on embedded configurations, growing attention has turned to surface-bonded arrangements, particularly in the context of practical deployment. These studies investigate a range of factors affecting strain transfer, such as the design of the protective jacketing, bonded length, adhesive properties, interrogator resolution, and the strain field conditions. A notable study by Wan et al. (2008) introduced enhanced methodologies for optical interferometric and FBG strain sensors, addressing challenges in small shear lag scenarios and stiff adhesive applications. Similarly, Li et al. (2009b) proposed a strain transmissibility formula that accounts for substrate stiffness and bonding layer characteristics. Their work highlighted that strain transmission loss is minimal with stiff, thick substrates but increases with thin, low-modulus materials, common in semiconductor packaging. The underestimation of strain due to FBG effects was also underscored in their findings.

Recent studies have delved deeper into modeling mechanics of surface-bonded DFOS, particularly in addressing complex considerations. Her and Huang (2011) investigated the Mach-Zehnder interferometric type of surface-bonded FOS by modeling a more complex segment of surface-bonded optical fibre that accounted for up to four distinct layers, comprising the core fibre, coating, adhesive, and substrate, while also considering the implications of potential gaps in the adhesive layer in Finite Element Method (FEM) geometry considerations. Their research indicated that both increasing bond length and coating stiffness enhances strain transmission to the optical fibre.

Falcetelli et al. (2020) critiqued traditional models for assuming zero strain at the bonded length's ends and proposed a novel analytical model that incorporates these real-world effects. Their model was validated experimentally and numerically, utilizing Rayleigh backscattering for strain profiling. A recent study by Du et al. (2023) proposed a model for surface-bonded DFOS with multilayered structures, focusing on the effects of different strain distributions on sensor performance. This study offered practical guidelines for optimizing cable design, particularly in varying strain gradients like uniform, parabolic, and bilinear distributions.

Research on strain transfer in crack detection and specialized environments has focused on advancing the understanding of DFOS and their application in extreme conditions. Feng et al. (2013) and Billon et al. (2015) researched the strain transfer phenomenon in the context of crack detection and quantification utilizing DFOS monitored by BOTDR and OFDR interrogations, respectively. They emphasized the vital role of interrogator resolution in accurately analyzing strain transfer for effective crack detection. Moreover, Tan et al. (2021b) developed closed-form solutions to characterize strain transfer in DFOS under varying strain fields, revealing that the strain transfer ratio can exceed 1 in areas with abrupt strain changes, an important finding for crack monitoring. Building on the application of DFOS in challenging environments, Yang et al. (2021) proposed a three-shear lag model with temperature-dependent properties for cryogenic conditions. Extending the investigation to embedded DFOS systems, Zhang et al. (2022) examined strain

transfer in concrete, identifying variations in force-displacement behaviour, with some cables exhibiting linear and others nonlinear responses, particularly under high strain. Their study emphasized the need for further exploration of viscosity sources and the development of more advanced nonlinear models, especially for long-term monitoring scenarios.

Overall, the literature highlights significant progress in understanding the strain transfer mechanisms of surface-bonded DFOS, with a focus on optimizing sensor designs for practical applications. Key findings include the importance of adhesive properties, substrate stiffness, bond conditions, and bonded length in optimizing strain transmission, as well as the need for improved models that account for real-world complexities such as null strain effects, temperature or strain gradients, and non-linear behaviour in extreme conditions. Future work is crucial to refine these models and address the challenges of long-term monitoring, particularly under varying environmental and structural conditions.

2.3. Surface-bonded DFOS on Reinforcing Bars

The successful deployment of DFOS in large-scale structures underscores its potential as a critical tool for long-term SHM. This growing recognition has increased demand for DFOS-instrumented reinforcing bars, which serve as integral components in advanced monitoring systems, offering sufficient resilience of the sensing unit to fracture-induced damage throughout the service life. By integrating strain and crack monitoring directly into reinforcement elements, DFOS-instrumented bars create multifunctional systems that combine structural performance with built-in sensing capabilities. Through bonding or internal embedding DFOS cables onto reinforcing bars, ongoing experimental research seeks to develop construction materials capable of continuously monitoring strain variations caused by structural damage, particularly cracking, without relying on external sensors. These developments offer a promising pathway toward more efficient and reliable methods for maintaining structural integrity over time.

In this context, it is essential to strike a thoughtful equilibrium between DFOS protection and ensure optimal utilization to obtain precise strain measurements throughout different phases of concrete performance to propagate field applications of DFOS-instrumented reinforcing bars. Aiming at achieving permanently accurate strain data acquisitions, these systems continue to undergo diverse experimental studies to address challenges and deficiencies in accurately monitoring strain and cracks. Researchers commonly embed DFOS within reinforcing bars, often comparing their outputs with those obtained through parallel sampling methods using well-established monitoring tools such as strain gauges.

In a recent experiment, Barrias et al. (2018b) tested and validated two OFDR-based, PI-coated DFOS-instrumented steel RC beams under realistic loading scenarios, evaluating the effects of two adhesive types: cyanoacrylate and two-part epoxy. The study demonstrated the feasibility and reliability of using thin, PI-coated DFOS directly bonded to reinforcing bars in both uncracked and cracked conditions, with cyanoacrylate outperforming the two-part epoxy. A spectral shift quality (SSQ) threshold was proposed to identify unreliable data at damage locations in the beams, which occurred after significant stiffness changes and detection of damage in the reinforcing bar.

Bado et al. (2018) similarly focused on the practical application of DFOS bonded to steel bars and demonstrated the strong potential of DFOS for internal strain measurements in RC members. A series of experimental tests were conducted to investigate the physical causes of strain reading anomalies (SRAs), aiming to improve monitoring efficiency in DFOS-instrumented steel reinforcement. The findings underscored the influence of bonding adhesives, such as cyanoacrylate and silicone, on DFOS performance and identified strain thresholds and structural deformation changes as key contributors to anomalies.

An experimental study by Bassil et al. (2019) assessed the performance of six-layer DFOS cables installed near the top and bottom reinforcing steel bars in RC beams. The system effectively

detected different crack types through crack-induced strain, crack opening displacement, and shear lag indicators, without requiring prior knowledge of the crack location.

Berrocal et al. (2021a) compared the performance of robust OFDR-based DFOS cables with PI-coated sensors bonded to reinforcing bars and embedded in concrete. The study evaluated their ability to detect cracks and deflections in RC beams under four-point bending and compared results with conventional methods, including digital image correlation (DIC). Findings showed that the sensors estimated beam deflections with errors between 6.8% and 12.5%, and strain peaks successfully identified crack locations. While robust cables performed well in uniaxial tensile tests, strain peaks at cracks were somewhat attenuated due to shear lag effects from the protective layers.

A comprehensive study from the Chair of Concrete Structures and Bridge Design at ETH Zurich summarised six years of DFOS research in structural concrete testing. The study presented best practices for instrumentation, fibre type selection (PI and acrylate coatings), and distributed sensing techniques. DFOS embedded in reinforcing bars via small longitudinal grooves, avoiding passage through the ribs, proved highly effective, preserving material properties while ensuring measurement accuracy. PI-coated DFOS, chemically bonded between jacket and core fibre, demonstrated high sensitivity and minimal slip, making them suitable for accurate strain transfer. Additionally, investigations into the compression zone of RC beams under pure bending revealed that strains at crack locations were significantly higher than between cracks, producing sharp, localized peaks (Galkovski et al. 2021).

Liu et al. (2021) evaluated six DFOS-instrumented RC specimens under uniaxial tension to assess OFDR sensing for monitoring concrete cracking and reinforcing bar deformation. Various DFOS cable types were tested for structure, sensitivity, and survivability. The study introduced a method for accurately estimating crack widths at defined load levels using both sensitive and less sensitive cables. Results showed that OFDR strain sensing, combined with advanced data processing, could

visualise distributed microcracks and estimate crack widths reliably. Moreover, stiff, less sensitive DFOS demonstrated good durability and maintained accuracy under higher loads, indicating their suitability for internal damage monitoring.

These studies collectively validate the feasibility of DFOS-instrumented reinforcing bars for detailed strain and crack monitoring, while also revealing persistent challenges related to bonding quality, sensor durability, and data reliability under real-world loading conditions.

2.4. Applications of FRP in RC Structures and FOS Monitoring

Corrosion of steel reinforcement in concrete structures, driven by moisture and chloride ion exposure, degrades steel properties and compromises structural safety through cross-sectional loss, steel-concrete bond deterioration, and concrete cracking or spalling, often necessitating costly repairs. In cold climates like Canada, factors such as temperature fluctuations, freeze-thaw cycles, moisture, and de-icing salts further accelerate corrosion (Rodrigues et al. 2021; Kristufek et al. 2022). In 2013, the estimated cost of repairing corroded structures in Canada and the U.S. was nearly $500 billion (Koch et al. 2016).

To address corrosion-related maintenance issues, alternative reinforcement materials, particularly fibre reinforced polymer (FRP) bars, have been increasingly used in buildings and bridges for over 50 years due to their corrosion resistance and superior mechanical properties. FRP bars are composites made of a polymer matrix, typically a thermoset resin like epoxy or polyester, reinforced with load-carrying fibres such as carbon (C), glass (G), basalt (B), and aramid (A).

FRP composite materials are heterogeneous and anisotropic without plastic deformation, and the FRP composite properties depend on the properties of both the fibres and the resin, as well as the volume fraction of each. FRP bars exhibit significantly lower weight, higher strength, corrosion resistance, and easier transportation, installation, and handling at the site job process compared to

conventional steel reinforcing materials (Canning and Luke 2010; Siddika et al. 2020; Uthaman et al. 2024). FRP composites can be prefabricated into various shapes and employed in concrete structures under two different conditions: internal applications (for new construction) with FRP bars, rods, and tendons and external applications (for existing structures, typically steel-reinforced concrete structures) with FRP plates, fabrics, wraps, and near-surface mounted (NSM) FRP bars.

In Canada, the National Research Council began exploring FRP materials for civil engineering in the late 1980s, leading to widespread use in infrastructure projects. Notably, FRP bars were used in the deck reinforcement of the Confederation Bridge in Prince Edward Island and for the rehabilitation of the Alexandra Bridge in Ottawa. Over the last decade, FRP bars have been successfully utilized in hundreds of bridge structures across Canada and the United States, including deck slabs, barriers, and girders, to extend the service life of bridges.

GFRP bars have also been used for continuously reinforced concrete pavement (CRCP) in Canada, as the Ministry of Transportation of Quebec (MTQ) has emphasized building long-lasting pavements suited to local traffic and climatic conditions. This emphasis led to the construction of a 150-metres-long section of eastbound Highway 40 in Montréal. Moreover, the first cable-stayed bridge in Canada is the Nipigon River Bridge, ON, where a new four-lane cable-stayed bridge replaced the old two-lane, four-span plate girder structures, and GFRP bars were used as the main reinforcement in the deck slab. GFRP bars have also been used for structures such as parking garages and hospitals, where the electromagnetic nature of FRP bars avoids interference with magnetic resonance imaging (MRI) machines (Nanni et al. 2014; Zingoni 2016; Ortiz et al. 2023).

Despite the favourable properties of FRP composites, design approaches must account for differences in behaviour compared to steel, including their lower elastic modulus and lack of plastic deformation. FRP bars are primarily utilized for tensile reinforcement in concrete structures, where their high tensile capacity effectively addresses flexural demands. They are less

effective as compression reinforcement due to the anisotropic nature of the materials and the potential for fibre micro buckling. Careful consideration of bond behaviour is also critical to ensure effective load transfer. Enhanced surface treatments can improve the bond strength between FRP bars and concrete. Considering the high strength-to-stiffness ratio of FRP reinforcing bars, serviceability criteria such as deflections and crack control tend to govern the design of FRP-RC flexural members (Tavares et al. 2008; AlNajmi and Abed 2020; Ilki et al. 2022; Dong et al. 2024).

Moreover, harsh environmental conditions, including extreme temperatures, UV radiation, moisture, alkaline, acidic, and saline solutions, can further adversely affect FRP reinforcement in RC members by degrading the polymer matrix, weakening the fibres in a composite structure, and ultimately compromising the performance and durability of the reinforcing bars. The damage can cause a loss of stiffness, strength, bond quality, and ductility in the FRP-RC components (Johnson et al. 1997; Duo et al. 2021). To account for the weaknesses in FRP caused by environmental exposure and severe mechanical loading conditions, design standards have established different environmental, creep rupture, and strength reduction factors for various types of FRP bars, thereby reducing the ultimate resistance considered in the design process (Ilki et al. 2023).

Glass fibre has become the preferred material for structural reinforcement among FRPs due to its cost-effectiveness, versatility, and suitable mechanical properties. E-glass leads the market by balancing tensile strength, durability, and affordability. In contrast, S-glass is selected for higher-performance needs, while AR-glass offers superior alkaline resistance in chemically aggressive environments. Although glass fibre has lower tensile strength than CFRP, it remains attractive because of its lower cost and environmental impact. Glass fibre production is less energy-intensive, has a smaller carbon footprint, and relies on abundant raw materials. While both GFRP and CFRP face recycling challenges, GFRP is more amenable to mechanical recycling, allowing partial material recovery, whereas CFRP's complexity limits its recyclability and sustainability (Karataş and Gökkaya 2018; Ji et al. 2023).

The growing global interest in using FRP composites for RC structures has driven a surge in research on integrating FOS for strain monitoring. This approach aims to advance sustainable built environments and effective structural maintenance. The studies cover both internal reinforcement with FRP bars and external strengthening using near-surface mounted (NSM) FRP bars. This research highlights the rising demand for more resilient and efficient monitoring solutions to enhance the integrity and performance of FRP-reinforced and strengthened concrete structures.

The development of self- and external-sensing FRP bars using FOS has gained significant popularity. These terms refer to embedding permanent in situ sensors, offering a valuable health management tool that allows structural components to monitor and report their own condition. Researchers have explored a wide range of approaches, including both integration techniques of embedding in manufacturing process or post-installation, and various FOS, mostly point-based types, to integrate optical fibre sensors into FRP bars, aiming to create self- or external-sensing composites capable of real-time monitoring (Jaradat et al. 2023).

Belarbi et al. (2001) embedded fibre-optic interferometric sensors in a pultruded carbon fibre core, which was then surrounded by filament-wound carbon fibres, to produce pseudo-ductile and smart hybrid FRP rods. Testing has confirmed that these rods, along with FRP-reinforced concrete beams, can accurately measure internal strain using the FOS.

Kalamkarov et al. studied and validated the pultrusion of GFRP reinforcements with embedded point-based FBG and Fabry-Perot fibre optic sensors in three key papers focusing on fabrication, reliability assessment, and long-term performance evaluation. The researchers concluded that embedded optical fibres, including glass core and cladding fibre with a PI protective jacket, had no significant effect on the tensile properties of the pultruded GFRP rods. They observed good agreement between strain data from sensors and traditional strain monitoring devices under cyclic loading, but weak long-term creep behaviour of Fabry-Perot sensors. They also validated the

durability and ductility of Fabry-Perot FOS integrated into GFRP tendons for long-term infrastructure health monitoring, comparing them to other strain measurement equipment like extensometers, electrical resistance strain gauges, and LVDTs. The experimental strain distribution aligned with theoretical predictions, demonstrating no bond slip between GFRP reinforcement rods and surrounding concrete (Kalamkarov et al. 1999, 2000, 2004).

Chhoa et al. (2001) explored and verified Brillouin scattering DFOS systems for measuring the strain of steel reinforcing cages in concrete beams. They addressed issues associated with the fragility of optical fibres in harsh concrete environments, developing protection methods such as embedding DFOS cables in pultruded GFRP rods, which has also been studied by Torkan (2011) and Rahmatian (2014), or bonding them to steel bars using epoxy. The study found that direct bonding to steel bars yielded more accurate results than GFRP rods, which experienced slippage. The study also noted challenges in maintaining fibre straightness during concrete pouring, which can affect signal integrity, and recommended further research on improving signal processing and assessing the long-term durability of DFOS in various conditions.

Zhou et al. (2003) examined the performance of self-sensing reinforcing bars, including pultruded FBG-GFRP bars and FBG-CFRP bars, while they were embedded in RC beams subjected to third-point static load conditions for monitoring strain of FRP bars, concrete cracking, slip between FRP bars and concrete, and strain distribution of the beams. The results indicated that FRP-FBG is an excellent construction material for civil engineering applications, serving as smart sensing elements without the challenges of embedded installation in concrete structures, and it can be conveniently utilized in RC structures as both sensors and reinforcing bars.

For the development of smart hybrid CFRP (HCFRP) rods as an innovative approach for both structural components and sensing materials with self-diagnosis and damage detection capability, a study by Yang et al. (2006) explores the dual functionality of the HCFRP rods to sense strain

and detect fractures through changes in electrical resistance. The utilization of clip gages and BOTDR-based DFOS for measuring crack initiation and propagation in HCFRP rod-reinforced concrete beams has been investigated, offering promising implications for SHM.

In the context of another research by Zhou et al. (2007), the authors have developed an affordable and highly dependable BOTDA-FRP-FOS rebar. Through experimental and theoretical investigations, they examined the surface bonding, mechanical strength, and strain transfer from the host to the optical fibre. Finally, their developed BOTDA-FRP-FOS were successfully utilized in the Tiyu West Road civil structure in Guangzhou and the Daqing Highway. The researchers found that the accuracy of strain coefficients in the BODTA system was significantly influenced by gauge length and spatial resolution. Therefore, further research is required to explore the practical applications of the BOTDA system with various gauge lengths.

Wang et al. (2009) embedded FBG sensors into GFRP bars during pultrusion and found that tensile, bond, and flexural tests showed close agreement between average strains from strain gauges and FBG sensors, with strain gauges reading slightly higher. They concluded that smart GFRP bars effectively measure strains for SHM under service loads but emphasized the need for FOS with wider strain measurement ranges and finer spatial resolution for destructive testing.

The studies by Tang et al. (2010) and Tang and Wu (2016) verified the crack monitoring capabilities of self-sensing basalt-FRP bars with BOTDA-based DFOS embedded during the industrial fabricating process. These studies highlighted the importance of sustained bonding and proposed key areas for further investigation, such as long-term strain-sensing performance, including accuracy and stability under diverse temperature, moisture, and strain scenarios.

In 2016, a comprehensive book edited by Rajan and Prusty (2016) explored FOS for monitoring the structural health of composite materials, synthesizing research and expert insights. It highlights self-sensing FRP bars with excellent strain sensitivity, ideal for strain monitoring in structural

applications. Key challenges discussed include strain transfer between the host material and sensor, discrepancies in measurements due to ply architecture, and the need for optimized FOS integration. The book also covered DFOS applications in manufacturing quality control, addressing challenges like sensor intrusiveness, resolution, and cross-sensitivity. It called for improved DFOS network systems, enhanced transversal strength in FRP bars, and advanced signal processing methods (e.g., ANNs) to boost monitoring accuracy and reliability.

For retrofitting and SHM of a heritage building, the Monastery in Sant'Angelo d'Ocre, L'Aquila, Coricciati et al. (2017) used self-sensing patches made of GFRP strengthening sheets embedded with FBG sensors at the centre of the plate, along with smart pultruded GFRP rebars incorporating OFDR-based DFOS along the rebar axis. The systems were monitored over five months, consistently detecting signals and demonstrating their reliability.

In another related study, Waters et al. (2022) showed that inexpensive single-mode, acrylate-buffer-coated FBGs can withstand brief exposure to high temperatures during FRP pultrusion and accurately measure flexural and tensile elastic strains up to 4000 microstrain. Experimental results revealed that the polymer buffer, combined with potential interfacial slippage, failure, or relaxation between the buffer and the fibre, hindered effective axial strain transfer from the host material to the optical fibre. This resulted in reduced strain readings under sustained higher loads and contributed to a noticeable discrepancy between measurements obtained from the extensometer and those recorded by the FBG sensors.

Zhou et al. (2023) conducted a comprehensive study on the bond performance of GFRP and stainless-steel reinforcements in concrete, using DFOS glued to the substrate rather than integrated within the matrix. This paper continues a line of hybrid studies, such as that by Rolland et al. (2018), examining the bond behaviour between GFRP bars and concrete while also evaluating the performance of OFDR-based DFOS in functionalising GFRP for real-time strain monitoring.

Comparison of experimentally tested parameters in GFRP–concrete bond tests revealed that epoxy resin was the most effective adhesive for DFOS bonding, outperforming cyanoacrylate and silicone. Additionally, PI-coated DFOS proved ideal for localized strain measurements, whereas acrylate-coated DFOS was better suited for larger specimens. The study recommends further research into environmental effects on DFOS performance, adhesive bond integrity, and compatibility with various FRP reinforcement types.

2.5. Summary and Research Gaps

All the above studies reported satisfactory performance of DFOS for strain monitoring in reinforcing bars, highlighting their role as multifunctional sensing systems and a transformative advancement in the SHM of RC structures, capable of detecting minute strain changes and accurately tracking crack formation and propagation. However, further investigations have been recommended to advance strain data analysis techniques, improve sensor integration methods, evaluate monitoring reliability under complex strain conditions, and explore integration strategies to fully realise the potential of these multifunctional systems.

The investigation into the mechanical principles of fibre optic sensing encompasses a wide range of localized and distributed optical technologies applied across various host materials, installation methods, and coating types. Although significant progress has been achieved in understanding strain transfer mechanisms, existing research increasingly highlights the need for more comprehensive studies that tackle the complexities encountered in real-world FOS implementations. The field remains dynamic and continues to evolve, with ongoing efforts focused on developing generalised predictive models to support a broad spectrum of applications.

The integration of FOS with non-corroding FRP bars, both in internal self-sensing and surface-bonded configurations, has proven effective for long-term monitoring of previously unmeasurable localized and distributed strains. However, in the case of OFDR-based surface-bonded DFOS on

GFRP bars, which offers sub-millimetre spatial resolution and employs a cost-effective, low-carbon FRP composite, most existing studies have concentrated on the linear elastic behaviour of the intermediate layer material. As a result, the long-term performance of DFOS under non-linear conditions, such as plastic shear deformation of the adhesive, followed by bondline degradation due to excessive loading or creep under repeated stresses, remains largely unaddressed.

The long-term durability and interfacial mechanics of DFOS in GFRP bars, particularly under severe strain conditions, have not been rigorously evaluated, raising concerns about their reliability in practical applications. Current research on DFOS strain transfer mechanics is limited by simplifying assumptions, such as idealised bonding between intermediate layers and purely elastic adhesive behaviour. These assumptions limit the study of bond quality and long-term effects of complex elasto-plastic behaviours, especially in surface-bonded DFOS GFRP bars that undergo wide in-service strain ranges due to their high strength and low elastic modulus (Qureshi 2022).

A more realistic mechanical strain transfer analysis is therefore essential. The long-term performance of bonding agents (e.g., adhesives) used in surface-bonded sensor attachments can be significantly compromised by degradation mechanisms such as bondline deterioration and ageing under sustained loading beyond critical bond strength, all of which can severely limit the durability of the sensing unit and the sustainability of its measurements (Zhou et al. 2007). A clear understanding of the multilayered interfacial stress and strain transfer within the core optical fibre, especially in surface-bonded DFOS GFRP reinforcing bars as studied here, is crucial to enhancing the stability, performance, and long-term durability of these sensing systems.

Addressing these gaps requires a comprehensive theoretical and experimental investigation into the strain monitoring and mechanical transfer performance of OFDR-based DFOS bonded to GFRP bars under diverse conditions, with a focus on sensor durability, optimal integration strategies, and the complex interplay of strain transfer behaviours in various loading environments.

Chapter 3

Experimental Program and Numerical Analysis Methodology

3.1. Experimental Program

3.1.1. Introduction

The experimental program was designed to evaluate the performance and reliability of a sensor-integrated structural system combining surface-bonded DFOS with GFRP reinforcing bars, monitored using optical frequency domain reflectometry (OFDR), under varying axial strain conditions. The primary objectives were to identify the upper performance limits, establish the effective operating range, and evaluate the consistency and repeatability of DFOS distributed strain measurements. Additionally, the study examined potential degradation of the sensor's bondline during testing and its effect on the accuracy of DFOS measurements.

A series of controlled uniaxial tension tests, including monotonic, sustained, and cyclic loading regimes, were applied across both service-level and extreme stress ranges. Each specimen was tested in a free-in-air setup using a universal testing machine (UTM), with tensile loads applied at both ends of the GFRP bar specimen. The tests aimed to characterize the strain-sensing performance of surface-bonded DFOS on GFRP bars and to establish a comprehensive performance profile. To achieve this, strain transfer efficiency and consistency between the GFRP substrate and bonded optical fibre were assessed, considering variations in sensor path, attachment method, adhesive type, DFOS coating, and the magnitudes, types, and histories of applied loading across tension test samples.

The experiments were conducted in two phases: initial pilot tests followed by Stage II, with DFOS measurements validated against reference data obtained from an extensometer. All tension test samples were fabricated and tested in the Structural Laboratory at the University of Ottawa.

3.1.2. Uniaxial Tension Test Requirements

The high possibility of transverse crushing in the UTM's steel jaws due to anisotropic characteristics of FRP bars preclude the conventional method of directly gripping the reinforcing bars to conduct tension tests. Thus, to ensure consistent, reproducible testing conditions that accurately reflect material performance under tensile stress and preventing early failure, ASTM D2705M defines criteria for proper selection of steel anchorage, specified via required tube size and length for FRP bars of varying diameter, and loading rates (ASTM D7205 2021). The monotonic loading rate is specified as 300 *MPa/min*.

According to the standards criteria, each GFRP test specimen, which were one metre long, were anchored at both ends of the bar with two pieces of 270-*mm*-long steel pipes, as shown in **Figure 3-1**. As per the ASTM recommended minimum outer diameter and anchor filler for the steel pipes, a series of trial anchor samples were conducted to find the most effective anchorage configuration, ensuring reliable load transfer and minimal failure at the anchorage interface.

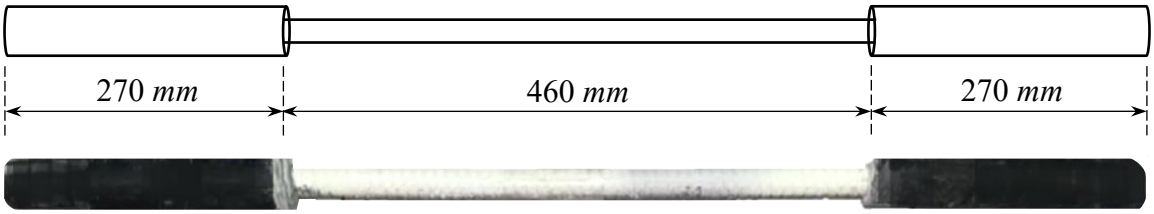

Figure 3-1. Schematic of GFRP bar specimen with steel pipe anchors at both ends

As shown in **Figure 3-2**, the failure results of the trial samples included: a) early anchors' failure due to bond slip between epoxy, used as the filler material, and steel tubes; b) compression failure and high deformation of thin *Sch 40* (*1 in*.) steel tubes filled with expansive, cementitious grout, occurring above 1000 *MPa* stress applied to GFRP #16; and c) tensile failure of GFRP in grout-filled steel tubes, with *Sch 80* (*1 in*.) for #16 GFRP, and *Sch 40* (*3/4 in*.) for #12 GFRP. Based on the last mentioned achieved failure mode, the anchorages were then selected for tension tests.

a) b) c)

Figure 3-2. Failure modes observed in the trial anchor: a) epoxy filler bond slip, b) compression failure and deformation of *Sch 40* (*1 in*.) steel tube for #16 GFRP, and c) tensile failure of GFRP

3.1.3. Pilot Tension Tests

The integration of surface-bonded DFOS systems with GFRP bars raises a critical question about the extent to which the physical and mechanical properties of the host material influence the overall performance, accuracy, and reliability of the sensing system. Factors such as surface treatment, material stiffness, strain transfer characteristics, and bar size may impact the signal quality and spatial resolution of the DFOS system. To explore these factors, a series of GFRP bars with varying properties were tested as hosts for a PVC-coated DFOS cable under uniaxial tensile loading. Both static and dynamic stress conditions were applied to identify key trends, challenges, and parameters affecting the reliable operation of DFOS in GFRP bars, as illustrated in **Figure 3-3**.

The loading protocol used in this phase of the investigation, referred to as Protocol A, consisted of five stages: 1) initial monotonic loading up to approximately 70% of the ultimate strain of the

GFRP bar, $0.7\varepsilon_{fu}$, reported by the manufacturer, 2) 10-minutes-long sustained load, 3) monotonic unloading to $0.1\varepsilon_{fu}$, 4) six fast loading cycles between $0.1\varepsilon_{fu}$ and $0.5\varepsilon_{fu}$, and 5) final monotonic loading up to the failure of the sample. The ASTM standard loading rate of 300 *MPa/min* was applied during all monotonic loading and unloading stages of the defined testing protocols, while for the fast and cyclic loading phases, the rate was increased to 900 *MPa/min*, continuing at this rate until the point of failure.

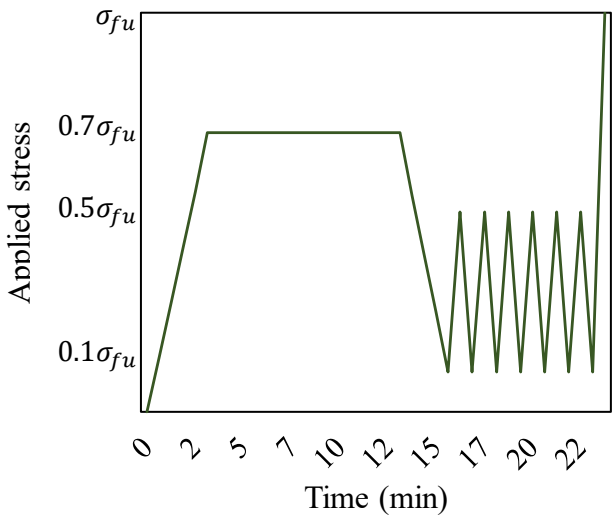

Figure 3-3. Applied loading protocol "A" for the pilot test specimens, shown as stress–time plot relative to the GFRP bar's ultimate tensile strength (σ_{fu})

Eight specimens were fabricated to evaluate the efficacy of a PVC-coated DFOS, visualized by OFDR, for logging strain data in GFRP bars. The study compared the effect of the bar's diameter, bar surface features, and DFOS attachment method (surface-mounted versus groove-embedded). A single-mode telecommunication-grade optical-fibre cable (900 μm diameter) was bonded within 400 *mm* of each GFRP bar's free length using two-part epoxy. The sample notation follows the format "x-Y-z," where "x" donates the surface treatment (SC for sand-coated, SP for ribbed spiral), "Y" indicates the bar diameter (12 *mm* or 16 *mm*), and "z" represents the DFOS attachment technique ("g" for groove-embedded, "s" for surface-mounted). A summary of the pilot test samples is provided in **Table 3-1**.

Table 3-1. Matrix of pilot test specimens

Test ID	Phase	Sample label	GFRP bar variables				DFOS layout	Loading protocol
			Surface texture	Dia. (mm)	Tensile strength[*1]	Tensile modulus[*2]		
T01	Pilot	SC-12-g	SC	12	1424	62	g-PVC-EP	A
T02	Pilot	SC-12-s	SC	12	1424	62	s-PVC-EP	A
T03	Pilot	SC-16-g	SC	16	1503	63	g-PVC-EP	A
T04	Pilot	SC-16-s	SC	16	1503	63	s-PVC-EP	A
T05	Pilot	SP-12-g	SP	12	1405	65	g-PVC-EP	A
T06	Pilot	SP-12-s	SP	12	1405	65	s-PVC-EP	A
T07	Pilot	SP-16-g	SP	16	1339	66	g-PVC-EP	A
T08	Pilot	SP-16-s	SP	16	1339	66	s-PVC-EP	A

[*1,2] Nominal values reported by the manufacturers- units: [*1](*MPa*) and [*2](*GPa*)

3.1.4. Stage II Tension Tests

Another critical inquiry regarding DFOS-bonded GFRP bar systems involves the role of the sensor's attachment configuration, specifically, the adhesive bonding and protective jacket of the sensing cable, in influencing the efficiency and stability of strain transfer between the core optical fibre and the GFRP substrate under varying stress conditions. To evaluate the effect of these intermediate layers on monitoring performance at given strain levels, a second group of tension tests was conducted on four tension test specimens subjected to different loading histories.

The investigated parameters included the sensor attachment technique (surface-mounted or groove-embedded), DFOS coating type (PI or PVC), adhesive material (two-part epoxy or cyanoacrylate), and loading method (sustained or cyclic). In this test phase, all GFRP bar specimens had a uniform diameter of 16 *mm* and were instrumented with four single-mode DFOS cables featuring varying coating types and attachment configurations, as detailed in **Table 3-2**.

A two-part notation system is used in this phase to distinguish the specimens: the first part indicates the GFRP bar's surface type, "SP" for ribbed spiral and "MST" for helical spiral finish, while the

second part denotes the loading protocol, “S” for sustained and “C” for cyclic loading. The DFOS layout labeling convention used in this phase follows the format “x-y-z,” where “x” indicates the DFOS attachment technique (“g” for groove-embedded, “s” for surface-mounted), “y” specifies the cable jacket type (“PVC” or “PI”), and “z” represents the adhesive used (“EP” for two-part epoxy or “CN” for cyanoacrylate).

Table 3-2. Matrix of Stage II test specimens

Test ID	Phase	Sample label	GFRP bar variables				DFOS layout	Loading protocol
			Surface texture	Dia. (mm)	Tensile strength[*1]	Tensile modulus[*2]		
T09	Stage II	SP-S	SP	16	1339	66	g-PVC-EP	S
T09	Stage II	SP-S	SP	16	1339	66	s-PVC-EP	S
T09	Stage II	SP-S	SP	16	1339	66	g-PVC-CN	S
T09	Stage II	SP-S	SP	16	1339	66	s-PVC-CN	S
T10	Stage II	SP-C	SP	16	1339	66	g-PVC-EP	C
T10	Stage II	SP-C	SP	16	1339	66	s-PVC-EP	C
T10	Stage II	SP-C	SP	16	1339	66	g-PVC-CN	C
T10	Stage II	SP-C	SP	16	1339	66	s-PVC-CN	C
T11	Stage II	MST-S	MST	16	1000	60	s- PVC-EP	S
T11	Stage II	MST-S	MST	16	1000	60	s-PI-EP	S
T11	Stage II	MST-S	MST	16	1000	60	s-PVC-CN	S
T11	Stage II	MST-S	MST	16	1000	60	s-PI-CN	S
T12	Stage II	MST-C	MST	16	1000	60	s-PVC-EP	C
T12	Stage II	MST-C	MST	16	1000	60	s-PI-EP	C

[*1,2] Nominal values reported by the manufacturers- units: [*1](MPa) and [*2](GPa)

The loading protocols in this phase were commonly designed based on five strain targets: 1) 0.2%, representing the nominal yield strain of steel reinforcing bars, 2) $0.3\varepsilon_{fu}$, corresponding to the serviceability limit for GFRP reinforcement as defined in ACI 440.11-22, 3) $0.5\varepsilon_{fu}$, 4) $0.7\varepsilon_{fu}$, and 5) the ultimate failure strain of the GFRP bars (ε_{fu}). To evaluate recovery behaviour and ensure consistent monitoring, each loading step was followed by unloading to 1 kN. The sustained

loading protocol, “S,” involved the application of incremental static loads held for 10 minutes before unloading. The cyclic loading protocol, “C,” consisted of four loading ranges, each involving six cycles of loading to a peak stress, based on the five target strain levels, and unloading back to 1 *kN*, applied at a rate of 900 *MPa/min*. **Figure 3-4** illustrates these protocols.

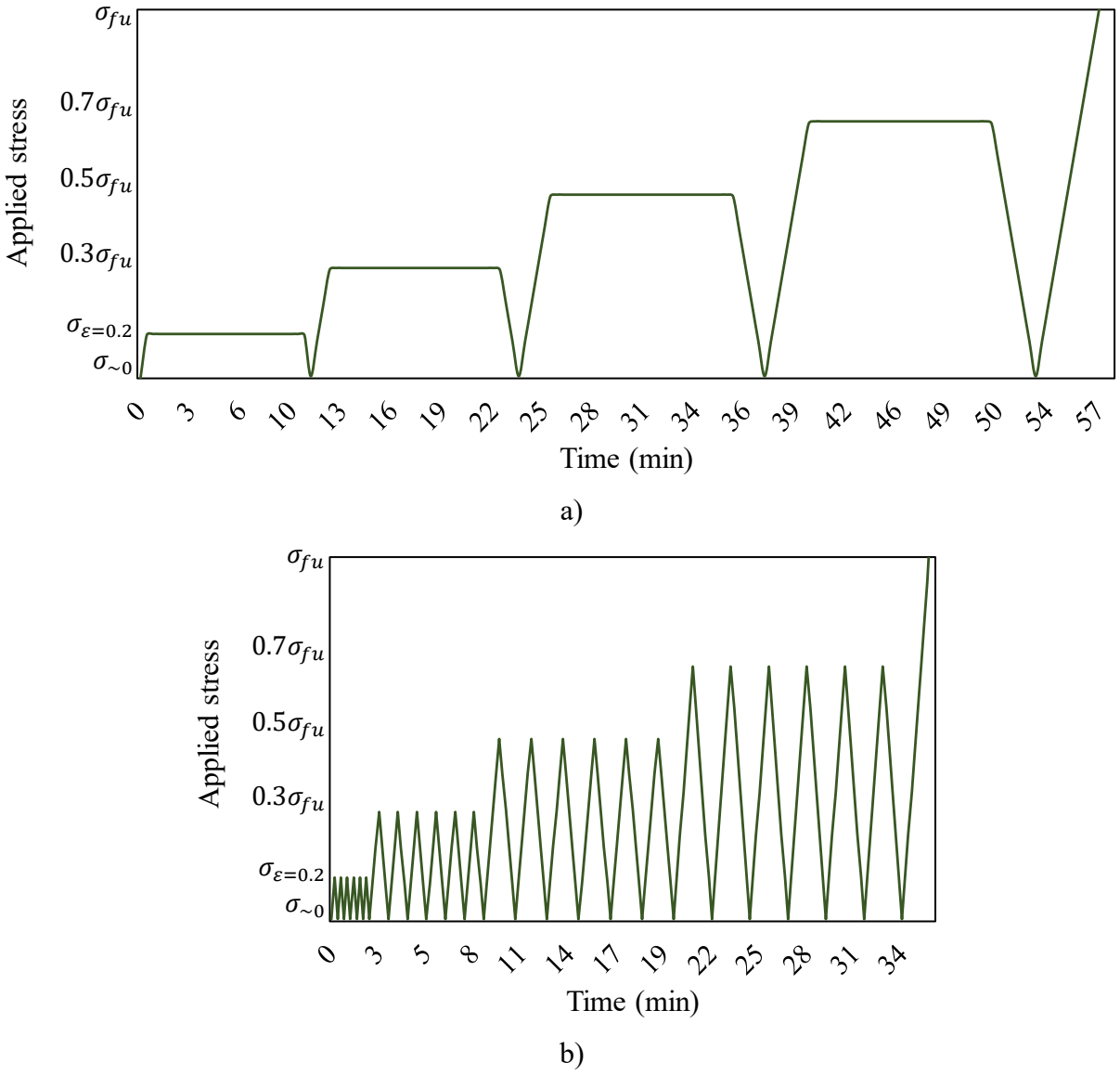

Figure 3-4. Applied loading protocols for Stage II test specimens, shown as stress–time plot relative to the GFRP bar’s ultimate strength (σ_{fu}): a) “S” (sustained) and b) “C” (cyclic)

The applied short-term yet extended loading protocols, comprising monotonic, sustained, and cyclic loading and unloading sequences, were collectively designed to evaluate the reliability and

repeatability of DFOS measurements under varying mechanical loading conditions. While long-term effects like creep were not expected due to the short test duration, these protocols aimed to assess the impact of varying loading histories on DFOS performance and verify the sensor's ability to provide reliable, stable, and consistent strain readings under both constant and fluctuating loads.

3.1.5. Materials and Fabrication Process

The overall design of the sensor installation is based on widely accepted and well-documented configurations for surface-bonded DFOS, as supported by numerous sources in the literature and thoroughly reviewed in the previous chapter, particularly in **Section 2.3**. Experimental studies have consistently affirmed the use of DFOS embedded in shallow longitudinal grooves on the surface of reinforcing bars, bonded with structural adhesives.

The test specimens consisted of pultruded GFRP bars made of continuous E-glass fibres embedded in vinyl ester resin matrix, supplied by three manufacturers, with ultimate tensile strengths ranging from 1000 to 1500 *MPa* and various surface treatments including SC, SP, and MST, as shown in **Figure 3-5**. At the initial preparation stage, a 1.5 × 1.5 mm^2 (depth × width) grooves were machined into the bars to embed the DFOS cable, as depicted in **Figure 3-5c** and **e**. This configuration allowed for the evaluation of potential improvements in distributed strain transfer performance, as well as any adverse effects on the mechanical properties of the GFRP bars.

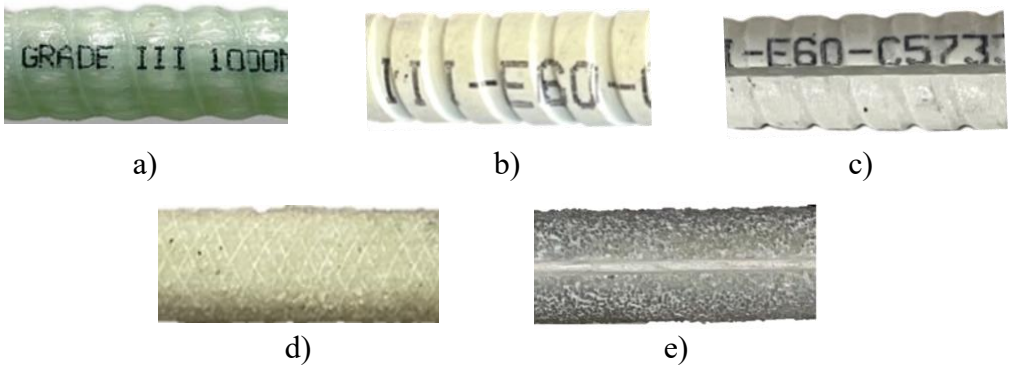

Figure 3-5. GFRP bar textures: a) MST, b) SP, c) grooved SP, d) SC, and e) grooved SC

Steel pipes of appropriate dimensions were selected for each bar. The GFRP bar was carefully centered within the pipe, and the entire assembly was positioned vertically to ensure uniform grout filling. Dexpan expansive grout, with an expansive strength of approximately 125 *MPa*, was then poured into the pipe. To maintain precise alignment, a bracing framework, as shown in **Figure 3-6**, was employed. and two silicon pieces were built and positioned at each pipe end, followed by sealing gaps with fresh silicon. About four hours after grout casting in one anchor tube, once the grout had sufficiently bonded the steel pipe and bar, the specimen was inverted to repeat the same procedure on the opposite side. All samples were subsequently cured for a minimum of 24 hours.

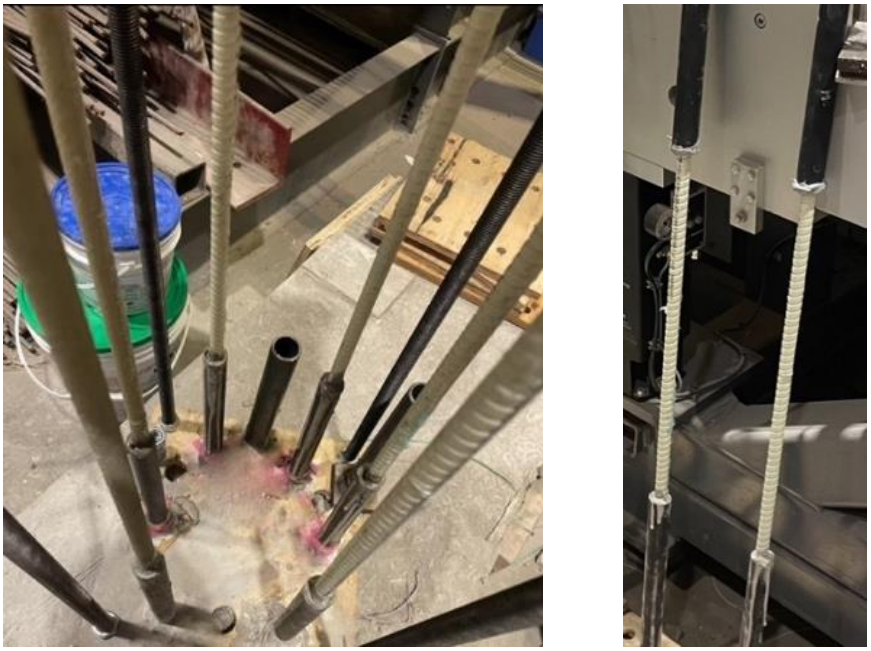

Figure 3-6. Grout casting for anchors of GFRP bars

After the grout anchors had cured, optical fibre cables were bonded along the 400 *mm* free length of the GFRP bars using either two-part epoxy (EP) or cyanoacrylate (CN) , as shown in **Figure 3-7**, and the specimens were placed horizontally to cure the adhesive for at least 24 hours, as illustrated in **Figure 3-8**. These adhesives were chosen based on established recommendations, as they are recognized for ensuring effective shear transfer between the sensor and substrate, while offering distinct properties in strain transfer and protective performance.

The test optical fibres were single-layer cables, tight-buffered with either a 900 μm PVC coating or a 380 μm PI coating, as depicted in **Figure 3-9**. Most of the test specimens were instrumented using PVC-coated DFOS cables due to their satisfactory monitoring performance and being more user-friendly for extensive measurements because of their much lower cost and less fragile nature than PI-coated cables. However, the very thin PI jacket which also has a chemical bond with the core fibre can enhance the STE, resulting in more accurate and responsive strain data.

EP, known for its excellent mechanical properties, forms a strong, durable bond with high tensile and shear strength, and resists temperature changes and moisture. However, its high viscosity limits penetration into surface gaps, resulting in a thicker bond layer that also protects the sensor. Proper curing requires heat and sustained clamping, which is impractical for fragile sensors; therefore, room-temperature curing under hand pressure increases adhesive thickness and may introduce shear lag effects. In contrast, CN resin's low viscosity and fast curing allow it to form a thin, strong bond layer under light clamping, enhancing strain transfer. However, its lower resistance to environmental factors, along with limited sensor protection, reduces its long-term reliability. Despite this, CN enhances interfacial cohesion and strain transfer efficiency by maintaining a thin, well-cured bond interface.

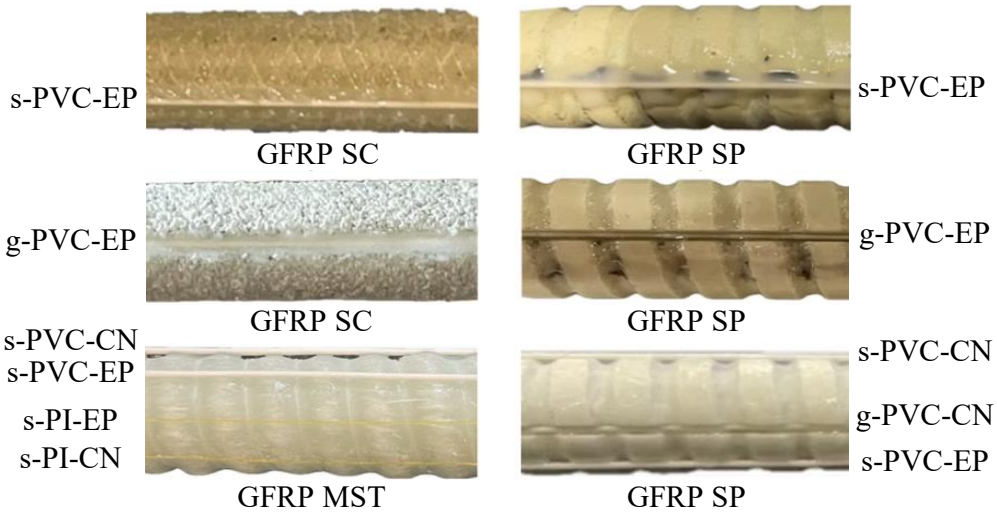

Figure 3-7. Close view of different DFOS test layouts

Figure 3-8. A depiction of horizontal placement of tension specimens during adhesive curing

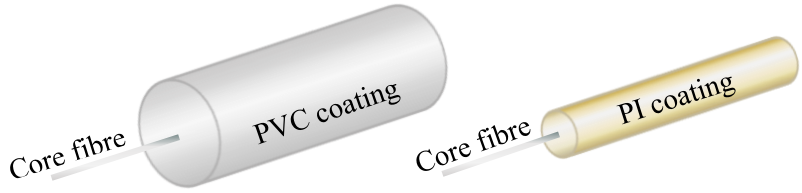

Figure 3-9. Tight buffered SMF28 fibre optic cable

3.1.6. Testing Procedure

Figure 3-10 illustrates the test setup. All samples were tested under uniaxial loading applied by a Galdabini UTM. During each test, tensile strain reading data were recorded continuously every 0.2 second by both DFOS and an extensometer mounted on the GFRP bar specimen's mid-length section. The DFOS data were acquired using LUNA ODiSI 6104 technology with an OFDR-based system set to 2.6 *mm* spatial intervals, while the extensometer measured average deflections over its gauge length and was connected directly to the UTM. Since the tests were performed indoors over relatively short durations, temperature was assumed constant throughout all experiments. The test specimens were securely clamped between the UTM grips, their vertical alignment was verified using a level ruler, and all strain sensors were calibrated under zero-load conditions prior to testing. The test session ended when the GFRP bar ruptured.

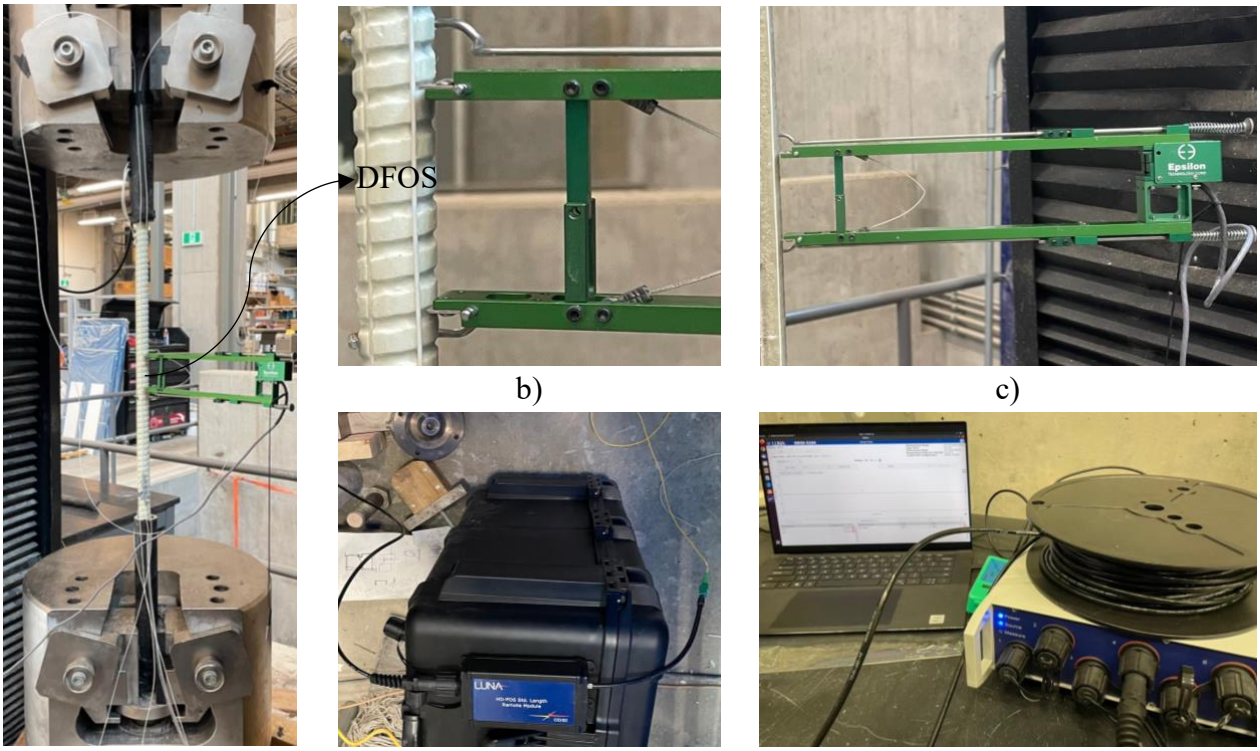

Figure 3-10. Uniaxial tension test setup: a) mounted sample on UTM, b) close-up of middle area of DFOS-bonded GFRP bar, c) extensometer, d) DFOS connection to remote module, and e) LUNA ODiSI 6104 mainframe

3.1.7. Testing Machine Description

The UTM machine applies a controlled load to the sample, which can be either tensile or compressive. The Galdabini machine is configured with two main parts: the loading unit, a robust dual-column frame that supports the entire testing apparatus, and the control panel, as shown in **Figure 3-11**. The machine features a movable crosshead driven by a motor with screw mechanism, allowing the precise application of tensile or compressive forces to the specimen. Integrated into the loading unit setup is a high-precision load cell that measures the applied force and converts it into an electrical signal for display and recording. The grips used for the tests feature a wedge action mechanism, which tightens on the specimen as the applied load increases, ensuring a secure hold and preventing slippage during testing, with the tightening screws on the sides allowing for manual adjustment to accommodate different specimen sizes.

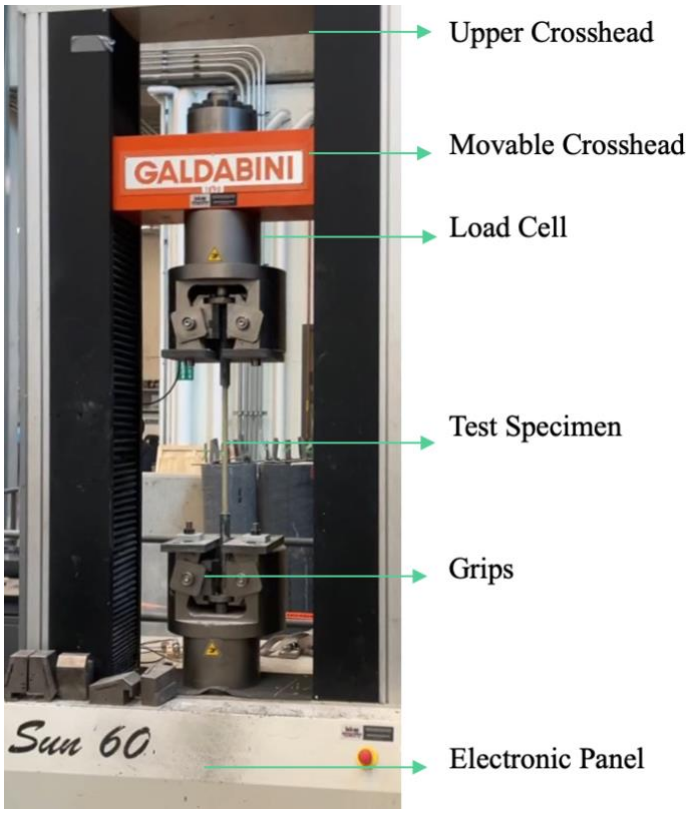

Figure 3-11. The UTM machine used in this study

3.1.8. Strain Sensors Overview

- **DFOS**

Luna Innovations' Optical Distributed Sensor Interrogator (ODiSI) series 6104, based on OFDR principles, employs swept-wavelength coherent interferometry to measure temperature and strain using optical fibre cables, ranging from 1 to 20 metres long, as sensors at intervals as small as 0.63 *mm*. By comparing measurements taken at different times, the ODiSI calculates and displays changes in strain or temperature. **Figure 3-12** depicts the key components of the Luna ODiSI.

The system consists of an ODiSI controller with application software (Linux OS), running on a computer, ODiSI mainframe, which is a comprehensive data acquisition solution offering extensive features for data logging and integration with external systems available in 1, 2, 4, or 8 channels, rugged standoff cables, used for each channel to connect the mainframe to the remote

module, remote module, serving as an interface to the optic-fibre sensors cable, and DFOS cables, which are capable of high-definition strain and temperature measurements. The light source module involves a laser source, injecting light into FUT, photodetectors, converting light into electrical signals, optical filters, and amplifiers to send conditioned signals to ODiSI mainframe, which has an analogue-to-digital converter (ADC).

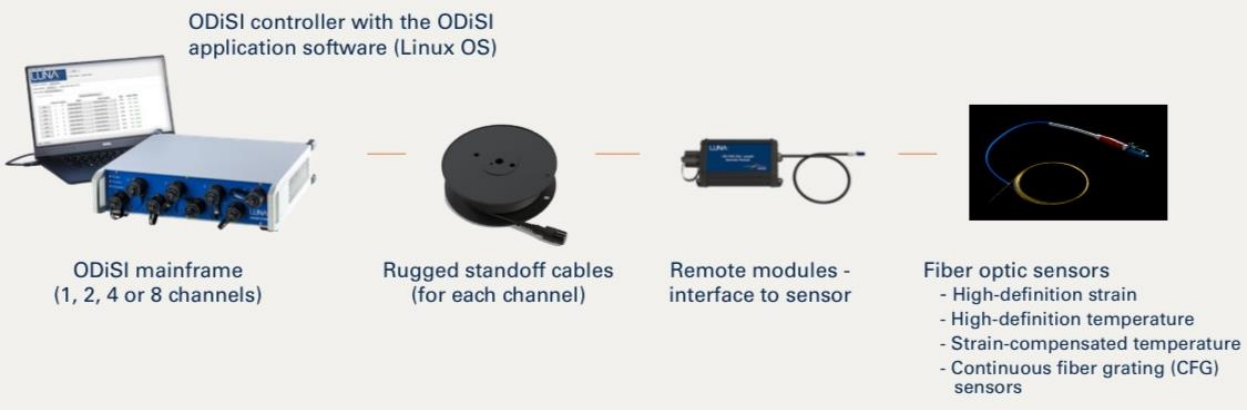

Figure 3-12. ODiSI system instrumentation units, from Luna manual

A fusion splicer was used to fuse the sensing DFOS cable to the connector, as shown in **Figure 3-13**. The splicing process starts with preparing the DFOS and connector cables by removing protective coatings, followed by cleaving and cleaning the core fibres. The splicer then aligns the fibre precisely and uses a controlled electric arc to fuse them together in fusion splicing, creating a seamless optical connection. After inspection, a protective sleeve is applied to secure the splice for mechanical stability and protection from environmental damage.

The Luna ODiSI system provides an advanced, reliable solution for continuous strain and temperature measurement. This system allows users to capture and store measurement data either as raw optical data or as processed strain and temperature values, depending on the analysis needs. A core feature of the ODiSI system is its event trigger functionality, which ensures that critical data is captured when specific, predefined conditions are met, such as exceeding a strain threshold

or detecting rapid temperature changes. This data is then logged, allowing for precise and timely analysis. Additionally, the ODiSI system supports continuous data streaming through protocols that enable real-time data integration into custom applications. This is achieved via a circular log file that maintains a fixed number of entries, with the oldest data being overwritten as new data is recorded. As the system operates, it continuously updates the log file, ensuring that the most recent strain and temperature readings are always available. This real-time data logging capability, combined with event-triggered data capture, allows the ODiSI system to provide up-to-date, accurate measurements across the sensing region without interruption over Ethernet. The system's ability to integrate seamlessly into custom programs further enhances its versatility, making it an invaluable tool for applications that demand continuous monitoring and real-time data processing.

Figure 3-13. The splicer used in this study

- **Mechanical Extensometer**

Mechanical extensometers, commonly employed in conjunction with a UTM, are precision instruments designed to externally attach to a test specimen. Their primary function is to measure strain by detecting the relative elongation (Δl) between two predefined gauge points on the specimen's surface. This process provides an averaged strain value over the specified gauge length.

The measurement is influenced by parameters such as the gauge length (l) and the gauge factor (k), which calibrate the instrument to account for the mechanical and geometrical characteristics of the setup, ($\varepsilon = k\Delta l/l$). These extensometers provide reliable strain data, though averaging may slightly affect accuracy depending on material behaviour and test conditions.

The uniaxial mechanical extensometer used for this experimental study was manufactured by Epsilon with a gauge length of 50 *mm*. The Epsilon extensometer was clamped onto the test sample at specific gauge points, using knife edges and springs that ensure a firm and stable attachment to measure the change in length (deformation) of the sample as the load is applied. The Epsilon extensometer was clamped onto each test sample at specific gauge points, using knife edges and springs that ensure a firm and stable attachment to measure the change in length (deformation) of the sample as the load is applied. During each test, the extensometer (EX) was strategically dismounted from the sample when the applied load approached approximately 60-70% of the anticipated failure load during the final monotonic loading. This precaution was taken to safeguard the equipment and ensure the integrity of the measurement apparatus against potential damage resulting from severe fibre rupture in the GFRP bar.

This extensometer, also known as a strain-gauged transducer, uses a full Wheatstone bridge configuration to enhance measurement accuracy and sensitivity by converting small resistance changes into a measurable electrical signal, powered by an excitation voltage. Its output, proportional to the excitation, is amplified to a high-level DC voltage and converted into strain units by digital systems and data acquisition hardware. Calibration is needed to verify that the amplification and conversion processes are precise, ensuring that the voltage accurately reflects the actual strain. This calibration process is generally straightforward. A mechanical calibration was conducted by comparing the UTM readings and corresponding known and precise displacements, measured by a caliper, when the extensometer device was connected to the testing machine. The gauge factor was derived to be 2.3 to adjust the deformation data.

3.2. Theoretical Methodology and Numerical Modeling

3.2.1. General

Key assumptions in shear-lag theory for optical fibres, as reported across various investigations, include that the optical fibre is axially stiff and resists deformation, and strain is transferred through pure shear stresses in the existing intermediate layers from the host to the sensing core. Key findings in the literature repeatedly marked that influential factors in strain transfer commonly include the bonded length as well as the adhesive and coating stiffness and thickness. Shorter bonded lengths may result in incomplete strain transfer, whereas stiffer adhesive facilitates better strain transfer and may amplify strain localization detections. Optical fibre coatings can dampen strain transmission due to their higher ductility and lower elastic modulus relative to the core fibre, resulting in reduced stiffness (Chapeleau and Bassil 2021; Clauß et al. 2021; Yang et al. 2021).

Numerical and experimental studies consistently show that strain transfer efficiency (STE) decreases near the ends of the bonded region due to bond discontinuities and localized stress concentrations. In these zones, the core fibre's strain lags behind the host material strain, as the bond redistributes the load over a characteristic length known as the strain (shear) transfer length. Surface-bonded DFOS systems capture this behaviour through distributed strain profiles that reflect the gradual transmission of strain along the bonded length, while regions beyond remain unaffected, directly representing the strain transmitted from the substrate to the core fibre.

Two characteristic regions are typically distinguished along the bonded length. The strain transfer length, or low-sensing zone, occurs near the bond free ends, where fibre strain increases from near-zero to values approaching those of the host. This transition, shaped by interface properties and boundary effects, is governed by a shear lag parameter that quantifies the rate of strain transfer. As bonding efficiency improves and strain loss through the intermediate layers decreases, this

region shortens, and the strain transition becomes steeper. The second region, known as the effective sensing length, is the central portion of the bonded length extending inward from the low-sensing zones on either side, beginning at the point where the core fibre's strain reaches at least 95% of the host strain (Falcetelli et al. 2020; Du et al. 2023). These defined regions form the basis for interpreting DFOS readings and are applied consistently throughout this study.

Previous analyses often assume an ideal bond between the layers of surface-bonded DFOS systems, including the adhesive interface between the host and sensor. However, surface irregularities at the bonding interface can significantly affect adhesive confinement and reduce the effective contact area. During manual installation and adhesive application, microvoids commonly form at the host–sensor interface, creating localized contact points that alter both the adhesive's performance and the actual bonded area between the sensor and the host material.

In cases of GFRP reinforcement in concrete structures, a stable bond between the bars and the surrounding concrete is essential for effective load transfer. Surface treatments, typically applied to enhance mechanical interlock, increase the surface roughness of GFRP bars. While this improves bonding with concrete, it can negatively impact the strain transfer to surface-mounted distributed fibre optic sensors (DFOS). Increased surface roughness introduces irregularities and microvoids that reduce adhesive contact quality, often due to insufficient surface energy for proper adhesive wetting. These inconsistencies diminish interfacial strength and STE, compromising the accuracy of DFOS measurements (Vollebregt 2014). Thus, a balance must be achieved between mechanical anchorage for structural performance and reliable sensor integration for monitoring.

Establishing a reliable bond between the optical fibre and the substrate is essential for effective strain transfer and the continuous acquisition of accurate measurements in surface-bonded DFOS

systems. Bond imperfections, such as air gaps and micro- or macro-voids within the adhesive layer, are often introduced during installation due to surface irregularities and can worsen further over time. Service-induced challenges, including inelastic shear deformation of the adhesive under sustained high loads, exacerbate these defects, increasing STE loss and disrupting the critical transfer of strain from the host material to the fibre. This degradation can significantly compromise the long-term accuracy and reliability of strain measurements.

Key factors influencing bond quality include the degree of adhesive wetting (i.e., overcoming surface energy barriers), uniform pressure distribution during sensor installation, appropriate adhesive selection and application, and the effective contact area at the sensor–host interface, which can also be affected by the sensing system's loading history. A thorough understanding of bondline behaviour and its evolution under critical conditions during testing and service is therefore vital for predicting the long-term performance and reliability of surface-bonded DFOS systems (Wan et al. 2008; García Garino et al. 2013).

Due to inherent material discontinuities at the adhesive interface, sharp stress concentrations, and in some cases, stress singularities, can develop, particularly near the bond edges. These localized stresses may exceed the adhesive's yield strength, resulting in plastic deformation and progressive degradation of the bondline. The extent and severity of this damage are influenced by factors such as load distribution, surface preparation, and the adhesive's inelastic mechanical properties. When stresses exceed a critical threshold, interfacial damage often initiates at high-stress points and can propagate along the bondline, particularly in the presence of localized defects such as voids.

While the inelastic behaviour of adhesives, such as stress relaxation, can mitigate the impact of stress concentrations by redistributing loads more evenly, this capacity is limited. Under high sustained loading, stress relaxation enables the adhesive to accommodate localized plastic

deformation and dissipate concentrated energy at the bond edges, reducing the risk of premature failure. However, once this localized damage progresses beyond a critical threshold and adjacent weak zones exist along the bondline, the adhesive may lose its ability to effectively transfer strain in a distributed manner or maintain bondline integrity. This degradation can significantly reduce strain measurement accuracy in surface-bonded DFOS systems and may permanently compromise sensor functionality. Moreover, additional factors such as repeated mechanical overloading, impact events, and environmental degradation (e.g., moisture ingress or corrosion) can further accelerate bondline deterioration (Da Silva et al. 2018).

This study presents a comprehensive mechanical analysis of a surface-bonded DFOS strain transfer model, developed for a three-layered sensing system in which the adhesive layer functions as a shared interface between the adherends. The modeled configuration comprises an elastic host material subjected to uniform tensile stresses, an adhesive bond interface exhibiting elasto-plastic behaviour, an elastic protective jacket, and a central core fibre layer, including the fibre and its cladding, with an elastic modulus significantly higher than that of both the intermediate and host layers. This refined model enables detailed evaluation of strain transfer mechanisms under sustained large-scale strain fields, accounting for bondline degradation and adhesive inelastic response beyond the yield threshold. Model validation is performed using experimental data from uniaxial tensile tests on DFOS-bonded GFRP bar specimens subjected to varying loading protocols, as described in **Section 3.1**.

3.2.2. Geometry and Stress States

In the analysis steps, the parameter i is substituted by $h,\ a,\ j,$ and c to donate corresponding parameters of the host material, adhesive, jacket material, and the core optical fibre, respectively. The term $2L$ represents the bonded length of the DFOS cable, symmetrically spanning the segment $-L \leq x \leq L$ relative to the midpoint of the bonded segment. The mechanical model considers a

three-layered sensing system composed of the substrate (host) layer, adhesive interface, jacket layer, and the core optical fibre layer. The host and jacket layers are bonded through a cohesive adhesive interface of negligible thickness t_a, consistent with cohesive zone modeling (CZM) reviewed in prior studies, such as previous papers by Lu and Xu (2013) and Lißner et al. (2019), as illustrated in **Figure 3-14**. Shear stresses are assumed continuous across the interfaces; hence, the shear stress at an element near the interface is taken as the interfacial shear stress.

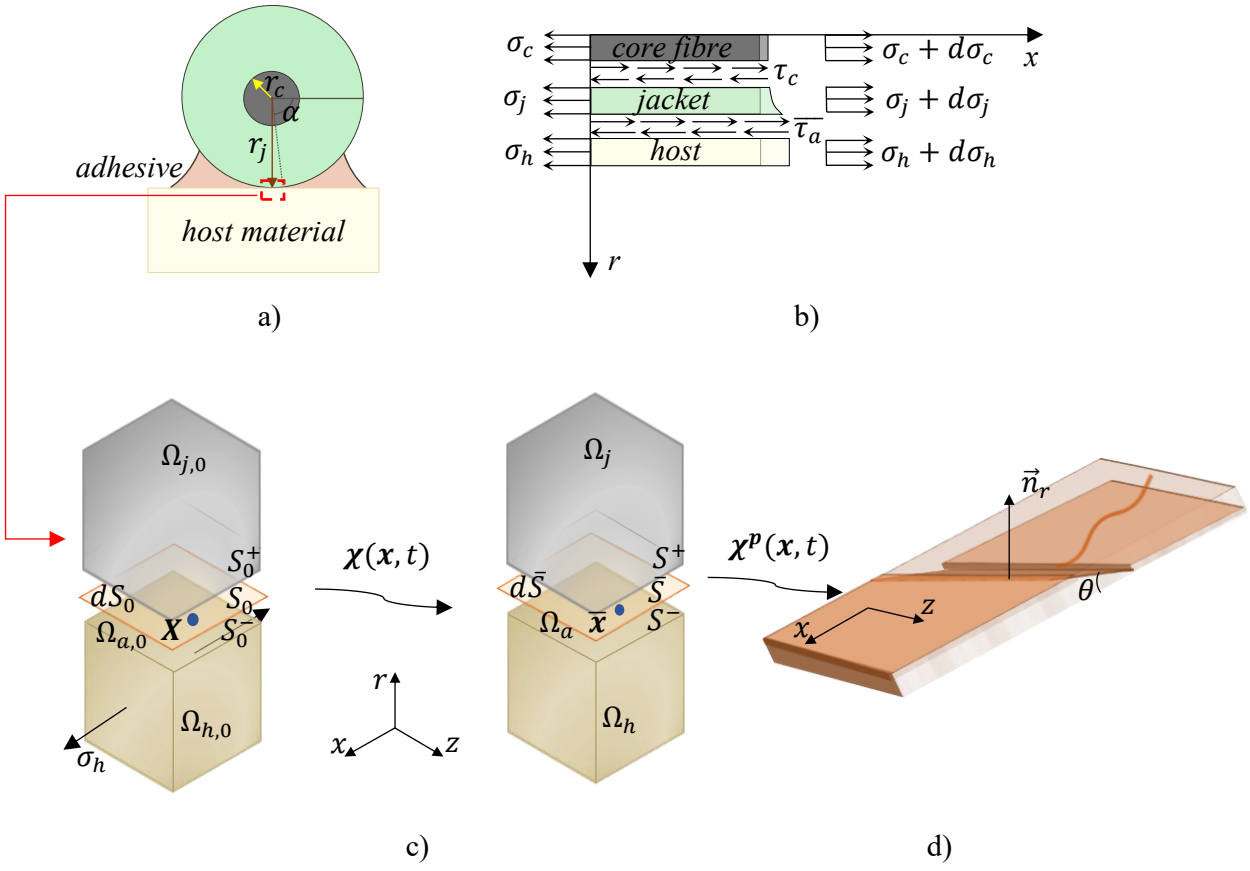

Figure 3-14. Conceptual schematics illustrating strain transfer in a surface-bonded DFOS system: a) cross-section of the DFOS–substrate assembly, b) stress state of each layer, c) illustrative kinematic behaviour of the adhesive interface, and d) schematic representation of inelastic shear localization within the adhesive

In **Figure 3-14a**, α represents the half−angle (in radians) of the unbonded regions along the jacket's perimeter, where no adhesive contact occurs, such that the effectively bonded perimeter

is given by $\pi - 2\alpha$. **Figure 3-14b** depicts the governing stress states, including normal (σ) and shear (τ), within microsections of each layer under applied tensile loading in the host, along two perpendicular axes: the radial direction, denoted by the independent variable r, and the direction of the externally applied load, represented by the independent variable x. $\overline{\tau_a}$ is the effective (or equivalent) shear stress across the interfacial adhesive surface.

The strain experienced by the host within each segment defined by the interrogator's spatial resolution (dx) is typically assumed to be uniform. The elastic behaviour of both the host and jacket layers are characterized, with an elasto-plastic adhesive interface between the host and the jacket, and a perfect bond between the jacket and core. According to **Figure 3-14b**, the equilibrium condition for the microsection of the core fibre ($0 < r < r_c$) leads to,

$$(\sigma_c + d\sigma_c)\pi r_c^2 - \sigma_c \pi r_c^2 + \int_0^{2\pi} \tau(x, r_c) r_c d\theta . dx = 0 \qquad \textbf{Eq. (3-1)}$$

$$\tau_c(x, r_c) = -\frac{r_c}{2}\frac{d\sigma_c}{dx} \qquad \textbf{Eq. (3-2)}$$

Similarly, by considering the equilibrium equations of the jacket and substituting the shear stress from the core layer, the shear stress in the jacket layer ($r_c \leq r \leq r_j$) can be expressed as,

$$\left(\sigma_j + d\sigma_j\right)\pi\left(r_j^2 - r_c^2\right) - \sigma_j \pi\left(r_j^2 - r_c^2\right) + \int_{\alpha}^{\pi-\alpha} \tau(x, r) r d\theta . dx - \int_0^{2\pi} \tau(x, r_c) r_c d\theta . dx = 0 \qquad \textbf{Eq. (3-3)}$$

$$\tau_j(x, r) = -\frac{\pi}{(\pi - 2\alpha)}\left(\frac{r^2 - r_c^2}{r}\frac{d\sigma_j}{dx} + \frac{r_c^2}{r}\frac{d\sigma_c}{dx}\right) \qquad \textbf{Eq. (3-4)}$$

At the adhesively bonded jacket–host interface, the interfacial shear stress is assumed to be equal to the shear stress induced by the adhesive $\tau_j\left(x, r_j\right) = \overline{\tau_a}$. The interfacial behaviour between the host material and the DFOS GFRP sensor is strongly influenced by the mode and rate of applied loading, which govern the dynamic response of the adhesive layer. This response involves a

combination of elastic deformation, plastic yielding, and bondline degradation beyond the yield point. Collectively, these mechanisms govern stress transfer across the interface and can be parameterized to simulate different adhesive bond responses. As such, the adhesive interface functions as a complex system, where the interaction between elastic and plastic processes directly impacts bonding effectiveness, stress distribution, and the overall structural performance.

The effect of elastic modulus mismatch becomes particularly pronounced in GFRP bars, where the significant difference between the adhesive and substrate moduli increases the likelihood of plastic deformation in the softer adhesive layer beyond its yield point. Under purely elastic deformation, contact between surfaces remains nearly uniform, and stress transfer across the interface is dominated by the relative stiffness of the materials. However, once yielding initiates, the adhesive exhibits elasto-plastic behaviour, characterized by an instantaneous elastic response corresponding to recoverable strains and a concurrent accumulation of irreversible plastic shear strains. This localized plastic deformation, illustrated in **Figure 3-14d** and discussed in the following section, occurs within the adhesive joint (Da Silva et al. 2018).

Such phenomena promote damage propagation along the bonded interface, leading to interlaminar cohesion loss following a characteristic spatial pattern. Consequently, strain measurements obtained from DFOS can become persistently inaccurate, compromising the reliability of monitoring applications and degrading long-term sensing performance (Wang et al. 2019).

According to CZM, the adhesive interface is governed by a traction-separation law, which defines the relationship between applied loads and displacement across the interface. The system geometry accounts for the complex kinematics of the adhesive and the progression of interfacial failure along the jacket–host interface by integrating adhesive continuum mechanics, micromechanical processes, and traction–separation behaviour. The jacket and the host body are defined as Ω_j and Ω_h, respectively, separated by a shared interface S, of adhesive layer which occupies a region

denoted as $\bar{S}$, in the deformed configuration Ω_a, as shown in **Figure 3-14c**. In the schematic representation, $\boldsymbol{X}$ represent an adhesive particle initially positioned on the surface S_0. During a motion characterized by the displacement field $\boldsymbol{u}$, initial material points shift to corresponding points in $S^{\pm}$ at time $t \in I = [t_0, T]$ through, $\boldsymbol{x}^{\pm} = \boldsymbol{X} + \boldsymbol{u}^{\pm}$ $(S_0 \longrightarrow S^{\pm})$, where $\boldsymbol{x}^{\pm}$ denotes the relocated positions of the upper (jacket) and lower (host) surfaces, $S^{\pm}$, in the deformed configuration, Ω_j and Ω_h, respectively. The deformation map χ, describes the position $\overline{\boldsymbol{x}} = \chi(\boldsymbol{X}, t) = (1/2)\boldsymbol{x}^{+} + \boldsymbol{x}^{-}$of the interface $\bar{S}$, with the relative displacement across the cohesive surface defined as $\boldsymbol{\delta} = \boldsymbol{x}^{+} - \boldsymbol{x}^{-}$.

Due to the DFOS's sensitivity primarily to axial elongation, the relative displacement is approximated by its axial component $\bar{\delta} = \boldsymbol{x}_x^{+} - \boldsymbol{x}_x^{-}$. In the elastic regime, this displacement corresponds to the relative elastic displacement $\bar{\delta}^e$. In the inelastic regime, deformation is described by an irreversible mapping, where the adhesive undergoes permanent plastic deformations. Under prolonged overload, localized plastic zones form initially at the bond edges due to stress concentrations and subsequently grow in response to internal resistance and loading conditions. As a result, the relative displacement across the cohesive surface increases irreversibly, causing a reduction in effective STE (Lu and Xu 2013).

3.2.3. Interactions within Adhesive Interfaces

This section focuses on incorporating the characteristics of the adhesive interface, emphasizing inelastic responses and the interfacial mechanisms that govern inelastic strain transfer from the host material to the DFOS. The constitutive formulations and theoretical foundations presented here draw upon well-established principles in material behaviour and plasticity, shear band localization and growth, interfacial damage evolution via CZM, as well as fracture mechanics and energy release criteria for adhesive joints. These concepts have been extensively developed in prior research, including works by Lu and Xu (2013) and Lißner et al. (2019).

Research on the failure processes and simulation of adhesive joints under elastic-plastic deformation has provided valuable insights into interfacial interactions, damage progression, and failure mechanisms. For example, the study by Johar et al. (2014) on adhesive joints under shear loading reveal that a characteristic sequence of fibrillation, plastic shear flow, and sliding precedes complete separation and failure onset.

The aforementioned studies identify the inelastic regime as encompassing both localized plastic deformation within the adhesive and microdamage mechanisms driven by dislocation motion at the microstructural level, in addition to elastic deformation. This enables the material to plastically deform without requiring additional stress beyond that necessary to initiate dislocation movement. Adhesive joints, which often exhibit non-uniform shear stress along the bondline, are particularly susceptible to shear localization in regions of elevated stress. This leads to the formation of plastic shear bands at stress concentration points, which can significantly reduce the bondline's capacity to carry load. These localized shear bands typically form at well-defined angles, commonly reported as $\theta = 45°$ relative to the principal stress direction, and serve as indicators of localized shear damage, as illustrated **Figure 3-14d**.

Progressive damage analysis by Panigrahi and Pradhan (2007) highlighted significant three-dimensional stress effects in adhesively bonded joints near the free surface. These variations, distinct from those within the interior, emphasize the complex stress transfer in the joint, where localized phenomena at the bond edges dominate and aid in predicting potential damage initiation sites. The study also indicated that adhesive layer failure is the primary site of failure. Consistent with findings from other studies, including the work by Lißner et al. (2019), results based on the strain energy release rate (SERR) indicate that interfacial damage in adhesive joints is predominantly governed by Mode II (shear-driven sliding) or Mixed Mode (a combination of Modes I and II). These modes play a critical role in characterizing the interfacial failure mechanisms and defining the dominant damage behaviour within the adhesive bond.

Markolefas and Papathanassiou (2009) extended prior research by investigating the development of plastic zones within the adhesive layer. Their study formulated and validated the stress and plastic strain distribution, demonstrating the formation of one or two plastic zones at the bonded region's ends, transitioning into elastic zones along the remaining bond length. This behaviour reflects the onset and progression of localized interfacial damage within the adhesive layer. In addition to these findings, other studies, such as the work by Budzik and Myhre Jensen (2014), further emphasized the critical role of plastic shear band formation at stress concentration points and its influence on energy dissipation and failure mechanisms in adhesively bonded joints.

The non-uniform distribution of shear stress and strain along the adhesive bondline contributes to the joint's durability and its ability to accommodate localized damage without significantly compromising global structural strength. When defects such as porosity, voids, or under-cured regions are present within the adhesive, the affected areas respond by redistributing the applied stress internally and toward adjacent regions along the bondline, rather than efficiently transferring it to the top adherend. This internal redistribution does not affect the peak shear stresses concentrated near the bond ends, which remain the dominant stress locations. However, if a chain of defects forms near the bond edge, driven by accumulated plastic deformation, plateau energy dissipation, or interfacial factors such as surface energy and work of separation, the adhesive stress field adjusts accordingly. Such redistribution facilitates continued load transfer and helps preserve the overall load-bearing capacity of the joint despite local degradation.

Proper surface preparation, controlled installation, and careful management of loading thresholds can effectively confine localized damage and prevent its propagation within the bondline. However, when the adhesive joint is subjected to continuous loading beyond its yield point, progressive damage initiates and becomes more pronounced in shorter bonded lengths, where a larger portion of the bondline is influenced by proximity to the free ends. In such cases, introducing an overload into the loading history accelerates the propagation of interfacial failure along the

bondline beyond the initial plastic zones. This reduces resistance to damage growth and increases localized instability near the bond edges, causing degradation to advance further into the bondline. Under these conditions, the adhesive interface must be analysed using a nonlinear framework that captures spatial and temporal changes in material properties and accounts for the accumulation of interlaminar deformation or separation. This necessitates iterative solutions to accurately model the progressive behaviour of the joint.

In this study, the adhesive's response to shear stresses near the bond edges is assumed to exceed the material's elastic limit due to elevated stress concentrations and localized geometrical discontinuities. Under sustained loading beyond the adhesive's yield point, the evolution of localized shear damage along the DFOS bondline is investigated. This behaviour is schematically illustrated in **Figure 3-14d**. The analysis captures the non-uniform shear stress redistribution, bond damage progression, and the resulting inelastic strain transfer from the host to the DFOS.

The analysis is conducted incrementally using an iterative solution to model damage evolution over time, improving the understanding and prediction of DFOS monitoring reliability under elevated strain levels and constant temperature. This approach quantifies the inelastic-dominated region of the adhesive interface, where damage from interlaminar sliding propagates inward along the bondline, weakening the interfacial interaction between materials and compromising strain transfer to the bonded sensor. Two key considerations are highlighted:

1) Damage progression is primarily examined under high sustained loads, though localized edge damage can also occur under varying loading modes at elevated stress levels. This underscores the complexity of adhesive behaviour, where edge-initiated damage may remain confined and not immediately propagate across the entire bondline.

2) Inelastic analysis becomes relevant only after the adhesive yields and the applied load is held constant. Prior to this, the DFOS bonded length is modelled elastically with no interfacial damage,

and the elastic solution is treated independently. Once yielding occurs, stress redistribution and the resulting relative displacement (or separation) between adherends are linked to host deformation. This enables simultaneous modelling of strain transfer and damage evolution. However, once unloading begins, the post-yield response becomes critical, as the material cannot simply revert to its pre-yield state.

The stress redistribution that occurs under sustained loading, along with the resulting damage length and the permanent plastic relative displacement between the adherends, must be defined as the final state before unloading begins. This final damage state, representing accumulated plastic deformation and interlaminar separation, directly influences strain transfer during unloading. As a result, it is essential to incorporate the finalized damage state when modeling the unloading phase, since the permanent displacement alters the DFOS response and affects strain transfer in subsequent loading cycles. Therefore, post-unloading strain transfer requires another revised analytical approach that accounts for the irreversible changes in the adhesive interface.

As the damage propagates, the damage length, defined as $L_d(t)$, represents the impaired region of the bondline at any time t, extending from the bond edge to the point where interfacial degradation has occurred. Within this portion, the adhesive has lost its cohesive and adhesive strength due to the presence of weak zones, often originating from insufficient initial bonding strength along the shared interface between the host and the DFOS. $L_d(t)$, which may initiate from one or both bond free ends, is treated as a time-dependent variable representing the accumulation of damage within the DFOS bondline under sustained loading, analogous to short-term fatigue conditions.

As $L_d(t)$ evolves, it alters the structural performance of the bonded joint. Following interfacial failure, and as noted by LeBlanc (1999), key regions along the DFOS bonded length, including the strain transfer length and the effective sensing length, must be redefined to reflect the evolving interfacial conditions. These adjusted lengths apply to the remaining undamaged, central elastic

region of the bondline, that is, the portion beyond $L_d(t)$ where no interfacial damage has yet developed and the adhesive continues to transfer strain effectively.

As outlined in the previous section, and drawing on the foundational work of Da Silva et al. (2018) and Malkiel and Rabinovitch (2021), the adhesive configuration at the host interface, marked by discontinuous edges and stress concentrations, results in a gradual attenuation of damage intensity. This is accompanied by a corresponding non-uniform redistribution and reduction of shear stress and relative displacement. The effect becomes increasingly significant moving from the free edge toward the central region, where the adhesive's stiffness becomes the dominant factor controlling the minimum shear stress level and thus shaping the spatial distribution of damage.

In this study, the adhesive interface is analyzed under Mode II-dominated loading, where interfacial shear stress is treated as the principal traction component, and relative shear displacement between adherends defines the deformation mode. The analysis accounts for DFOS sensitivity to axial displacements while incorporating separation and traction effects across the adhesive bond, represented by equivalent shear stress and relative displacement.

To model this behaviour, a bilinear CZM is adopted, consistent with the traction–separation frameworks discussed in Da Silva et al. (2018) and Romano et al. (2020), to describe the relationship between shear stress and relative displacement during damage evolution. In the elastic regime, this relationship is governed by a reversible traction–separation law, valid even in the absence of interfacial damage. Here, the elastic interfacial shear stress is expressed through a formulation that combines the core principles of the traction–separation law, Goodman's relation, and the Effective Modulus (EM) method, as previously developed by Markolefas and Papathanassiou (2009) and Wang and Xiang (2016). Thus, the elastic adhesive's interfacial shear stress, $\bar{\tau}_a^e$, can be rewritten as,

$$\bar{\tau}_a^e = K_{a,e}\bar{\delta}^e \qquad \textbf{Eq. (3-5)}$$

where $K_{a,e}$ denotes the effective elastic stiffness of the adhesive interface, characterizing the current state of interfacial adhesion. When $K_a \to 0$, the interface lacks stiffness and mechanical interaction; conversely, when $K_a \to \infty$, it represents a perfectly bonded interface. In the elastic phase, shear stress and relative displacement are assumed uniform along the bonded length.

As the applied load reaches a critical threshold, localized damage initiates at the interface, reducing the adhesive's ability to resist shear, commonly referred to as softening. This softening alters the spatial distribution of both shear stress and separation. Beyond the elastic regime, the shear stress (traction) and separation evolve spatially, calibrated by local variables to reflect the damage intensity and corresponding degradation of adhesive properties along the bonded length.

To incorporate this behaviour into a practical DFOS strain transfer model, a simplified representation is adopted. The spatial distribution of shear stress and separation is modeled using an exponential decay function with a decay factor q, applied separately to each half of the adhesive bonding length, treated as a semi-infinite joint. According to Da Silva et al. (2018) and Romano et al. (2020), the equivalent shear stress and separation distribution, donated as $\bar{\tau}_a^d(x,t)$ and $\bar{\delta}^{\,d}(x)$, respectively, under uniaxial loading within the damaged regions (excluding the central elastic portion), can be expressed as,

$$\bar{\tau}_a^d(x,t) = \bar{\tau}_{a,max} e^{-q(|L|-|x|)} \qquad \textbf{Eq. (3-6)}$$

$$\bar{\delta}^{\,d}(x) = \bar{\delta}_{max}\, e^{-q(|L|-|x|)} \qquad \textbf{Eq. (3-7)}$$

where, $\bar{\delta}^{\,d}(x) = \bar{\delta}^{\,e} + \bar{\delta}^{\,p}(x,t)$, with $\bar{\delta}^{\,p}(x)$ representing the permanent (plastic) separation, $\bar{\tau}_{a,max}$ and $\bar{\delta}_{max}$ denote the maximum shear stress and relative displacement (separation) at the bond edges, respectively. The decay parameter q is determined based on material properties and experimental observations.

Accurate modeling of damage progression in adhesive joints requires the integration of both spatial and temporal factors along the bondline. Drawing on the foundational work of Simo (1988), which emphasizes spatial covariance and plastic dissipation under non-uniform stress fields, various studies have adopted stepwise, incremental strategies to capture the complex nature of adhesive failure. These include the Griffith criterion, traction–separation laws, stochastic modeling, and energy release rate evaluations near the damage tip (Zotti et al. 2016).

In this study, a unified incremental–iterative framework is employed to simulate the initiation and progression of bond damage, as well as the resulting loss of STE along the adhesive bondline. Inspired by perturbation-based analyses of interlaminar damage growth developed by Bigoni (2012), the method iteratively updates shear stress and relative displacement distributions by accounting for spatial deformation inhomogeneity and void propagation along the interface. The incremental energy release rate, $\dot{G}_{II}$, is used to evaluate damage progression. Furthermore, stress singularities at the bond ends, arising from sharp geometric transitions and elastic assumptions, are considered. While idealized, these singularities underscore regions of elevated stress critical to understanding and predicting adhesive failure behaviour.

In adhesively bonded DFOS systems, interfacial damage progression under sustained high loads results in complex stress-separation interactions. Unlike the classical traction-separation law, which assumes a monotonic decrease in traction, this incremental formulation captures localized shear stress increases due to material stiffening phenomena, such as hardening or toughening effects, prior to complete decohesion. It also incorporates the time-dependent evolution of shear stress and relative displacement, enabling a balanced, straightforward, yet promising analysis of damage accumulation and stress redistribution. The model incrementally updates the damage state near the damage tip, specifically the bond edges, where stress singularities and localized damage peak. This unified framework addresses both fracture propagation and shear band formation under consistent assumptions, providing a comprehensive perspective on adhesive behaviour.

Studies such as Bigoni (2012) and the detailed handbook by Da Silva et al. (2018) demonstrate that shear localizations, when aligned with the material's principal orthotropy axes, behave analogously to Mode II cracks, thereby offering solutions for finite-length shear bands in pre-stressed, nonlinear elastic materials. The adhesive interface's inelastic response is cohesively modeled, reducing uncertainties related to assumptions of perfectly plastic behaviour or micro-crack evolution. Shear bands, conceptualized as slip discontinuities or fracture surfaces within the adhesive, are pre-stressed by field constraints and subjected to incremental Mode II loading. As these inelastic shear localizations propagate, stress concentrations at the damage tips accelerate interfacial degradation and drive damage progression. This approach provides a robust framework to analyze interfacial damage under short-term sustained loads, effectively capturing the interplay between stress localization, energy release, and damage evolution, while aligning to the analysis procedure for DFOS strain transfer mechanics.

Accordingly, perturbation equations are derived to model the time-dependent evolution of inelastic localization and the damage zone, defined by the damage length $L_d(t)$. Within the context of slip discontinuity or fracture surface mechanics, the change in potential energy associated with void growth in an anisotropic, pre-stressed body, subject to boundary conditions and stress localization, is expressed through an incremental gradient potential, such as the incremental stress intensity factor, $\dot{K}_{II}$. The subsequent equations, ultimately solved using time-harmonic Green's functions and further refined based on general formulations of edge damage, are adapted for a thin adhesive interface of thickness, t_a, following Bigoni (2012) and Da Silva et al. (2018). These formulations incorporate shear-induced effects on adhesive interfacial interactions, described as follows,

$$\hat{\tau}_a = \frac{\dot{K}_{II}}{\sqrt{2\pi t_a}}, \qquad \dot{K}_{II} = 1.12\bar{\tau}_a^{e,Yield}\sqrt{\pi L_d(t)} \qquad \textbf{Eq. (3-8)}$$

$$\hat{\delta} = 1.12(2+2\nu)\frac{\bar{\delta}^{e,Yield}\sqrt{\Delta l - \widetilde{r_a}}\sqrt{L_d(t)}}{2\sqrt{2}t_a}\mathrm{lm}(x) \qquad \textbf{Eq. (3-9)}$$

where $\hat{\tau}_a = \bar{\tau}_{a,max}(t)$ and $\hat{\delta} = \bar{\delta}_{max}(t)$ represent the incremental shear stress and relative displacement at the damage tip (focused on the bond endpoints), respectively. The term $\bar{\delta}^0 \cong \bar{\delta}^e_{max}$ denotes the adhesive's initial total homogeneous shear deformation at the bond edge prior to the onset of localized damage. The radial distance from the damage tip, $\widetilde{r_a}$ is taken as $\widetilde{r_a} = t_a$ the adhesive thickness, for this application. $\hat{\delta}$ applies to the shearing damage surfaces over a small incremental damage growth Δl. The $\mathrm{lm}(x)$ represents a mathematical component that regularizes the displacement field near the damage tip by eliminating singularities and incorporating the influence of rotational shear deformation, thereby ensuring a physically realistic representation of stress and strain distributions in the vicinity of the damage zone. For simplicity in this analysis, $\mathrm{lm}(x)$ is approximated as $1\ m^{-1}$.

In this incremental approach, the damage state is continuously updated based on the evolving damage length, which serves as an indicator of bond flaw severity. This allows precise tracking of both shear stress and interfacial damage progression along the adhesive bondline, as the incremental stress intensity factor, $\dot{K}_{II}$, evolves with damage growth. In the specific case presented, the damage length is updated at each incremental step, thereby modifying the local stress field near the damage tip at the adhesive edges.

Accordingly, the stress expression presented in the preceding equation is updated incrementally as damage progresses. At each step, the shear stress and interfacial separation (or shear displacement) at the bond edges are recalculated based on the evolving damage length, ensuring accurate tracking of stress and damage development over time. As the interfacial damage propagates, the shear stress redistributes along the bondline, while the peak values remain concentrated near the damage tip.

This process transforms the initially uniform distribution, particularly the final state at the adhesive's yield plateau, $\bar{\tau}_a^{e,Yield}$, into a progressively non-uniform profile as damage initiates and shear localization intensifies. The bondline is thus divided into two spatial segments corresponding

to damaged and intact regions, each sapping $\pm x \epsilon [\pm L, \pm L_d(t)]$ and $\pm x \epsilon [\pm L_d(t), 0]$, respectively, where the positive and negative signs denote symmetry. It is noted that $L_d(t)$ may differ on each side, reflecting the potential asymmetry in damage evolution.

Under short-term sustained loading conditions that exceed the adhesive's yield strength, interfacial damage emerges between the DFOS and the host substrate. As loading persists, energy accumulates at the interface, resulting in micro-scale separation or weakening of the bond. If the load remains above the adhesive's strength threshold, the damage zone continues to grow, further degrading the bondline and potentially leading to interfacial failure, particularly if the strain energy release rate exceeds a critical value. This damage progression is governed by a combination of material properties, interface geometry, and applied loading.

Although damage may not always manifest as a visible crack, it frequently arises through a combination of material instabilities, ultimately resulting in a loss of interfacial integrity and a compromised bondline. If the strain energy release rate increases with the growing damage length, rapid and unstable damage propagation can develop, potentially leading to complete interfacial failure. Conversely, a decreasing energy release rate may cause damage arrest at a lower energy level, significantly slowing progression. This behaviour aligns with experimental findings that often show an initial rapid damage advance followed by a slower propagation phase.

Finally, to capture the adhesive's elasto-plastic response under loading, shear stress and interface-relative displacement (or separation) functions are formulated using switching functions. These functions build upon the relationships established in **Eqs. (3-5)** to **(3-9**) and reflect distinct behaviours in the elastic and perturbed inelastic regimes. The relative displacement, $\bar{\delta}$, can be rewritten as $\bar{\delta} = u_h - u_j$, where u_i donates the axial displacement in the x-direction, of the host and jacket surfaces, respectively. By substituting this relation into the governing equations and rearranging the terms accordingly, the following expressions are obtained,

$$\bar{\delta}(x) = u_h - u_j = \begin{cases} u_h(1-\alpha_e^{\Delta}) \\ 1.12u_h(1-\alpha_e^{\Delta})(1+\nu)e^{-q(|L|-|x|)\frac{\sqrt{t_a}\sqrt{L_d(t)}}{\sqrt{2}t_a}}\mathrm{lm}(x) \end{cases} \quad \textbf{Eq. (3-10)}$$

$$\overline{\tau_a}(x) = \begin{cases} K_{a,e}u_h(1-\alpha_e^{\Delta}) \\ 1.12u_h\left(\left(K_{a,e}(1-\alpha_e^{\Delta})\right)_{Yield}\right)e^{-q(|L|-|x|)}\sqrt{\frac{L_d(t)}{2t_a}} \end{cases} \quad \textbf{Eq. (3-11)}$$

where α_e^{Δ}, is the adhesive's elastic displacement transfer ratio, used to simply quantify the efficiency of displacement transmission across the adhesive interface. A set of switching functions is applied to the appropriate regimes and segments, distinguishing between the elastic region and the localized, perturbed (damaged) inelastic region within the range $\pm L \leq x \leq \pm L_d(t)$.

Furthermore, in many analyses, the strain in the DFOS cable at the bonded length ends is often assumed to be zero, with simplified boundary conditions set as $\varepsilon_c(\pm L) = 0$. However, when quasi-static plastic deformations occur in the adhesive at the sensor–host interface, the DFOS far-field (edge) strains shift from these original zero values to permanent, constant magnitudes that develop rapidly during initial homogeneous plastic deformation. The accumulation of incremental plastic deformation in the adhesive at the bond ends causes the axial DFOS strains to increase significantly and then stabilize, maintaining this steady state with only minor further changes as bondline degradation progresses, as also observed by LeBlanc (1999). The evolution and stabilized value of these deformations can be experimentally determined, as demonstrated further in this study. In the analysis process, the edge strain can be expressed as a fraction, $Z_{b:\pm L}$, of the substrate strain, such that $\varepsilon_c(\pm L) = \varepsilon_p = Z_{b:\pm L}\varepsilon_h$.

3.2.4. Strain Transfer Mechanics Analysis

Now that the formulation of the adhesive interface is set up, we start analyzing the strain transfer mechanics. The general formulation presented in this section is consistent with the analyses

conducted in various studies, including those by Du et al. (2023), Wang and Xiang (2016), and Chapeleau and Bassil (2021). At the adhesively bonded jacket-host interface, the interfacial shear stress is equal to the shear stress induced by the adhesive $\tau_j(x, r_j) = \overline{\tau_a} = \{\bar{\tau}_a^e \text{ or } \hat{\tau}_a\}$, according to **Eq. (3-11)**. Substituting $\bar{\tau}_a^e$ and $\hat{\tau}_a$ into **Eq. (3-4)**, each at their relevant regime, the expression of stress gradient $d\sigma_j/dx$ related to each phase is obtained as,

$$\frac{d\sigma_j}{dx} = \begin{cases} -\frac{(\pi-2\alpha)}{\pi} K_{a,e} u_h (1-\alpha_e^{\Delta}) \frac{r_j}{r_j^2-r_c^2} - \frac{r_c^2}{r_j^2-r_c^2}\frac{d\sigma_c}{dx} \\ -\frac{(\pi-2\alpha)}{\pi} 1.12 u_h \left(\left(K_{a,e}(1-\alpha_e^{\Delta})\right)_{Yield}\right) e^{-q(|L|-|x|)} \sqrt{\frac{L_d(t)}{2t_a}} \frac{r_j}{r_j^2-r_c^2} - \frac{r_c^2}{r_j^2-r_c^2}\frac{d\sigma_c}{dx} \end{cases} \quad \textbf{Eq. (3-12)}$$

Within the jacket layer, the radial displacements are minimal compared to the axial displacements, and the radial displacement gradients can be neglected. Thus, using the jacket shear modulus, G_j, Hooke's law can be simplified as, $\tau_j(x, r) = G_j\gamma_j = G_j(\partial u/\partial r)$. Integrating this equation within the region from r_c to r_j, it can be obtained,

$$u_j - u_c = -\frac{1}{G_j}\frac{\pi}{\pi-2\alpha}\left[\left(\frac{r_j^2-r_c^2}{2} - r_c^2 ln\frac{r_j}{r_c}\right)\frac{d\sigma_j(x)}{dx} + r_c^2 ln\frac{r_j}{r_c}\frac{d\sigma_c(x)}{dx}\right] \quad \textbf{Eq. (3-13)}$$

Substituting $u_j = u_h - \bar{\delta}$ into **Eq. (3-13)**, with corresponding $\bar{\delta} = \{\bar{\delta}^e \text{ or } \hat{\delta}\}$ from **Eq. (3-10)**, while replacing the related expression of $d\sigma_j/dx$ from **Eq. (3-12)**, and rearranging the parameters, it can be rewritten as,

$$\frac{r_c^2}{G_j}\frac{\pi}{\pi-2\alpha}\left[\frac{r_j^2}{r_j^2-r_c^2} ln\frac{r_j}{r_c} - \frac{1}{2}\right]\frac{d\sigma_c(x)}{dx} - u_c = -u_h\beta_1(x,t) \quad \textbf{Eq. (3-14)}$$

$$\beta_1 = \begin{cases} 1 - \left((1-\alpha_e^{\Delta})\left(1 + \frac{f(r)}{G_j}K_{a,e}\right)\right) \\ 1 - \left((1-\alpha_e^{\Delta})_Y \left[\frac{(1+\nu)}{\sqrt{2}} + \frac{f(r)}{G_j}\left(K_{a,e}\right)_Y\right] \times 1.12 \times e^{-q(|L|-|x|)}\sqrt{\frac{L_d(t)}{2t_a}}\right) \end{cases} \quad \textbf{Eq. (3-15)}$$

where Y denotes the parameters associated specifically with the adhesive yield point, and β_1 is a

defined parameter to characterize the adhesive's interfacial strain transfer effects, within both elastic and inelastic regimes. It is estimated using the proposed switching function, where β_1 can be treated as a constant elastic parameter (donated as $\beta_{1,e}$ in the first case), or a time- and position-dependent variable, $\beta_1(x,t)$, representing slip discontinuities associated with shear band formation or fracture surface growth in the second case. $f(r) = r_j[(1/2) - (r_c^2/(r_j^2 - r_c^2) \times ln\,(r_j/r_c))]$ is a defined expression based on the contributing parameters.

The axial strain of the micro-section can be defined as the ratio of the axial displacement, u_i or its differential form du_i for micro-scale considerations, to the original length (dx), such that $\varepsilon_i = du_i/dx$. Accordingly, using the relation $\sigma_c = E_c(d\varepsilon_c/dx)$, where E_c is the elastic modulus of the core fibre, and taking the first-order derivative of **Eq. (3-14)**, the following expression is obtained,

$$\frac{1}{\beta_2^2}\frac{d^2\varepsilon_c(x)}{dx^2} - \varepsilon_c = -\beta_1(x,t)\,\varepsilon_h \qquad \textbf{Eq. (3-16)}$$

$$\beta_2^2 = \left(\frac{\pi}{\pi-2\alpha}\frac{E_c r_c^2}{G_j}\left(\frac{r_j^2}{r_j^2-r_c^2}ln\frac{r_j}{r_c} - \frac{1}{2}\right)\right)^{-1} \qquad \textbf{Eq. (3-17)}$$

where β_2 is a defined constant parameter related to $d^2\varepsilon_c(x)/dx^2$. **Eq. (3-16)** is a standard second-order nonhomogeneous differential equation. The general solution for the homogeneous part can be written in terms of hyperbolic functions since the characteristic equation has real roots. Replacing particular solution with $\beta_1\varepsilon_h$, **Eq. (3-16)**, final solution gives,

$$\varepsilon_c(x) = A\,sinh(\beta_2 x) + B\,cosh(\beta_2 x) + \beta_1\varepsilon_h \qquad \textbf{Eq. (3-18)}$$

where A and B are constants determined by the boundary conditions (BCs). Furthermore, the strain transfer coefficient, Z_x or $Z(x)$, is defined as the ratio of transferred strain from the host to the core fibre, representing the STE between the two components under load, formulated as,

$$Z(x,t) = \frac{\varepsilon_c(x,t)}{\varepsilon_h} \qquad \textbf{Eq. (3-19)}$$

For setting the BCs, we can refer to the previously defined bonded length, $2L$, spanning from $-L$ to L. Besides, the damage length, $L_d\ (t)$, represents the region affected by inelastic localization within the adhesive interface, initiating at the bond edges due to stress concentrations and progressing inward.

Each symmetric half of the bonded length is divided into distinct regions. Except at the center ($x = 0$), the boundaries separate the perturbed (damaged) and intact interface zones, with spatial ranges defined as $\pm x\ \epsilon[\pm L, \pm L_d(t)]$ for the perturbed region and $\pm x\ \epsilon[\pm L_d(t), 0]$ for the intact region. Parameters related to these boundary points are denoted by "$\pm b$," leading to the expressions of $Z_{\pm b}(t) = \{Z_{\pm L}(t)$ or $Z_{\pm L_d}(t)\}$, $x_{\pm b}(t) = \{\pm L$ or $\pm L_d(t)\}$, and $\beta_{1,\pm b} = \{\beta_{1,\pm L}(t)$ or $\beta_{1,\pm L_d}(t)\}$.

Assuming symmetry in the strain field ($\varepsilon_c(-x) = \varepsilon_c(+x)$), a simplification that may not strictly hold in real-world applications but is adopted here for analytical convenience, the BCs at $x = \pm b$ for each region can be assigned with common values for $Z_{\pm b}(t)$, $x_{\pm b}(t)$ and $\beta_{1,\pm b}(t)$ in **Eq. (3-18)**. Under this assumption, we obtain $A = 0$ and $B = \varepsilon_h(Z_{\pm b}(t) - \beta_{1,\pm b}(t))\ / cosh(\beta_2 x_{\pm b}(t))$. Substituting these values for A and B into the expression for $\varepsilon_c(x)$ and then inserting the resulting $\varepsilon_c(x,t)$ into the strain transfer function from **Eq. (3-19)**, the corresponding expression for $Z(x)$ is obtained as,

$$Z(x,t) = \frac{\varepsilon_c(x,t)}{\varepsilon_h} = (\beta_1(t) + \frac{\left(Z_{\pm b}(t) - \beta_{1,\pm b}(t)\right)}{cosh(\beta_2 x_{\pm b}(t))} cosh(\beta_2 x)) \qquad \textbf{Eq. (3-20)}$$

Chapter 4

Results and Discussions of the Uniaxial Tension Testing Program

4.1. General

Chapter Four presents the results and discussion of the tension tests, exploring the monitoring performance and strain transfer characteristics of the OFDR-based DFOS bonded to the surface of GFRP bar samples under various loading conditions. The chapter is structured into four main segments: discussion of failure results, pilot test outcomes, Stage II test results, and a final summary and discussion. Each sub-chapter of the pilot and Stage II test results begins with a verification of DFOS strain readings against measurements from the extensometer, referred to as EX, and ends with detailed demonstrations and analysis of the obtained DFOS strain distributions across diverse stress conditions of the test specimens.

4.2. Failure Results

All specimens exhibited a tensile failure of the GFRP bar, accompanied by varying failure modes and the subsequent rupture of the sensing cables, as depicted in **Figure 4-1**. As the applied load approached a critical threshold, around 90% of the ultimate strength, an audible cracking sound became noticeable, signaling the onset of material distress. This was typically followed by the failure of the adhered DFOS cable, leading to a progressive loss of signal integrity.

Signal attenuation in the DFOS system steadily worsened as the applied load increased, progressively weakening the signal until total loss and sensor rupture. At ultimate failure, typically corresponding to strain levels above 17000 microstrain ($\mu\varepsilon$), the GFRP bars experienced a sudden, brittle fracture, marked by an abrupt drop in applied load. This failure caused the bars to fragment along their free length, dislodging small glass fibres and pieces of the impregnation material that were visibly scattered around the fractured specimens.

Figure 4-1. Overview of sample failures, and fibre cable breakage

The most common failure mode was full tensile failure, with fibre rupture and matrix cracking along the entire free length, breaking the GFRP bar into jagged segments. Another observed mode involved partial or localized fibre fracture followed by fibre-matrix debonding, with fibres either snapped at the surface or separated along the length. In some cases, failure involved both the steel anchors and GFRP bar, indicating combined failure under stress concentrations. The GFRP bar did not fully fail within its free length, and DFOS readings continued; instead, it fractured along with the steel pipe, indicating the pipe reached its ultimate strength or had stress concentrations. These failure modes occurred only in samples with the SC GFRP bar, as shown in **Figure 4-2**.

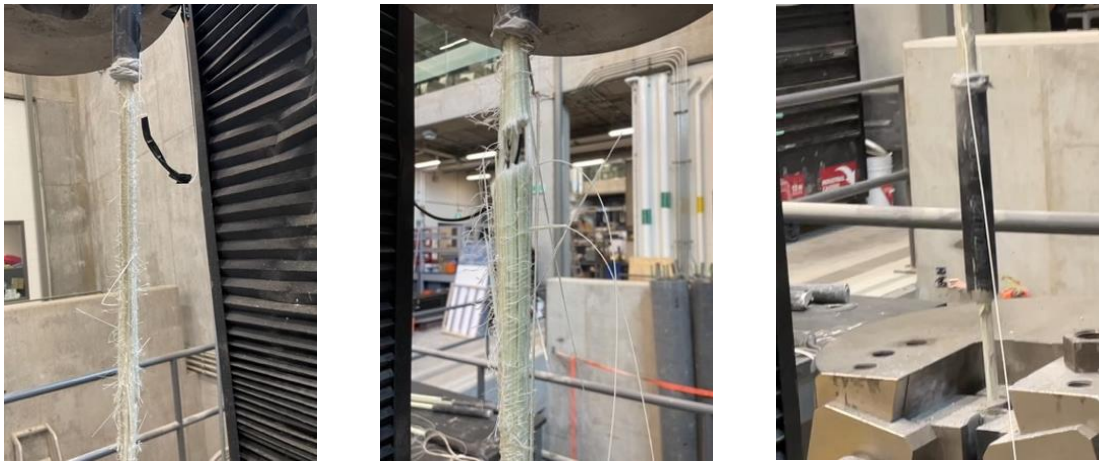

Figure 4-2. Non-typical failure modes observed in SC GFRP bar specimens

4.3. Pilot Test Results

4.3.1. Point-based Strain Measurement Verifications

The graphs shown in **Figures 4-3** and **4-4** present comparative point-based strain data recorded by the DFOS and EX instruments for the GFRP #12 and #16 sample configurations, respectively, throughout the entire test, with time on the horizontal axis.

These graphs focus on the measurements from the central area of the test samples, where EX device was mounted, and the DFOS achieved full strain transfer along their bonded length. The DFOS data represents measurements taken at the midpoint of the bonded length along the bar, while the EX data corresponds to the measurements recorded over its gauge length. Additionally, for sample SC-16-g, the reported DFOS reading near the midpoint of the bonded length was chosen, and the corresponding curve is labeled as DFOS-SC-16-g' in **Figure 4-4**, representing a portion of the bonded length that showed distinct monitoring behaviour, maintaining full signal integrity and consistent readings throughout the test.

Both DFOS and EX measurements generally exhibited a clear, linear relation between strain and applied load up to specimen failure. During initial monotonic loading, a consistent correlation was observed, with both methods effectively capturing strain development as the load increased, showing close agreement in their overall strain trends. However, beyond approximately 2000 to 3000 $\mu\varepsilon$, EX consistently recorded higher strain values than DFOS. Measurement discrepancies between the two systems typically ranged from 2% to 7% across test samples and strain levels. Notably, the error magnitude increased with strain, indicating a trend of growing deviation at higher levels. The observed differences may be attributed to errors associated with the physical characteristics and operational principles of each sensor, despite both being calibrated according to manufacturer specifications, the EX manually in the laboratory as a mechanical device, and DFOS through pre-calibrated wavelength-based measurements.

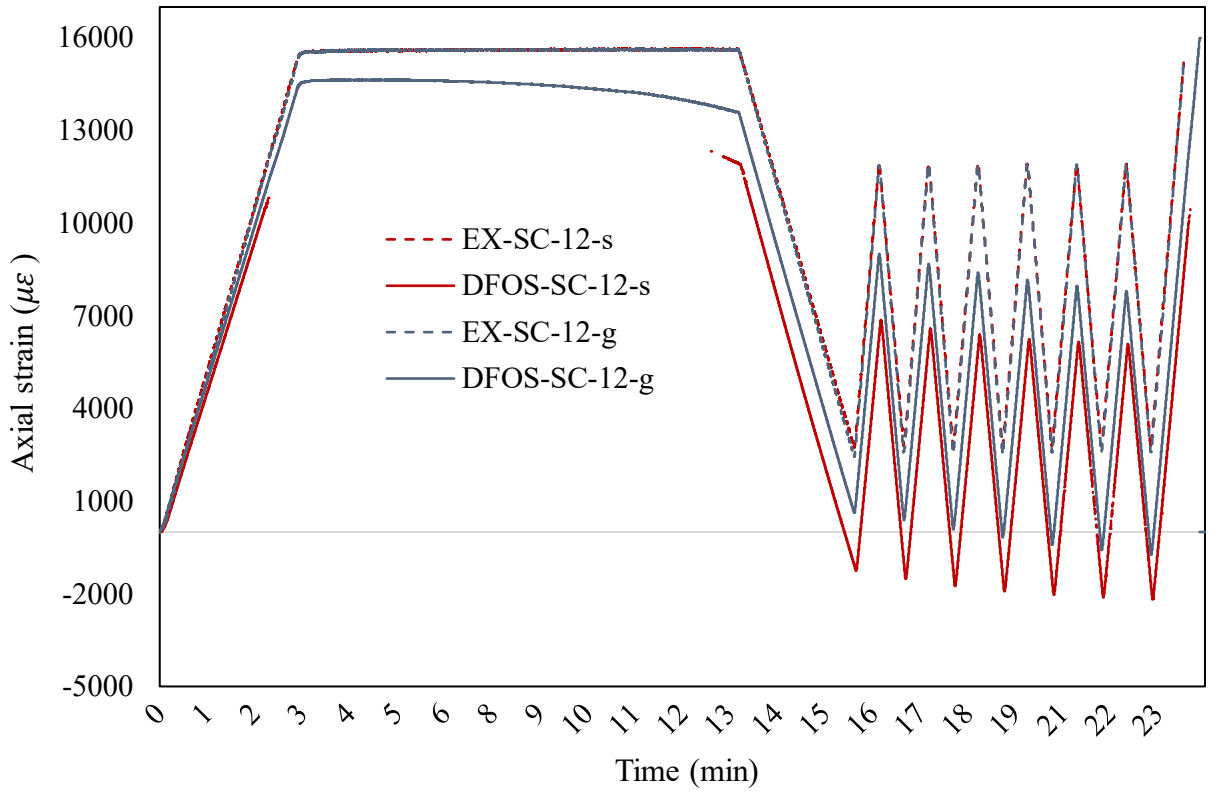

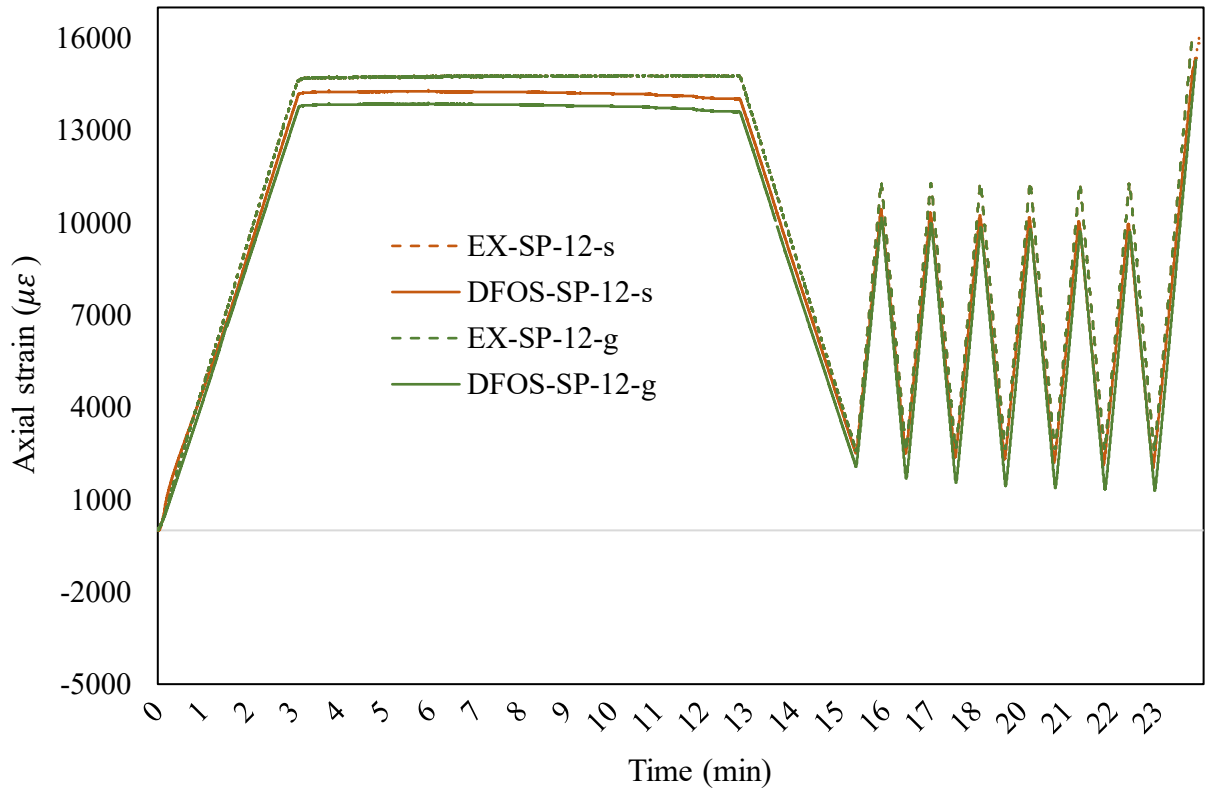

Figure 4-3. Point-based strain/time profiles obtained from DFOS and EX for GFRP #12 samples

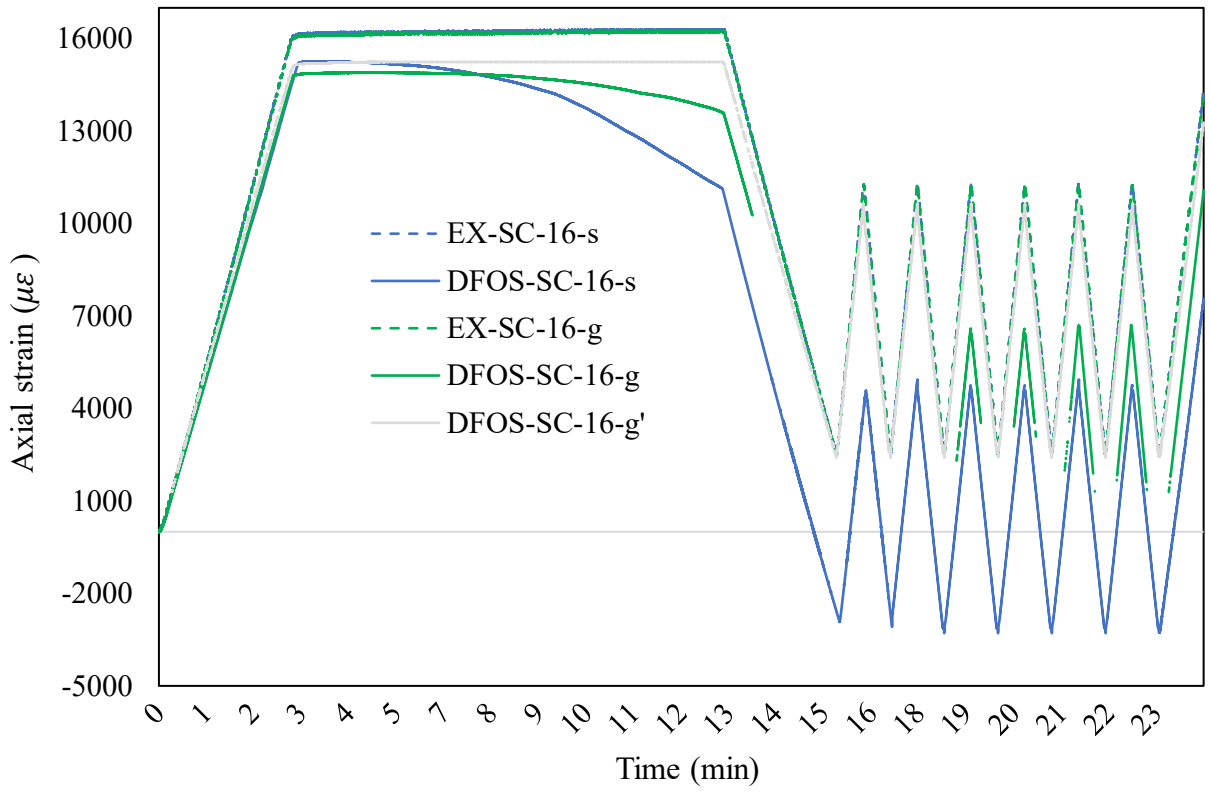

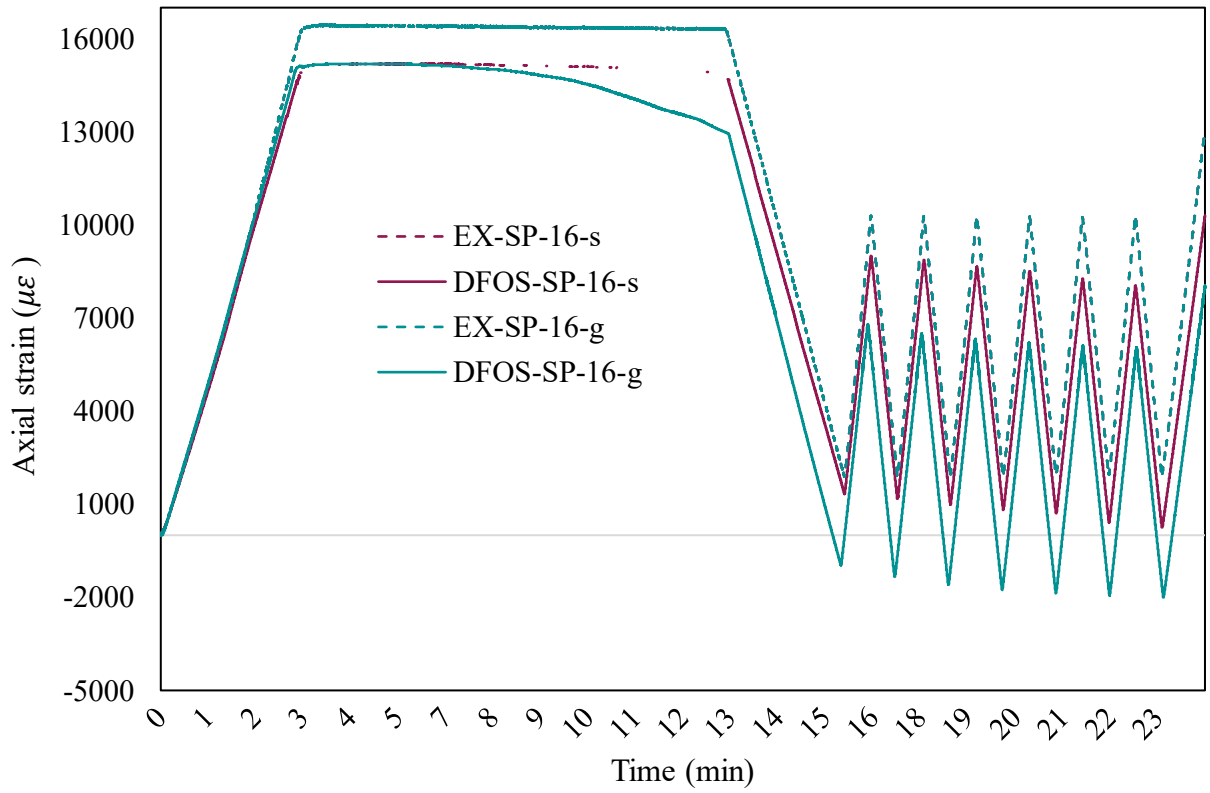

Figure 4-4. Point-based strain/time profiles obtained from DFOS and EX for GFRP #16 samples

The EX device, despite calibration, may introduce biases due to its physical configuration, potentially causing localized stress concentrations or inertial effects at the contact points with the GFRP bars, leading to strain overestimation. Mechanical uncertainties, such as misalignments, knife positioning variations, or minor bending, further contribute to measurement errors. On the other hand, the DFOS systems exhibit errors and strain transfer loss, due to the complex interaction between the optical fibre and intermediate layers, further amplified by sensor installation's inconsistencies and adhesive bond defects.

The inherent differences in the sensing principles, spatial resolution, and response characteristics likely amplify possible errors, leading to the divergence in measurements. Similar to the experimental conditions of this study, a recent study by Zhou et al. (2023), also observed a progressive deviation in DFOS and EX strain measurements, with values reaching 10000 $\mu\varepsilon$ for DFOS and 11000 $\mu\varepsilon$ for EX at a 70 kN load stop. Therefore, since the exact source of error and a full validation of the instrumentation in this study cannot be conclusively determined, the EX measurements are utilized as a reference for correlating and comparing reading patterns with the DFOS data, rather than relying on absolute strain values.

While both the EX and the additional DFOS point on sample SC-16-g recorded stable data and maintained a steady correlation with load steps during testing, with the additional DFOS point of sample SC-16-g also exhibiting marginally higher, yet noticeable, strain values compared to its DFOS midpoint, DFOS measurements at the midpoint of all samples, though initially consistent, progressively lost reliability under sustained high strain exceeding 13000 $\mu\varepsilon$. In this regime, the sensor exhibited a growing decline in measured strain for the same load intervals, with the rate of degradation varying across different sensing systems.

Based on the experimental results presented above, the samples can be ranked according to the extent of DFOS measurement degradation, interpreted as the loss in strain transfer efficiency

(STE), from least to most severe as follows: SC-16-g, SP-12-s, SP-12-g, SP-16-s, SC-12-g, SP-16-g, SC-12-s, and SC-16-s. This trend indicates a strong correlation between the mechanical quality of the sensor installation, the condition of its underlying path, and the bond strength of the bond between the sensor and the host material, all of which contribute to the long-term stability of DFOS measurements under elevated and sustained loading. Specifically, smoother surfaces, higher geometric and bonding uniformity, and greater anchoring rigidity were associated with reduced STE loss. Samples exhibiting lower degradation rates generally featured enhanced sensor attachment conditions, such as continuous groove channels in GFRP bars or relatively flat surfaces between spiral grooves in SP GFRP bars. These configurations contributed to improved interfacial stability between the sensing cable and the host, thereby minimizing STE loss effects and preserving DFOS measurement integrity under prolonged high-strain exposure.

Although samples with DFOS bonded to GFRP in a longitudinal groove or on a flat surface between spiral grooves generally exhibited low to medium rates of STE loss and monitoring reliability degradation, the observed variability in degradation rates indicates that additional factors were influencing the quality of the sensor installation. Despite consistent path conditions, varying rates of degradation were recorded, suggesting that factors such as installation quality, beyond the geometric configuration of the sensor installation path, contributed to the differences in performance. Specifically, the contrast between the DFOS midpoint and the additional DFOS point on sample SC-16-g, which exhibited higher readings and greater stability, suggests a potentially stronger bond between the optical fibre and the host material at that location, facilitating more effective strain transfer from the outset of the test.

During the cyclic stress phase, DFOS midpoints repeatedly recorded strain oscillations, with values deviating from the initial readings, and compressive strain emerging at the troughs of cyclic loading, like those observed during lower load steps in the unloading phase after sustained loading. The influence of strain history played a critical role in the subsequent readings as the system

transitioned from the severe static loading phase to the onset of cyclic loading. As the sensing system entered cyclic loading, the earlier discrepancies in recorded strain and STE loss due to bond degradation between the sensor and host material affected the sensor's response to the fluctuating loads. Consequently, DFOS readings reflected both the lasting cumulative effects of previous loading and the immediate changes resulting from the cyclic loading. Although a continued decrease in recorded strain was still evident after each cycle for some samples, it evolved at a significantly slower rate compared to the former phase.

As explained in **Section 3.2**, the progressive decline in monitoring efficiency over time is primarily attributed to the propagation of shear bond damage along the adhesively bonded joint line. This process led to interfacial failure between the sensor and the host material, disrupting effective strain transfer. The underlying cause was the adhesive's permanent plastic localizations, triggered by sustained excessive loading on the sensor's bond joint. Over time, this resulted in the gradual deterioration of bond integrity. These progressive bond degradations, varying in severity among test samples, impaired the sensors' ability to accurately reflect the strain within the host GFRP material. The employed DFOS systems continued to capture these relatively stable interlaminar plastic deformations throughout the remaining stages of the testing period until the end (Panigrahi and Pradhan 2007; García Garino et al. 2013; Da Silva et al. 2018).

As described by Krempl and Gleason (1996), when a material is subjected to stress beyond its yield strength, it undergoes irreversible plastic deformation that continues to influence its behaviour during unloading. In such cases, the material does not return purely elastically when the applied load is removed. Instead, as unloading occurs, the tensile stresses reverse direction, leading to the development of compressive stresses. This happens because the material, attempting to return to its original, unstressed state, is hindered by the effects of plastic deformation, which prevents full recovery. Consequently, residual internal forces emerge in the opposite direction,

manifesting as compressive stress. This behaviour is analogous to the adhesive bond between the DFOS and the host material across samples in this investigation.

The absence of a highly strong bond allowed the adhesive to undergo significant inelastic deformation under prolonged loading, especially as the load exceeded the critical local bond strength. Upon removal of the sustained applied loads, the weakened adhesive bond failed to recover elastically, resulting in increased redistribution of internal stresses within the adhesive interfaces. This behaviour led to the recording of compressive strains by the DFOS during the unloading phase in samples exhibiting greater STE loss, such as SC-12-s, SC-16-s, and SP-16-s. These samples, which are likely associated with weaker initial bonding between the DFOS and the host material, consistently recorded a broader range of compressive strain during unloading. The magnitude of the recorded compressive strain varied with the severity of STE loss among the samples, reflecting the differing extents of prior inelastic damage and bond degradation.

4.3.2. DFOS Strain Distributions

This section presents strain distributions from pilot test samples to analyze DFOS measurements, assess STE, and evaluate the uniformity and stability of distributed measurements under varying underlying sensor path conditions. Strain profiles are illustrated in the two-dimensional graphs where the *x*-axis represents the DFOS bonded length, and the y-axis shows axial strain values.

The subchapters are designed based on five durations of loading phases: initial monotonic loading, sustained loading period, monotonic unloading, fast cyclic loading, and final loading to failure. They include comparative demonstrations of strain distribution curves, allowing for analysis of strain patterns and the primary strain responses across the surface-bonded DFOS GFRP bar samples. Additional strain profiles with detailed load intervals and corresponding measurements for each sample are provided in **Appendix A**, providing a more gradual view of the observed monitoring behaviour under varying loading conditions.

4.3.2.1. First Monotonic Loading

Figure 4-5 presents DFOS strain profiles from pilot test samples under initial monotonic loading, with data shown at stress increments of approximately 175 *MP*a. The simultaneous EX readings, averaged from both samples of the same GFRP host, are represented as a strain level line ($\overline{\varepsilon_{EX}}$).

The DFOS data captured progressive strain variations across the samples as the applied load increased, providing insight into consistent monitoring behaviour under gradual, incremental loading. Despite minor differences and spatial inconsistencies which are due to installation-related deficiencies, a common trend is evident in the strain/length curves at this loading stage, in which strain is distributed relatively uniform along the DFOS central bonded length, flanked by steep gradients near the extremities (strain transfer zones). This pattern suggests effective stress transfer and measurement accuracy across the gauge length, regardless of the mounting method and indicates elastic response of the adhesive joint and reliability of DFOS to capture reliable strain of the host material. Throughout this period, the DFOS strain profiles remained predominantly stable.

In samples SP-12-g and SC-12-s, signal loss within the entire DFOS bonded length began at strain levels beyond approximately 8000 $\mu\varepsilon$, with progressively increasing severity. Additionally, nearly all DFOS GFRP samples experienced signal integrity loss within strain transfer zones, where strain transitions from zero at the free length to that of the host material, beyond almost 3000 to 4000 $\mu\varepsilon$. The former signal loss is attributed to poor physical interaction between the fibre and host material at elevated strain levels, while the latter results from the optical resolution limits of DFOS in capturing steep strain gradients within short distances.

Regarding signal loss in DFOS, Herbers et al. (2024) identified conditions where correlation quality between reference and measurement degrades within virtual gauges due to vibrations, micro-slippages, high strain gradients, or external factors such as splices and poor fibre terminations. In such cases, dropouts occur, with unreliable data replaced by NaN values.

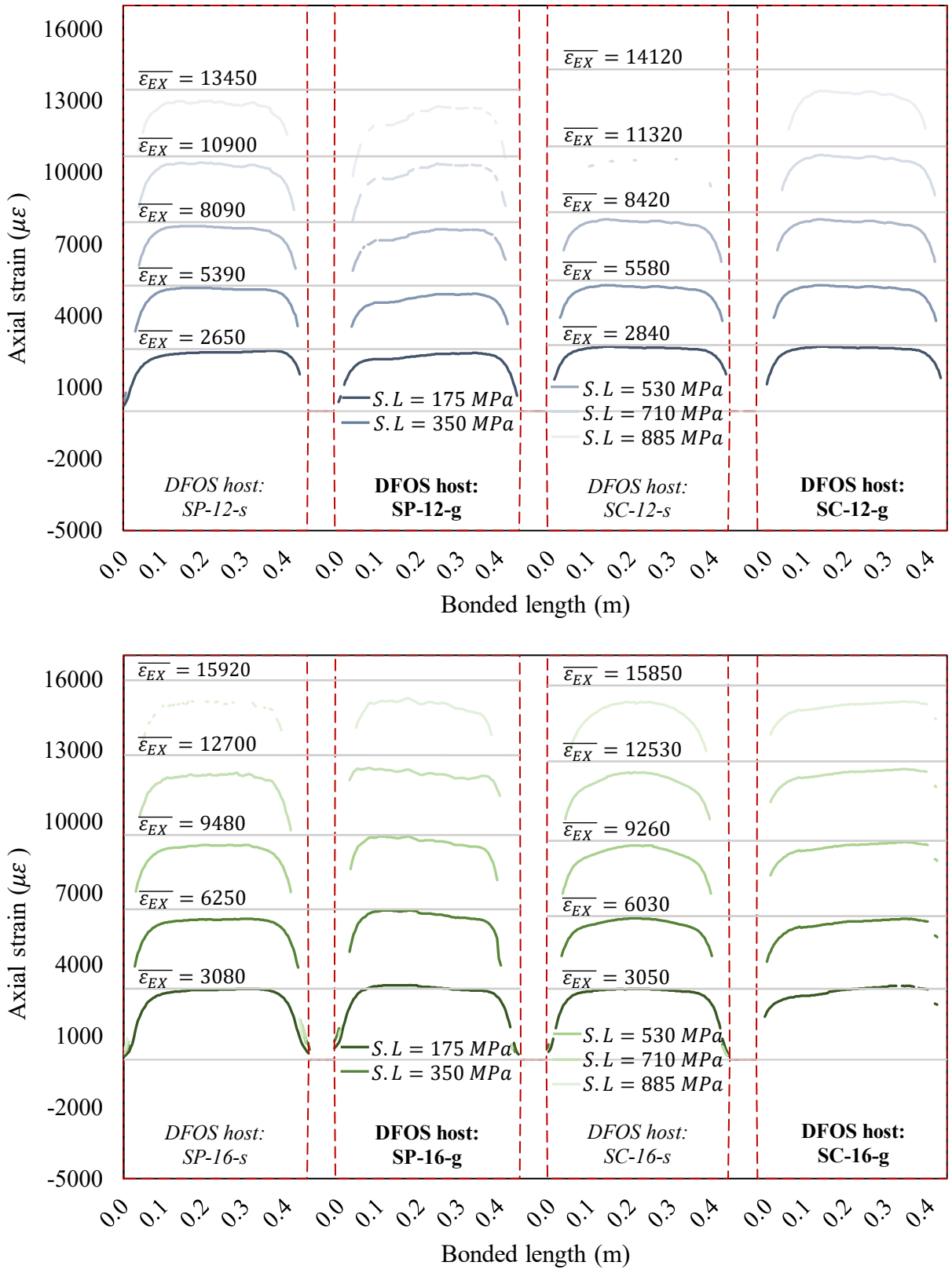

Figure 4-5. DFOS strain distribution curves captured during initial monotonic loading ($S.L :=$ stress level, $\overline{\varepsilon_{EX}} :=$ simultaneous EX average strain reading)

DFOS measure strain via changes in backscattered light, but due to Rayleigh scattering frequency and photonic constraints, it struggles to resolve high strain gradients over short distances. When the strain in the host material increases rapidly across a narrow zone, the fibre's spatial resolution may not be sufficient to accurately capture these steep transitions, even with 0.63 *mm* provided by OFDR. The Rayleigh frequency, which defines the smallest measurable strain change over a given length of fibre, is constrained by the physical properties of the optical fibre, including its scattering characteristics. As a result, DFOS may struggle to resolve the sharp variation in strain across the strain transfer zone, leading to complete loss of the strain data in this region.

Additionally, slippage between intermediate layers, especially within adhesive contact interface where imperfections in installation such as poor bonding or localized voids can lead to attenuation or irregular light scattering, preventing the sensor from recording accurate data in certain sections. This can be applied to sample SC-12-s that contained the highest volume of voids caused by surface roughness that resulted in complete signal loss that evolved since relatively early stages, after 8000 $\mu\varepsilon$ level. Dropouts are particularly concerning as they create data gaps, undermining the accuracy and completeness of strain measurements. In critical applications, such as monitoring localized damage or stress concentrations, frequent dropouts can compromise the reliability of the analysis, potentially leading to misinterpretations of material behaviour.

Among the test specimens, the grooved embedded DFOS sample, except SC-12-g, exhibited noticeably reduced accuracy along half of the bonded length. This performance reduction is likely due to the installation constraints specific to the grooved embedding process. In this configuration, the DFOS cable had to be embedded in a groove and extend through both ends, where it was constrained by the steel pipe anchors at the GFRP bar ends. Instead of allowing for downward pressure during adhesive curing, this setup may have caused outward pressure on the fibre at the ends, potentially leading to incomplete embedment. As a result, the bondline integrity may have been compromised, with micro-voids or insufficient adhesive contact partially affecting strain

transfer and reducing the sensing accuracy in these samples. However, this issue was addressed in the Stage II samples, and the results will be presented in **Section 4.4**.

4.3.2.2. High-level Sustained Loading

This section examines strain distribution in samples under high-level sustained strain, with measurements taken at five 2.5-minute intervals to track changes over time, as depicted in **Figure 4-6**. This phase aimed to understand a preliminary simulation of the long-term stability of DFOS distributed measurements and any potential drift in strain readings of the host GFRP material.

Initial strain distributions were uniform across all samples, indicating reliable sensing performance with minimal influence from microstructural variations within the intermediate layers of the sensing system. Over time, however, all specimens exhibited a gradual decline in effective sensing length and STE, reflected in the progressive reduction of distributed strain measurements and the evolving strain profiles during constant loading.

All samples, except SC-16-g, experienced a complete loss of well-bonded sensing regions as bond damage began at the edges and propagated toward the midpoint, ultimately leading to a significant reduction in the strain values recorded by DFOS along the entire bonded length. This continuous degradation is believed to result from progressive bondline damage due to accumulated plastic shear deformations within the adhesive layer, followed by partial separation or slippage of the DFOS cable along the full bonded length, which compromised STE across the entire bonded length. The gradual loss of distributed STE varied across the samples, reflecting differences in bondline strength under the applied high sustained stress, as well as variations in overall installation quality and adhesive performance.

Furthermore, two samples, SC-12-s and SP-16-s, showed continuous signal attenuation from the start of loading, ultimately leading to almost complete signal loss along the central region of th bonded length during the period of sustained high-stress application.

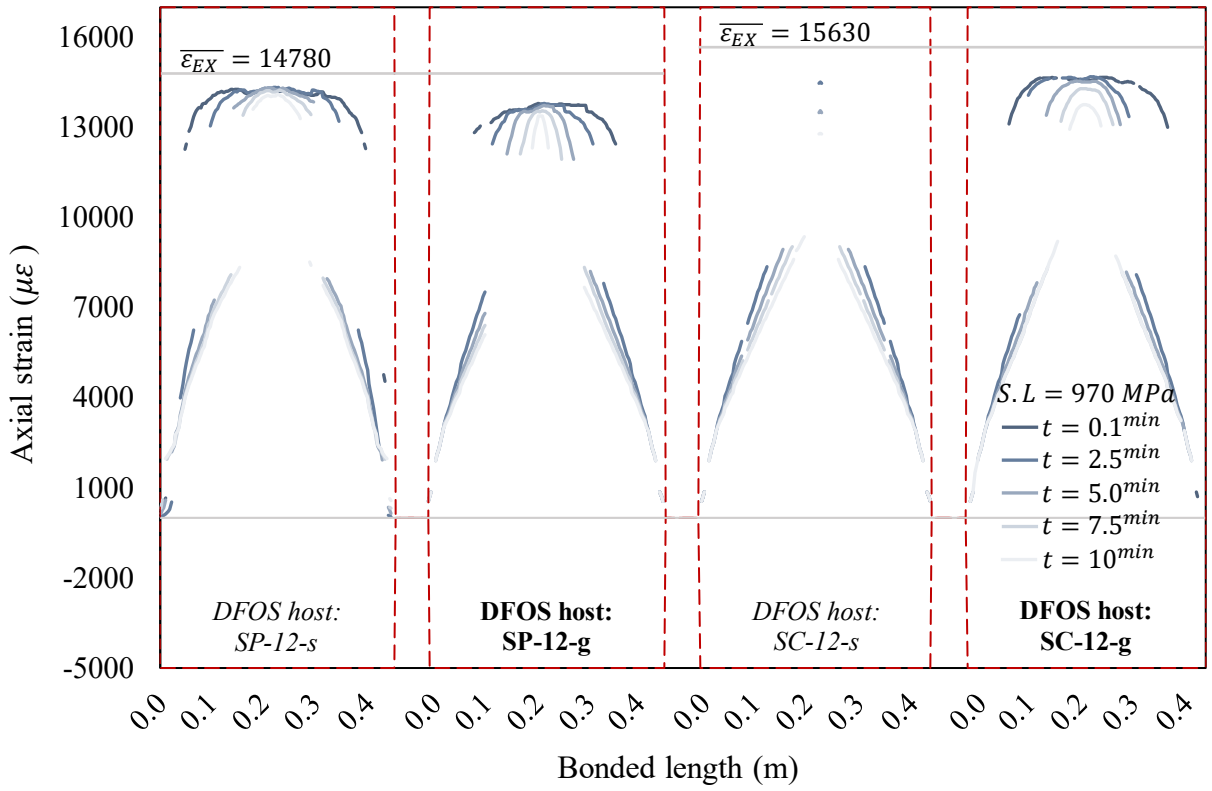

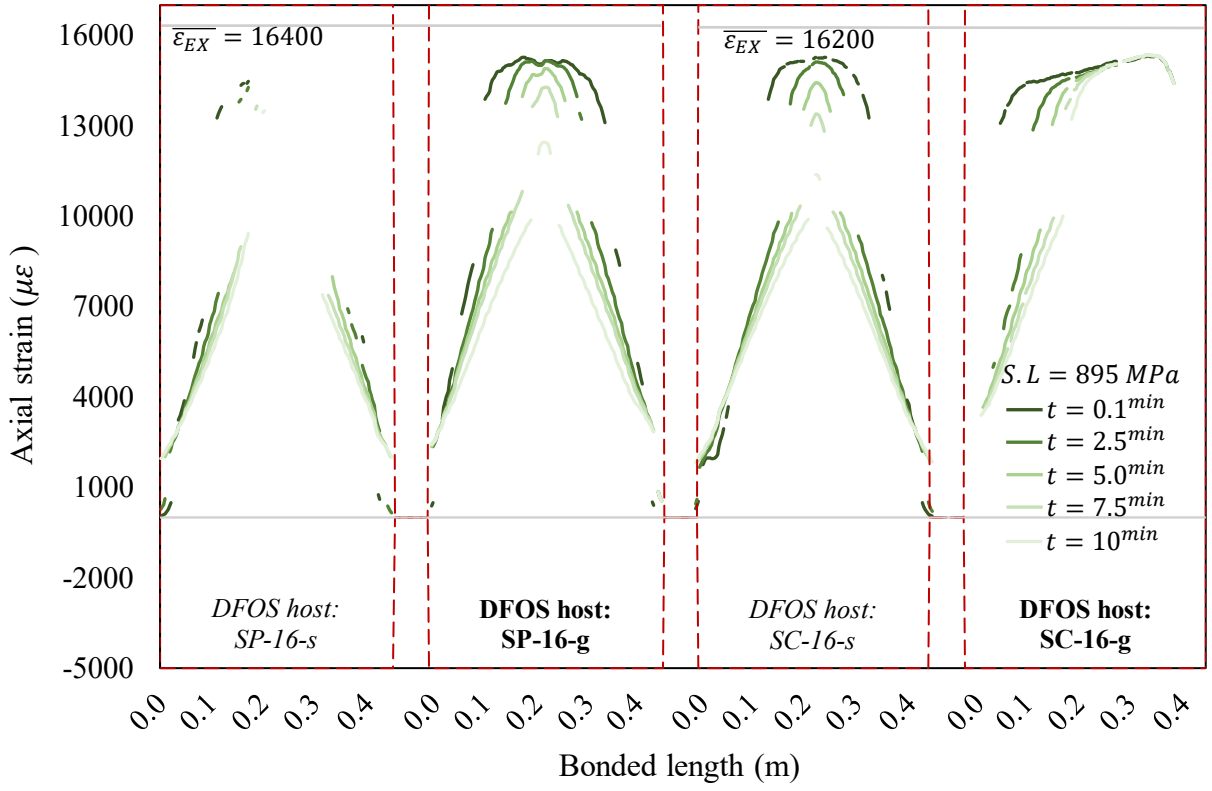

Figure 4-6. DFOS strain distribution curves captured during sustained load period

Remarkably, interfacial failure along the sensor–host interface appeared to develop symmetrically along the DFOS bonded length in all test samples, initiating at the bond edges, where stress concentrations were present, and progressing inward. However, specimen SC-16-g showed bondline degradation over only half of the bonded length on one side. This asymmetrical strain pattern in sample SC-16-g is primarily attributed to installation-related inconsistencies and the extent of void filling achieved, which may have also hindered uniform strain transfer along the entire bonded length during the earlier monotonic loading phase, as previously noted.

In comparing the effect of sensor installation path on performance stability under severe loading, samples with smoother sensor paths, such as grooves or flat surfaces between SP GFRP ribs, generally exhibited more robust and stable STE than those mounted on the rough surfaces of SC GFRP bars. Notably, SC-16-g consistently maintained elevated strain levels along its remaining effective sensing length, with identical initial and final DFOS readings. In contrast, the rough and irregular texture of the SC GFRP surfaces in samples SC-12-s and SC-16-s introduced microvoids, gaps, and uneven adhesive distribution, which hindered the formation of a well-confined adhesive and effective sensor–host contact. These conditions compromised bond quality during installation, reducing both adhesive and cohesive strength along the bondline and accelerating progressive bond degradation under sustained high loads. This issue is particularly evident in the significant variability between the initial and final strain readings at the midpoint of the DFOS bonded lengths for samples SC-12-s and SC-16-s, which typically represents one of the last regions to experience bond damage, where DFOS measurements decreased by around 1800 and 4000 $\mu\varepsilon$, respectively.

The direct surface-mounting method proved more effective for SP GFRP specimens, which have a more uniform surface treatment. The consistent groove spacing and smoother surface of spiral-ribbed GFRP bars enhanced bonding with surface-mounted DFOS, improving bond strength and STE stability under challenging loading conditions, thereby reinforcing the critical bond between the host and the sensor compared to SC GFRP bars. However, for SP GFRP bars, groove-

embedded DFOS samples exhibited relatively lower performance stability compared to surface-mounted counterparts, likely due to increased peeling stresses at the sensor's free ends, where the DFOS cables exited the groove and encountered mechanical constraints.

4.3.2.3. First Unloading

The graphs displayed in **Figure 4-7** show the strain profiles captured during monotonic unloading after the sustained load stop. The results highlight how distributed strain measurements, which were uniform across the DFOS GFRP bar samples during first monotonic loading, show distinct non-uniformities with similar trends due to the previously experienced bondline degradation.

Bondline damage had substantial consequences for the reliability and interpretation of DFOS data, particularly after prolonged and severe loading conditions. The strain distribution curves in these graphs clearly demonstrate that interfacial failure between the DFOS and the GFRP bar introduced discrepancies along the bonded length, following a common and predictable pattern. In the central segment, all samples registered strain values lower than those recorded during the initial monotonic loading phase. This suggests that permanent shear deformations in the adhesive layer led to lower-than-expected strain measurements.

Additionally, all samples recorded consistent, non-zero strain near the edges of the DFOS bonded length, indicating residual strain and localized effects from loading history. These arose from permanent shear deformations in the adhesive bondline, especially near bond free ends, where irreversible changes caused the DFOS to register plastic strain of the underlying adhesive after formation and stabilization during previous damage progression. Detailed graphs are provided in **Appendix A**. These observations reveal the complex interactions between history of mechanical stress, present bond quality, and strain transfer in DFOS systems. This insight is crucial for understanding how well distributed sensing can perform in high-demanding SHM applications when structures face previously prolonged overstress conditions in the monitoring history.

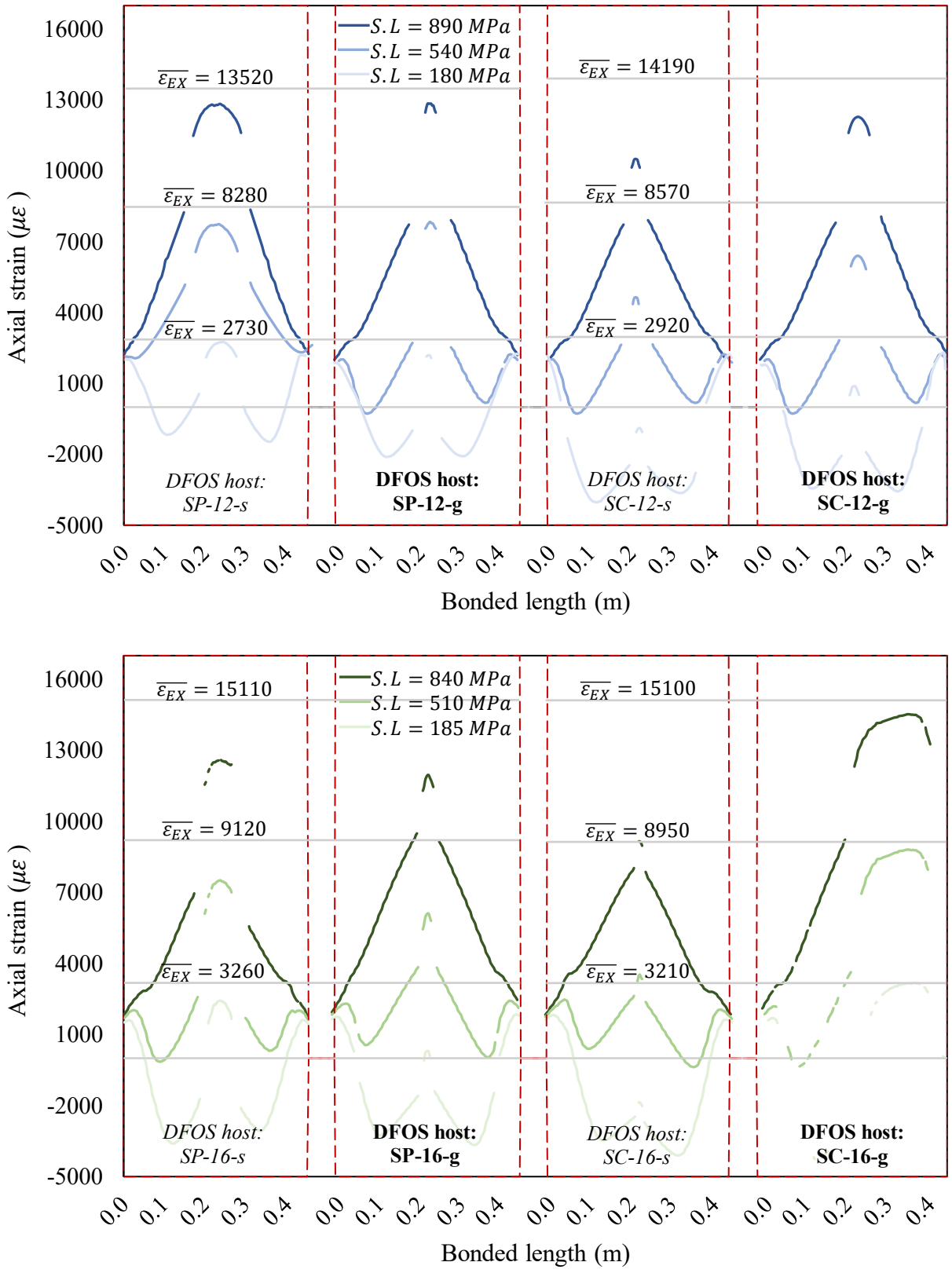

Figure 4-7. DFOS strain distribution curves captured during unloading after sustained load stop

4.3.2.4. Fast Cyclic Loading

The charts shown in **Figure 4-8** present strain profiles of the test samples, recorded at critical points during fast cyclic loading, capturing the variations at the peaks and troughs of multiple repetitive load cycles. Despite the impact of bond damage on strain readings, the distributed measurements remained relatively consistent throughout the cyclic loading phases. This is evidenced by the close agreement between strain profiles from the initial and final cycles, as shown by the overlapping trends and stable distribution patterns in the recorded data. This consistency is notable because it suggests that while interfacial failure affects absolute strain values, the relative patterns or trends in the strain distribution remain recognizable over time and across cycles. This implies that cyclic loading alone did not disrupt the integrity of the sensing systems to a catastrophic extent. Instead, the DFOS recorded strain patterns that, while distorted by adhesive bond shear plastic deformations, retained identifiable characteristics from one cycle to the next.

The consistent distributed strain transfer behaviour, distinct from the linear, elastic response captured initially before exposure to sustained high loading, is evident in the first and sixth (final) 'trough' and 'peak' curves in each graph. Each cycle appears to re-establish a similar distribution pattern, with minor shifts. The shifts observed from the start to the end of this phase include slight improvements in distributed STE in the side zones, reflected by marginally higher recorded strain values, and reduced strain in the central zone, likely due to further accumulation of plastic shear deformations. The increase in strain at the sides and decrease in the central zone suggests a gradual redistribution of stress along the adhesive joint, moving toward a more balanced state over time.

These patterns show the bonded sensing system's ability to deliver repeatable data across multiple load cycles. Minor drifts in strain readings stem from adhesive shear stress redistribution due to prior plastic deformations, not issues during cyclic loading. Despite this, stable strain readings under repeated cycles suggest the surface-bonded DFOS system is suitable for monitoring environments with frequent stress variations, as will be further shown in **Section 4.4.2.2**.

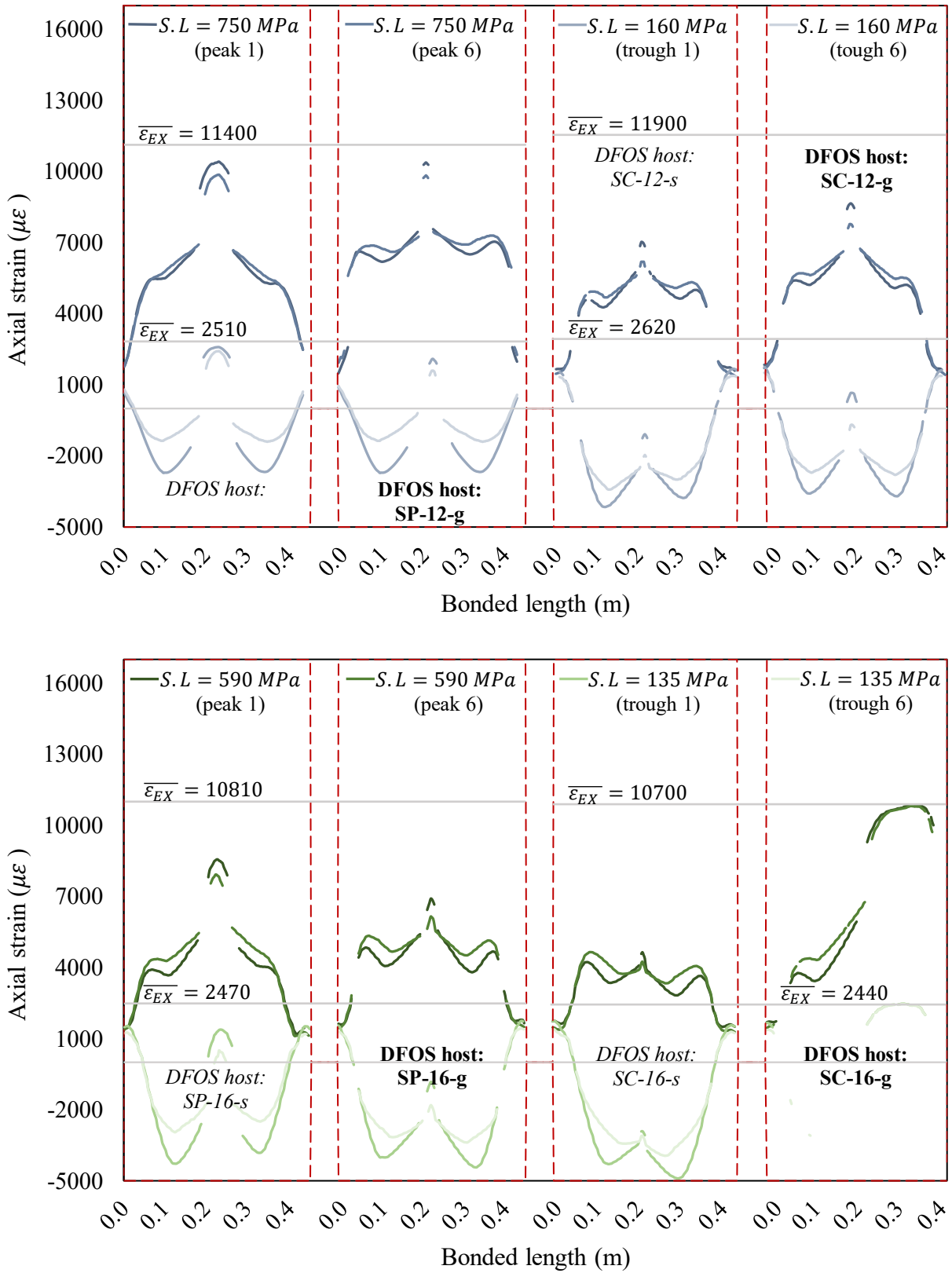

Figure 4-8. DFOS strain distribution curves captured at cyclic loading peaks and troughs

Furthermore, during this phase, at stress troughs, all samples recorded negative strains along the DFOS bonded length due to the sign change in stress in response to previous overloading conditions, indicating compressive behaviour of the damaged sensing system during unloading to significantly lower loads. However, this compressive response was not observed in the central regions of all samples. Specifically, within the remaining effective sensing length, the DFOS layout on sample SC-16-g consistently recorded the same strain values at peaks and troughs as those captured during initial monotonic loading, implying a more robust capability to capture strains following complex loading histories.

4.3.2.5. Last Monotonic Loading to Failure

Finally, the graphs presented in **Figure 4-9** capture the strain distributions across pilot test samples as they underwent monotonic loading to failure. Throughout this final loading phase, each sample exhibited a clear escalation in strain, with the DFOS layouts capturing evolving strain profiles along their bonded lengths on the GFRP bars, clearly demonstrating the progressive intensification of strain leading up to failure with extreme values.

Once again, the curves indicate that strain distributions increased consistently with progressive load intervals, though they remained non-uniform along the DFOS bonded length because of previously absorbed bondline damage. Each sample exhibited a characteristic 'arching' strain pattern, with peak recorded strain values concentrated at the central region of the bonded length. This central concentration reflects the higher STE in that region, where the bonded DFOS system remained more effective at capturing the host material's strain due to reduced degradation in transmission through the adhesive interface. In contrast, the accumulation of plastic shear deformation was more pronounced toward the bond edges, leading to reduced accuracy in those zones. As loading progressed, the smoothness of the strain curves declined, showing sharper peaks and more abrupt slope changes. Additional detailed graphs are provided in **Appendix A**.

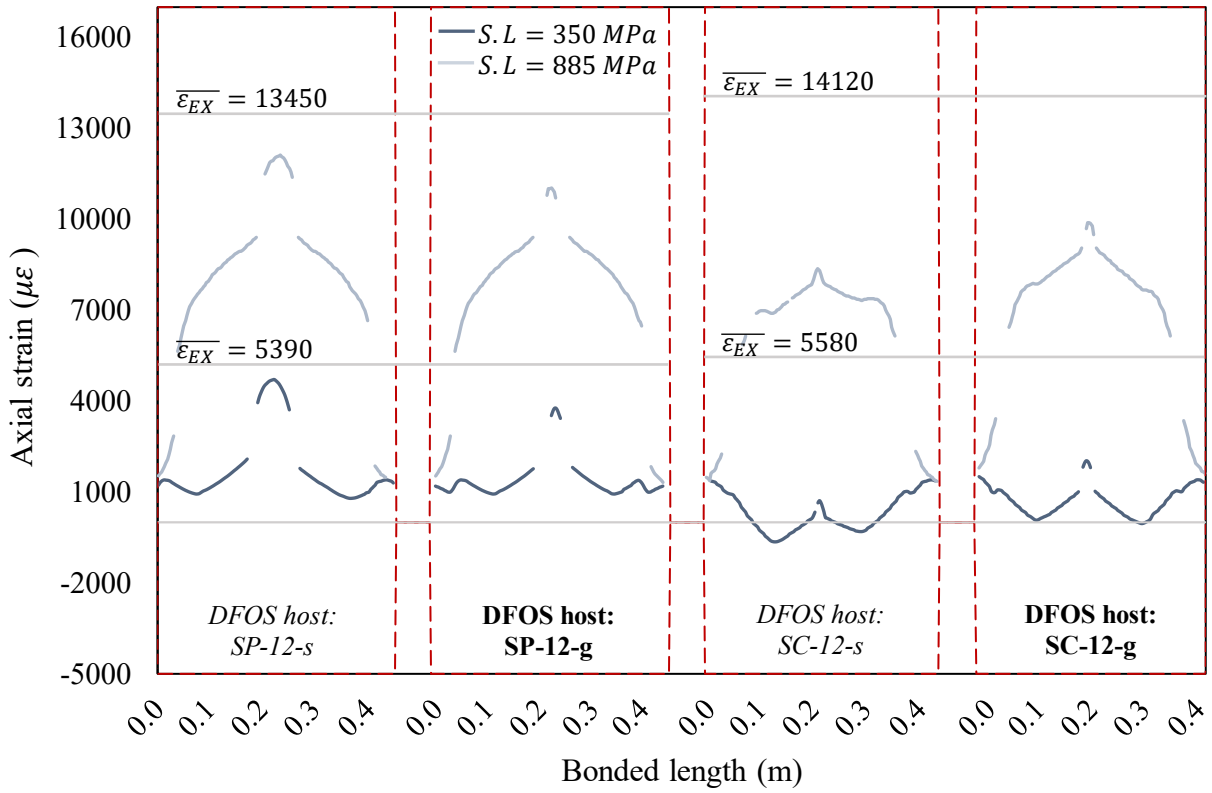

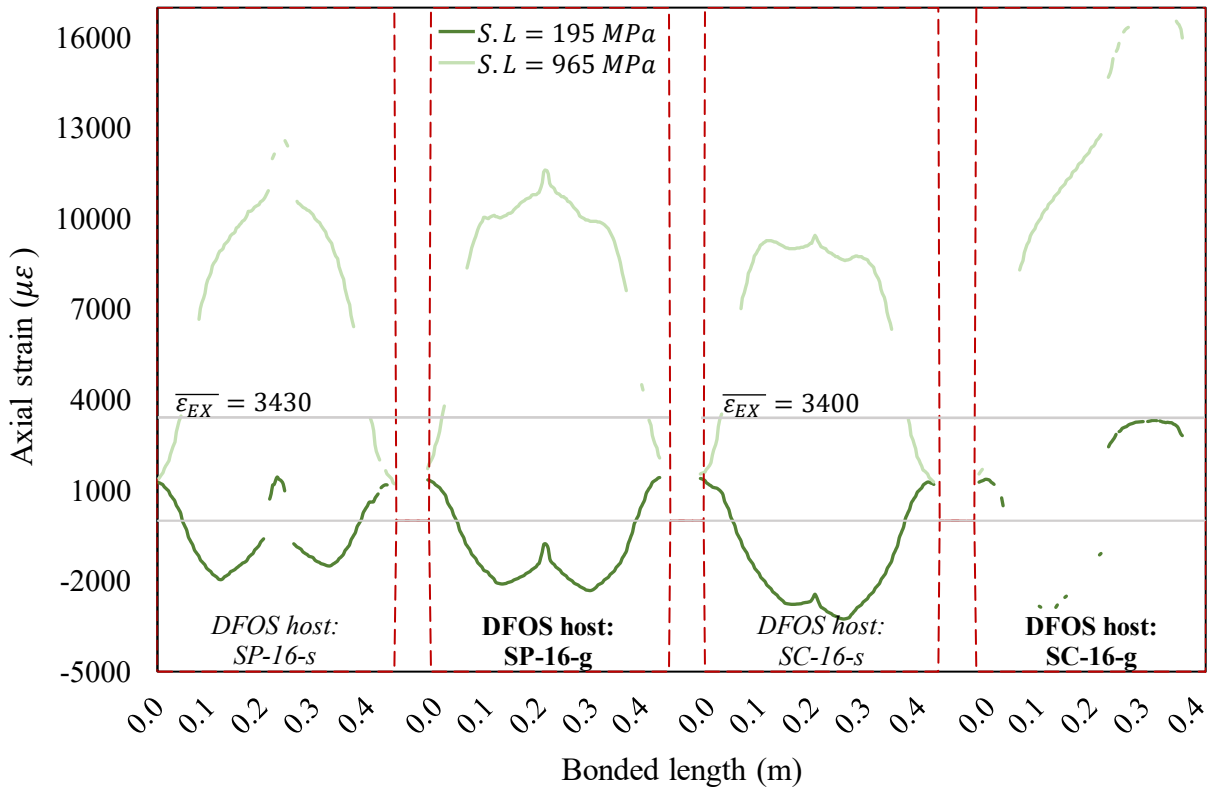

Figure 4-9. DFOS strain distribution curves captured during final loading to failure

4.4. Stage II Tension Tests

4.4.1. Point-based Strain Measurement Verifications

In the Stage II tension tests, DFOS-instrumented specimens with four varying DFOS configurations, except specimen MST-C with only two DFOS layouts, were analyzed. This phase focused on assessing the performance of the various DFOS configurations under distinct loading protocols, including cyclic and sustained histories. The results provide insight into the influence of sensor layout and loading type on DFOS measurement behaviour.

Figures 4-10 and **4-11** compare strain measurements from various DFOS layouts with EX readings at the midpoint of all test samples, showing a strong correlation across the full strain range with ~ ± 2–5% agreement. No progressive deviation in DFOS measurement response was observed at elevated strain levels, indicating stable elastic behaviour and reliable performance of the bonded sensing systems at the midpoint under increasing sustained load steps.

However, the g-PVC-CN and s-PVC-EP layouts on sample SP-S failed to maintain reliable strain measurements during the final sustained load step, where strain levels exceeded 14000 $\mu\varepsilon$. As observed in the pilot tests, this behaviour corresponds to a prolonged overloading condition for the adhesive bond interface, during which gradual accumulation of plastic shear deformations beyond the adhesive's yield strength reached a critical threshold. As a result, bond degradation progressed to affect the entire bondline, including the midpoint, which typically resists damage the longest.

Remarkably, all DFOS configurations within each test sample showed a high degree of consistency in measured strain values, with only slight variations, typically higher readings from polyimide (PI)-coated DFOS and cyanoacrylate (CN)-adhered DFOS layouts compared to their counterparts. This suggests that, where adhesive inelasticity did not compromise cohesion at the midpoint of the bonded length, the OFDR-based sensing units reliably captured strain throughout the entire testing.

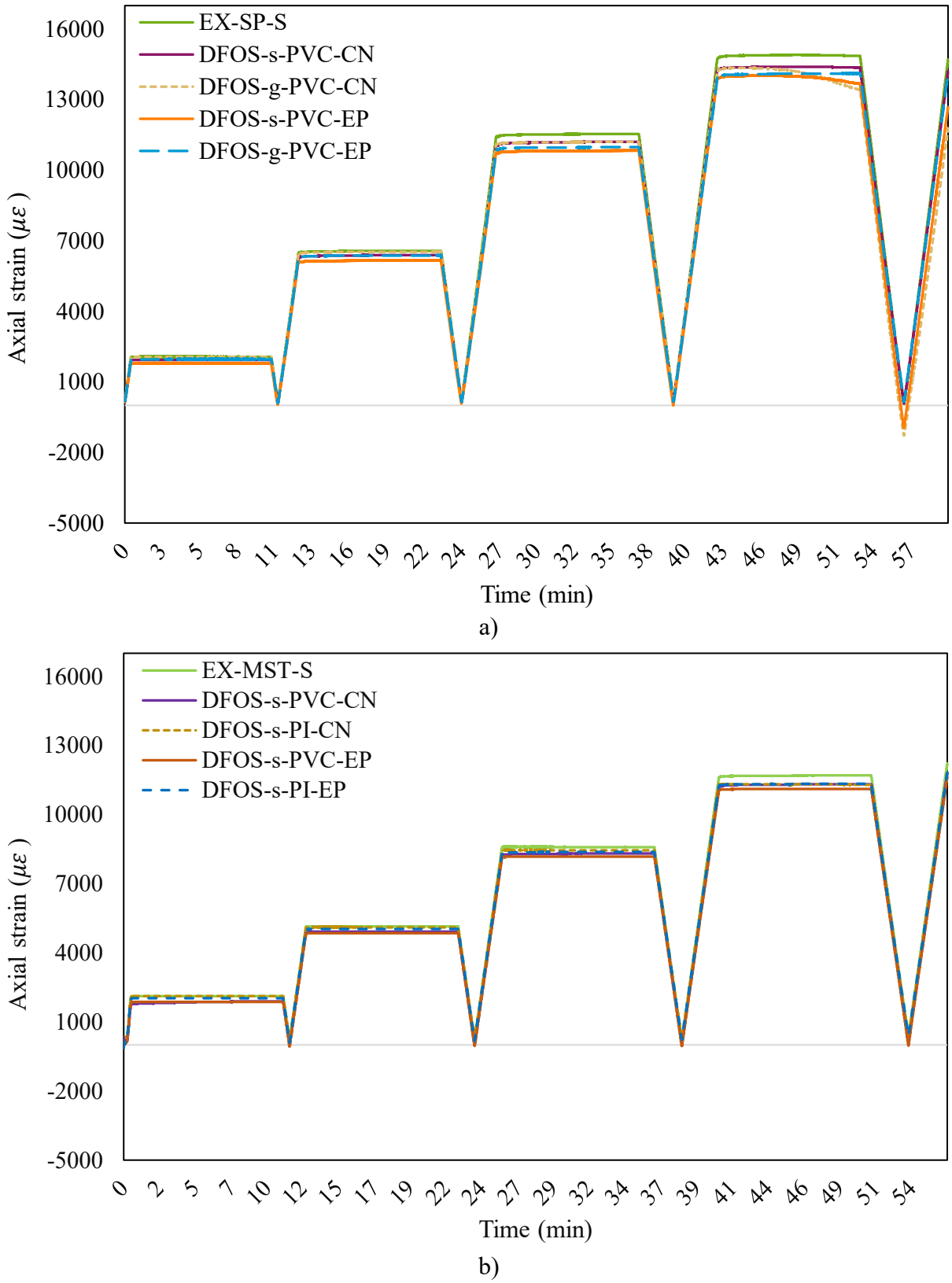

Figure 4-10. Point-based strain/time profiles obtained from DFOS and EX for Stage II test samples subjected to loading protocol S: a) SP-S and b) MST-S

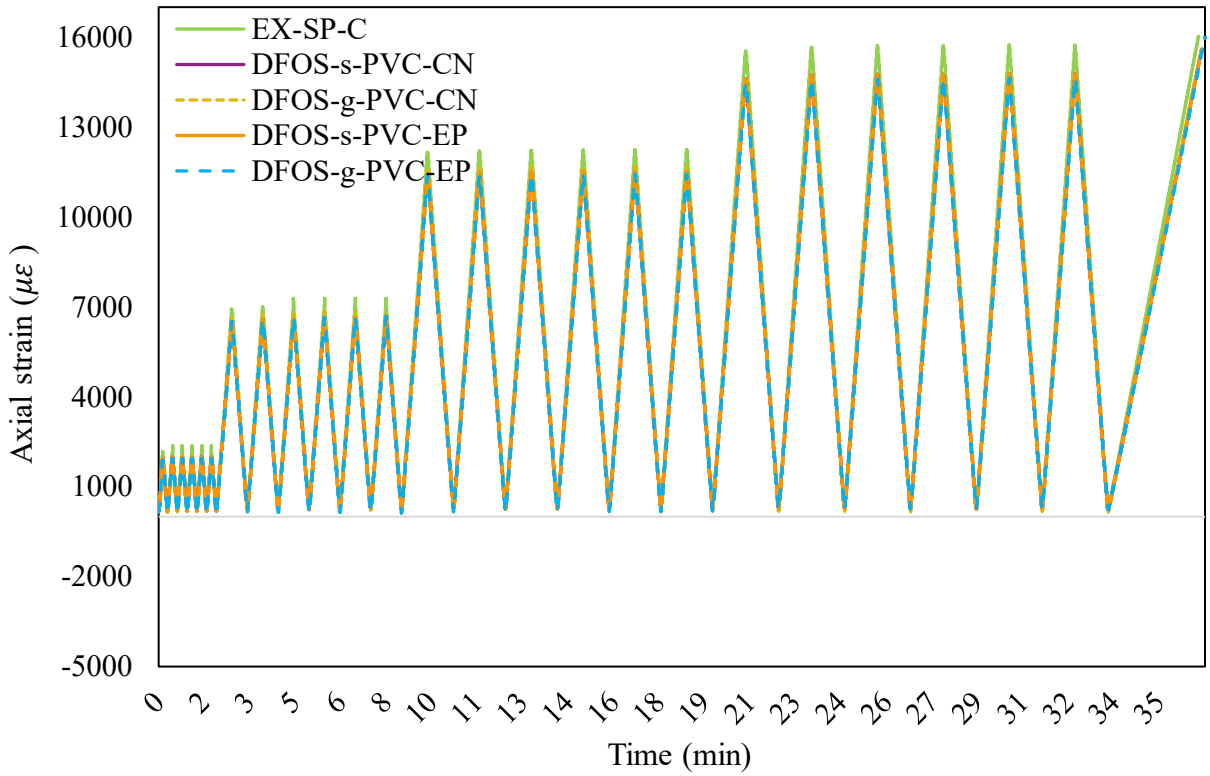

a)

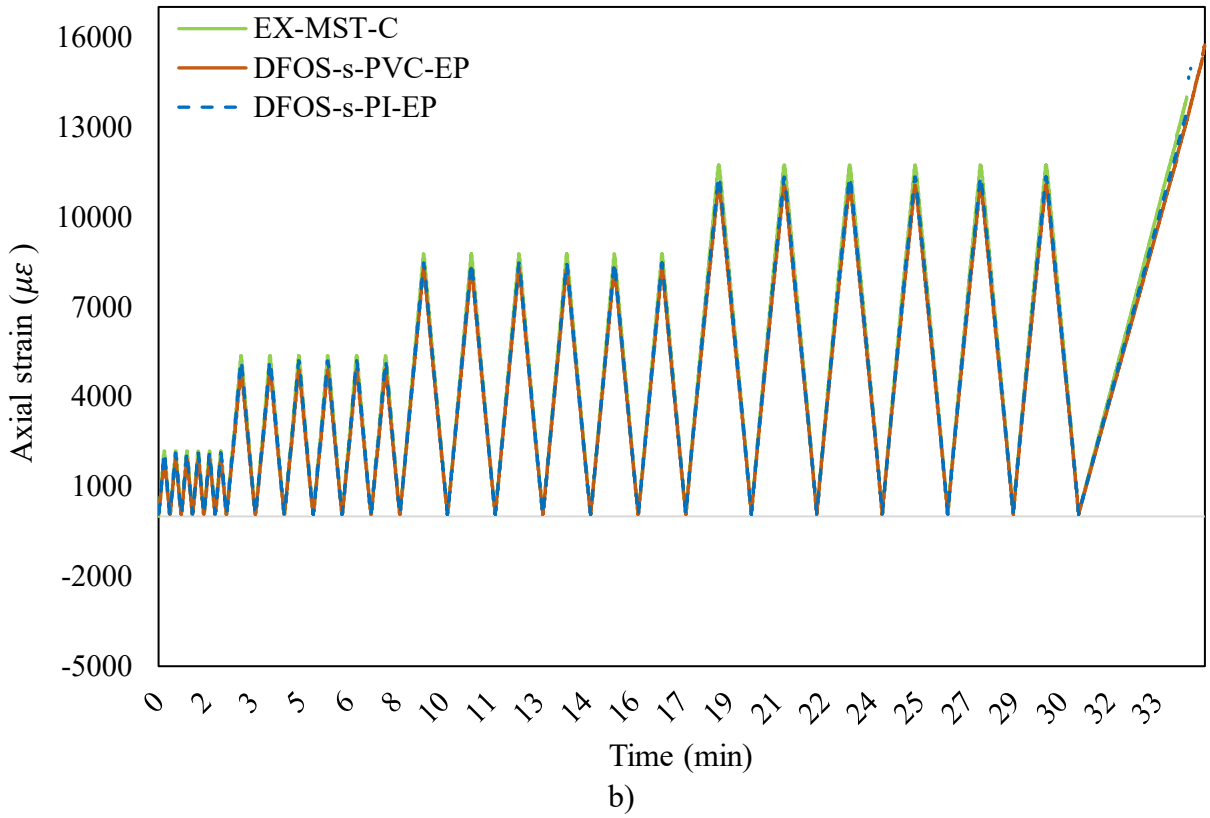

b)

Figure 4-11. Point-based strain/time profiles obtained from DFOS and EX for Stage II test samples subjected to loading protocol C: a) SP-C and b) MST-C

Before further interpretation of the results, it is important to note that the sustained strain levels were designed to be equivalent relative to the ultimate tensile strengths of the respective SP and MST GFRP host bars and were applied in accordance with manufacturer specifications. However, MST bars exhibited experimentally higher mechanical properties, such as ultimate strain (ε_{fu}) and modulus of elasticity, than initially anticipated. Consequently, the recorded strain data for the corresponding DFOS layouts in these samples remained below the 12000 $\mu\varepsilon$ threshold throughout the test, up to the final loading to failure. This outcome inadvertently allowed 12000 $\mu\varepsilon$ to be assessed as a practical threshold for maintaining full sensing efficiency under sustained loading.

Across the four bonded DFOS layouts in each sample, the measurement deviations remained stable and internally consistent throughout the strain range. In contrast, measurements from the EX showed a progressively increasing deviation with increasing strain levels. At lower strain levels, a clear alignment was observed between the EX and the higher-performing DFOS layouts, particularly those incorporating CN adhesive or a PI jacket in the intermediate layers, within certain strain ranges. However, beyond approximately 7000 $\mu\varepsilon$, a progressively more pronounced divergence in measurements was observed. DFOS layouts that initially exhibited strong correlation with the EX showed increasing measurement errors of up to 3–4% as strain levels approached the final sustained or cyclic peak loading. In contrast, less accurate layouts, such as those bonded with EP adhesive, experienced larger errors, reaching 5–6%.

This divergence contrasts with the inter-DFOS measurement errors, which remained layout-dependent and generally consistent with theoretical expectations at a conceptual level during the initial evaluation stages. In comparison, the increasing discrepancy between EX and DFOS readings appeared systematic. Thus, the progressively increasing error can be attributed to experimental setup limitations associated with the EX system, including decoupling effects, frame slippage, and other sources of additive elongation that influence EX measurements. To examine

the intercorrelation among the DFOS layouts, a reference layout, selected for its highest recorded strain, was used to quantify absolute measurement deviations, interpreted as error. This analysis revealed three distinct and repeatable error trends as strain levels increased: 1) nearly constant absolute error, where certain layouts exhibited a relatively fixed absolute error regardless of the strain level, observed in EP-adhered layouts; 2) progressively increasing error, characterized by absolute strain deviations that grew proportionally with increasing strain levels, consistent with classical shear lag theory, discussed in **Section 3.2**. The shear lag theory and strain transfer model developed in the previous chapter describe the STE of a bonded DFOS system, where the strain difference between the core optical fibre (ε_c) and the host material (ε_h) is governed by a defined strain transfer coefficient, $Z(x) = \varepsilon_c(x)/\varepsilon_h$, where the strain difference scales with the host strain as $\varepsilon_c(x) - \varepsilon_h = \big(1 - Z(x)\big)\varepsilon_h$; and 3) decreasing error magnitude, based on the selected layout reference, with some layouts showing reduced absolute error as strain levels increased.

In samples SP-S and MST-S, where g-PVC-CN and s-PI-CN were selected as the reference layouts, lower-performing layouts, such as s-PVC-EP, exhibited a nearly constant absolute strain error across all loading stages, between –250 to –360 $\mu\varepsilon$. This error may stem from installation-related issues, such as interfacial gapping, compliance, or loosening of the optical fibre cable (i.e., initial slack), all of which can cause a constant optical path error independent of actual strain. This fixed internal offset represents a residual, strain-independent error term, manifesting as consistent strain underestimation across the entire loading range. In contrast, layouts such as g-PVC-EP in sample SP-S and s-PI-EP in sample MST-S, demonstrating higher STE, showed strain measurements more closely aligned with the reference and exhibited error behaviour primarily governed by a proportional, strain-dependent component.

In samples SP-C and MST-C, all layouts exhibited progressively increasing absolute strain errors relative to their respective selected references, s-PVC-CN and s-PI-EP, respectively. For example,

in sample SP-C, where measurements from all DFOS layouts were closely aligned, the errors relative to the reference s-PVC-CN were approximately –8, –67, and –108 $\mu\varepsilon$ at the peak of the first cyclic loading cycle for the g-PVC-EP, s-PVC-EP, and g-PVC-CN layouts, respectively. The absolute errors for each layout increased progressively, ultimately reaching –245, –375, and –448 $\mu\varepsilon$, respectively, at the peak of the final cyclic loading cycle. This is a classic manifestation of shear lag inefficiency, where increasing strain leads to an increased discrepancy between the host strain (ε_h) and the fibre strain (ε_c). This behaviour is consistent with the strain transfer (shear lag) model, where $\varepsilon_h - \varepsilon_c(x = 0) = \big(1 - Z(0)\big)\varepsilon_h$, with $x = 0$ representing the theoretical midpoint of the DFOS bonded length. This model defines the core optical fibre's measurement error as a percentage-based error rather than a fixed value, where the absolute strain error is proportional to the experienced strain level. $Z(x)$ is influenced by adhesive interface stiffness and jacket rigidity.

A third trend, characterized by decreasing absolute deviation from the reference layout with increasing strain, was observed in configurations such as s-PVC-CN and s-PI-EP in sample MST-S, and s-PVC-CN in sample SP-S. For instance, in sample MST-S, the absolute error relative to the selected reference layout decreased for both s-PI-EP and s-PVC-CN, from –238 and –85 $\mu\varepsilon$, respectively, at the first sustained load stop to –60 and –35 $\mu\varepsilon$ at the final sustained load stop. This reduction suggests a nonlinear strain transfer behaviour, likely driven by evolving interfacial dynamics within either of the two compared layouts over the course of the test.

In summary, DFOS measurements under sustained loading generally exhibited either constant or decreasing error trends, apart from the g-PVC-EP configuration in sample SP-S, which displayed an error pattern mainly consistent with the shear lag model. Cyclic loading, in turn, induced progressively increasing errors, also in line with predictions from shear lag theory. Thus, the overall behaviour of the sensing system appears to be influenced by key factors such as the quality of the initial bonding and the type of applied loading.

These factors likely determine whether the dominant source of measurement error is a fixed offset due to bonding inefficiency or a strain-proportional deviation due to limited shear transfer, as described by shear lag theory. For instance, the g-PVC-EP configuration in sample SP-S appears to have been governed more by shear lag effects than by fixed bonding loss. As will be discussed in the following section on DFOS strain distributions, this layout also exhibited superior bondline integrity under high sustained loading compared to the others. Taken together, these characteristics suggest that g-PVC-EP in sample SP-S may represent one of the most effective bonded sensor installations, closely aligning with the ideal assumptions of shear lag theory, particularly in terms of proportional strain transfer. Additionally, it demonstrated stable bond performance under elevated sustained stress, further supporting its effectiveness. Similarly, the close agreement among all DFOS layouts in sample SP-C may further support the presence of higher overall installation quality, enabling consistent behaviour in line with shear lag predictions.

Overall, these findings confirm that measurement discrepancies are primarily influenced by the mechanical properties of intermediate layers, geometric factors, and installation quality. Notably, inter-DFOS errors remained consistently low within an acceptable range, following distinct stable trends for each configuration, driven by interfacial interactions. In contrast, EX readings diverged at higher strains. These insights highlight the potential of bonded DFOS systems to provide reliable and accurate strain measurements, particularly within the stress ranges corresponding to the serviceability limits of GFRP bars, contingent on controlled installation quality and verified configuration-specific performance for both laboratory and practical applications.

Notably, in sample SP-S, which experienced short-term sustained stresses exceeding 12000 $\mu\varepsilon$, two out of four fibres under test (FUTs) continued to deliver stable and reliable strain measurements at the midpoint of the DFOS bonded length. In contrast, only one out of eight FUTs maintained such performance under similar loading in the earlier pilot tests across eight samples.

Collectively, these findings emphasize the crucial role of installation quality and bond strength in ensuring accurate strain measurements and maintaining monitoring performance, especially for manually bonded DFOS on GFRP reinforcing bars in high-stress environments. When bond strength is compromised, the likelihood of microstructural dislocations increases. Adhesive particles can shift and reorganize, alleviating stress concentrations by shear redistribution along the bondline. This process often accelerates the progression of shear plastic deformation, gradually weakening bondline integrity. While the mechanisms and extent of bondline damage may vary with conditions, this degradation typically accelerates under sustained high-level loading, ultimately affecting the durability and long-term reliability of the bonded sensing system.

Several factors contribute to this outcome, one of the most significant being the curing process, which plays a pivotal role in determining the quality of the bond between the host material and the FUT. Additionally, the quality of installation improved as experience and expertise increased between the pilot tests and the stage II tension specimens. This was reflected in better control over adhesive thickness, alignment, and fulfillment degree, achieved through more frequent practice and a deeper understanding of the optimal bonding conditions.

The expertise of trained engineers is therefore indispensable for ensuring the long-term performance and reliability of DFOS systems in these applications. Proper hand-operated installation ensures optimal signal transmission and maximizes the longevity of the monitoring system. Inaccuracies in bonding or alignment can lead to accelerated progression of shear plastic deformations, which in turn cause a degradation of monitoring efficiency along the bonded length of the FUT. Consequently, these observations provide valuable insights for refining the fabrication processes of surface-bonded DFOS GFRP bar systems. They highlight the need for rigorous control and expertise to ensure compliance with project specifications and to maintain the long-term stability of monitoring systems over time.

4.4.2. DFOS Strain Distributions

This subchapter evaluates the overall monitoring performance and distributed STE of bonded DFOS on GFRP bars, based on experimentally captured strain profiles from various DFOS layouts. Furthermore, the effects of sensor placement, adhesive type, jacketing coating, strain levels and conditions, as well as loading history on the performance of DFOS distributed strain measurements, are discussed herein and are comprehensively elaborated upon in **Section 4.5**.

4.4.2.1. Specimens Subjected to Loading Protocol S

- **Sustained Load Steps**

This section presents strain profiles recorded by DFOS layouts in samples SP-S and MST-S during each sustained loading level, evaluating the stability and accuracy of strain measurements across layouts, as shown in **Figure 4-12** for sample SP-S and **Figure 4-13** for sample MST-S.

All DFOS configurations of both samples demonstrated a high degree of stable accuracy and consistency within the serviceability stage and sustained stresses undergoing strain levels of less than 12000 $\mu\varepsilon$. However, the recorded distributions during the final sustained loading of sample SP-S revealed signal loss and a gradual reduction in the span of effective sensing length, along with a decline in reliable strain transfer from the host to the DFOS core. At the onset of the first sustained load step, with strain levels around 2000 $\mu\varepsilon$, the DFOS strain distributions were relatively smooth in appearance and consistent along their bonded lengths. As the load was applied over the extended period, the final DFOS strain curves showed that the readings remained stable.

Starting from low strain levels, the strain distribution curves from the PI-coated FUT, especially in the s-PI-CN layout, showed minor yet noticeable nonuniformity, likely due to the sensor cable's small diameter and the stiff, thin CN adhesive interface, which increased sensitivity to surface irregularities and uneven adhesive application, causing slight strain transfer inconsistencies.

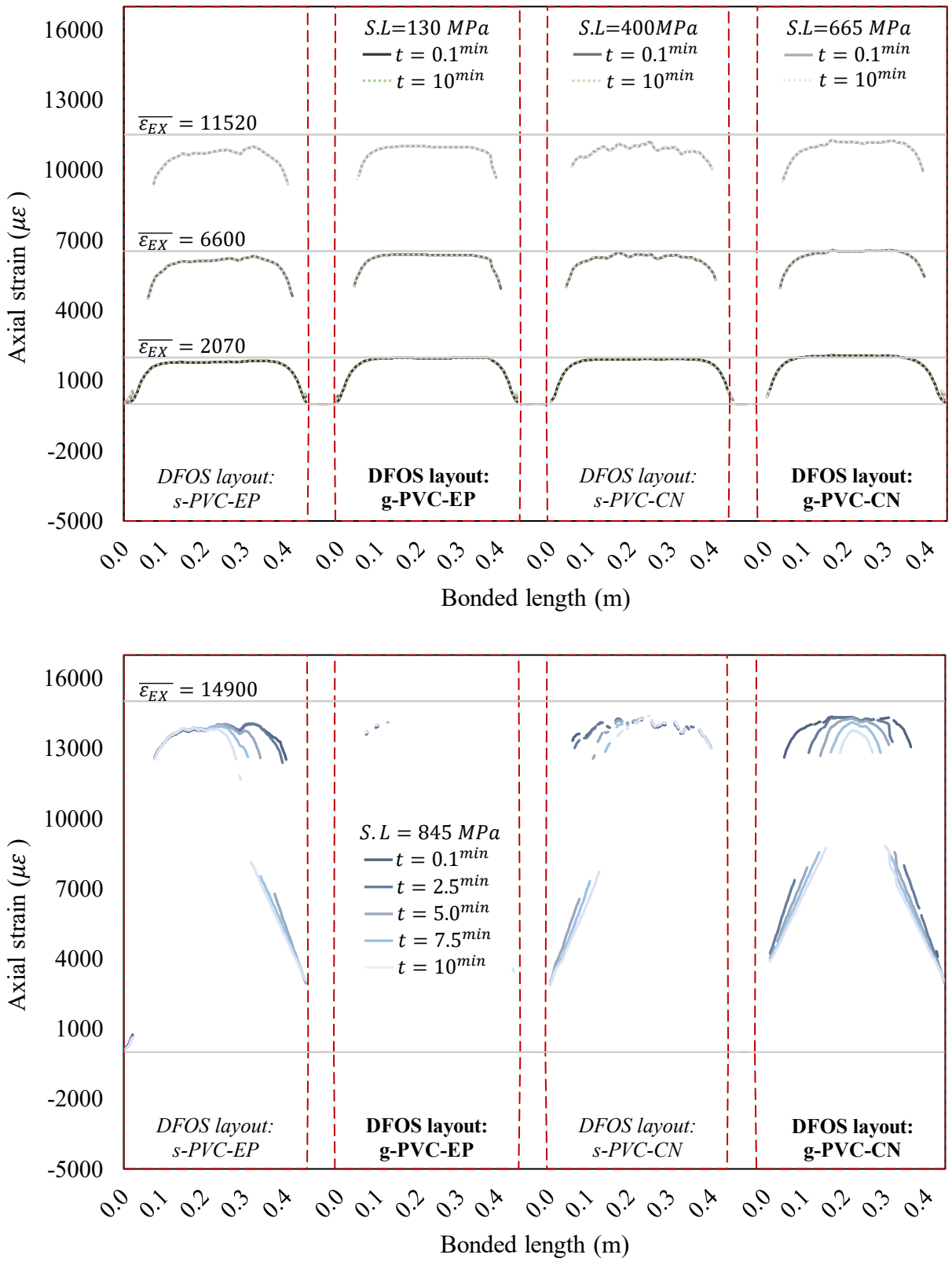

Figure 4-12. DFOS strain distribution curves for sample SP-S captured during different levels of sustained load periods

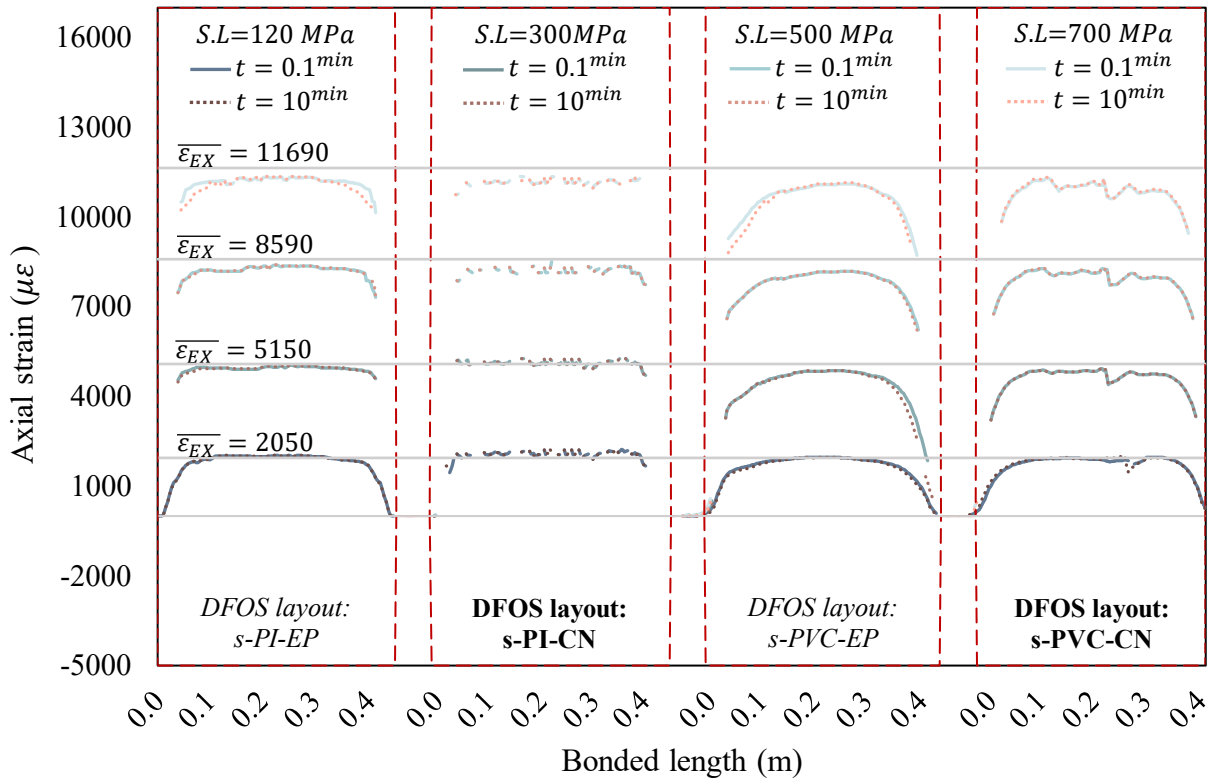

Figure 4-13. DFOS strain distribution curves for sample MST-S captured during different levels of sustained load periods

By comparing the initial and final strain distribution readings after applying the second static load (with strain levels between 5000-6000 $\mu\varepsilon$), notable differences in monitoring performance and stability can be observed between the DFOS layout configurations. In particular, despite noisier distributed measurements, the PI-coated DFOS demonstrated superior STE, recording higher strain values than the PVC-coated DFOS. Moreover, the consistency of strain reading along the DFOS bonded length was improved when PVC-coated DFOS cables were embedded within a pre-drilled groove in the GFRP bar or attached using two-part epoxy (EP). In contrast, the use of CN adhesive and PI-coated DFOS improved STE within the intermediate layers, as reflected by higher average strain readings. However, this improvement was accompanied by reduced uniformity in distributed strain measurements along the bonded length, likely due to non-uniform bond conditions on irregular surfaces and greater sensitivity to surface texture and imperfections.

Considering the third sustained load, which followed unloading to 1 *kN* from previous static load steps and monotonic loading to the corresponding stress levels, it can be observed that strain in all DFOS built up again and continued to be logged with the same degree of uniformity along their DFOS bonded lengths throughout the extended static stress durations.

Finally, as the samples were loaded to the final designed constant load stops, initial DFOS distribution readings exhibited higher noise levels in both surface-mounted sensors and those attached using CN. In contrast, the g-PVC-EP DFOS layout in sample SP-S completely lost signal integrity across nearly the entire bonded length. Additionally, while the final strain distribution curves from the bonded DFOS in sample MST-S closely matched the initial ones, those from sample SP-S, subjected to higher sustained stress, displayed a distinct pattern, as observed in the pilot test results. These curves indicated damage progression, characterized by a gradual reduction in effective sensing length and STE from the substrate to the DFOS along the bonded length.

The distribution curves for sample SP-S, captured at 2.5-minute intervals, show that the effective measurement lengths of DFOS progressively shortened as shearing damage spread from one free end in s-PVC-EP and s-PVC-CN layouts, and from both ends in the g-PVC-CN configuration. Notably, the s-PVC-EP and s-PVC-CN layouts lost almost half or less of their effective sensing lengths asymmetrically by the end of this static stop; the remaining segments of these sensor layouts continued to capture strain data from the host material constantly and reliably. However, the progressive increase in damage length in the g-PVC-CN DFOS layout led to a corresponding reduction in the effective sensing range, resulting in a noticeable decline in the reliability of DFOS strain measurements along the entire length compared to the originally recorded data.

Similar to the pilot samples' results, a noticeable pattern in signal loss can be observed through the strain distributions. The OFDR-based data acquisition system showed a loss of capability in capturing signal integrity within the portion of strain transfer lengths where the strain gradients

were high. At higher strain levels of the host material, within strain transfer segments, which have a length depending on β_1 and β_2 (parameters describing the effects of the mechanical properties of intermediate layers like thickness and modulus elasticity of adhesive and protective jacket as detailed in **Section 3.2**, strain gradients increased significantly as each sensing layout tried to provide uniform conditions of the host material's strain. The DFOS strain distributions recorded beyond 3000 $\mu\varepsilon$ levels frequently demonstrated signal loss at both ends of bonded lengths.

- **Final Monotonic Unloading**

included a final monotonic unloading to 1 kN to evaluate prolonged monitoring stability after exposure to various sustained load levels. As depicted in **Figure 4-14**, after unloading both SP-S and samples MST-S, the strain readings decreased to lower levels, with some layouts exhibiting full elastic recovery while others continued to track strain without returning to the initial state. Following this, the g-PVC-EP DFOS layout in sample SP-S regained signal integrity, while the s-PI-CN DFOS layout in sample MST-S showed increased signal attenuation. Sample MST-S showed almost uniform strain redistributions during the final unloading, which are in satisfactory agreement with initial measurements during the test. However, the s-PVC-EP layout of this sample demonstrated partial loss of uniform and accurate strain reading within a small region between strain transfer length and effective sensing length on the left side. After the severe, sustained stress in sample SP-S, strain distributions continued to show pronounced SRAs and permanent STE loss within the damaged bonded region, attributed to plastic shear deformation in the adhesive. In contrast, the remaining well-bonded DFOS segments maintained effective strain transfer and provided reliable data. Configurations such as s-PVC-EP, g-PVC-EP, and s-PVC-CN recorded strain values consistent with pre-damage levels, indicating stable bonding and efficient strain transfer across the undamaged sensor interface. Furthermore, similar to the pilot test samples, a key observation was signal loss between DFOS segments with and without bond damage, suggesting steep strain gradients and improved STE across the boundary.

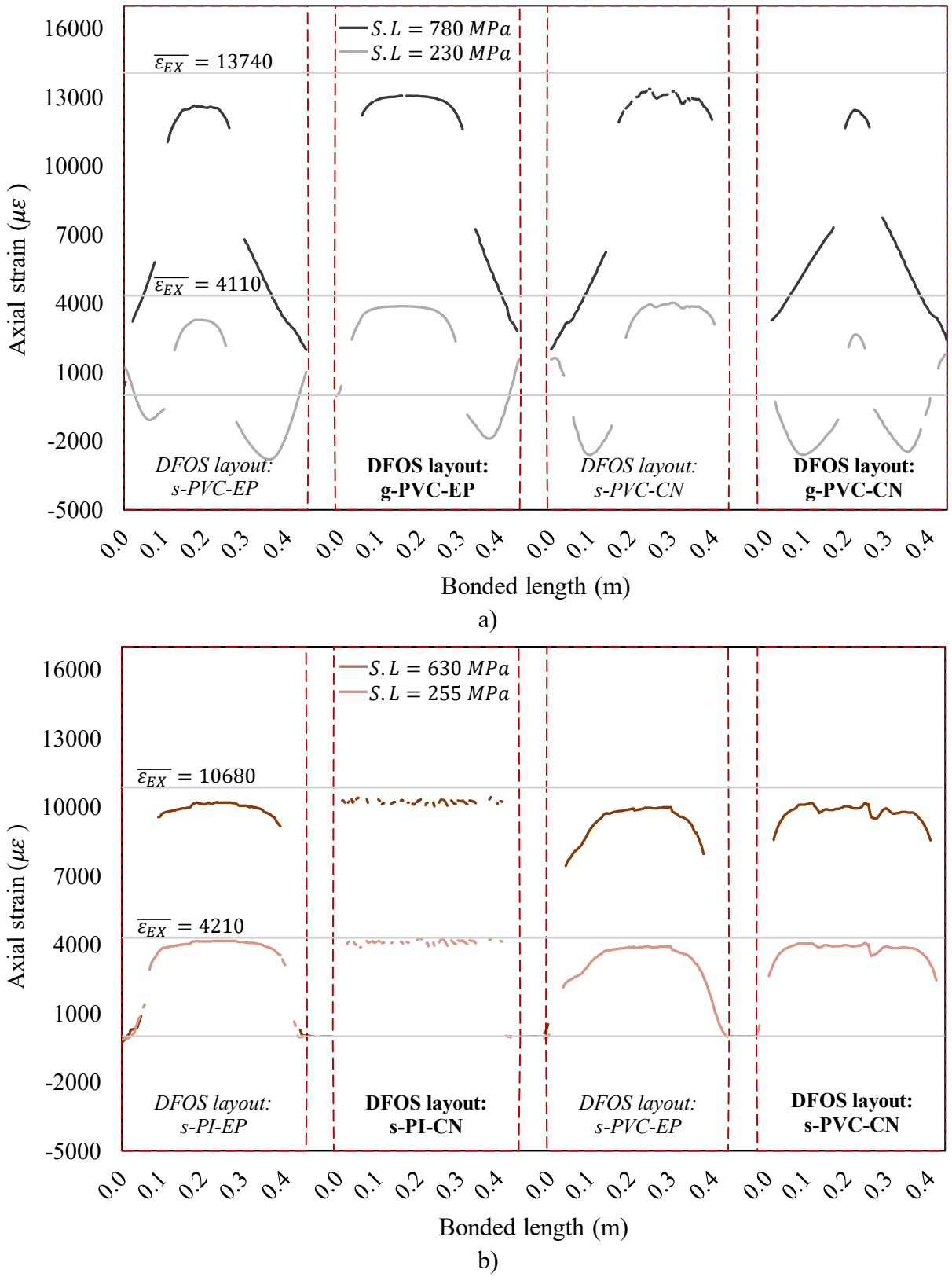

Figure 4-14. DFOS strain distributions captured during unloading after final sustained load step: a) SP-S and b) MST-S

- **Final Monotonic Loading Stage to Failure**

During the final loading to failure of samples SP-S and MST-S, all FUTs exhibited consistent monitoring behaviour, capturing both reliable and erroneous strain data along their bonded lengths, similar to patterns observed during the previous unloading phase, as illustrated in **Figure 4-15**. Although compression strain data within damaged areas of sample SP-S were removed, these regions still failed to provide accurate strain readings. Additionally, signal loss in the PI-coated DFOS layout occurred more rapidly toward failure than in the PVC-coated DFOS.

As in earlier loading stages, CN-based DFOS configurations in both samples showed higher average strain values and more localized variation in strain profiles than their EP-based counterparts. This behaviour results from the CN layer's stiffness and thinness, which increase STE and overall sensitivity to surface irregularities and local deformation. In contrast, the thicker and more ductile EP bond interface facilitates strain averaging across the DFOS bonded length, reducing the impact of local surface defects and leading to smoother, more uniform strain transfer along the sensor. These findings highlight the trade-off between local sensitivity and measurement consistency, underscoring the role of adhesive choice in reliable DFOS performance.

4.4.2.2. Specimens Subjected to Loading Protocol C

- **Cyclic Load Steps**

The strain responses observed under the cyclic loading protocol "C" for samples SP-C and MST-C are presented in detail in **Figures 4-16** and **4-17**, highlighting the distributed monitoring behaviour across DFOS bonded lengths through cycle peaks and troughs. Overall, the graphs demonstrate the reliability of surface-bonded DFOS systems in capturing the distributed strain behaviour across all ranges of cyclic loading. Additionally, as previously observed, CN-based DFOS configurations showed less uniform strain distributions, whereas EP-adhered DFOS layouts produced smoother and more consistent strain profiles.

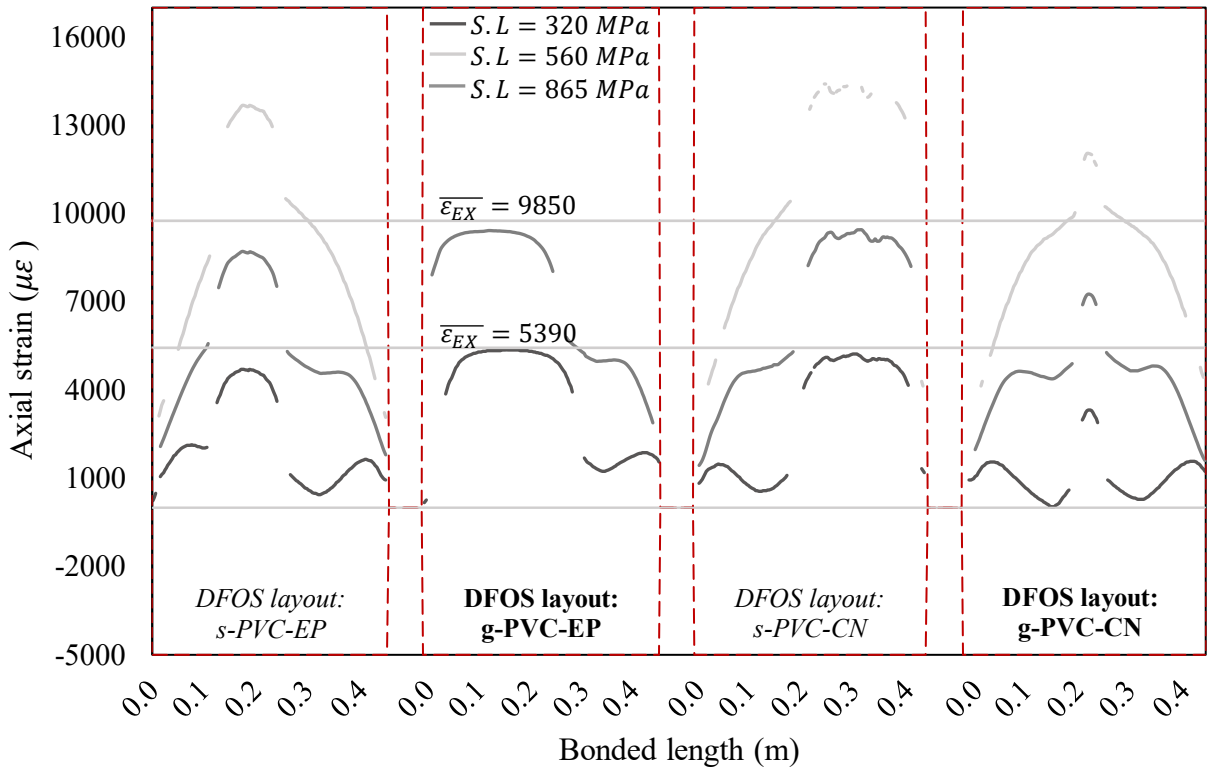

a)

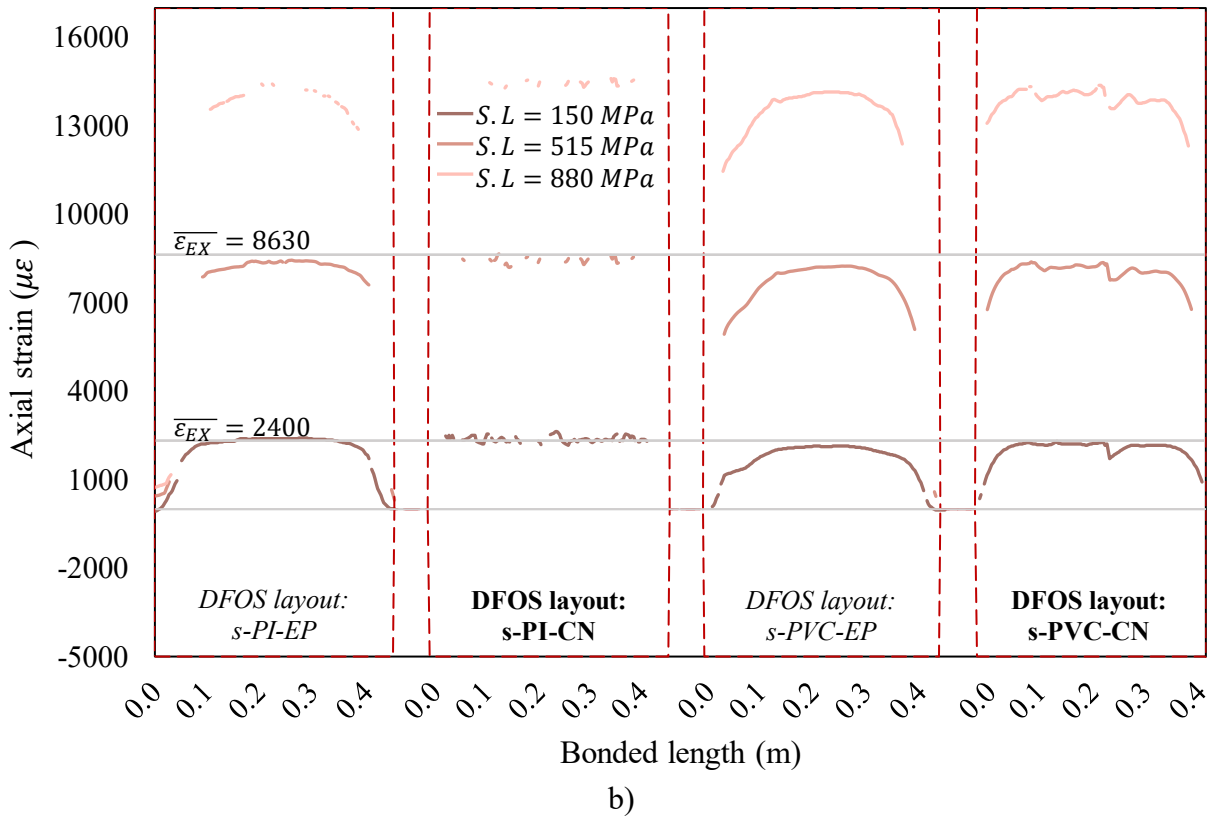

b)

Figure 4-15. DFOS strain distributions captured during last monotonic loading to failure: a) SP-S and b) MST-S

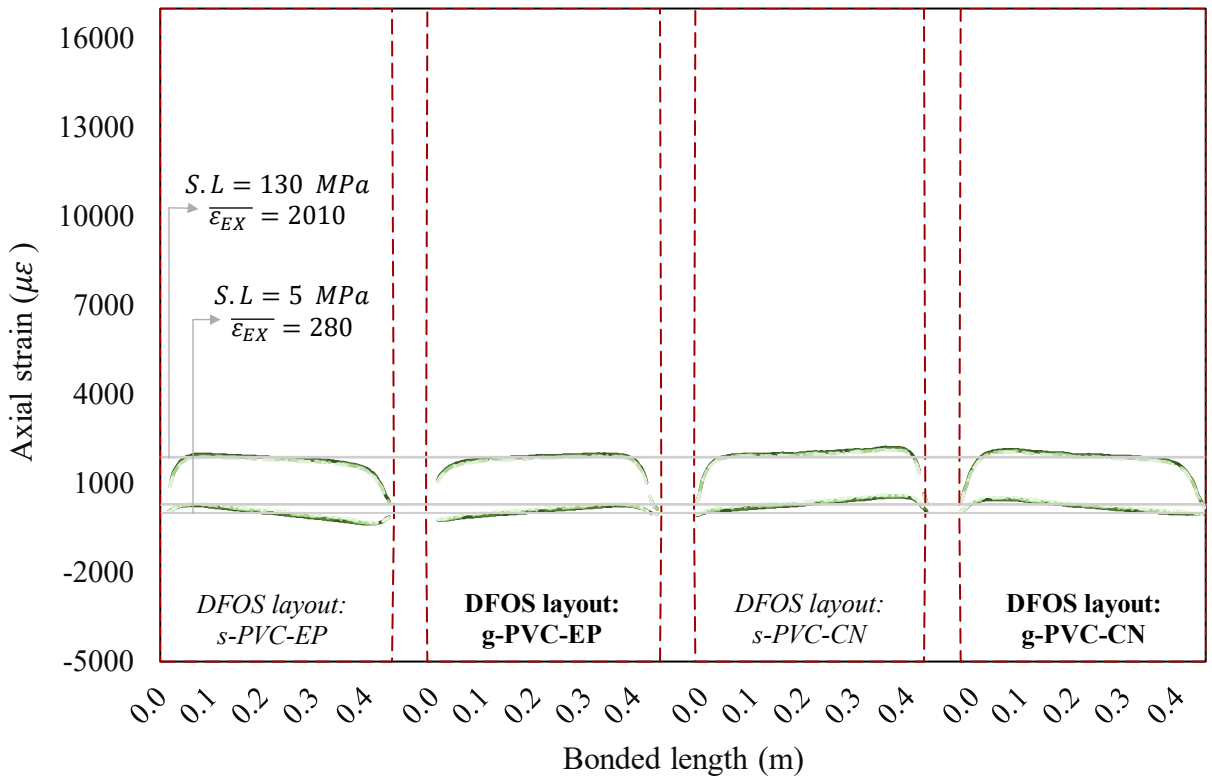
16000
13000
10000
7000
4000
1000
-2000
-5000
Axial strain ($\mu\varepsilon$)
$S.L = 130\ MPa$
$\overline{\varepsilon_{EX}} = 2010$
$S.L = 5\ MPa$
$\overline{\varepsilon_{EX}} = 280$
DFOS layout: s-PVC-EP
DFOS layout: g-PVC-EP
DFOS layout: s-PVC-CN
DFOS layout: g-PVC-CN
0.0 0.1 0.2 0.3 0.4
Bonded length (m)

a)

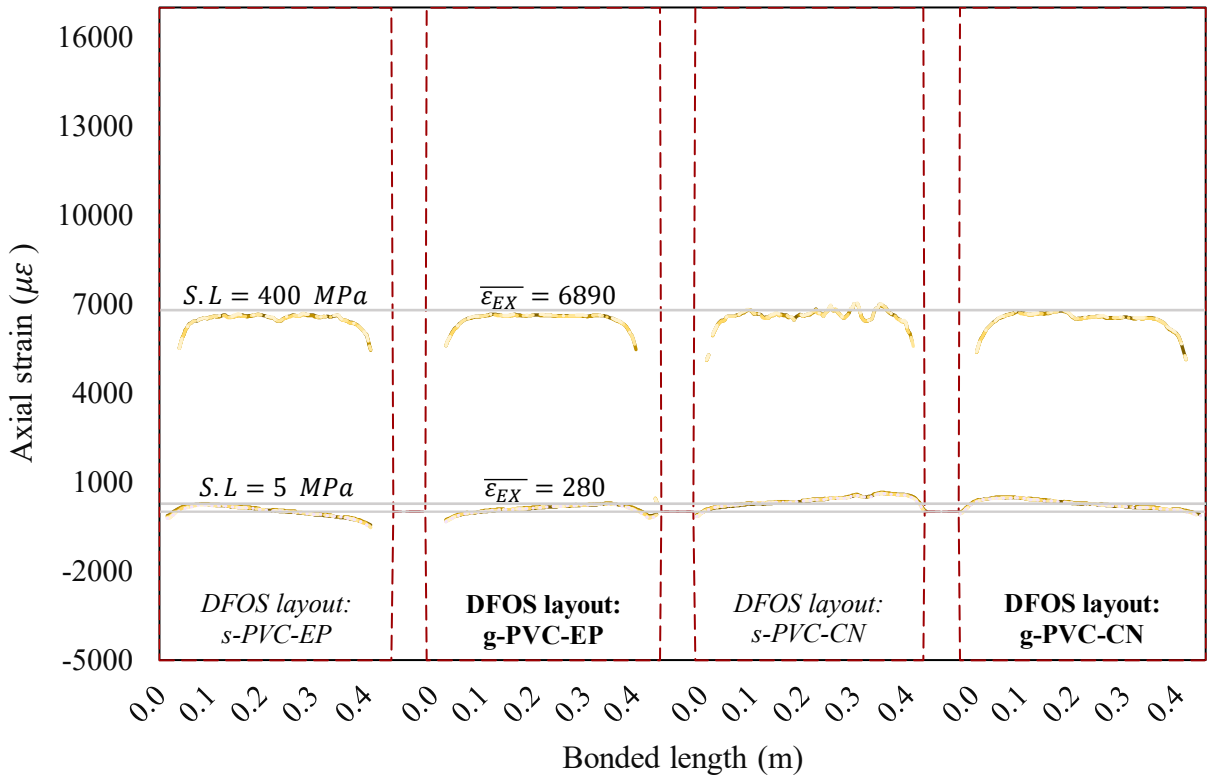
16000
13000
10000
7000
4000
1000
-2000
-5000
Axial strain ($\mu\varepsilon$)
$S.L = 400\ MPa$
$\overline{\varepsilon_{EX}} = 6890$
$S.L = 5\ MPa$
$\overline{\varepsilon_{EX}} = 280$
DFOS layout: s-PVC-EP
DFOS layout: g-PVC-EP
DFOS layout: s-PVC-CN
DFOS layout: g-PVC-CN
0.0 0.1 0.2 0.3 0.4
Bonded length (m)

b)

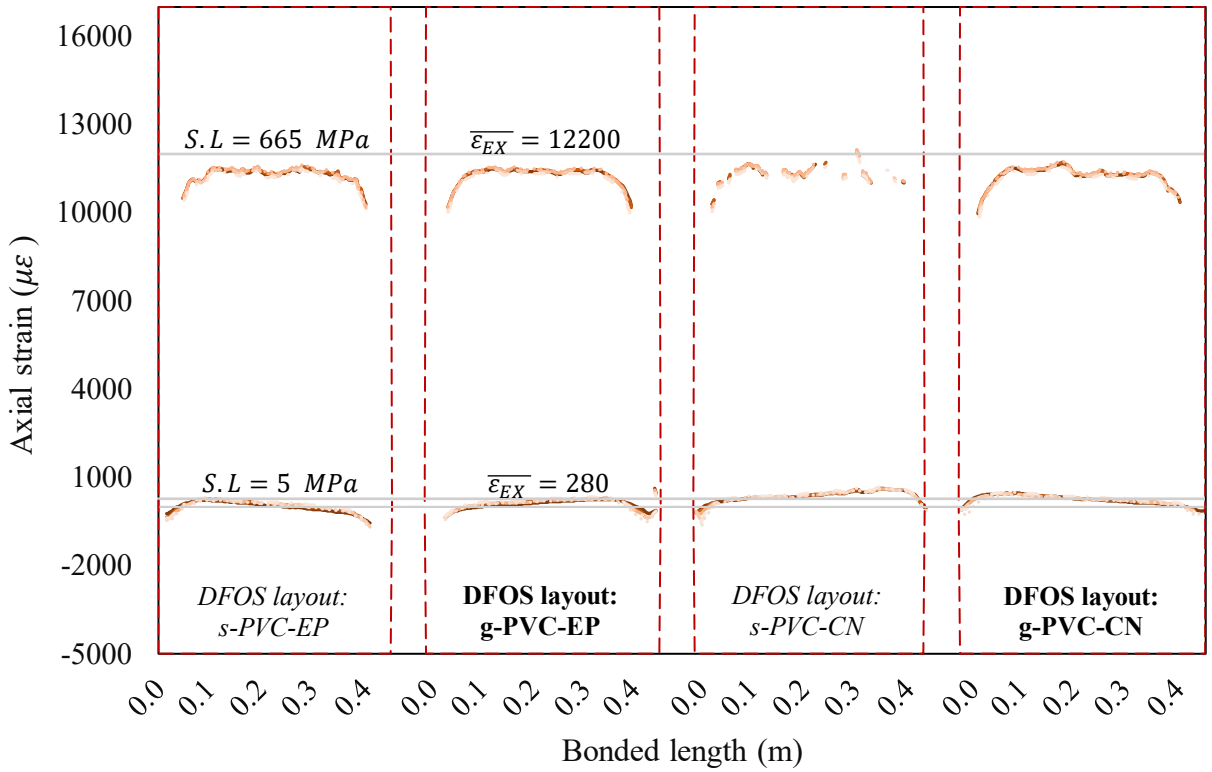

c)

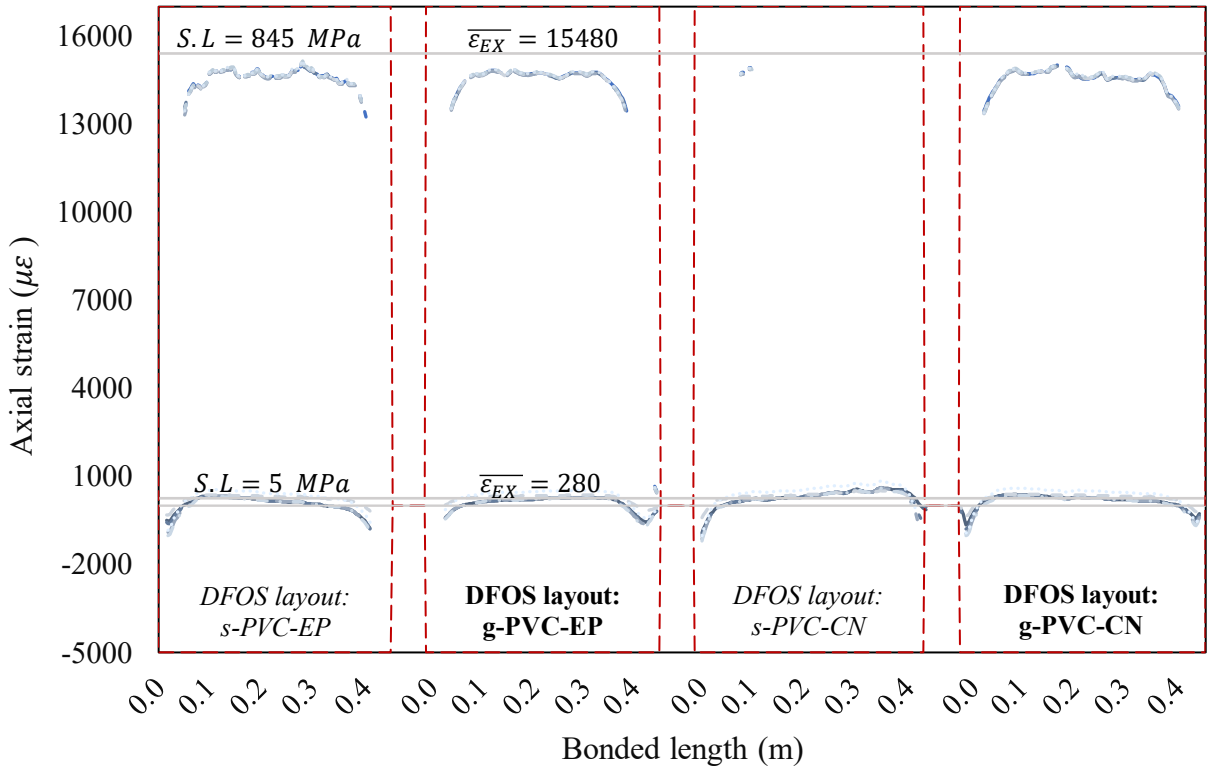

d)

Figure 4-16. DFOS strain distribution curves for sample SP-C captured during cyclic loading ranges: a) 1st, b) 2nd, c) 3rd, and d) 4th

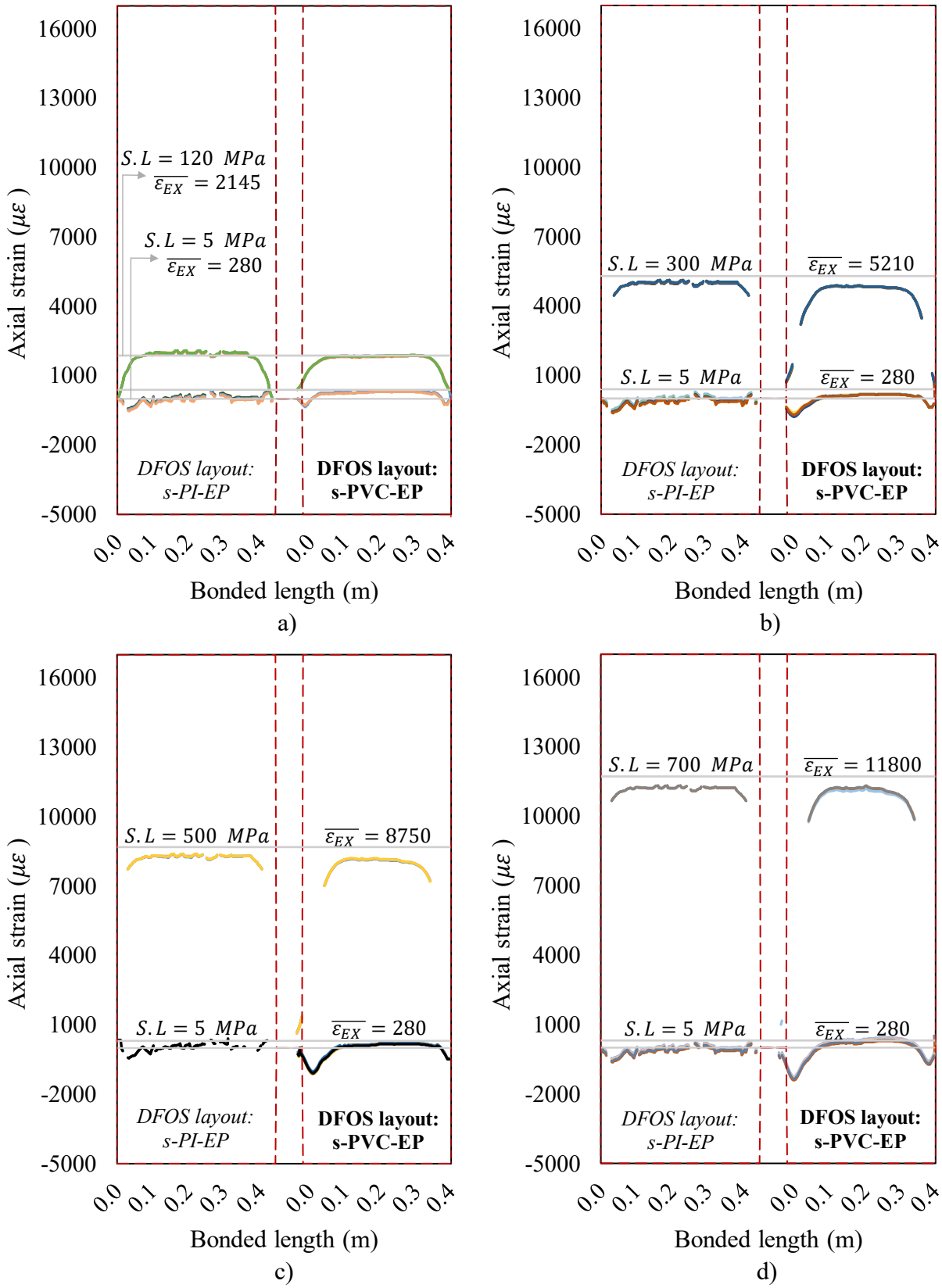

Figure 4-17. DFOS strain distribution curves for sample MST-C captured during cyclic loading ranges: a) 1st, b) 2nd, c) 3rd, and d) 4th

In both samples, distributed strain readings at cyclic peaks exhibit roughly well-defined plateaus, indicative of consistent strain transfer to the sensors. The alignment of repetitive strain responses with the applied cyclic peaks validates the DFOS's capacity to capture distributed strain behaviour effectively. As expected, trough-cycle strain minima were generally low in magnitude but showed subtle SRAs near the bondline ends that progressively intensified, peaking during the fourth loading cycle. The transient strain recovery behaviour captured by DFOS at the bondline edges during unloading often deviated from purely elastic recovery. They typically showed a shift to compressive strain near the bonded-to-free transition of the DFOS, followed by a return to zero strain in the outer free length.

The observed edge compressive SRAs most likely indicate progressive localized bond damage and recovery mismatch at the adhesive interface edges under cyclic loading. This reflects early-stage degradation in adhesive joints, where damage initiates at free edges due to stress concentrations and strain reversals, while the interior remains unaffected until creep, fatigue, or bondline failure develops. Localized degradation arises from geometric discontinuities, material mismatches, and shear or out-of-plane deformation effects, rather than a uniform global stress field, as discussed in **Section 3.2**, with references such as Panigrahi and Pradhan (2007) and Da Silva et al. (2018). Repeated cycling of high shear and peel stresses at the adhesive edges causes localized damage zones, including microcracking, interfacial separation, or plastic shear deformation.

Therefore, the compressive strains observed by DFOS near the ends of the bonded region during the unloading phase can be interpreted as indicators of progressively increasing localized bond damage. These strain patterns likely resulted from residual internal shear stress redistribution as the system attempted to recover its original configuration. Although the adhesive exhibited partial elastic recovery, residual stress fields caused by plastic shear deformation, microscale debonding, or cohesive degradation remained. In some cases, these stresses led to localized, temporary reversals in strain direction, indicating the interplay of recovery and residual damage.

With continued cyclic loading, particularly at higher peak stresses, the adhesive edge zones exhibited increasingly nonlinear behaviour, disrupting strain transfer and causing localized compressive SRAs at the DFOS bonded length ends during unloading, due to configuration constraints and complex interfacial interactions. In contrast, the central bonded region remained elastic and stable, highlighting the confined nature of the damage and its minimal impact on overall bonded sensing system performance under load.

Nonetheless, as per experimental observations, during loading, the induced SRAs near the ends of the bonded length gradually disappeared. This is attributed to the dynamic interplay of changing internal stress states. During loading, the applied tensile force dominates, uniformly stretching the adhesive, cable jacket, and core optical fibre, ensuring stable strain transfer along the bonded length and minimizing relative motion between layers. However, during unloading, the release of tensile force creates a brief window for transient strain phenomena and reveals residual stress effects, followed by pronounced boundary influences and emerging strain discontinuities.

- **Final Monotonic Loading Stage to Failure**

Similar to all other tests, the final testing stages of samples SP-C and MST-C included loading to failure of the host GFRP bar which was commonly followed by culmination of structural performance, wherein the material and bonded sensing system responded to rapidly intensifying stresses and strains during the last moments. The charts depicted in **Figure 4-18** represent these phases. One of the key characteristics of this stage is the onset of signal loss and cable breakage, indicating the physical limitations of the sensing system as structural collapse approaches.

The signal loss is typically attributed to severe deformations in the optical fibre caused by extreme strain concentration. This behaviour marks the transition from measurable strain to the point of failure. While the strain readings ultimately cease due to cable breakage, the preceding data offers a comprehensive picture of the load-bearing capacity and failure dynamics of the structure.

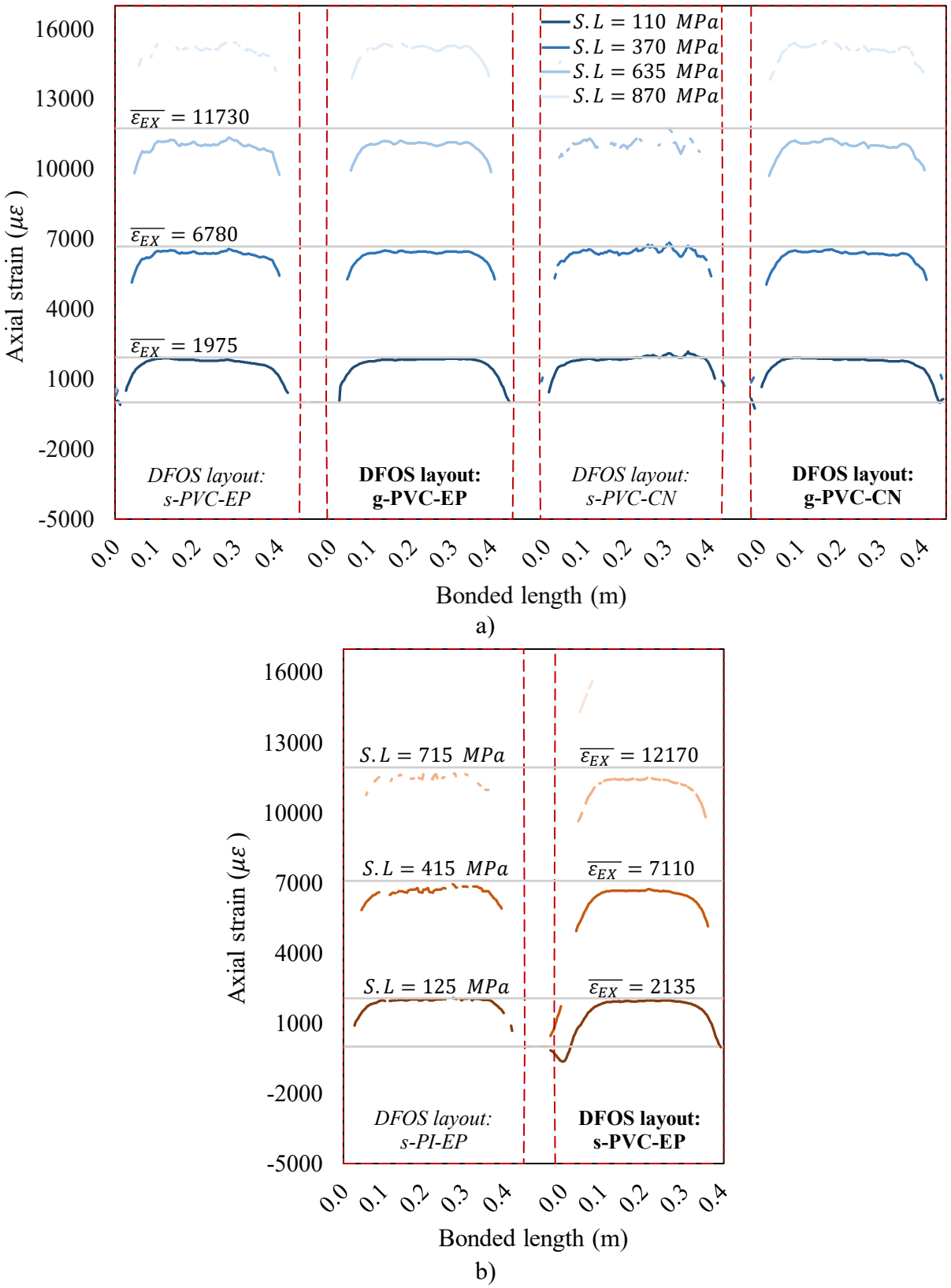

Figure 4-18. DFOS strain distribution curves captured during last monotonic loading to failure: a) SP-C and b) MST-C

4.5. Summary and Discussion

4.5.1. Overall Monitoring Behaviour Examinations

Through a series of experiments conducted on twelve DFOS-instrumented GFRP bar specimens subjected to uniaxial tension, it was determined that the distributed strain readings can be captured with a sufficient and acceptable level of accuracy across a wide range of varying strain conditions, except at high levels of sustained strains beyond 12000 to 13000 $\mu\varepsilon$. The results generally demonstrate the robust performance of surface-bonded DFOS on GFRP bars under repeated mechanical loading, reinforcing their suitability for high-strain field applications.

One important aspect of the overall evaluation involves assessing the measurement error between the DFOS and the EX. While both systems generally captured similar strain patterns within the defined ranges of DFOS efficiency, discrepancies in absolute strain values were observed, particularly at higher strain levels. Overall, agreement between DFOS and extensometer readings was acceptable within specific strain ranges, with error margins from about 0.6% at low strains to as high as 6-7% at higher strains. This increasing deviation can be attributed to compounded uncertainties in both systems. On average, the observed measurement error generally aligns with findings reported in the existing literature on DFOS applications.

On the DFOS side, strain transfer inefficiencies, often from suboptimal installation, caused lag or localized errors. Conversely, while the EX offers high precision, its configuration and setup may have introduced sensitivity to mounting effects, alignment issues, and minor variations in effective gauge length. These factors, which are negligible at low strains, can amplify uncertainty at higher strains due to increased influence of seating stability and surface interaction. These observations underscore the need for proper sensor integration, calibration, and validation. While DFOS offers strong distributed sensing capabilities with acceptable accuracy, both systems require critical evaluation of their limitations across varying test setups.

Furthermore, it is believed that beyond the identified strain limit, the inelastic behaviour of the adhesive interface, coupled with progressive bondline degradation and flaw propagation, induced dynamic changes in the strain transfer mechanisms within the bonded layers of the DFOS system. Hence, as bond damage increased, STE was impaired, either partially or entirely along the DFOS bonded lengths, ultimately affecting the accuracy of the DFOS strain measurements.

Monitoring stability in adhesively bonded DFOS was primarily governed by the precision and quality of sensor installation, rather than the specific bonding layer or attachment method. This was evident from the loss of full monitoring efficiency or partial retention of capability under challenging conditions, regardless of bonding parameter variations. The observed performance degradation is mainly attributed to the adhesive interface's response to sustained high-level stresses, where prolonged loading promotes progression of inelastic shear deformations.

As the adhesive interface undergoes these deformations, energy is released, progressively altering the interfacial interactions. The progressive decline in the adhesive’s ability to maintain bondline integrity compromises the mechanical performance of the host–sensor interface and reduces the effectiveness of distributed strain transfer from the host to the core optical fibre. In this experimental context, Stage II testing demonstrated improved durability of monitoring and distributed measurements along the DFOS bonded length, achieved through enhanced manual bonding of sensors to the GFRP bars. This stronger adhesion minimized adhesive bond degradation, enhancing STE and ensuring more consistent long-term performance.

It should be noted that larger discrepancies in stability between surface-mounted and groove-embedded DFOS layouts were observed in the test specimens with sand-coated GFRP host bars. The sand-coated texture significantly influenced sensor installation path quality and adhesive bondline effectiveness, leading to increased sensor detachment challenges. Microvoids and gaps degraded the bond quality by interrupting adhesive continuity, weakening bond strength, and

increasing the risk of sensor detachment when stresses exceed the critical bond threshold. These findings highlight that even minor initial imperfections in bondline integrity, adhesive thickness, curing conditions, or sensor alignment can cause significant deviations in bonded sensor performance under high sustained stresses and large deformations.

4.5.2. Implications for DFOS Applications in Structural Monitoring

While automated integration of DFOS, such as embedding during pultrusion, has been widely proposed in the literature to enhance sensor protection and manufacturing efficiency, this study specifically focused on surface-bonded DFOS due to its practical advantages in experimental validation and flexible field deployment. The findings indicate that surface-bonded DFOS systems are highly valuable and reliable tools for distributed strain measurement in GFRP bars, particularly within their serviceability range, corresponding to strain levels below 0.7%, and up to elevated strain levels of 1.2%–1.3% under various loading conditions, consistently demonstrating strong signal integrity and stable prolonged monitoring performance.

Furthermore, observations revealed that, while effective in distributed strain measurement within defined operational limits, surface-bonded DFOS can exhibit progressive SRAs, particularly under sustained or cyclic high-level loading. These effects are most likely due to the elasto-plastic response of the adhesive interface and bondline degradation, surpassing the critical resistance of the adhesive joint. Shear plastic deformation along the adhesive interfaces of the bonded DFOS system was observed under high, sustained strain levels, well beyond those typical in DFOS-GFRP systems, resulting in a gradual decrease in the measured distributed strain values.

These feasibility results highlight the crucial role of proper DFOS installation in instrumenting structural components, especially GFRP bars, to enhance bondline strength and ensure reliable monitoring under demanding conditions. In long-term SHM, the drift resulting from the evolution and progression of shear plastic deformation along the bondline adhesive interfaces can lead to a

gradual underestimation of strain in the host material. For high-demand applications, engineers and researchers should consider correction factors or advanced bonding techniques to mitigate interfacial failure effects in the sensing system's intermediate layers, enhancing DFOS data reliability over extended loading ranges.

Overall, experimental DFOS strain distribution curves provided crucial insights into the behaviour of DFOS-bonded GFRP bars under static and dynamic loads, underscoring the importance of bond integrity and interpretation of the present cohesive strength for accurate strain measurements. While damage progression and the inelastic behaviour of the sensor bond joints pose challenges, the consistent repeatability of strain patterns with stabilized values suggests that, with careful calibration and consideration of the adhesive bond's inelastic behaviour, DFOS can still provide reliable, consistent data for structural monitoring. This approach remains valuable during short, critical periods before repairs that are needed to address inefficiencies in sensor attachment.

While some inconsistencies in measurement stability and defined strain thresholds for accurate monitoring were noted, these limitations do not undermine the overall viability of DFOS for SHM. Instead, they highlight key areas for further refinement and development. With standardized installation protocols, meticulous surface preparation, adhesive selection, and rigorous calibration routines, the performance and reliability of surface-bonded DFOS can be significantly enhanced.

These measures can mitigate installation variability and improve long-term data consistency. In this context, surface-bonded DFOS remains a highly adaptable and accessible sensing approach. Its field applicability, repairability, and ability to deliver high-resolution strain data make it especially suited for SHM where flexibility and responsiveness are critical. Ultimately, these insights contribute to defining best practices for surface-bonded DFOS use and stress the importance of developing supportive regulatory and quality assurance frameworks to ensure consistent performance in long-term SHM applications.

4.5.3. Sensitivity and Parametric Examinations and Recommendations

4.5.3.1. Effects of Sensor Installation Path Conditions

The study investigated how variations in host bar size and surface characteristics along the DFOS cable installation path influence the performance of the sensing system. Generally, despite the differences in mechanical properties of the host material, the prolonged strain monitoring performance of the integrated DFOS layouts of varying GFRP bar's diameter remained consistent. The bar diameter did not influence the overall feasibility of accurate DFOS reading.

The impact of sensor path conditions on strain measurements was investigated by comparing surface-bonded DFOS on different GFRP finishes, smooth, flat spiral-finished surfaces versus rough, irregular sand-coated (SC) surfaces, and groove-embedded DFOS. The results highlighted key differences in long-term stability of distributed STE between two types of DFOS attachment techniques based on bondline integrity and strength: 1) consistent bondline quality a medium to full extent of sensor-to-host integration, depending on whether sensors were mounted on flat areas between spiral grooves or embedded within machined grooves; and 2) disrupted bondline quality caused by micro-gaps within the adhesive interface, which result from the rough SC surface finish and lead to poor sensor-to-host integration.

The sensors directly bonded on the rough texture of SC GFRP samples could record relatively accurate strain readings during the initial monotonic tensile loading. Nonetheless, under sustained high-level loading conditions, surface-bonded DFOS on SC GFRP bars exhibited significant gradual drifts and reductions in strain measurements across the entire bonded length. In contrast, groove-embedded DFOS within SC GFRP samples displayed more stable strain data. Notably, sample SC-16-g demonstrated superior resistance to loss of distributed STE. This was primarily due to the preservation of a portion of the effective sensing length, which allowed the sensor to continuously capture near-actual strains in the host. The improved stability can be attributed to the

more rigid anchoring of the sensor and higher degree of adhesive fulfilment, effectively controlling drift development by minimizing adhesive particles' dislocations and interfacial slippage.

Both sensor placement configurations with consistent bondline quality, surface bonding on spiral-finished GFRP and groove embedding along a refined path, demonstrated the potential to maintain partial bondline integrity and effective strain transfer under elevated static loads. In these cases, the bond strength facilitated partial energy dissipation along the bonded length, especially within the partially damaged zone that developed from one free edge, where localized plastic deformation was not effectively confined. The primary distinction between the two approaches lay in the consistency of strain readings along the DFOS-bonded length. Groove embedding produced smoother, more continuous strain profiles, regardless of adhesive type, reducing the risk of misinterpreting crack locations and extents in concrete reinforced with DFOS-bonded GFRP bars.

Furthermore, although not directly observed in this study, groove-embedded DFOS layouts offer additional potential advantages over surface-mounted configurations by providing physical protection to the FUT against external damage and environmental interference. This added protection contributes to more stable and reliable strain measurements under both cyclic and sustained loading conditions, enhancing the suitability and robustness of groove-embedded systems for long-term SHM applications.

4.5.3.2. Effects of Sensor Bonding Material

The choice of adhesive played a small but noticeable role in the DFOS performance, mostly in terms of measuring strain values rather than maintaining bondline integrity and monitoring stability. The two adhesive types investigated, EP and CN, demonstrated similar probabilities for the evolution and progression of shear plastic deformation into the bondline under sustained loading conditions exceeding the critical bond strength, though they differed slightly in the degree of STE and the distributed uniformity within their elastic regimes.

CN adhesive enabled direct bonding of the sensor to the host material due to its rapid curing and minimal bondline thickness, attributed to its high viscosity. Although CN possesses a lower shear modulus, which may typically limit STE, it occasionally demonstrated superior performance. In specific instances, such as sample SP-S, strain measurements from DFOS layouts bonded with CN and EP adhesives showed comparable performance.

Overall, CN proved more effective in mitigating STE losses associated with suboptimal sensor installation or incomplete embedment, issues more likely to occur with EP due to its slower curing process. The rapid setting of CN promoted stronger adhesive confinement, and when combined with its relatively stiff bonding layer, governed by the interplay between shear modulus and bondline thickness, it effectively reduced interfacial shear strains. This resulted in higher average strain readings from DFOS bonded with CN compared to those bonded with EP.

However, CN was less effective in achieving uniform strain distribution along the bonded sensor cable. Strain measurements from DFOS directly surface-bonded with CN exhibited increased variability along the DFOS bonded length, particularly under elevated strain conditions exceeding 3000–4000 $\mu\varepsilon$. In contrast, EP provided more consistent strain distribution, supporting satisfactory STE and yielding smoother strain profiles across a wide range of loading conditions.

The increased noise observed in the strain distribution curves of CN-bonded DFOS layouts can be attributed to heightened sensitivity to irregularities along the sensor path and host surface, amplified by the adhesive bondline's higher stiffness, which promotes more localized strain transfer at discrete points along the sensor–host interface. As shown in the strain distribution results, the groove embedding technique effectively mitigated these inconsistencies by minimizing surface roughness and bonding irregularities. This reduction in noise allows CN-bonded DFOS systems to maintain high strain sensitivity and accurately capture localized variations without being distorted by surface-induced effects. With proper installation techniques, such as groove

embedding, CN adhesive demonstrates strong potential to outperform EP in DFOS-based crack monitoring, consistent with findings by Clauß et al. (2021).

The mentioned study demonstrated that adhesives like EP, which exhibit lower interfacial stiffness and higher thickness, cause strain to diffuse over a broader area of the adhesive, rather than being directly transmitted to the optical fibre. This strain-spreading effect reduces the precision of local strain measurements, particularly at deformation zones, leading to a smoothing of the strain profile and a slight distortion of absolute values. Similar behaviour was observed in the present study, where EP-bonded DFOS layouts produced smoother and more stable strain curves, while CN-bonded counterparts exhibited increased sensitivity to surface irregularities, reflected as localized noise in the strain profiles. Moreover, the referenced study noted that strain-spreading can cause de-localization, displacing strain peaks from the actual deformation site, such as a crack, and diluting strain intensity in critical regions.

Experimental observations, supported by previous crack monitoring studies, underscore the critical role of adhesive interface stiffness in determining the accuracy of distributed strain measurements in DFOS-instrumented reinforcing bars. While lower-stiffness adhesives typically produce smoother and more continuous strain profiles, they may fail to capture localized strain peaks, such as those at crack sites. In contrast, stiffer adhesives, such as CN and high-stiffness epoxies, enable more precise detection of localized strains. However, the use of CN, in particular, increases the risk of DFOS cable damage due to its brittleness and reduced flexibility, potentially compromising sensor protection and coverage.

Understanding the trade-off between strain localization (high stiffness) and measurement continuity (low stiffness), along with careful consideration of sensor protection and layout design, is therefore essential when selecting adhesives for applications such as high-load testing or localized structural monitoring.

4.5.3.3. Effects of Sensor Protective Jacket

The DFOS coating type has a subtle but measurable effect on strain-sensing performance. Both PVC- and PI-coated fibres have similarly thin single layers; however, PI-coated DFOS showed slightly better strain response. This is due to the PI coating's finer thickness and chemical bonding to the core fibre, which improves strain transfer and reduces shear lag. In contrast, the PVC coating lacks this bonding, resulting in slightly less efficient strain transmission. Consequently, PVC-coated FUTs occasionally underestimated strain relative to PI-coated fibres and consistently exhibited a shorter effective sensing length, reducing the bonded length contributing to accurate readings. PI-coated DFOS also exhibited reduced signal integrity and higher local strain gradients in low-sensing (strain transfer) areas, a trade-off to preserve a longer effective sensing length.

Nevertheless, PVC-coated FUTs consistently provided reliable strain measurements under various loading conditions without noticeable degradation. Due to their greater robustness, easier handling, and significantly lower cost, PVC-coated fibres present practical advantages for field applications. These benefits make them a favorable and cost-effective choice for many SHM scenarios, despite exhibiting slightly lower STE compared to more sensitive but delicate PI-coated counterparts.

4.5.3.4. Effects of Sensor Strain Conditions

The DFOS monitoring performance, assessed under short-term simulations of both service-level and extreme stress conditions, showed consistent behaviour across monotonic tensile loading/unloading and rapid cyclic stress scenarios. Within service-level strain ranges, measurement accuracy appeared largely independent of strain level and condition, with only minor variations attributed to DFOS layout. However, as strain levels increased, particularly under sustained or extreme loading, loss of distributed measurement efficiency became more pronounced. This suggests a performance threshold around 12000–13000 microstrain, beyond which readings become increasingly perturbed and less reliable.

Under high sustained stresses, adhesive shear stresses can exceed 90% of their ultimate strength, triggering irreversible bond damage. This is attributed to the inelastic response at the adhesive interface, where interlaminar instability and sliding (or slippage) between DFOS and the host GFRP typically initiate near free bond ends, zones of elevated stress concentration. These instabilities propagate inward over time, progressively reducing cohesive bond strength. The result is significant permeant shearing lag, strain redistribution, and the emergence of SRAs along the bonded length, ultimately reducing the effective sensing length and compromising DFOS reliability under elevated or sustained loading.

4.5.3.5. Effects of Sensor Strain History

Observations from the three loading histories examined in this experimental study underscore the critical influence of prior mechanical exposure on the interpretation of real-time strain data from DFOS-bonded GFRP bars. Although the DFOS-integrated systems exhibited consistent and reliable performance under monotonic loading, frequent stress variations, and low-to-moderate sustained stress conditions, their accuracy progressively declined following extended overstress. Persistent distortions in strain readings, particularly along bonded regions affected by plastic interfacial deformations, were observed even after unloading or transitioning to milder loading regimes. This indicates that loading history can compromise monitoring durability when it introduces lasting degradation in bond integrity or the sensor–host interface. As bond deterioration and damage length increase, the DFOS system may require recalibration or compensation strategies to mitigate the effects of sustained overstress and halt the progression of SRAs, thereby restoring reliable measurements for the remainder of the service or testing period.

4.5.4. Performance Efficiency Thresholds

The comparative feasibility study of surface-bonded DFOS systems on GFRP bars has provided valuable insights into their performance under varied conditions, as well as the practical challenges

associated with their implementation. To consolidate these findings, **Table 4-1** provides a detailed summary of the primary obstacles impacting the long-term monitoring reliability and stability identified throughout the investigation. This table presents key evaluation parameters, including signal attenuation integrity, the durability of bonded FUT for stable monitoring under mechanical stressors, and distributed strain transfer uniformity via strain thresholds for efficiency delivery and signal fidelity. Complementing this, **Table 4-2** synthesizes comparative observations into a unified framework. The results indicate that, while DFOS technology holds significant promise for real-time strain monitoring in GFRP bars, its performance is subject to multiple influential factors. By consolidating critical findings and challenges into concise references, these tables provide a valuable resource for guiding future research aimed at optimizing DFOS-integrated GFRP systems for structural health monitoring and smart infrastructure applications.

Table 4-1. General parametric evaluation of test samples of surface-bonded DFOS GFRP bar

NO.	*Evaluative parameter*	*General Deficiency*	$\varepsilon_{\mathrm{eff,th}}$[2]	*Possible cause of deficient observation*
1	Signal integrity within the effective sensing length ($\varepsilon_{DFOS} \geq 0.95\varepsilon_{host}$)	Increased signal loss at higher strain levels, varying in magnitude	12000	- Natural attenuation - Micro/macro bends - FUT breakage (when reaching specimen failure) - Poor splice/ connector faults - Uneven cable laying or interfacial slippage - Scattering or reflection loss
2	Signal integrity within the strain transfer length ($\varepsilon_{DFOS} \leq 0.95\varepsilon_{host}$)	Signal attenuation under high strain	4000	- Strain gradient exceeds OFDR interrogator gauge pitch limit (resolution limitations)
3	Effective sensing length ($\varepsilon_{DFOS} \geq 0.95\varepsilon_{host}$)	Gradual decline under sustained high stress	12000	- Progressive damage length induced by adhesives' inelastic response at host-sensor interface
4	Stable distributed strain transfer within intermediate layers	Full/partial failure along length under sustained high stress	12000	- Significant increase in shear stresses and interfacial failure affected by adhesives' shear plastic deformation progression
5	Uniformity of distributed readings along effective sensing length	Prone to slight accuracy decline at elevated strain levels	2000	- High sensitivity of the technology to existence of any integrity inconsistency within bonded length

[1] *(the segment of the optical fibre cable extending from one endpoint to where DFOS records 0.95 of the host material's strain)*

[2] $\varepsilon_{eff,th}$ ($\mu\varepsilon$): *Probable strain threshold for efficient delivery*

Table 4-2. General influence of variable DFOS configurations across test samples

NO.	*Parameter*[1]	*General observed pros and cons*	*Field application*[2]
1	Surface-mounted attachment technique	✓ Sensor installation simplicity × Increased non-uniformity in the strain distributions recorded by DFOS	Speedy implementation of SHM unit
2	Groove-embedded attachment technique	✓ Improved smoothness in DFOS-recorded strain distribution profiles ✓ Consistent installation, anchorage, and alignment of FUT ✓ Enhanced protection of the DFOS cable against mechanical damage ✓ Reduced interference with the bond between concrete and reinforcing bar when embedded in RC members	Improved reliability in crack visualization and quantification due to minimized strain peak misinterpretation
3	EP adhesion	✓ Uniform distributed strain measurements along the DFOS bonded length × Increasing shear lag effects within layered strain transitions	Enhanced sensor protection against mechanical stress and increased adhesive interface resistance to environmental factors
4	CN adhesion	✓ Improved STE and accuracy of DFOS distributed strain measurements ✓ Increased effective sensing length and reduced low-sensing segments along the DFOS bonded length (PI only) × Increased non-uniformity in the strain distributions recorded by DFOS × Increasing signal attenuation, installation complexity, and possibility of losing the sensor during service (PI only)	Enabled precise localized strain data for SHM, with enhanced sensor sensitivity, reduced smoothing of strain variations, and improved concrete crack assessment
5	PI jacket		
6	PVC jacket	✓ Enhanced sensor stability, cost-efficiency, ease of use, and improved resistance to environmental noise and potential damage × Increasing shear lag effects within layered strain transitions × Reduced effective sensing length and increased low-sensing segments along the DFOS bonded length	Ideal for large-scale SHM due to durability, satisfactory STE, low cost, and ease of installation

[1] *DFOS layout investigated parameter*

[2] *The relevant requirement for field application (when embedded in RC member)*

Chapter 5

Results and Discussions of the Numerical Analysis

5.1. General

This chapter presents results from numerical simulations of theoretical strain transfer in DFOS GFRP test specimens. **Section 3.2** details the governing equations describing both elastic and inelastic interlaminar strain transfer. The strain transfer mechanism from the monitored host materials through intermediate layers to the core optical fibres, considering both elastic and inelastic adhesive interface behaviour under practical operational conditions, is examined using detailed graphical illustrations. The charts in this chapter depict the spatial distribution of strain transfer coefficients, $Z(x) = \varepsilon_{DFOS}(x)/\varepsilon_h$, across various conditions and test samples for DFOS-bonded GFRP bar systems. These visualizations capture both elastic strain transfer and the progressive inelastic degradation characterized by localized damage along the DFOS bonded length. Key parameters, namely the interfacial transfer coefficient (β_1) and the shear lag parameter (β_2), were derived from the material and geometric properties of the adhesive interface and the fibre cable, respectively, each reflecting a distinct aspect of the overall strain transfer mechanism.

The numerical analysis conducted within the inelastic regime of bonded joints, examines the strain transfer behaviour under different scenarios of localized permanent shear deformation or interfacial separation at host-sensor interface. This investigation examines potential interfacial failure along the DFOS bonded length and the growth of perturbations that drive damage propagation. By incorporating critical experimental observations obtained by DFOS, particularly related to damage length, this chapter offers a comprehensive analysis of the system's response to high-demanding loading conditions. The outcomes of the numerical modeling are assessed and compared against experimental data, with the observed trends consistently corroborating the theoretical predictions, thereby validating the model's analytical robustness.

5.2. Numerical Study Setup

5.2.1. Inelastic Analytical Model Relevance and Applicability

Before implementing the proposed numerical model incorporating inelasticity, its relevance is evaluated by analyzing experimentally measured strain profiles along the DFOS bonded length. Special emphasis is placed on initial strain reading anomalies (SRAs) observed at the onset of distributed measurement degradation to assess their correlation with underlying adhesive interface mechanisms, specifically localized plastic slip and progressive separation. It is noted that in the following material response clarification, the explanations for adhesive behaviour are implied from the studies by Burke (1999) and Da Silva et al. (2018).

The inelastic part of the numerical model presented in this study is designed to accurately capture the complex strain transfer mechanism of adhesively bonded DFOS systems under relatively high-level sustained loading, with a particular focus on the initiation and progression of interfacial damage. One of the key features of this model is its ability to consider localized damage that begins at the bond edges and propagates along the bonded length. This phenomenon is critical in adhesively bonded DFOS configurations, where interfacial damage typically initiates at regions of high stress concentration, such as the edges of the adhesive bond. This localized damage can progressively lead to bond degradation under elevated, sustained loading conditions, permanently compromising the performance and reliability of the sensing system.

Generally, as the high sustained stresses pushed the adhesive interfaces into their inelastic regime, initially all tested samples exhibited a shift in strain readings at their ends (previously defined as ε_p in **Section 3.2**). **Figure 5-1** illustrates an example of this behaviour, captured with integrated DFOS signals, highlighting the initial strain localization at the adhesive bond edge, where the material first experiences the influence of the applied load strain. Localized strain concentrations indicate the initial stages of interfacial degradation, where the adhesive initially loses its ability to

transfer strain efficiently. This signals the onset of inelastic shear strain, characterized by a non-homogeneous response and localized shear redistribution, gradually reducing the bondline's stiffness during sustained overload. Such localized strain increases were commonly observed in adhesive joints under overloading and have been validated by numerous experimental studies.

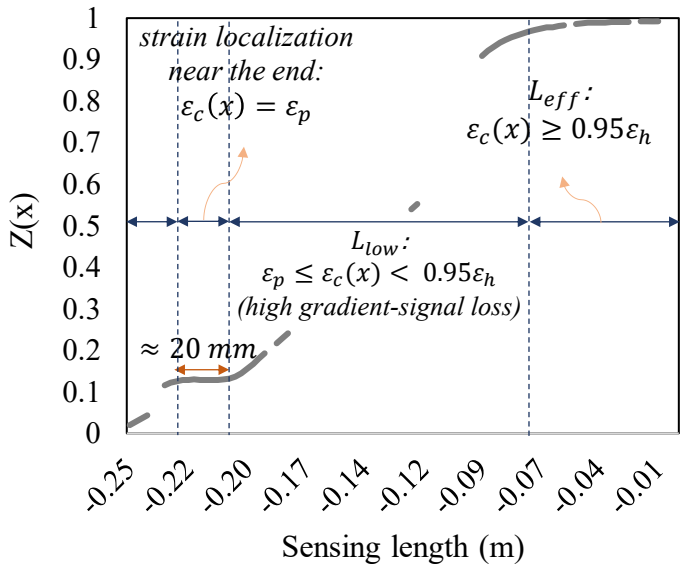

Figure 5-1. Formation of adhesive's strain localization near the bond edge, as detected by DFOS (L_{eff}: effective sensing length, L_{low}: low-sensing length. The plotted $Z(x)$ values are based on the assumption of $\varepsilon_{c\ or\ DFOS}(x = 0) = \varepsilon_h$)

For both experimentally investigated adhesive types, two-part epoxy (EP) and cyanoacrylate (CN), the bond interface exhibited strain localization and damage when subjected to stresses exceeding a certain threshold, particularly when sustained strains surpassed 12000 microstrain ($\mu\varepsilon$). However, their responses were influenced by their distinct molecular structures, leading to notably different interfacial behaviours near the bond ends. Despite these differences, both exhibited a similar damage evolution pattern, characterized by shear stresses acting parallel to the interface that initiated interfacial degradation. This process led to the formation of damage zones and the progressive development of localized shear deformation or separation, accompanied by stress redistribution and gradual energy dissipation within the adhesive interface, consistent with traction–separation behaviour observed in cohesive zone models (CZM).

As demonstrated in the previous chapter, experimental results show that damage consistently initiated near the bond edges, where shear deformations were most concentrated. When pre-existing weak zones or interfacial defects were located near these regions, they were incorporated into the expanding damage front, accelerating its progression into the adhesive interface. These imperfections contributed to local strain concentrations and facilitated plastic slip between adherends. The extent of damage varied across specimens, reflecting differences in initial bondline quality. These findings illustrate the model's ability to represent the progressive nature of interfacial failure at host-sensor interface, in which the adhesive accommodates excess loading through localized shear plastic deformation, dissipating energy while maintaining partial strain transfer. In some cases, this allowed portions of the bonded length to remain elastic, as damage localized within a confined region rather than propagating along the entire interface.

In the case of DFOS cables, the free length adjacent to the adhesive interface remains mainly unaffected by the adhesive bond, experiencing minimal strain due to its lack of direct involvement in the load transfer. Although this condition predominated within elastic responses of the adhesive, the experimental observations obtained at elevated sustained stresses from most EP-embedded test layouts frequently revealed that after initiation of the adhesive's inelastic response, within a small segment of the DFOS free length of about 5-7 *mm*, there was a shift in DFOS strain reading from zero to a strain value approximately equal to the bond edge's localized strain, as shown in **Figure 5-2**. The strain measurements in this region indicate inelastic behaviour, stemming from the adhesive's progressive localized deformations under sustained severe stress. This occurs despite the region not being initially bonded, reflecting the increasing intensity of shear-induced alterations in localized areas near bond edges, such as plastic deformation and shear flow.

The relatively ductile nature of EP appears to accommodate more gradual accumulation of plastic deformation at the bond free ends under load. As polymer chains approach their deformation limits, shear flow within the adhesive may develop, influenced by stress redistribution and

kinematic constraints. This process can lead to a gradual build-up of localized deformation near the bond edges, with the extent of redistribution varying according to the molecular structure and arrangement of the adhesive polymers. As localized plastic shear deformation accumulates and progresses along the adhesive bondline, it appears to engage longer unbonded DFOS segments near the bond edges, gradually increasing their strain readings from near zero to higher values, as shown in **Figure 5-2**. This increase reflects the gradual transition of strain from the bonded region to the unbonded DFOS segments, influenced by the accumulation of plastic deformation and the inherent spatial averaging of the sensor over a limited sensing length. The evolving plastic deformation at the adhesive interface most likely governs this strain transition in the fibre optic sensor, corresponding approximately to the plastic strain in the adhesive itself.

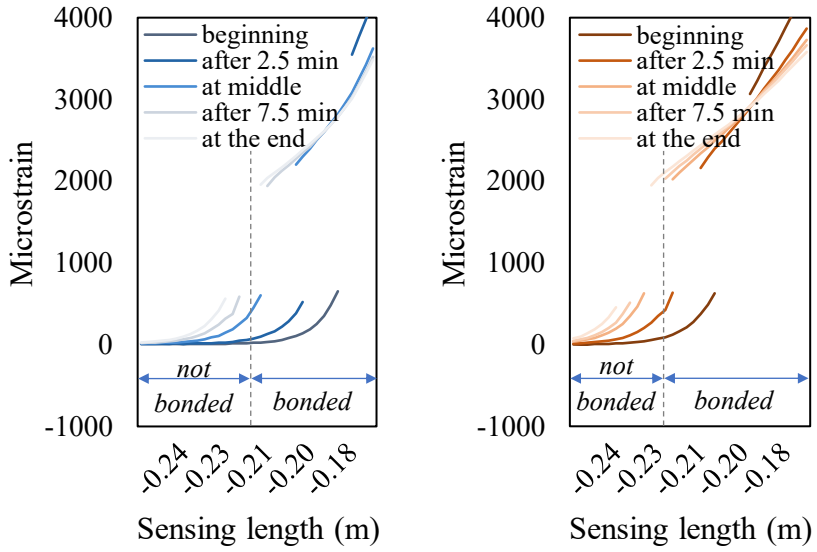

Figure 5-2. Representative DFOS measurements near bond edges indicating local accumulation of inelastic deformation in the adhesive and redistribution of strain transmission, capture within the range $-L + (-L') \leq x \leq -L + L''$ (L'~0.03m, L''~0.05)

In contrast, CN interfaces exhibited a stiffer and sudden response. Although experimental observations revealed similar overall patterns of bondline damage growth compared to EP, CN showed markedly sharper and more abrupt transitions from elevated, localized strain at the bond edges to near-zero strain along the adjacent free length. In both CN-adhered test layouts, DFOS

signal integrity was compromised; however, measurements near the CN bond edges specifically revealed that these transitions occurred over just a few sensing intervals, indicating a rapid buildup of irreversible strain once the adhesive yield threshold was exceeded. This behaviour aligns with the tightly crosslinked polymer structure of CN, which limits gradual, extensive plastic flow and leads to more abrupt strain localization at stress concentration points near the bond edges.

Furthermore, experimental observations following unloading cycles show that the DFOS segments near the ends of the bonded regions, which accumulated delayed shear strains, remained "locked" at the obtained strain readings for the rest of the tests, as shown in **Figure 5-3** and detailed in **Appendix A**. These findings suggest that the DFOS bonding interfaces were likely influenced by the plastic deformation, hardening or toughening effects of the adhesive interfaces as the accumulated strains were irrecoverable. As damage zones developed, the adhesive underwent permanent deformation, causing the DFOS segments to become fixed in the adhesive's new deformed state. This resulted in the strain readings remaining constant, reflecting the final condition of the adhesive after damage had occurred.

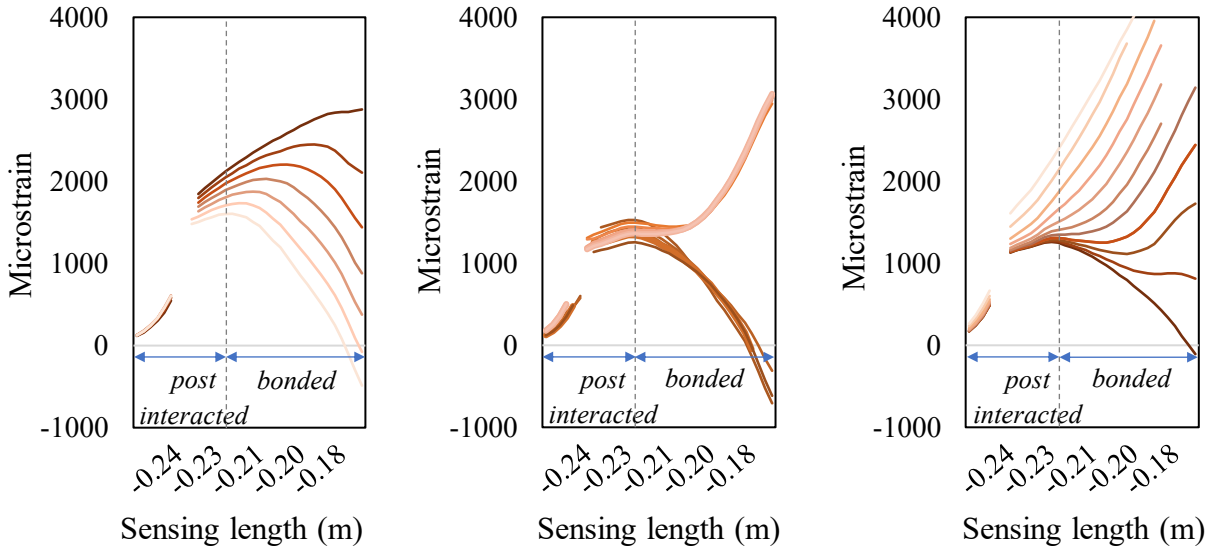

Figure 5-3. Localized DFOS strain profile near free ends of bondline interface captured by a representative sample after relieving constant overloading: a) initial unloading, b) peaks and troughs of cyclic loads, and c) final loading (with load progression shown by a color gradient)

Furthermore, during the elastic strain transfer regime, end points of the DFOS bonded lengths consistently remained near zero, regardless of the applied load. Thus, it implies that these regions correspond to newly formed bond edges, which no longer exhibit dynamic responses to subsequent loading. These observations reinforce the model's applicability for capturing the accumulation of irreversible shear deformation across both adhesive types.

Consequently, the findings show that both EP and CN adhesives, despite their differing polymer structures, exhibited localized inelastic shear deformation from the onset of sustained high loads. This initiated bondline degradation through similar mechanisms, as insufficient confinement of plastic shear strain at the bond edges under sustained high-level loading promoted interfacial damage propagation and progressively reduced cohesion between the host material and the DFOS at the microstructural level.

In the damage zone of adhesive joints, localized deformations may involve polymer chain alignment, plastic shear deformation, void formation, and micro-fracturing, often interacting in complex ways, all of which contribute to changes in stress distribution and ultimately lead to bond degradation and loss of overall bondline integrity. Although these behaviours manifest differently depending on the adhesive material and application, they can all be understood within a unified framework of interlaminar bond damage localization and progression. Therefore, the analytical model developed in **Section 3.2**, which considers localized, non-homogeneous shear deformations within the adhesive interface incrementally and iteratively, can effectively capture the observed accumulative plastic shear lag effects and strain transfer efficiency (STE) loss mechanisms.

This preliminary validation confirms the inelastic component’s applicability for analyzing interfacial interactions along DFOS bonded lengths, establishing its readiness for subsequent numerical modeling. The model thus provides a promising framework for simulating adhesive bond interface under sustained loading, focusing on localized damage initiation and progression.

5.2.2. Input Parameters and Analysis Approach

- **Domain and Sequence of Analysis**

By leveraging the symmetry of the system, the analysis is performed over the bonded length of $-L \leq x \leq 0$. Although minor discrepancies and inconsistencies were occasionally observed in the strain distribution curves of some experimental samples, arising from installation-related issues, these differences were generally negligible and were therefore disregarded, as they did not significantly affect the overall analysis. However, in cases where more pronounced variations occurred, particularly in samples exhibiting interruptions in the strain curves during high sustained loads with only one half of the bonded length affected while the other half remained intact, these instances are specifically highlighted and discussed in the following sections. These variations influence the interpretation of strain transfer and distribution patterns across the adhesive interface. It is also noted that both surface-mounted and groove-embedded configurations are analyzed using the same procedure, and the potential differences are not factored in.

Prior to applying the refined strain transfer model to characterize the inelastic regime, the analysis begins with the implementation and validation of strain transfer behaviour under elastic conditions. Given that the mechanics of elastic strain transfer are well-established in the literature, this phase primarily serves to validate the model framework, ensure alignment with known behaviour, and confirm the accuracy of input parameters.

- **Estimation of Host Strain (ε_h) and $Z_{ex}(x)$ Calculation**

When incorporating and plotting experimental strain transfer coefficient distributions, referred to as $Z_{x,ex}$ or $Z_{ex}(x)$, it is essential to establish a reliable assumption for the strain experienced by the host material, ε_h, since $Z_{ex}(x)$ is defined as $Z_{ex}(x) = \varepsilon_{DFOS}(x)/\varepsilon_h$. The selection of this reference strain is critical, as it forms the basis for aligning experimental observations with the numerical model and ensuring consistency in the interpretation of the data.

A practical estimation of the host strain can be obtained using the relation $\varepsilon_h = \varepsilon_{DFOS}(x=0)/Z_{ex}(x=0)$, evaluated at the location of maximum strain transfer along the DFOS bonded length. This formulation enables a direct correlation between experimental data and theoretical predictions, under the assumption that $Z_{ex}(x=0) = Z_{th}(x=0)$. Then, by initially assigning a value for $Z_{th}(x=0)$, the input parameters of the theoretical model, particularly those governing the adhesive interface properties, can be calibrated to satisfy this condition.

Extensometer (EX) data were not used as the primary reference for the host strain due to growing discrepancies with DFOS measurements at higher strain levels. While relative errors remained below 1% at low strains, they increased to 6–7% in less correlated samples. To establish a consistent baseline, essential for verifying the inelastic component of the model and evaluating its performance across different test samples, a common, conservative measurement accuracy of 96% at the specimen midpoint, corresponding to $x = 0$ theoretically, was adopted, setting $Z_{ex}(x = 0) = Z_{th}(x=0) = 0.96$. This value balanced the average deviation between EX and DFOS, providing a realistic estimate of maximum STE without overestimating DFOS accuracy or approaching the upper limits of EX performance. While accuracy may vary across test samples, it served as a reliable reference for calibrating the model in the elastic regime. Additionally, a 93% accuracy, observed under the worst-case alignment, was adopted as a lower bound for the credible performance of the bonded DFOS systems across varying conditions.

Consequently, the host strain (ε_h) was estimated by assuming a maximum STE of 96% at the bonded length midpoint ($Z(x=0) = 0.96$), using the relation $\varepsilon_h = \varepsilon_{DFOS}(x=0)/0.96$. This enabled the calculation of the experimental STE distributions along the bonded length ($Z_{ex}(x)$).

- **Determination of β_2 and Input Parameters for the DFOS Cable**

The parameter β_2, which characterize the gradient of DFOS strain transfer along the bonded length, was computed using **Eq. (5-1)**, previously derived as outlined in **Section 3.2.4**.

$$\beta_2 = \left[\frac{\pi}{\pi-2\alpha}\frac{E_c r_c^2}{E_j}\left(1+\nu_j\right)\left(\frac{r_j^2}{r_j^2-r_c^2}ln\frac{r_j}{r_c}-\frac{1}{2}\right)\right]^{-0.5} \quad \textbf{Eq. (5-1)}$$

where $\pi - 2\alpha$, representing the engaged portion of the jacket's perimeter, was approximated as π due to the small diameter of the DFOS cables used in this study, and ν_j, the jacket's Poisson ratio, was taken as a typical value of 0.25 for both jacket types investigated.

As described in the equation, the parameter β_2 is derived from DFOS cable specifications, particularly the radial geometry and elastic modulus of both the jacket and core fibre layers, which directly influence distribution of STE. The material properties were obtained from established literature sources, including studies by Padilla Michel (2015), Wang et al. (2016), Tan et al. (2021b), Chapeleau and Bassil (2021), and Zhang et al. (2021b). These values were treated as fixed constants for all test samples, with the appropriate parameters selected according to the jacket type tested, either polyimide (PI) or PVC.

The input parameters and the β_2 value are summarized in **Table 5-1**. Additionally, the defined radial geometry function in the final Z_x formulation, given by $f(r) = r_j[(1/2) - ((r_c^2/r_j^2 - r_c^2) \times ln\,(r_j/r_c))]$, was computed at this stage for both DFOS cable types, providing the required values for subsequent calculations.

Furthermore, as mentioned in the study by Zhang et al. (2021b), the parameter α_j was defined as an empirical calibration factor applied to the DFOS jacket's modulus to effectively reduce the interface stiffness between the fibre cladding and the jacket, thereby simulating the effects of excessive shear deformation in the intermediate layers. The specific value of alpha for each testing type, as outlined in the referenced study and adjusted with experimental correlations in this context, is incorporated into the model, as described in **Table 5-1**. The role of this parameter is crucial, as elaborated in the subsequent section; neglecting it leads to inaccurate results, causing the model to yield improper interpretations of the strain transfer mechanics.

Table 5-1. DFOS cable input parameters

No.	Definition	Label	Input/Output Value	Unit
1	Radius of the core fibre	r_c	0.0000625	m
2	Young's modulus of the core fibre	E_c	70	GPa
3	Radius of the PVC jacket	$r_{j,PVC}$	0.00045	m
4	Radius of the PI jacket	$r_{j,PI}$	0.00015	m
5	Young's modulus of the PVC jacket	$E_{j,PVC}$	1.7	GPa
6	Young's modulus of the PI jacket	$E_{j,PI}$	2.5	GPa
7	empirical calibration factor (PVC)	α_{PVC}	0.001	–
8	empirical calibration factor (PI)	α_{PI}	0.0015	–
9	β_2 parameter of PVC-coated DFOS	$\beta_{2,PVC}$	≅40.5	m^{-1}
10	β_2 parameter of PI-coated DFOS	$\beta_{2,PI}$	≅100	m^{-1}
11	f(r) value of PVC-coated DFOS	$f_{PVC}(r)$	≅0.000207	m
12	$f(r)$ value of PI-coated DFOS	$f_{PI}(r)$	≅0.00004	m

- **Determination of $\beta_{1,e}$ and Input Parameters for the Adhesive Interface**

At this stage, $\beta_{1,e}$, which characterizes the interfacial strain transfer within the adhesive at the sensor–host interface in the elastic regime, along with the elastic mechanical properties of the adhesive interface, were determined. To achieve this, the value of $Z_{x=0,th}$ was determined using the previously established 96% measurement accuracy at the specimen midpoint. This value was calculated by substituting and adjusting the relevant input parameters in the following equation to yield $Z_{x=0,th} = 0.96$, described as,

$$Z_{x=0,th} = (\beta_{1,e} + \frac{(Z_{\pm b} - \beta_{1,\pm b})}{cosh(\beta_2 x_{\pm b})} cosh(\beta_2 \times 0)) \quad \textbf{Eq. (5-2)}$$

where the parameters associated with the boundary conditions (BCs), indicated by the subscript "$\pm b$", were defined at the $\pm L$ points because the bonded length remained unaffected by partial bondline damage during the elastic regime, and no additional BCs were required beyond these endpoints to segment the measurement length further. At the boundary points, the strain transfer

parameter was approximated as zero, $Z_{\pm b} = Z_{\pm L}(t) \approx 0$, based on the ideal assumption that no strain transfer occurs at these discontinuities. The parameter $\beta_{1,e}$was treated as constant along the adhesive interface, such that $\beta_{1,e} = \beta_{1,\pm L}$. This allowed $Z_{x=0}$ to be simplified to,

$$Z_{x=0} = \beta_{1,el}\left(1 - \frac{1}{cosh(\beta_{2,j} \times -L)}\right) \quad \textbf{Eq. (5-3)}$$

In the equation above, since the bonded length used in this study was at least 0.4 m, such that $|L| > 0.2\ m$, the term $\left(1 - \frac{1}{cosh(\beta_2 \times -L)}\right)$ effectively tends toward zero, even when using the lowest calculated $\beta_{2,j}$ value of 40.5, as listed in **Table 5-1**. As a result, the maximum strain transfer coefficient at the midpoint was approximated as $Z_{x=0} = \beta_{1,e}$. The parameter $\beta_{1,el}$ was determined using the elastic-regime form of the switching function, previously defined in **Eq. (3-15)**, as,

$$\beta_{1,e} = 1 - \left((1 - \alpha_e^{\Delta})\left(1 + \frac{f(r)}{G_j} K_{a,e}\right)\right) \quad \textbf{Eq. (5-4)}$$

where α_e^{Δ} represents the defined adhesive interface's elastic displacement transfer ratio, and $K_{a,e}$ is the elastic interfacial shear stiffness of the adhesive interface.

Based on the above discussion, the elastic component of the analytical model, developed under simplified assumptions, reduces to the form $Z_{th}(x) = \beta_{1,e}(1 - \frac{cosh(\beta_2 x)}{cosh(\beta_2 \times -L)})$. This formulation incorporates the overall strain transfer performance primarily to the behaviour of the adhesive interface as a whole, rather than to the detailed distribution or gradient of strain transfer along the bonded length, such as that characterized by β_2 in the Z_x profile. Accordingly, the parameter $\beta_{1,e}$ was set to equal to $Z_{x=0} = 0.96$, based on the previously noted average experimental accuracy and consistent DFOS measurement error trends reported in the literature. By definition, $\beta_{1,e}$ ranges from 0 to 1, representing the quality of sensor bonding, with the adopted value reflecting typical interface performance under the tested conditions.

The adhesive interface stifness was incorporated using the relation $K_{a,e} = G_a/t_a$, as described by Lißner (2019), where G_a represent the adhesive shear modulus and t_a is the adhesive layer thickness. This formulation factors in the influence of adhesive thickness into the analysis while preserving the simplicity of a cohesive interface model that assumes negligible thickness in strain transfer mechanics. The relation also serves as a lower bound for estimating interface stiffness. This approach captures the interfacial effects of different adhesive joint configurations, such as the stiffer, thicker EP adhesive versus the more compliant, thinner CN adhesive, where the offsetting influences of stiffness and thickness reduce the overall differences in interface performance between these two specific adhesives.

Furthermore, the adhesive's elastic displacement transfer ratio, denoted as $\alpha_e^{\Delta} = u_{a/j}/u_{h/a}$, was introduced in this study as a simplified parameter to support the transition into the more complex inelastic regime. It represents a lumped numerical abstraction of shear displacement across the adhesive interface, aiding in the modeling of strain transmission from the host material to the sensor. Although not derived from a direct physical formulation, α_e^{Δ} serves as a practical tool to numerically modulate the output of the elastic phase and ensure compatibility with the inelastic model developed in the subsequent stage of analysis.

The parameters for E_a, t_a, and α_e^{Δ} were selected using a combination of justification strategies and a fitting approach aimed at satisfying the condition $\beta_{1,e} = Z_{x=0} = 0.96$. This approach ensured that the selected values reliably captured the mechanical behaviour of the adhesive interface in the elastic regime, while also establishing a robust foundation for incorporating the inelastic components developed later in the study. Moreover, it remained consistent with experimental observations within the defined accuracy and performance limits.

The fitting approach is outlined in the calibration flowchart in **Figure 5-4**, and the final input values for the adhesive interface's elastic mechanical properties are summarized in **Table 5-2**.

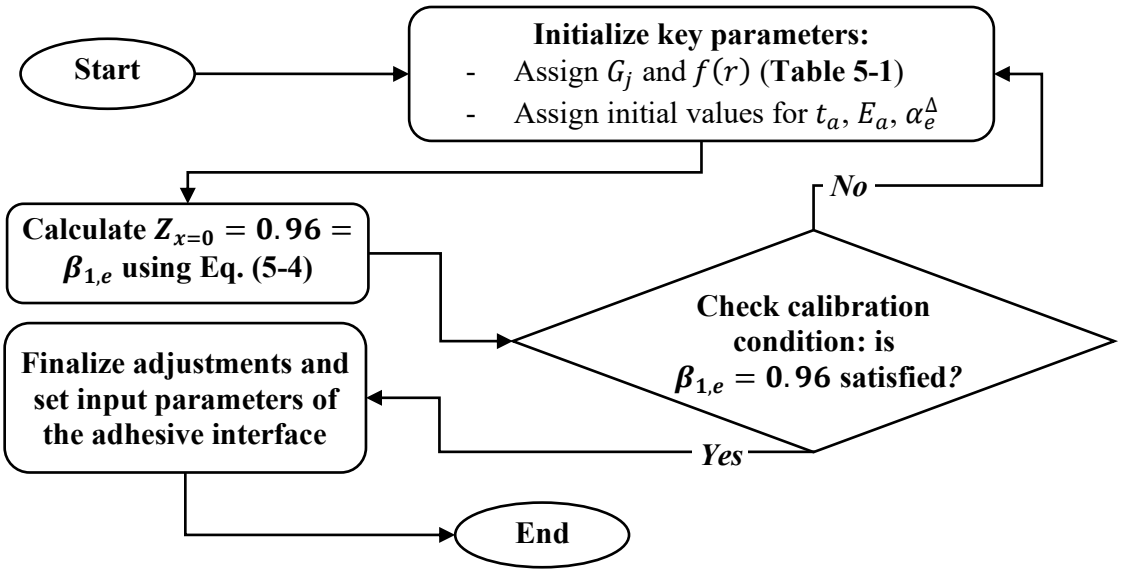

Figure 5-4. Calibration of adhesive interface parameters in the elastic response regime

Table 5-2. Adhesive interface input parameters

No.	Definition	Label	Input Value	Unit
1	Thickness of the EP adhesive interface	$t_{a,EP}$	0.0003	m
2	Thickness of the CN adhesive interface	$t_{a,CN}$	0.00015	m
3	Adhesive's Poisson ratio	ν_a	0.3	–
4	Elastic displacement transfer ratio	α_e^{Δ}	0.98	–
5	Young's modulus of the EP adhesive	$E_{a,EP}$	2.5	GPa
6	Young's modulus of the CN adhesive	$E_{a,CN}$	1.3	GPa

The selection strategy combined a review of relevant literature, including Komurlu et al. (2016), and adhesive product manuals to determine Young's modulus. Although a formal quantitative basis for adhesive thickness was lacking, it was chosen based on practical feasibility and fixed after assigning the corresponding modulus for each adhesive type. Given the strong interdependence between adhesive thickness and modulus, their combined effect, rather than individual values, was prioritized, as it governs the $\beta_{1,e}$, which in turn controls the measurement

accuracy through $Z_{x=0} = \beta_{1,e}$. This interdependence ensures that the model reliably captures the overall behaviour in DFOS systems, even if precise values vary in real-world applications.

Although the adhesive interface elastic input parameters are deterministically defined here for the initial setup, these values used in calculating $\beta_{1,e}$ may require refinement due to variations in adhesive properties and bonding quality under different conditions. A detailed justification for the chosen parameters, along with sensitivity analysis to evaluate their impact on elastic strain transfer mechanics, especially through the $\beta_{1,e}$ parameter, will be presented in the following section. This approach aims to account for potential uncertainties and variability, ensuring a thorough understanding of their influence on the model's response.

- **Determination of Elastic $Z_{th}(x)$**

Finally, the theoretical strain transfer coefficient distribution along the DFOS bonded lengths at each sensing point x was calculated using the simplified equation,

$$Z_{th}(x) = \beta_{1,e}\left(1 - \frac{cosh(\beta_2 x)}{cosh(\beta_2 \times -L)}\right) \quad \textbf{Eq. (5-5)}$$

Since both the theoretical and experimental calculations of Z_x inherently depends on $\beta_{1,e}$, which characterizes the adhesive bond interface and defines the maximum STE at $x = 0$ (midpoint of the DFOS bonded length), the following correlation analysis focuses on comparing overall measurement trends and distribution patterns, rather than the precise alignment of absolute Z_x values expected under field conditions. By calculating both $Z_{x,ex}$ and $Z_{x,th}$ using the same assumed value at $x = 0$, set at 0.96, and selecting the adhesive interface input parameters in the theoretical model to satisfy $Z_{th}(x = 0) = \beta_{1,e} = 0.96$, the resulting curves inherently align in terms of the targeted or observed accuracy range.

While the numerical implementation assumes uniform adhesive properties for consistency and streamlined integration of the newly developed inelastic model, it is acknowledged that, in

practical applications, minor uncertainties persist in the adhesive interface properties, which are defined here based on idealized assumptions and simplified models.

Unlike the well-defined properties of the jacket and core fibre, adhesive parameters, such as thickness, shear modulus, and curing quality, both between and within bonded lengths, can exhibit variability, making them the primary source of uncertainty in the model's input parameters.

A notable example of potential inconsistency in the mechanical properties of the adhesive bondline was experimentally observed in pilot test sample SC-16-g, where non-uniform strain measurements along the DFOS bonded length indicated localized deviations. Specifically, in this sample, approximately half of the DFOS bonded length showed a nearly consistent ~350 $\mu\varepsilon$ loss compared to the other half. This reduction also corresponded to the region affected by bondline degradation under high loading, while the remaining section retained bondline integrity. Similarly, in sample SP-S, comparisons between layouts (e.g., s-PVC-EP versus g-PVC-CN) revealed a near-constant deviation of about 250 $\mu\varepsilon$, largely independent of load level. A constant strain offset may arise from installation-related factors such as fibre loosening or interfacial gaps, and should be considered when interpreting strain data.

Despite the significance of these effects in high-accuracy strain interpretation and field calibration, they are not incorporated in the current numerical framework. The decision to omit them was made to maintain input consistency across all test cases and to avoid added complexity in the preliminary implementation of the inelastic component, which represents the primary novel contribution of the developed analytical model. By holding initial conditions constant, the model's performance and newly defined inelastic parameters can be evaluated in a controlled manner across all experiments. These simplifications ensure a focused assessment of the inelastic model's validity while laying the groundwork for future extensions that incorporate localized interface effects or probabilistic variability in adhesive properties for more comprehensive field-level accuracy evaluation.

5.3. Implications of the DFOS Strain Transfer Model

5.3.1. Numerical Analysis Results in the Elastic Regime

- **Pilot Test Samples**

To implement the formulation for $Z_{x,e}$ and evaluate the elastically-based analysis approach, encompassing the effects of parameters such as α_j, α_e^{Δ}, $\beta_{2,j}$, and $\beta_{1,e}$, pilot test samples are first utilized as case studies. These samples, consisting of PVC-coated DFOS cables bonded with EP adhesive, are employed to develop numerical models and establish experimental correlations under various sensor–host interface conditions. This provides a foundational understanding of the resulting curves and key influencing factors. The analysis of Stage II test samples is presented subsequently, examining the impact of intermediate layer properties, specifically comparing the differences between PI and PVC jackets and EP and CN adhesive interfaces.

The two charts in **Figure 5-5** present the theoretical and experimental strain transfer coefficient distributions, $Z_{th}(x)$ and $Z_{ex}(x)$, along half of the DFOS bonded length. Theoretical curves provide analytical baselines, while experimental curves are shown for two distinct loading stages during initial monotonic loading across various specimens.

Figure 5-5a presents data from DFOS layouts bonded to sand-coated (SC) GFRP bars, and **Figure 5-5b** corresponds to spiral (SP) GFRP bars. Each chart includes two sets of curves: Curve set 1 (s/1, g/1), recorded during the early stage of monotonic loading at a strain level of approximately 2000–3000 $\mu\varepsilon$, and Curve set 2 (s/2, g/2), captured at a higher strain level around 13000 $\mu\varepsilon$, near the point where the specimen experiences sustained high loading.

Overall, the experimental curves align well with the theoretical prediction, $Z_{th}(x)$, confirming the validity of the investigated model and input parameters. However, noticeable deviations are observed in the low-sensing length region, extending from the endpoints of bonded length till the

region with reliable measurements ($Z_{ex}(x) \geq 0.95$), particularly between $Z_{ex}(x)$ values of a single sample at the two strain levels. As the sensing length extends toward the effective region, discrepancies between the experimental curves and the theoretical baseline diminish, and the curves converge. This suggests that near the central bonded length, strain transfer stabilizes better, resulting in a more uniform system response with reduced shear lag and inconsistency effects.

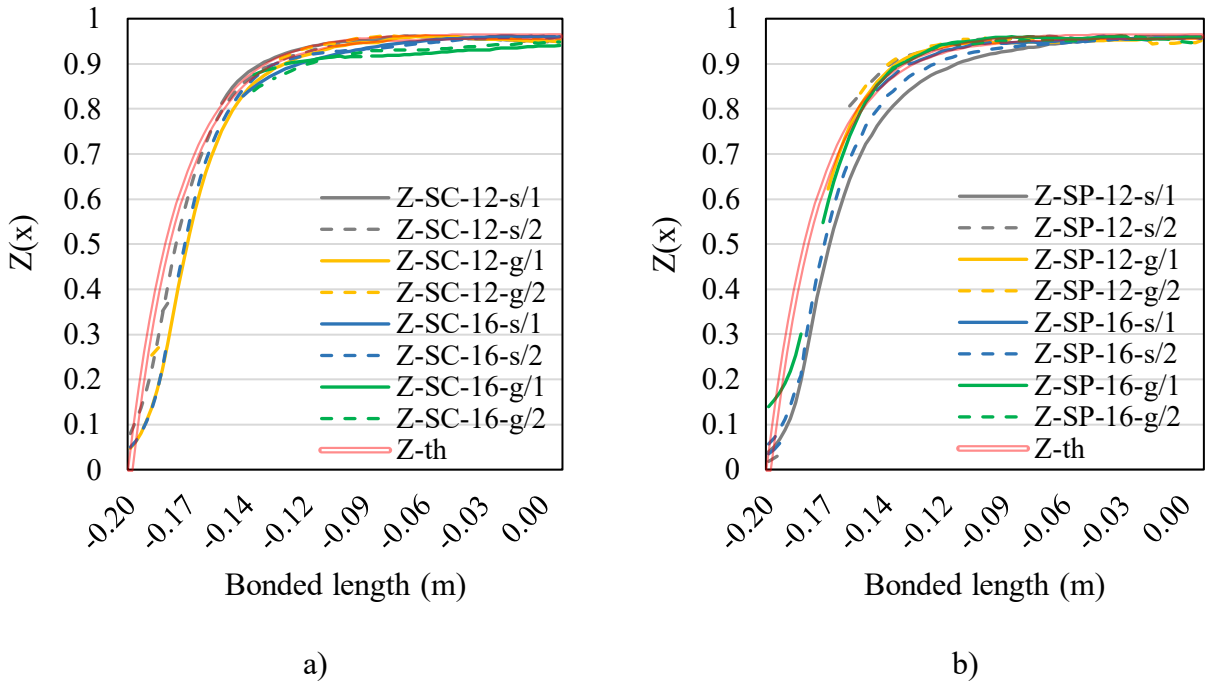

Figure 5-5. $Z_e(x)$ correlation analysis for pilot test specimens: a) GFRP SC and b) GFRP SP

Within the low-sensing (strain transfer) length range, approximately $-0.209\ m$ to $-0.147\ m$ in this particular case, as shown in **Figure 5-5**, the STE becomes more sensitive to the interaction between the core fibre and the host material, resulting in more noticeable deviations between theoretical and experimental results, particularly due to the simplified assumptions embedded in the theoretical model. Since the DFOS jacket is identical across all samples, any differences in the experimental results cannot be attributed to variations in the jacket itself. Instead, the deviations observed between the samples most likely have originated from differences in the adhesive interface and bondline quality conditions, which directly influence the STE.

Although the theoretical model defines the primary strain gradient through the DFOS jacket parameter $\beta_{2,j}$, by treating the adhesive as an interface rather than a shear layer, the adhesive's distributed response remains crucial in governing strain transfer along the entire sensing length. The defined parameter $\beta_{1,\mathrm{e}}$ captures the overall influence of the adhesive bond on strain transfer, meaning that this simplified elastic analysis does not account for local variations or distribution changes caused by suboptimal sensor installation.

The following summarizes key observations from experimental versus theoretical curves:

- The strong correlation between the experimental and theoretical curves confirms the reliability of the model and its input parameters. The observed differences can be attributed to factors such as microstructural effects, simplifications in modeling BCs where high-stress concentrations dominate the adhesive joint, and assumptions of uniformly distributed bonding conditions, adhesive response, and stress distribution.

- Sample SC-16-g exhibits the highest, albeit slight, deviation from the theoretical curve in the modeled half of the sensing length. However, the other half of the sensing length for this sample recorded slightly higher strain values, closely aligning with the middle point readings. It was the only sample with a partial sensing length that maintained steady readings throughout the sustained load and the entire loading protocol, as shown in the previous chapter in **Figures 4-6** and **4-7.** This is likely attributed to installation inconsistencies.

- Some experimental curves, such as Z-SC-12-g/1, Z-SC-12-s/2, Z-SC-16-s/2, Z-SP-12-S/1, and Z-SP-16-s/2 exhibited a more gradual rise in $Z_{ex}(x)$ from near-zero at the free ends toward the midpoint ($x = 0$) compared to the sharper gradient predicted by the theoretical curve. In sample SP-12-s, the gradient of $Z_{ex}(x)$ in the low-sensing length region increased when transitioning from strain level 1 (s/1) to strain level 2 (s/2). This contrasts with other samples that exhibited either a less pronounced difference or almost no change in response at all. This behaviour

suggests that at higher strain levels, the overall interaction between the sensing system and the host material may have become more effective, resulting in improved strain transfer. In contrast, at lower strain levels, the system may not have been fully engaged or stabilized, leading to slight inconsistencies and a more gradual response in the low-strain region.

- The deviation between the two experimental curves at different strain levels, or from the theoretical baseline, is generally slight but varies across the test samples due to factors such as variations in bond conditions, local imperfections along the bondline, complex interfacial engagement and behaviour, micro-slippage, and sensor positioning irregularities. These factors can influence how the adhesively bonded DFOS responds to tensile loads. However, along the effective sensing length, the impact of these factors diminishes, leading to a more uniform response across different DFOS layouts.

- **$\beta_{1,e}$ Sensitivity Analysis**

In the previous analysis, the parameter $\beta_{1,e}$ was set to 0.96, based on experimental observations showing an average strain deviation of 4% at the midpoint of DFOS-bonded specimens compared to EX readings. The experimental data were normalized accordingly to provide a consistent basis for comparison. This subsection investigates the sensitivity of adhesive interface elastic input parameters and assesses the influence of varying $\beta_{1,e}$ between 0.8 and 1.0 on both experimental results and corresponding theoretical predictions.

The parameter $\beta_{1,e}$ represents the overall efficiency of strain transfer from the host material to the core optical fibre through the adhesive interface, governed by the global characteristics and interfacial quality of the adhesive interface at the host-jacket boundary. Its value was found to depend largely on the displacement transfer ratio (α_e^{Δ}), a key parameter that quantifies how effectively displacement is transmitted across the adhesive interface. In this context, α_e^{Δ} is introduced as a reduced-order representation of interfacial behaviour, consistent with strategies

commonly used in multiscale modeling. While the introduction of α_e^{Δ} may affect analytical precision in the elastic regime, it enables a simplified yet realistic modeling approach. α_e^{Δ} captures the effective bonding and transfer efficiency, while the related $\beta_{1,e}$ scales the global strain transfer profile along the jacket. This abstraction, based on cohesive zone modeling (CZM) principles employed in this study, characterizes interfacial behaviour through traction–separation laws rather than internal stress distributions. It offers a streamlined yet robust framework to extend the model into complex inelastic regimes, effectively capturing evolving interfacial phenomena using cohesive zone theory. In practice, adhesive layers are typically thin and highly effective at transmitting strain, making this modeling approach a realistic and practical simplification. The concept is analogous to α_j introduced by Zhang et al. (2021b) for characterizing cohesion at the jacket–core interface, examined in the next section.

Table 5-3 summarizes the sensitivity analysis on key input parameters, including E_a, t_a, and α_e^{Δ}, based on the deterministic values previously mentioned in **Table 5-2**. The corresponding variation in the $\beta_{1,e}$ calculation was evaluated for both EP and CN adhesives. For both adhesives, variations in E_a and t_a by ±10% and ±20% resulted in only minor fluctuations in $\beta_{1,e}$ typically within a range of 0.004–0.008 from the baseline values. This suggests that within a reasonably expected range of uncertainty in adhesive properties, the model maintains its predictive consistency. However, when α_e^{Δ} was varied independently, the effect on $\beta_{1,e}$ was far more significant. A small reduction of 1% in α_e^{Δ} (from 0.98 to 0.9702) led to a noticeable decrease in $\beta_{1,e}$, and a 5% reduction caused a drastic drop, up to 12–15%, pushing $\beta_{1,e}$ well below experimentally acceptable bounds.

On the other hand, the sensitivity analysis of the E_a and t_a revealed a seemingly counterintuitive trend in the resulting interfacial transfer coefficient, $\beta_{1,e}$. Classical shear lag theory suggests that increasing the stiffness of the adhesive, either by increasing E_a or decreasing t_a, should enhance interfacial stress transfer, leading to sharper strain gradients and therefore higher $\beta_{1,e}$ values. However, as shown in the table below, the observed response under the current formulation

exhibits a slight but consistent decrease in $\beta_{1,e}$ with increasing adhesive interface stiffness. The apparent contradiction is resolved by revisiting the core modeling assumption that simplifies the adhesive from a continuous shear layer with distributed stress into a lumped strain transfer interface, characterized by α_e^{Δ} and $\beta_{1,e}$.

Table 5-3. Sensitivity analysis: adhesive interface's inputs vs. output $\beta_{1,e}$

Scenario	E_a	t_a	α_e^{Δ}	$\beta_{1,e}$	E_a	t_a	α_e^{Δ}	$\beta_{1,e}$
adhesive	EP				CN			
baseline	2.50	0.00030	0.980	0.960	1.30	0.000150	0.980	0.960
E_a+10%	2.75	0.00030	0.980	0.959	1.43	0.000150	0.980	0.958
E_a −10%	2.25	0.00030	0.980	0.962	1.17	0.000150	0.980	0.962
t_a+10%	2.50	0.00033	0.980	0.962	1.30	0.000165	0.980	0.962
t_a −10%	2.50	0.00027	0.980	0.958	1.30	0.000135	0.980	0.957
E_a+20%	3.00	0.00030	0.980	0.957	1.56	0.000150	0.980	0.956
E_a −20%	2.00	0.00030	0.980	0.964	1.04	0.000150	0.980	0.964
t_a+20%	2.50	0.00036	0.980	0.964	1.30	0.000180	0.980	0.963
t_a −20%	2.50	0.00024	0.980	0.956	1.30	0.000120	0.980	0.955
α_e^{Δ}+1%	2.50	0.0003	0.989	0.978	1.30	0.000150	0.989	0.978
α_e^{Δ} −1%	2.50	0.0003	0.970	0.941	1.30	0.000150	0.970	0.940
α_e^{Δ} − 5%	2.50	0.0003	0.931	0.864	1.30	0.000150	0.931	0.861

In the elastic regime, the shear stress at the interface is described as, $\tau_a = K_a\,\delta^e = K_a\,u_h(1 - \alpha_e^{\Delta})$, where $K_a = G_a/t_a$ is the interface stiffness, and u_h is the host material's axial displacement. This modeling approach introduced a known artifact in the sensitivity analysis: by holding α_e^{Δ} constant at 0.98, increases in adhesive stiffness led to higher interfacial shear stress for the same displacement, requiring greater traction to resist the applied force. This effect reduced the apparent interface integrity, as it altered the internal strain distribution without increasing the total transferred force. Although α_e^{Δ} depends on both interfacial stiffness and bond quality, it was treated as a fixed parameter in the sensitivity analysis. This simplification decoupled physically interdependent parameters, allowing adhesive property variations to influence only the interfacial stiffness, K_a, not α_e^{Δ}. Consequently, the observed decrease in $\beta_{1,e}$ with increasing adhesive

stiffness stemmed directly from the modeling assumptions used in the sensitivity analysis, where $\beta_{1,e}$ was computed under the constraint of a fixed α_e^{Δ}. This counterintuitive trend reflects the abstraction's inherent limitations rather than a contradiction in the model.

Furthermore, **Figure 5-6** shows theoretical curves generated for various $\beta_{1,e}$ values within the range 0.8–1.0. The corresponding experimental data were normalized by dividing each set by the respective $Z_{x=0} = \beta_{1,e}$ value used in that case. Since both the theoretical and experimental curves were scaled simultaneously, they moved together in a way that maintained their relative positions. This analysis therefore focused not on discrepancies between theory and experiment but on how different $\beta_{1,e}$ values, affect the general trend and reflect adhesive-related parameter influences. For clarity, only theoretical curves are labeled, as the experimental data follow the same relative pattern governed by the selected $Z_{x=0} = \beta_{1,e}$.

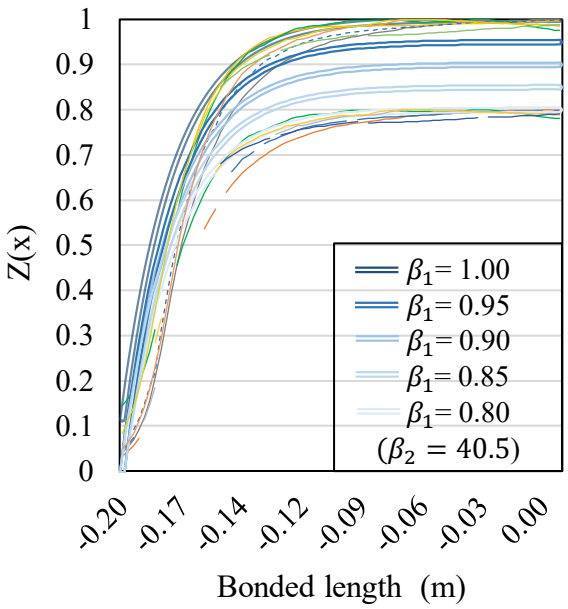

Figure 5-6. Graphs illustrating the effect of varying $\beta_{1,el}$

The graph clearly demonstrates that $\beta_{1,e}$ functions as a linear scaling factor controlling the overall elastic STE along the bonded length. When $\beta_{1,e}$ equals 1, full strain transfer is achieved, with Z_x reaching 1 over the effective sensing length. In contrast, if $\beta_{1,e}$ is reduced to 0.98 or 0.8, the entire

Z_x profile is proportionally scaled, and the peak value reaches 0.98 or 0.80, respectively. This scaling effect demonstrates how changes in adhesive interface performance directly impact the maximum achievable STE, while preserving the overall shape of the Z_x distribution. It also explains why theoretical and experimental curves maintain consistent trends once $\beta_{1,e}$is calibrated, modifying magnitude without altering distribution form.

Realistically accounting for physical mechanics and numerical modeling, a stiffer adhesive interface combined with a higher displacement transfer ratio (α_e^{Δ}) contribute to an increased $\beta_{1,e}$. Lower $\beta_{1,e}$ values, often resulting from a less stiff adhesive interface, suboptimal sensor installation, or any inconsistencies within bondline, reduce STE, causing the strain in the host material to not be fully reflected in the core fibre at the maximum reading location.

The decision to adopt α_e^{Δ} = 0.98 in the deterministic model was grounded in both physical reasoning and experimental data, reflecting an overall STE of approximately 96% ($\beta_{1,e}\approx$ 0.96) as indicated by an average 4% deviation between DFOS and EX measurements at the bonded midpoint. The selected value corresponds to a high, but realistic, interfacial efficiency under elastic conditions, consistent with the expected performance of thin adhesive layers in DFOS applications. Given that adhesive layers are often only tens of microns thick, and assuming a moderate to good bond, strain is transmitted to the sensor with minimal loss. In this context, α_e^{Δ} = 0.98 provides a practical and effective representation of that behaviour. Moreover, since α_e^{Δ} is introduced as a lumped parameter to capture the effective stiffness and bonding quality of the adhesive interface, rather than being derived directly from mechanical theory, it also supports the flexibility required to integrate $\beta_{1,e}$ formulation with the subsequent inelastic modeling stages.

While this sensitivity analysis was performed virtually, it provides meaningful insight into the model's responsiveness and establishes a foundation for future investigative work. In practical

applications, these parameters may be refined through field calibration, uncertainty quantification efforts, or to assess sensor installation quality in structurally complex environments.

A notable advantage of incorporating the β_1 parameter in STE analysis, particularly within the elastic regime, is its ability to simply and effectively account for interfacial strain losses in the intermediate layers of a DFOS sensing system, including both the adhesive and jacket layers, in addition to its established relevance in a temporal and spatial function-responding mode in inelastic regime analysis. By normalizing the maximum probable STE across a range of jacket materials and adhesive bond conditions, this parameter diverges from the conventional strain (shear) lag approach, which relies on gradient-based modeling. While the gradient-based shear lag parameter suggests that strain transfer from the host material to the core fibre becomes complete beyond a certain bonded length, it may neglect the residual influence of imperfect bonding and adhesive layer mechanics. Instead, the defined elastic interfacial transfer coefficient ($\beta_{1,e}$) captures these residual effects by calibrating overall STE across the bonded interface, with an average 4% deviation from the EX reference at the point of maximum response (x = 0) observed in this study.

- **Comparative Analysis and Stage II Test Samples**
  - **SP GFRP Bar Samples**

This section examines the case study samples SP-S and SP-C, which were subjected to sustained and cyclic loading, respectively. Each sample features four DFOS configurations, varying in attachment technique (groove-embedded vs. surface-mounted) and adhesive type (EP vs. CN). To ensure consistency in evaluating STE across these configurations, the highest strain reading at the middle sensing point across all layouts was selected as the representative value to incorporate the strain of the host material, $\varepsilon_h = \varepsilon_{DFOS,max}(x = 0)/Z_{max,x=0}$. For each layout, two experimental curves were generated, as shown in **Figure 5-7**, corresponding to the strain levels at the end of the first and third designated load steps, approximately 2000 and 11000 $\mu\varepsilon$, respectively.

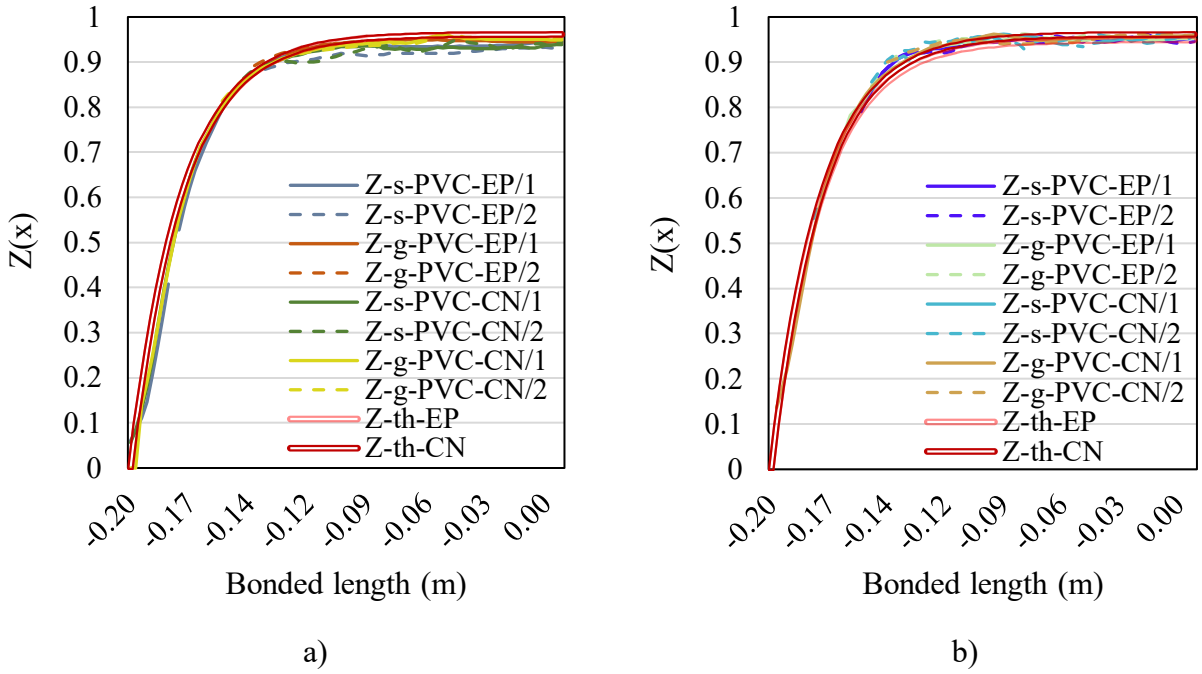

Figure 5-7. $Z_e(x)$ correlation analysis for Stage II test specimens: a) SP-S and b) SP-C

Theoretical curves for CN and EP adhesives were initially calculated separately, accounting for the potential different properties of each adhesive type. These curves reflect the combined effects of adhesive stiffness and thickness. When the adhesive thickness t_a and Young's modulus E_a were varied together, as specified in **Table 5-2**, the resulting curves were nearly identical, both plotting with $\beta_{1,e} \approx 0.96$. This supports the concept of a balanced interaction between the adhesive's mechanical properties, where variations in thickness and stiffness, with opposite effects on strain transfer, result in similar overall impacts on STE for each adhesive type.

Overall, as shown in the charts, improvements in installation quality and bonding conditions led to more accurate alignment between the theoretical and experimental curves for distributed STE. This was especially evident in sample SP-C, where the experimental curves converged along the effective sensing length and maintained consistent STE across different DFOS layouts. In the presence of a detectable signal, better alignment was also observed at lower sensing lengths for both samples compared to pilot test samples. However, slight, negligible deviations were observed

in the surface-mounted layouts of sample SP-S, indicating that the groove-embedded layout offered a more consistent STE across the bonded length due to improved interfacial effectiveness. These effects were further amplified by manual installation inconsistencies inherent in this study.

These parametric results, with $\beta_{1,e} \approx 0.96$ across all DFOS layouts, demonstrate consistent and balanced STE along the DFOS effective sensing length, reflecting the combined effect of adhesive properties like thickness and modulus. This internal dependency ensured uniform strain transfer behaviour across varying configurations while preserving agreement with theoretical predictions.

Furthermore, while sample SP-C showed no notable additional shear lag effects across all experienced strain levels along the bonded length, it is acknowledged that the cyclic loading protocol in this study was relatively short, under one hour. Given the known rate-dependency of adhesive properties, the observed elastic behaviour may not fully reflect long-term effects, and results should be interpreted with caution.

- **MST GFRP Bar Samples (*Investigating α_j, r_j, E_j, $\beta_{2,j}$ Effects*)**

In fibre optic cables, the jacket-cladding interface exhibits distinct interfacial shear resistance that affects strain transfer mechanisms. The extent of shear deformation at this interface is heavily influenced by the material properties of the coating, which can vary depending on the polymer type used, such as PVC or PI in this study. To properly replicate these behaviours in numerical models, the shear modulus of both PVC and PI coatings must be properly calibrated.

In addition to the insights gathered from the literature review, practical observations during the installation process further indicated that PVC jackets could be removed with hand pressure during mechanical stripping. This suggests a lower shear modulus and weaker adhesion, leading to shear deformation occurring more readily at lower stress levels. These observations emphasize the need for proper calibration in numerical models to account for such material behaviours.

In contrast, PI-coated DFOS have shown higher adhesion and resistance to mechanical stripping, requiring thermal assistance, such as localized heating with a flame, to degrade the PI coating without damaging the core optical fibre. This indicates that the PI coating sustains higher shear stresses before significant deformation and detachment occur, reflecting a higher shear modulus and a stronger interfacial bond. Therefore, the effective shear modulus for the PVC jacket should be set lower to represent its weaker shear resistance, while a higher effective shear modulus is required for PI to capture its stronger interfacial bond and greater resistance to shear deformation.

To account for variations in the jacket's effective shear modulus and avoid directly modeling nonlinear interfacial behaviour, Zhang et al. (2021b) introduced a calibration parameter, α_j, to adjust interface stiffness for excessive shear deformation. This approach is adopted in this analysis, as proper calibration is critical for capturing realistic STE along DFOS bonded lengths. As shown in the sensitivity analysis in **Figure 5-8**, varying α_j values notably affect the $Z_{th}(x)$ response, and incorporating a calibrated α_j greatly improves agreement between the model and observed data.

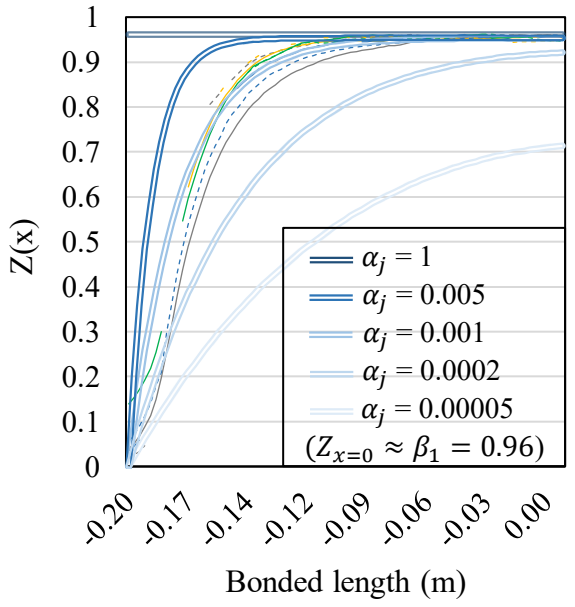

Figure 5-8. Effect of varying α_j on $Z_{th}(x)$ response (with unlabeled representative experimental curves and labeled theoretical curves)

Specifically, improper calibration, such as assuming α_j=1, resulted in a $Z_{th}(x)$ distribution that significantly deviated from the experimentally observed curves, incorrectly treating the entire bonded length as the effective sensing length and failing to capture the actual strain transfer mechanics. In contrast, calibrating α_j to match experimental data (e.g., α_j = 0.001) produced a $Z_{th}(x)$ curve that closely aligned with experimental observations.

Prior to the correlation and comparative analysis, a model refinement was implemented to improve alignment with experimental data, especially by updating BCs that were previously simplified as zero-strain. Following this modification, the charts shown later in **Figures 5-9** and **5-10** illustrate the improved correlation between experimental and theoretical results for Stage II samples with MST GFRP bar hosts, while comparing the effects of varying jacket effective shear modulus ($\alpha_j \times E_j$) and thickness among the investigated jacket types (PVC and PI) on the $Z_e(x)$ distributions. It is important to note that the final jacket effective shear modulus values were determined by curve fitting through adjustment of α_j, optimizing model curves to best match experimental data.

BCs were refined to revise the simplifying assumptions regarding strain behaviour at the bond region edges for the elastic regime. Previous correlation results revealed slight discrepancies between theoretical and experimental curves near the bonded edge at $x = -L$. A major issue was the assumption that strain at the fibre's extremities is zero, $\varepsilon_c(\pm L) = 0$, which introduces a discontinuity in the first derivative of the strain profile. Such a condition is physically unrealistic and unlikely in practical applications, as discussed by Falcetelli et al. (2020). Their study further explains that, due to the stiffness mismatch between the core optical fibre and surrounding components, deformation at the fibre boundaries is significantly less than at the outer layers. Because the core fibre is highly stiffer, it resists stretching, while the surrounding jacket tends to stretch the core. This interaction results in a self-equilibrating system where the core fibre experiences tensile strain, balanced by compressive strain in the other cable components.

This boundary effect diminishes after just a few cable diameters, as predicted by the Saint Venant principle, which states that stress redistributes along the structure. A more accurate strain profile can thus be obtained by applying non-zero strain for BCs, similar to the developed inelastic formulation for ε_p, described as $\varepsilon_c(\pm L) = p\varepsilon_h$. The parameter p reflects the residual strain in the core optical fibre at the free ends. With these BCs, the integration constants can be determined for strain transfer equation along the bonded length, resulting in a modified strain profile given by the similar formulation established for the inelastic regime, expressed as,

$$\varepsilon_c(x) = \varepsilon_h \left(\beta_{1,e} + \frac{(p-\beta_{1e})}{cosh(\beta_2(\pm L))} cosh(\beta_2 x)\right) \quad \textbf{Eq. (5-6)}$$

For regions beyond the bonded length ($x > L$ or $x < -L$), Falcetelli et al. (2020) described the strain profile as an exponential decay given by $\varepsilon_c(x,t) = ae^{-b|x|}$. This formulation is symmetrical with respect to the bonded region edges at $x = \pm L$. A simplified version of this model is adopted in the present study, where the parameters a, b, and p were determined through curve fitting to improve agreement with experimental data, particularly within 22 mm beyond $-L$ ($-0.22\ m$ to $-0.2\ m$). For a more comprehensive theoretical approach, Falcetelli et al. (2020) provide a full derivation of these parameters without relying on experimental correlation. In their method, the b parameter, governing strain decay outside the bonded region, is calculated similarly to the shear lag parameter but adjusted to account for the absence of an adhesive layer.

Building on the refined theoretical model, improved $Z_{th}(x)$ distribution curves were generated for the various DFOS layouts applied to Stage II test samples with MST GFRP bar hosts and compared against corresponding experimental data. The host strain for the experimental $Z_{ex}(x)$ curves was estimated using $Z_{max,x=0}$= 0.97, based on the PI-coated DFOS layouts with the highest midpoint readings, specifically s-PI-CN in sample SP-S and s-PI-EP in sample SP-C. Experimental results showed an average strain deviation of 3% at the midpoint compared to EX data, attributed to the

combined effect of the PI coating and the lower strain levels applied during sustained load steps, which reduced progressive divergence. Accordingly, host strain was calculated as $\varepsilon_h = \varepsilon_{DFOS,max}(x=0)/Z_{max,x=0}$. **Figure 5-9** presents the correlation results for sample MST-C, with experimental curves captured at two strain levels corresponding to peak readings from the first and final designated cyclic load steps, approximately 2000 $\mu\varepsilon$ and 11000 $\mu\varepsilon$. For sample MST-S, shown in **Figure 5-10**, the curves were plotted using near-final readings from each sustained load step, as each increment appeared to exhibit distinct strain transfer behaviour.

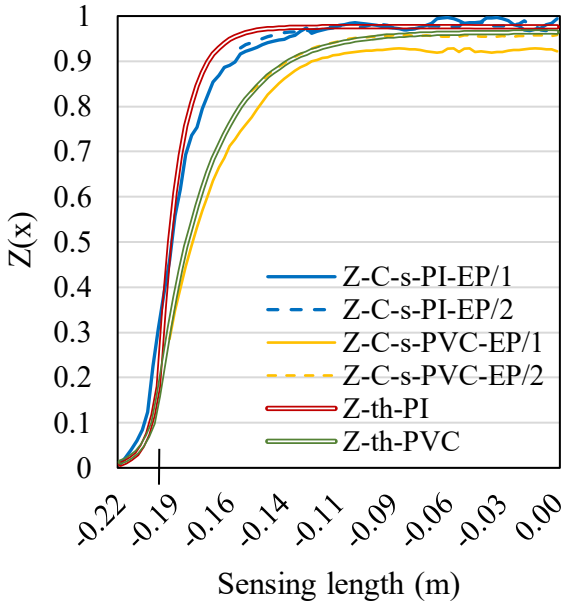

Figure 5-9. $Z_e(x)$ correlation analysis for test specimen MST-C ($\beta_{1,PI} = 0.976$)

Although PI-coated DFOS layouts feature stiffer interfaces, their $Z_{ex}(x)$ curves exhibited noticeable fluctuations, particularly at higher strain levels. This behaviour is likely attributed to the sensor cable's structurally delicate design, which is more prone to vibration and suboptimal surface embedment during manual installation, especially when bonded with CN adhesive on a non-uniform surface. In the case of the s-PI-CN layout on sample SP-S, which showed the most pronounced fluctuations, extreme data points were excluded to reduce noise while retaining the overall strain transfer trend.

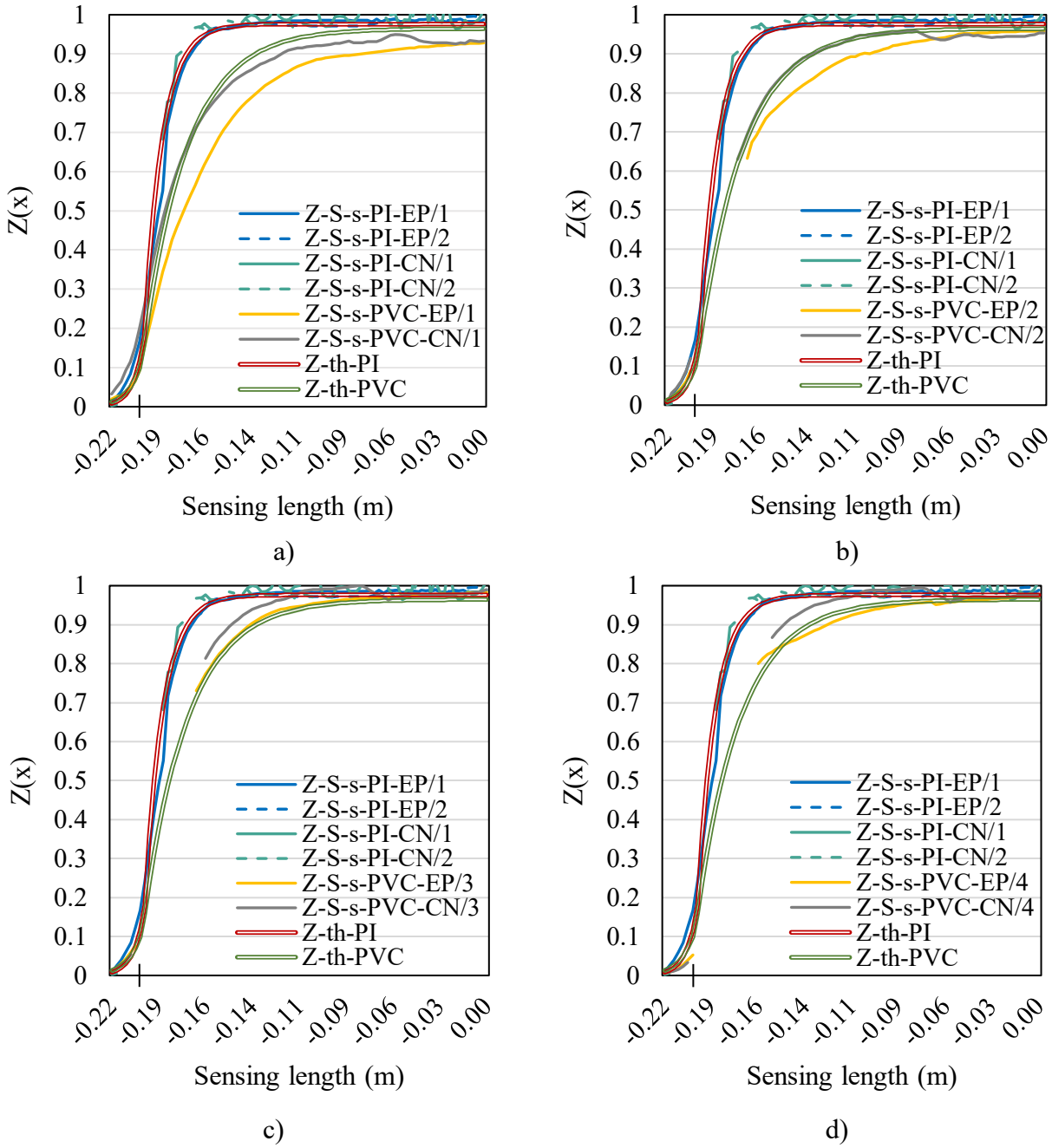

Figure 5-10. $Z_e(x)$ correlation analysis for test specimen MST-S at the end of sustained load steps: a) 1st, b) 2nd, c) 3rd, and d) 4th ($\beta_{1,PI}$=0.976 and $\beta_{1,PVC}$= 0.96)

The proper calibration of each jacket's effective shear modulus using the α_j parameter was confirmed by the strong correlation between theoretical predictions and experimental results. Specifically, the higher α_j value assigned to PI jackets reflected their greater interfacial rigidity

and more concentrated strain transfer, while lower α_j value for PVC jackets corresponded to their more gradual strain distribution. In addition, variation in jacket type led to an increase in the elastic β_1 value, from 0.960 to 0.976, under identical adhesive interface inputs, as the formulation accounts for both the jacket's Young's modulus (E_j or G_j) and its thickness function ($f(r)$).

Although a consistently distributed $Z_e(x)$ is theoretically expected along the bonded length across varying strain levels, experimental $Z_e(x)$ curves for PVC-coated DFOS layouts on sample MST-S revealed a slight deviation, most notably when comparing the final readings from the first and second sustained load steps. During the first sustained load step, PI layouts and EX recorded average midpoint strains of around 2070 $\mu\varepsilon$, while PVC layouts showed lower values between 1850 and 1950 $\mu\varepsilon$, resulting in a maximum STE of approximately 93%, slightly below the theoretical estimate of 96% along the effective sensing length.

The discrepancy between the theoretical curve for these layouts and corresponding experimental curves was largely resolved through additional data obtained from the final readings at higher strain levels, which showed improved alignment. The CN-bonded layout showed quicker convergence with the theoretical distribution along the bonded length, while the EP-bonded layout required an additional load increment to reach a comparable level of agreement. Although $Z_{x=0}$ for the s-PVC-EP approached the expected value during the second sustained load step, the overall $Z_{ex}(x)$ distribution along the effective sensing length remained below target and did not fully align. Installation-related inconsistencies, such as uneven bond condition or fibre misalignment, likely contributed to these discrepancies in correlation. These suboptimal installation effects are especially pronounced at lower strain levels, where absolute measurement errors become proportionally more significant, leading to larger relative deviations. Notably, as discussed in **Section 4.4.1**, s-PVC-EP layout showed a consistent ~ –250 $\mu\varepsilon$ strain deviation from s-PI-CN configuration, a difference that cannot be attributed to shear lag–induced error.

Furthermore, as illustrated in the preceding charts comparing $Z_e(x)$ responses across varying $\beta_{2,j}$ and elastic $\beta_{1,j}$ values, the parameter $\beta_{2,j}$ corresponds to the classical shear lag parameter, here redefined to isolate jacket properties from adhesive interfacial effects. This approach proved especially relevant in this study, as experimental observations indicated that variations in jacket type, rather than adhesive interface, primarily drove the reduction of the low-sensing segment within the bonded length. Consistent with this, theoretical analyses showed that differing $\beta_{2,j}$ values for each jacket type had the greatest impact on the $Z_e(x)$ distribution in the low-sensing region, specifically where the STE falls below 95%.

Previous studies, such as that by Chapeleau and Bassil (2021), suggest that such parameter as $\beta_{2,j}$ typically ranges from 30 to $300-400\ m^{-1}$, representing a spectrum of STE, ranging from poor (with softer intermediate layers) to excellent (with stiffer intermediate layers). Based on this established range, it is important to highlight that input parameter values like α_j=1, yielding $\beta_{2,j}$=1250 m^{-1}, are likely unrealistic. Such a scenario would imply perfect and full strain transfer along the bonded length with no shear lag effects, an idealized condition that does not reflect the practical limitations inherent in real-world applications.

PVC-coated FUTs exhibited an effective strain transfer length of 200 –260 *mm* within the ~ 400 *mm* bonded sensing length. This means that only a portion of the DFOS bonded length contributed to reliable measurement, while a substantial part experienced lower strain levels before fully engaging with the host material's the host material's deformation. In contrast, PI-coated DFOS layouts, with higher effective shear modulus and thinner jackets, showed a more efficient strain transfer. Theoretical and experimental $Z_e(x)$ for these layouts indicate that only about 10% of the bonded length falls within the low-strain transfer region, improving STE along the bonded length compared to PVC-coated fibres. To express the minimum effective sensing length, referred to as $L_{eff,min}$, defined as the bonded length required for $\varepsilon_c(x=0) = 0.95\varepsilon_h$, it can be formulated as,

$$L_{eff,min} = \frac{1}{\beta_2}\, cosh^{-1}\left(\frac{(\beta_{1,e}-p)}{\beta_{1,e}-0.95}\right) \qquad \textbf{Eq. (5-7)}$$

This equation provides a means of calculating the minimum effective sensing length, $L_{eff,min}$, which differs from the previously defined effective sensing length. While the latter represents a portion of the total sensing length, $L_{eff,min}$ determines the minimum length required to achieve 95% of the host strain, assumed at midpoint for the above equation. The consideration of $L_{eff,min}$ is particularly important in setups where full strain transfer along shorter DFOS attachment lengths is critical, such as in instrumented stirrups or localized reinforcement zones in RC beams. In these cases, a significant portion of the bonded length may fall within low-sensing regions, reducing strain measurement reliability. Conversely, in longer applications like longitudinal reinforcement over extended lengths, the impact of jacket properties on overall strain transfer diminishes, as a greater share of the bonded length operates within the effective sensing range.

Table 5-4 presents the observed $L_{eff,min}$ for each jacket type and the general impact of DFOS jacket's modulus and geometric parameters on the $Z_e(x)$ distributions. It also provides the final set of jacket input parameters used in the following analysis steps, where the adhesive interface's inelastic response governs the bonded sensing system's performance under high sustained loads.

Table 5-4. Comparison and finalization of jacket's input parameters for analysis

No.	Parameter	PVC jacket	PI jacket	Unit	Overall impact
1	r_j	0.00045	0.00015	m	$\downarrow r_j \Rightarrow \uparrow Z(x)$
2	E_j	1.7	2.5	GPa	$\uparrow E_j \Rightarrow \uparrow Z(x)$
3	α_j	0.001	0.0015	-	$\uparrow \alpha_j \Rightarrow \uparrow Z(x)$
4	$\beta_{2,j}$	40.5	100	m^{-1}	$\uparrow \beta_{2,j} \Rightarrow \uparrow Z(x)$
5	$f_j(r)$	0.000207	0.00004	m	$\downarrow f_j(r) \Rightarrow \uparrow Z(x)$
6	$\beta_{1,j}$	0.96-0.97	0.976-0.98	-	$\uparrow \beta_{1,j} \Rightarrow \uparrow Z(x)$
7	L_{low}[1]	~100	~10	mm	$\uparrow \beta_{2,j} \Rightarrow \downarrow L_{low}$

[1]Low-sensing length (or strain transfer length)

Reducing the jacket's radius (r_j) and its thickness function ($f_j(r)$) increased the STE, as shown by an upward shift in $Z(x)$. Similarly, greater effective jacket layer stiffness, measured by $\alpha_j \times E_j$, also enhanced STE. Together, these factors influenced the values of $\beta_{2,j}$ and β_1, with higher values indicating improved STE. Higher $\beta_{2,j}$ values corresponded to stronger interfacial bonding within the sensor cable itself, while β_1 represented improved interfacial effectiveness at the adhesively bonded jacket–host interface. The jacket's shear modulus calibration parameter (α_j) specifically calibrates the interface between the core fibre's cladding and the jacket, governing strain transfer there. It does not apply to the outer jacket–host interface, which is controlled by separate adhesive bondline properties independent of α_j.

- **Summary of key findings and essential input parameters for the next step**

In this section, the elastic strain transfer mechanism for both surface-mounted and groove-embedded DFOS configurations on GFRP bars under uniaxial tension was quantified using a numerical model developed for a three-layered sensing system, consisting of a host material, jacket, and core optical fibre. The results demonstrate strong alignment with experimental data, validating the reliability of the numerical approach. The analysis followed general formulations similar to those presented in previous studies, employing the well-established governing equation for DFOS strain transfer, derived in detail in **Section 3.2**, expressed as,

$$\varepsilon_c(x) = A\,sinh(\beta_2 x) + B\,cosh(\beta_2 x) + \beta_1 \varepsilon_h \qquad \textbf{Eq. (5-8)}$$

The approach was primarily based on theoretical formulation, with experimental calibration applied selectively to critical parameters. Parameters A, B, β_2, and β_1 were validated and refined via experimental validation to ensure consistency across conditions.

Although previous studies, such as Chapeleau and Bassil (2021), have treated surface-mounted and groove-embedded DFOS configurations separately, primarily due to differing assumptions

about strain transfer mechanisms through adhesive layers versus embedding materials, the numerical analysis presented above applied a unified modeling framework to both. This generalization is supported by the fact that the strain transfer process, governed by interfacial shear from the host material to the core optical fibre, remains mainly unchanged across configurations.

Instead of relying on a classical shear lag theory-based approach, the analytical model employed in the preceding numerical implementation decouples the strain transfer formulation across the adhesive interface. The strain transfer contribution typically attributed to shear lag theory, particularly from the protective jacket, is represented using a shear lag-like parameter (β_2). In contrast, interfacial interactions at the sensor–host interface are modeled separately using a distinct interfacial transfer coefficient (β_1), defined through a cohesive zone model governed by a traction–separation law. This approach enables representation of the adhesive or embedding interface without explicitly modeling it as a continuous shear-transmitting layer.

In groove-embedded configurations, the embedding material's fluidity and cohesion affecting interfacial bonding are similarly captured by $\beta_{1,e}$, representing interfacial effectiveness within the adhesive's elastic regime influenced by factors such as bondline quality. This enables the model to accommodate both installation types using the same analytical structure. Experimental validation across a range of specimens confirms the model's versatility and validity for both surface-mounted and groove-embedded applications.

This modeling strategy was particularly motivated by the potential variability during installation and the possibility of in-service degradation at the adhesive interface, such as the initiation and propagation of damage, which can significantly affect strain transfer in adhesively bonded DFOS systems. These effects are captured through β_1, which governs the overall STE along the effective sensing length within the adhesive interface's elastic response regime and allows for extension to its evolving inelastic behaviour along the bondline. It comprises two phases: a constant elastic

phase used to calibrate maximum STE, and a time- and position-dependent inelastic phase reflecting interfacial degradation and damage progression.

At the elastic analysis stage, experimental data confirmed the reliability and practical applicability of the model's preliminary elastic component and its underlying assumptions, while numerical results validated the experimental findings. Consistency across tested samples further demonstrates the model's robustness for different materials, particularly GFRP bars from various manufacturers, though minor variations may occur due to surface treatment or installation factors.

The stepwise integration of experimental and theoretical distributed strain transfer coefficients enabled accurate determination of key parameters within the elastic regime, establishing a solid foundation for subsequent inelastic analysis. Concurrent calibration of both formulations, achieved through $Z_{\max or\ x=0} \approx \beta_{1,e,\ CN\ or\ EP} = 0.96$, based on an average 4% experimental deviation from EX measurements, enabled the extraction and validation of key model parameters. These validated parameters were then incorporated into the numerical model for the next phase.

The numerical analysis within the elastic regime confirms the effectiveness of surface-bonded DFOS systems in accurately capturing structural strain responses under various loading conditions, especially during serviceability stages of high-strength materials like GFRP bars. These results align with prior research, reinforcing the reliability of DFOS for SHM. Moreover, the accuracy of surface-bonded DFOS can be improved by numerically calibrating shear lag and interfacial transfer effects among intermediate layers, including the DFOS jacket and adhesive bond.

By integrating key parameters such as α_j, β_2, and β_1 into the calibration process and quantifying the proportion of low-sensing (strain transfer) segments along the bonded length, the theoretical model, validated against experimental data, provides a robust understanding of strain transfer mechanics. This correlation enhances the accuracy of DFOS-based monitoring, especially in complex real-world scenarios involving varying materials and installation conditions. Importantly,

this approach enables systematic identification and exclusion of unreliable sensing regions, which typically contribute minimally to overall STE. This capability is critical when sensor attachment lengths are limited, allowing for optimized sensor deployment and improved performance.

Furthermore, strain readings can be normalized using the parameter $\beta_{1,e}$ via $\varepsilon_h \cong \varepsilon_c/\beta_{1,e}$, adjusting for variability in STE across different materials and interfaces. This correction ensures that measured strains more accurately represent the host material's deformation, mitigating the impact of suboptimal sensor installations and inconsistencies in the core fibre–host intermediate layers. As a result, the approach can significantly improve the reliability of distributed strain measurements, supporting long-term SHM and accurate assessment of host material behaviour.

5.3.2. Numerical Analysis Results in the Inelastic Regime

- **Review of the Analysis Framework**

In this section, the numerical modeling approach is extended to capture the inelastic behaviour of the adhesive interface for proper quantification of surface-bonded DFOS' STE under sustained overload conditions, assessing the impact of inelastic deformations and progressive damage at the adhesive interface on the overall degradation of the sensing system's performance. As the adhesive interface is subjected to sustained high-level stress, localized damage zones begin to form, progressively degrading the bond integrity. Over time, bondline degradation impacts both the mechanical properties of the bond and the efficiency of stress (and strain) transfer between intermediate layers, which is critical to the long-term stability and performance of DFOS.

The adhesive bondline's ability to maintain effective stress transfer is essential for ensuring reliable monitoring throughout the system's service life. In this application, where the adhesive bond cross-sectional area between the DFOS and the substrate is exceptionally small, often less than 10 mm^2, the sensitivity of the adhesive interface to localized stress concentrations becomes particularly

critical, amplifying the impact of any bond degradation or interfacial failure (partial or full debonding) during its service life due to different structural and environmental factors.

Thus, this transition in analysis framework from linear elastic to time-dependent, non-linear inelastic response can be essential for predicting the long-term performance of surface-bonded DFOS systems, especially in the context of FRP reinforcement (or strengthening) where the host material's behaviour, elastic modulus, and strain capacity are different from more conventional structural materials like steel.

The numerical model incorporates theoretical correlations that capture the evolving inelastic behaviour of the adhesive interface during strain transfer to the core optical fibre. This includes the initiation of interfacial damage and the gradual development of progressive inelastic shear localization within the bondline. These effects are particularly significant in regions where defects or installation inconsistencies are likely to be present. This approach enhances the accuracy STE prediction, particularly during the inelastic response of the bond interface, and offers insights into potential adhesive layer failure mechanisms under extreme conditions, providing a reliable framework for assessing failure in surface-bonded DFOS systems.

This type of criterion for designing surface-bonded DFOS systems has not been extensively addressed in the existing literature. While extensive research has focused on the general performance, material properties, and plastic behaviour of DFOS coating layers, particularly for crack quantification, where high strain levels in the jacket enable crack detection, an important gap remains. The critical role of the adhesive interface's elasto-plastic response in influencing in-service STE and the consequent SHM assessments has not been adequately explored. This gap is especially evident in scenarios where the sensor is adhered to reinforcement, as opposed to being applied directly to the cracked area. The absence of an analytical approach that incorporates factors

such as the evolving inelastic properties of the adhesive interface and bondline quality highlights the need for further advancements in DFOS strain transfer modeling and application.

This part of the model is intended to be applied only during severe (higher than the adhesive joint's ultimate local strength) sustained loading phases, focusing on the gradual damage progression. Once external stress surpasses a critical threshold at points of stress concentration, the strain transfer analysis must incorporate the effects of permanent shear deformation or bond damage between the sensor and host material. This marks a transition in the bondline integrity and alters the stress distribution for the remainder of the system's service life.

After the sustained load is removed, advanced modeling is required to address sensor decoupling and its impact on sensor performance and system reliability. Recalibration and refinement should then be performed to ensure accurate measurements moving forward.

It is noted that throughout the development of the numerical model using different trials, it became clear that incorporating an exponential function with a time-dependent decay factor was essential for reliably simulating the spatial decay of damage intensity (and stress redistributions) along the bonded length. The incorporation of this spatial decay function enhances the model's reliability while retaining simplicity by incrementally redistributing shear stress interactions and interfacial separations (or shearing relative displacements) along the bonded length, utilizing maximum stress localized at the edges at a given time during high-sustained loading.

As discussed in **Section 3.2.3**, damage typically concentrates in high-stress regions near the edges, resulting in an uneven redistribution of shear forces and shear-induced, delayed sliding between the adherends. In DFOS monitoring applications, where distributed sensing points along the optical fibre cable provide continuous strain measurements, the decay function enables a gradual attenuation of damage intensity along the bonded length, making it a practical, efficient, and straightforward method for capturing sensor bond damage and the gradual loss of distributed STE.

On the other hand, when it comes to adhesive joints, modeling approaches typically involve more complex techniques, such as FEM simulations, which are node-based and require extensive computational resources. These models are often tailored to predict localized behaviour under varying conditions, necessitating sophisticated analysis for accurate results. Consequently, a closed-form equation, such as the one defined in this study for distributed sensing along the DFOS cable, is not commonly used in the analysis of adhesive joints. Unlike FEM, which, while accurate, is computationally intensive and less suitable for continuous, widespread deployment, the proposed approach offers both simplicity and efficiency. Therefore, the analysis process investigated in this section provides potential benefits, particularly in extending its application to DFOS-based designs and service life monitoring for structural adhesive joints. This approach can offer a more practical solution for large-scale implementation, facilitating SHM capabilities.

- **Initial Parametric Assumptions**

For clarity and ease of discussion, this section adopts the following material properties (initially fixed): the PVC jacket, $\beta_{2,PVC}$ = 40.5 m^{-1}, $f_{PVC}(r)$ = 0.000207 m, $E_{j,PVC}$ = 1.7 *GPa,* EP adhesive interface, $E_{a,EP}$ = 2.5 *GPa,* $t_{a,EP}$ = 0.0003 m (tested under various conditions), and CN adhesive $E_{a,CN}$ = 1.3 *GPa,* $t_{a,CN} = 0.00015\ m$ (examined in a single sample with two configurations); for both adhesives, it was assumed that α_e^{Δ} = 0.98.

The PVC-coated DFOS configurations were experimentally subjected to severe, sustained loading conditions, which induced progressive damage zones along the bondline. This testing condition generated crucial data to assess the time- and position-dependent STE of the system. The experimental results provided key parameters related to the temporal evolution of damage length, $L_d(t)$, which are necessary for implementing the theoretically developed formulations. Thus, the analytical approach effectively bridges real-time sensor capabilities with theoretical models, providing valuable insights into the system's performance and longevity under prolonged stresses.

- **Review of DFOS Bonded Length Division and Key Formulations**

To properly model the adhesive behaviour under sustained loading beyond the adhesive joint's strength, the bonded length is categorized into two primary regions, as outlined previously: the damage zone and the intact zone. The intact region, which is centred in the middle and gradually decreases in length over time during the sustained loading period, is further divided into two sub-zones: a low-sensing zone and an effective-sensing zone. This division reflects the progression of damage and its influence on the stress distribution across the adhesive interface.

1) Damage (inelastic-dominated) zone ($\pm L < x < \pm L_d(t)$): This region is characterized by stress redistributions due to damage progression within the adhesive interface. As localized damage accumulates, shear stress and relative displacement between adherends become non-uniform, resulting in $\bar{\delta}(x)$ and $\hat{\tau}_a(x)$, reflecting the degradation of the adhesive interface. Inelastic shear-induced deformation or separation introduces a considerable, permanent shear lag effect, varying along the DFOS bonded length, further disrupting stress transfer and weakening the adhesive joint's load-bearing capacity. The formulations for this region are reviewed below, outlining the time-dependent, perturbed (i.e., plastic/inelastic) strain transfer coefficient, referred to as $Z_p(x,t)$, and parameter $\beta_{1,p}(x,t)$ for dynamic changes in STE between the host material and the core fibre over time, as detailed in **Section 3.2**,

$$Z_p(x,t) = \frac{\varepsilon_c(x,t)}{\varepsilon_h} = \left(\beta_{1,p}(x,t) + \frac{\left(Z_{\pm L}(t) - \beta_{1,\pm L}(x,t)\right)}{cosh(\beta_2(\pm L))} cosh(\beta_2 x)\right) \varepsilon_h \qquad \textbf{Eq. (5-9)}$$

$$\beta_{1,p}(x,t) = 1 - \left((1-\alpha_e^{\Delta})_Y \left[\frac{(1+\nu)}{\sqrt{2}} + \frac{f(r)}{G_j}\left(K_{a,e}\right)_Y\right] 1.12\, \lambda_{SC}(t) e^{-q(t)(|L|-|x|)} \sqrt{\frac{L_d(t)}{2t_a}}\right) \qquad \textbf{Eq. (5-10)}$$

Y denotes the parameters associated specifically with the yield point. The introduction of the scaling parameter, $\lambda_{SC}(t)$, and decay parameter, $q(t)$, in a time-dependent form for the exponential decay function, was observed to be crucial for accurately simulating the progression

of interfacial damage within the adhesive interface during the strain transfer process during prolonged overloading. This time-dependency consideration was essential, as damage often begins at localized edge points and progressively propagates along the bonded length over time, a pattern consistently observed in the test samples. The samples frequently demonstrated a progressive, permanent reduction in DFOS strain data across varying portions of the bonded length following the highest level of sustained load, with an initial strain level above approximately 12000 $\mu\varepsilon$ recorded by DFOS (**Chapter 4**). Without a method to capture evolving damage distribution, stress and shear displacement between the sensor and host would be misrepresented, undermining model reliability. $\lambda_{SC}(t)$ was introduced to adjust the magnitude of the damage over time as the $L_d(t)$ may lead to an overestimation of interfacial separation and efficiency loss, emphasizing the need of ensuring a smooth transition from localized damage near the edges to a more uniformly distributed degradation along the bonded length as the damage progresses.

The value of ε_p for each sample was determined based on experimentally, focusing on localized strain at the bond edge where damage initially formed, prior to the progression of damage and the emergence of a non-homogeneous STE response across the adhesive interface, as shown through fixed strain values at the bonded length ends in graphs provided in **Appendix A**. The value of $Z_{b:\pm L}(t_p) = \varepsilon_p/\varepsilon_h$ for different samples at the start of damage progression was around $0.14 \leq Z_{\pm L} \leq 0.24$, based on available DFOS data. In cases where signal integrity was occasionally compromised, the first sensing point with a valid signal was considered the bond edge.

2-1) Elastic low-sensing (strain transfer) length: This refers to the portion of the bonded length within the central well-bonded region that is characterized by linear elastic strain transfer between the host material and the DFOS through the adhesive interface. Within this portion, a distinct strain gradient develops, where strain is transferred from the host material to the core fibre according to newly redistributed shear lag effects, located between the damage zone and the

effective strain transfer region. The region is bounded between $L_d(t)$ and the first point where 95% of the maximum strain at the adhesive is transferred from the host to the core fibre. The steep strain gradient within this region reflects the gradual reconstruction of the effective elastic interaction between the host and the adhesive. This process is akin to the quantifications presented in the previous section, where the parameter $\beta_{2,j} \cong 40.5$ for PVC and 100 for PI effectively characterized this phenomenon, controlling the required length to achieve the maximum STE.

While the shear lag parameter (or strain gradient) remains applicable for analyzing the system in earlier stages (e.g., $\beta_{2,PVC} \cong 40.5$) when the bonded length is largely unaffected by damage zones, its effectiveness diminishes as damage progresses along the bonded length. As the damage intensifies, the sharpness of the strain gradient, as defined by this parameter without modification in the proposed inelastic-dominated model, may fail to capture the transition within this region accurately. This limitation was evident during model trials, where the remaining elastic strain distribution was underestimated as damage predominated along the bonded length. In such cases, stress redistribution occurs, and STE improves rapidly along the elastic-dominated length.

This highlighted the need for further refinement in the model, specifically concerning the proper incorporation of shear redistribution within the elastic region as damage progresses, ensuring that the strain response more effectively reflects the evolving bond conditions. To maintain analytical simplicity, a time-dependent coefficient, defined as $1 \leq \beta_3'(t) \leq 2$, was introduced to modify the pre-existing strain gradient, $\beta_3'(t) \times \beta_{2,PVC}$. The adjustment using this defined coefficient, determined empirically, enabled the model to straightforwardly simulate the actual gradient of the stress redistribution within the adhesive layer along with the original strain gradient defined based on the jacket's properties. These considerations are further clarified with practical implications, ensuring the model remains analytically robust and applicable to real-world scenarios where adhesive joint stress redistribution is crucial for maintaining the bond efficiency.

2-2) Elastic, effective sensing length: Beyond the strain transfer length, the effective sensing length represents the region where no interfacial damage or strain gradient exists, and the adhesive continues to transmit strain efficiently without significant shear lag or degradation effects. In this zone, the interfacial bond remains intact, and the adhesive performs effectively, maintaining reliable strain transfer.

The formulation used to describe the distributed elastic strain transfer coefficient, $Z_e(x,t)$, between the host and core optical fibre, applicable to both the strain transfer and effective sensing zones as a unified sensing length, is reviewed and presented as follows, ($\pm L < x < \pm L_d(t)$),

$$Z_{e\prime}(x,t) = \frac{\varepsilon_c(x,t)}{\varepsilon_h} = (\beta_1(x,t) + \frac{\left(Z_{\pm L_d}(t) - \beta_{1,\pm L_d}(t)\right)}{cosh\left(\beta_2\beta_3'(t)x_{\pm L_d}(t)\right)} cosh(\beta_2\beta_3'(t)x)) \qquad \textbf{Eq. (5-11)}$$

Finally, to illustrate the discretized zones within the defined sensing length, as conceptualized in the diagram and inspired by Da Silva et al. (2018), **Figure 5-11**, highlights the key zones: the damage zone, the elastic zone, and two sub-zones within the elastic region, the strain transfer or low-sensing length (referred as $L_{low}(t)$) and the effective sensing length for DFOS (referred as $L_{eff}(t)$), induces a rapid decay in damage intensity, followed by a reduction damage intensity and shear induced defective interactions from the free end of bonded length towards the middle area.

The figure depicts a highly magnified, conceptual schematic of the adhesive bondline under tensile loading on the host material beyond the adhesive's yield point (or ciritcal bond strength), illustrating the damage length at three given time intervals during the progression of damage across half of the DFOS bonded length, if applicable as it might stop to progress at any time if no pre-existing weak zone exist at the end of each time increment.

At the onset of high-level sustained loading, the adhesive bonding layer remains largely intact, with initial damage typically concentrated near the bond edges. As the load is maintained over

time, cohesive zone elements along the bondline begin to exhibit increasing levels of interfacial degradation, captured by the damage parameter, D. This parameter, which quantifies the extent of damage, typically ranges from zero (indicating no damage) to one (representing complete failure). Under a commonly used linear simplification, damage parameter is expressed as $D = \frac{\delta - \delta_{II,c}}{\delta_{II,f} - \delta_{II,c}}$, where $\delta_{II,c}$ and $\delta_{II,f}$ represent the critical and failure shear relative displacements, respectively.

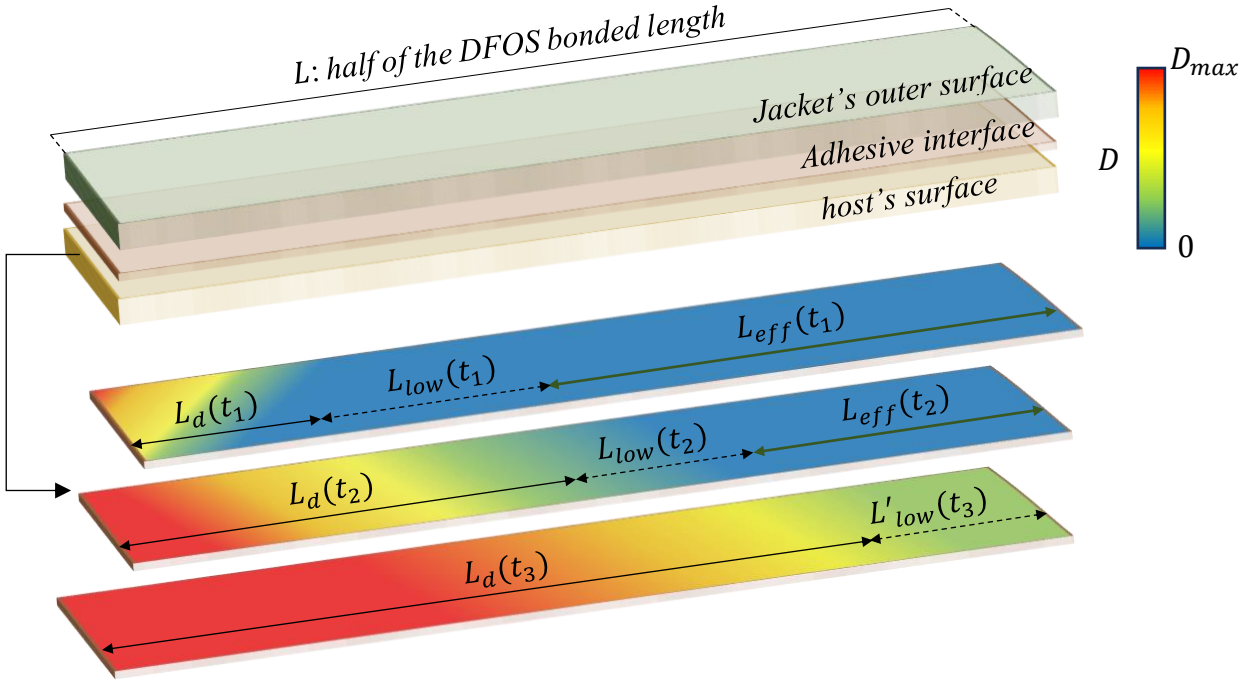

Figure 5-11. Proposed discretization within half of the DFOS bonded length into distinct zones, illustrating the adhesive configuration at the host interface and a schematical representation of spatial and temporal damage intensity, adapted from Da Silva et al. (2018)

In the depiction, D_{max} is used to represent a phase where the bond has not fully failed and strain transfer to the DFOS still occurs. The visual progression highlights the gradual expansion of the damage zone, reaching maximum degradation over time as the adhesive interface weakens under sustained loading. Outside of the central intact region, characterized by $L_{low}(t)$ and $L_{eff}(t)$, the STE from the host material to the DFOS is significantly compromised due to the adhesive's

excessive shear deformations or interfacial separations. In these areas, stress transfer follows distinct governing conditions, as described in **Eqs. (5-9)** and **(5-10)**, deviating from the uniform strain transfer observed within the undamaged region.

- **Complementary Theoretical Insights and Model Refinement Using $\beta_3'(t)$**

Figure 5-12 illustrates a representative case of model underestimation occurring during the progression of damage under conditions of severe and sustained loading. As illustrated by this selected sample, the underestimation is most pronounced when the effective strain transfer is confined to a small, well-bonded segment, particularly in a central region where the STE remains nearly unchanged from its initial state, amplifying the discrepancy between experimental observations and theoretical predictions.

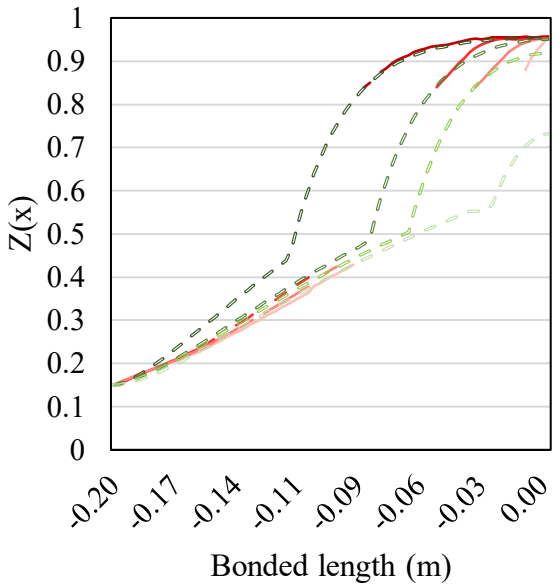

Figure 5-12. Underestimation for representative sample SP-12-g, showing minimal STE change in a concentrated middle region under severe, sustained loading (Experimental data (solid lines) vs. theoretical predictions (dashed lines), with STE progression shown by a color gradient)

Based on the book by Da Silva et al. (2018), the adhesive joint's shear stress distribution undergoes significant changes During damage progression, as illustrated in **Figure 5-13**, affecting the overall stress transfer mechanism. Initially, the adhesive shear stress follows a relatively stable profile,

with peak stresses occurring near the bonding edges. However, as a bond flaw develops, evidenced by the damage zone $\pm L_d(t)$, the stress distribution shifts due to local bond degradation.

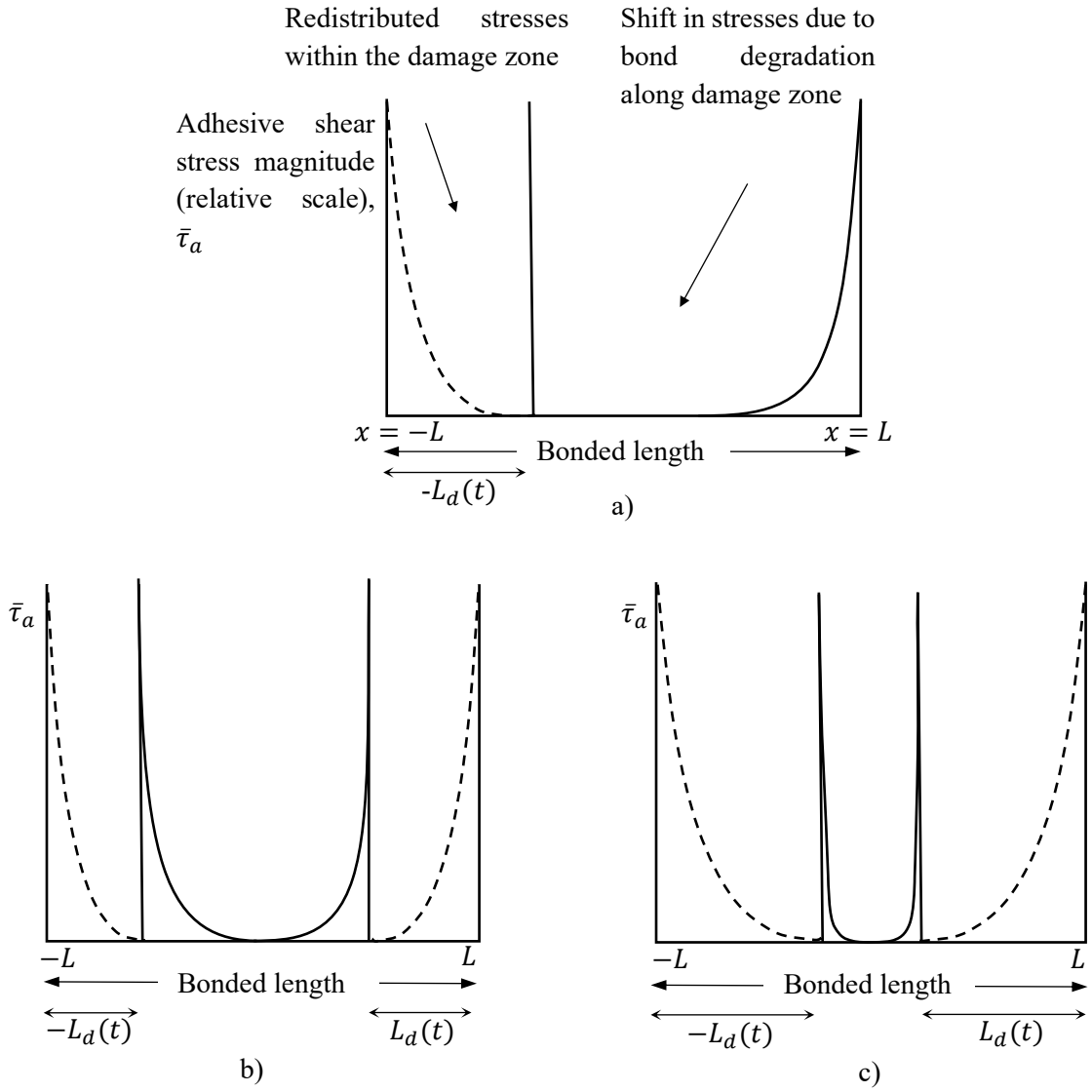

Figure 5-13. Redistributed adhesive stress profile after introduction of damage zone with amplified bond flaws: a) a general detailed description, b) and c) comparing stress gradient during damage progression, adapted from Da Silva et al. (2018)

As illustrated in the schematic, shear stress redistribution occurs when shear localization at the edge extends into the bondline, within both the damaged and intact zones, leading to a shift in the stress concentration. The shear stress in the damaged region decreases substantially, adhering to

its original distribution, where stress concentrations are concentrated at the edge and gradually decay toward the centre. Concurrently, the stress is redistributed to the adjacent bonded areas, with the peak shifting inward as the well-bonded length adjusts to bear a larger portion of the applied load. This redistribution further amplifies the shear stress gradient, resulting in the shear stress reaching its minimum at the centre of the bonded length. As the well-bonded region shortens over time, the shear stress gradient intensifies due to a steeper variation of stress concentration as the peak shifts inward toward the centre, where the minimum stress magnitude is located.

The shift in stress distribution due to partial bond degradation and the evolving stress redistribution highlights the need for a more refined analytical approach to the remaining elastic zone. This effect cannot be captured by the initially defined strain gradient ($\beta_{2,j}$), which was designed for the distributed interaction between the jacket and the core fibre.

To align theoretical predictions with observed behaviour, an amplification factor is required to account for the adhesive joint's actual stress (or strain) gradient. This factor must be time-dependent, as the localized stress field evolves with degradation, necessitating a variable correction to maintain reliability. Hence, the need for a time-dependent amplification coefficient for stress (strain) gradient ($\beta_3'(t)$) becomes apparent, as the redistribution occurs progressively with damage propagation. Incorporating this coefficient allows the model to dynamically adjust, capturing the shear stress redistribution and adapting to changing bond conditions while maintaining both computational efficiency and simplicity.

- **Practical Implications Illustrated by Test Sample Case Studies**

This subsection uses numerical modeling to assess the inelastic behaviour of the adhesive interface in the dynamic STE of DFOS under sustained overload, focusing on the experimentally tested samples in this study. The analysis offers a comprehensive quantification of the effects of inelastic, shear-induced interfacial separation, progressive damage within the sensors' bond interfaces, and

the accumulation of bond flaws on the overall functionality and performance of the surface-bonded DFOS systems. To support and validate the proposed model, a series of test case studies were conducted using test specimens subjected to high sustained loading conditions, designed to capture inelastic shear strain responses at the adhesive interface over time.

As previously noted in the numerical study setup, the analysis and corresponding graphs are based on half of the bonded length due to symmetry, $-L < x < 0$. However, $Z_p(x,t)$ curves derived from sample SP-S in Stage II are shown as full-field to highlight the asymmetric results.

As outlined in **Section 3.2.3**, the analysis is implemented through an incremental, iterative approach where the damage length ($L_d(t)$) in the derived $Z_p(x,t)$ equation, **Eq. (5-9)**, along with other utilized time-dependent parameters, including $\lambda_{SC}(t), q(t)$, and $\beta_3'(t)$, are continuously updated over time. The time-dependent inputs, derived from experimental correlations for each sample, are provided in **Tables 5-5** and **5-6** at four time intervals (2.5, 5.0, 7.5, and 10.0 minutes) to complement the $Z_p(x,t)$ curves. **Table 5-5** includes parameters detailing the crack length, $L_d(t)$, and the corresponding amplifier factor for the gradient along the remaining elastic length, $\beta_3'(t)$, as determined by the DFOS system. **Table 5-6** outlines the decay factor, $q(t)$, and scale factor, $\lambda_{SC}(t)$, which model the interfacial damage evolution and stress redistribution and scale $L_d(t)$ influence over time, enabling the system to capture the progressive bondline deterioration.

This analytical approach excels by incorporating time-dependent parameters into DFOS-based STE predictions, maintaining adaptability under prolonged loading and bondline degradation. The DFOS's inherent advantages, enabling distributed, real-time, and reliable strain data, are well-suited for this iterative and data-driven modeling process. The continuous updating of damage parameters ensures that the model reflects the present monitoring response of the surface-bonded DFOS system under high-level stress, offering a straightforward and efficient method for predicting the sensing system's long-term stability.

Table 5-5. Time-dependent input parameters for $Z_p(x,t)$ quantifications (*time unit: min*)

No.	Sample	$L_d(2.5)$	$L_d(5)$	$L_d(7.5)$	$L_d(10)$	$\beta_3'(2.5)$	$\beta_3'(5)$	$\beta_3'(7.5)$	$\beta_3'(10)$
		unit: m				-			
1	SC-12-s	0.10	0.13	0.15	0.18	No DFOS data to fit			
2	SC-12-g	0.05	0.09	0.14	0.18	-	1.40	1.30	1.30
3	SP-12-s	0.05	0.10	0.12	0.16	-	-	1.30	1.50
4	SP-12-g	0.09	0.12	0.16	0.18	-	1.30	1.40	2.70
5	SC-16-s	0.14	0.16	0.18	0.20	2.00	1.70	1.50	1.30
6	SC-16-g	0.09	0.13	0.16	0.18	1.10	1.30	1.30	1.70
7	SP-16-s	0.09	0.13	0.15	0.17	1.30	1.50	1.60	2.00
8	SP-16-g	0.11	0.14	0.15	0.17	1.40	1.40	1.20	1.10
9	SP-S/s-EP	0.04	0.09	0.12	0.14	no short remained intact regions that need amplified stress gradient			
10	SP-S/s-CN	0.01	0.06	0.09	0.11				
11	SP-S/g-CN	0.07	0.09	0.12	0.13				

Table 5-6. Time-dependent input parameters for $Z_p(x,t)$ quantifications (*time unit: min*)

No.	Sample	$q(2.5)$	$q(5)$	$q(7.5)$	$q(10)$	$\lambda_{SC}(2.5)$	$\lambda_{SC}(5)$	$\lambda_{SC}(7.5)$	$\lambda_{SC}(10)$
		unit: m^{-1}				-			
1	SC-12-s	6.80	6.00	5.70	5.10	1.00	0.87	0.83	0.75
2	SC-12-g	6.80	6.20	6.20	5.00	1.30	1.05	0.82	0.71
3	SP-12-s	6.80	6.20	5.60	5.10	1.25	0.97	0.89	0.75
4	SP-12-g	6.80	5.10	4.60	4.50	1.13	0.97	0.82	0.78
5	SC-16-s	6.80	5.80	5.30	4.20	0.90	0.82	0.77	0.65
6	SC-16-g	6.80	6.60	5.60	5.10	0.96	0.89	0.77	0.73
7	SP-16-s	6.80	5.70	5.50	4.30	1.05	0.90	0.82	0.74
8	SP-16-g	6.80	5.80	5.50	4.30	0.95	0.81	0.78	0.73
9	SP-S/s-EP	6.80	6.00	5.50	4.60	1.52	1.07	0.93	0.80
10	SP-S/s-CN	-	6.00	5.50	5.30	-	1.07	0.94	0.90
11	SP-S/g-CN	6.80	5.80	5.50	5.00	1.05	0.90	0.80	0.75

This approach demonstrates the DFOS system's strength in precisely tracking adhesive interface degradation, capturing localized damage, and ensuring reliable strain transfer measurements. Its adaptability to bondline changes and dynamic STE marks DFOS as a vital tool for real-time monitoring and structural health assessment. Combining experimental data with time-dependent

modeling enhances reliability and provides a robust foundation for long-term performance optimization. The charts sets in in **Figures 5-14**, **5-15**, and **5-16** present $Z_p(x,t)$ results for four time intervals under high sustained load, with each graph representing a sample. Solid lines represent experimental data, dashed lines indicate theoretical predictions, and the dark-to-light gradient illustrates STE loss over time and deviation from the initial, elastic $Z_e(x)$.

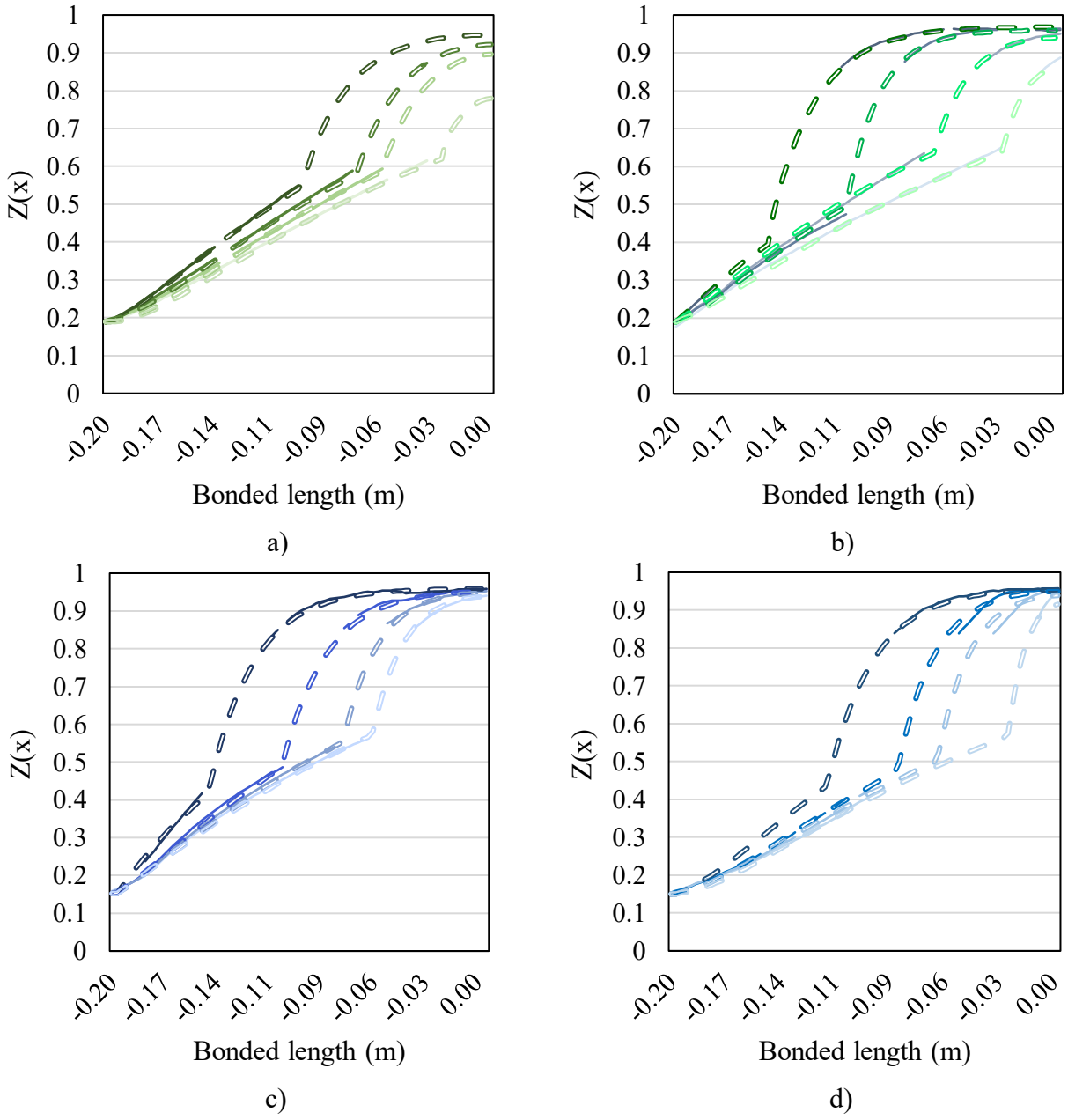

Figure 5-14. $Z_p(x)$ for GFRP #12 samples: a) SC-12-s, b) SC-12-g, c) SP-12-s, and d) SP-12-g

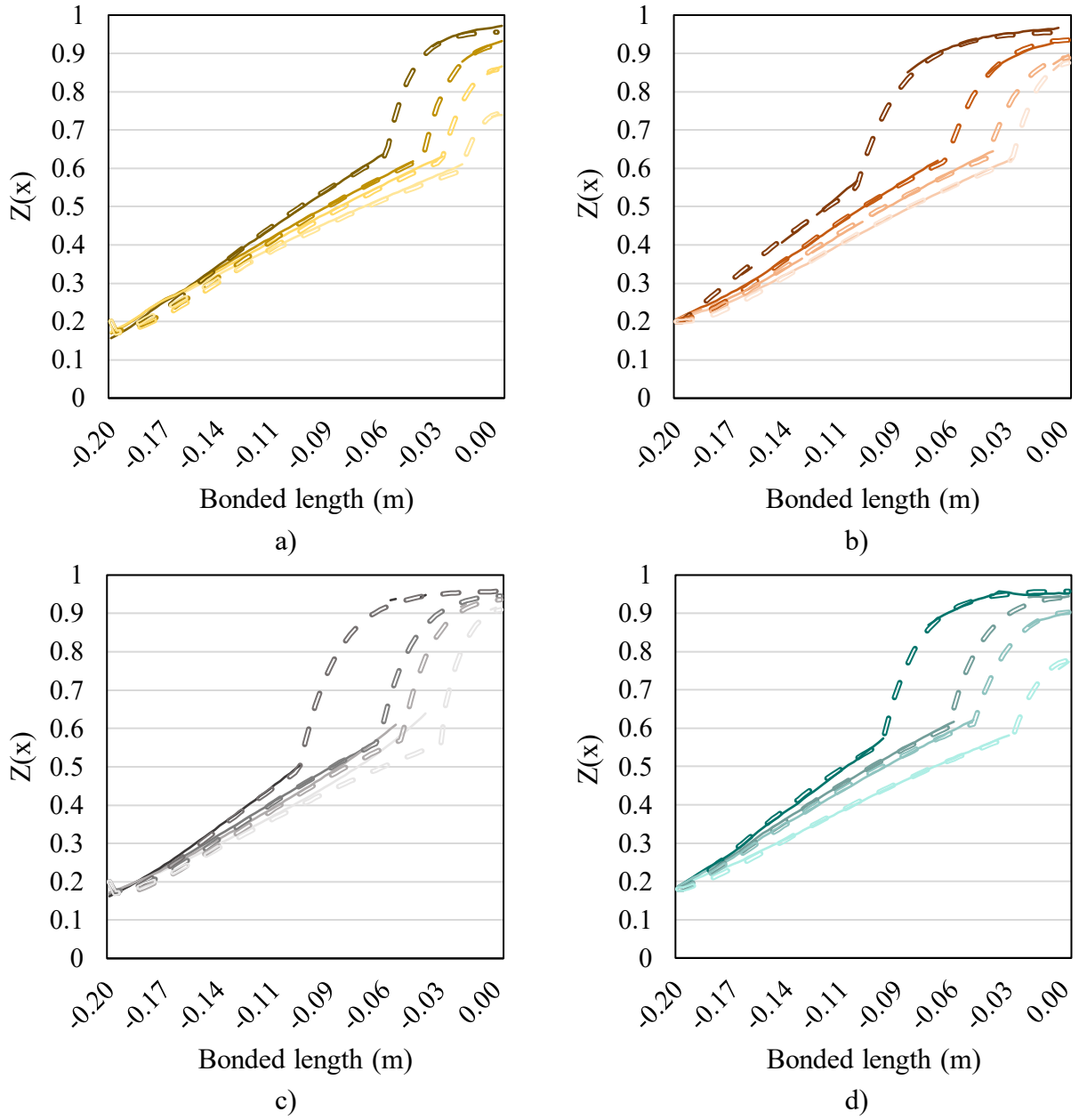

Figure 5-15. $Z_p(x)$ for GFRP #16 samples: a) SC-16-s, b) SC-16-g, c) SP-16-s, and d) SP-16-g

Model predictions showed strong agreement with the experimentally derived distributed strain transfer coefficient (Z_x), calculated using the assumption ε_h =1.04 $\varepsilon_{DFOS,x=0}$ at the bonded mid-length, measured at the onset of sustained loading. This assumption corresponds to $Z_{x=0} = \beta_{1,e} =$ 0.96, as previously defined and analyzed during elastic regime calibration, where experimental error bounds informed the parameter selection.

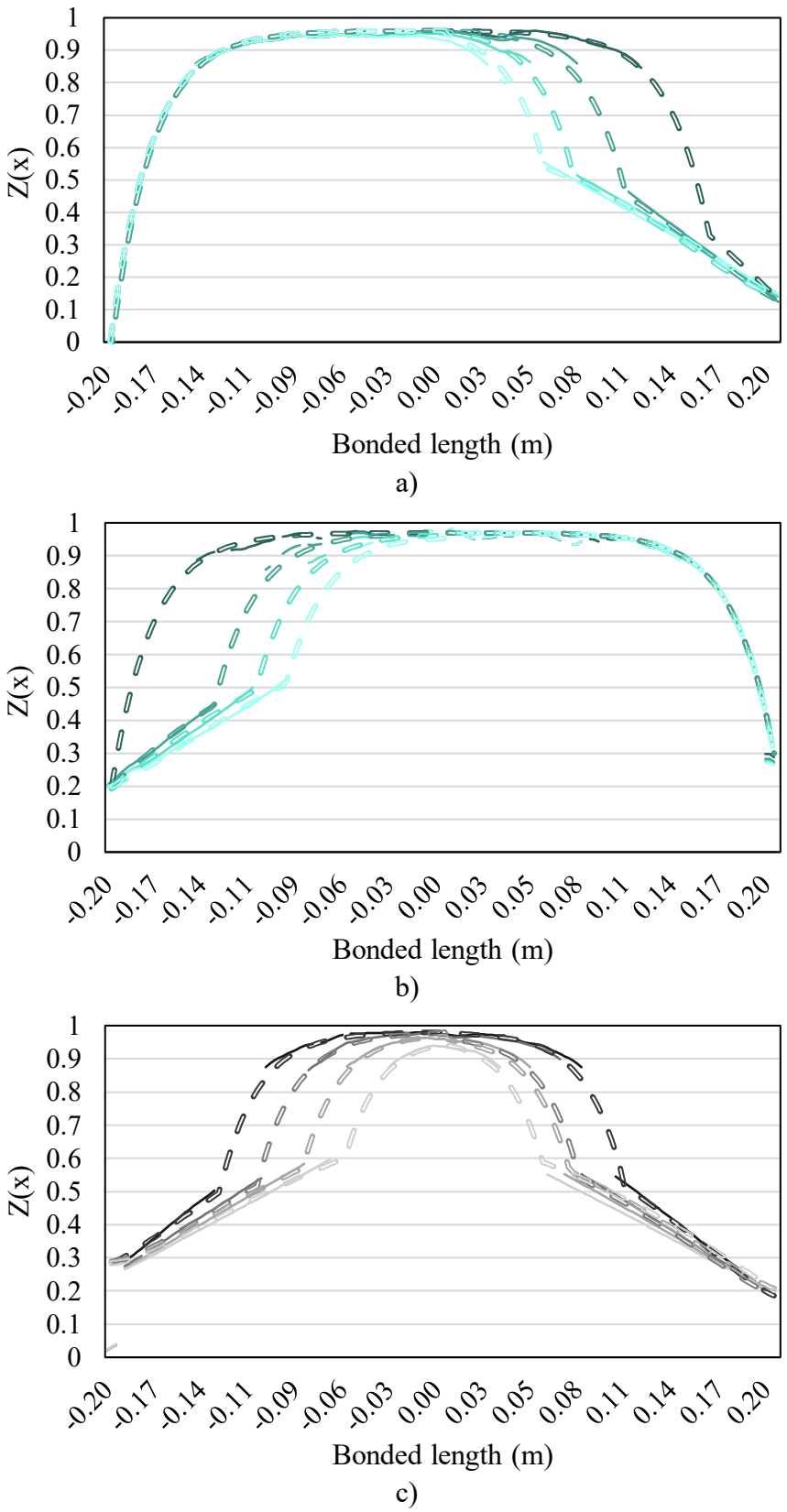

Figure 5-16. $Z_p(x)$ for layouts in sample SP-S: a) s-PVC-EP, b) s-PVC-CN, and c) g-PVC-CN

It can be seen that at various time intervals, the model successfully captures the damage progression and the gradual loss of local STE. Initially, the strain transfer was nearly uniform across the DFOS effective sensing length, as detailed in **Chapter 4**, under severe, sustained loading conditions. However, as the loading continued, localized concentrations of effective Z_x ($\geq$ 0.96) merged and progressively shrank over time, appearing in the central region of the bondline and converging toward the bondline center as damage progressed.

The close alignment between the theoretical predictions and experimental results further validates the model's ability to accurately predict strain transfer dynamics and the evolving behaviour of DFOS systems under prolonged high level stress. In is noted that for g-PVC-EP layout of sample SP-S, no DFOS data were available during the final sustained load phase, and consequently, no inelastic analysis was conducted for this configuration. However, as discussed in **Section 4.4.2.1,** building upon the DFOS distribution curves during unloading, when the signal was restored, this layout showed only partial damage along the bonded length, effectively preserving a long portion of the bonded length where STE was maintained, with a similar pattern as shown here.

Remarks on the results and the model performance:

- The numerical model demonstrated strong alignment with experimental results, effectively capturing bondline degradation and the evolution of the strain transfer coefficient over time in DFOS-bonded GFRP bars. Its predictive performance remained consistent across samples, reinforcing the model's reliability under sustained overloading conditions.

- The model was successfully validated using two distinct adhesives, EP and CN, both exhibiting similar initiation and progression of interfacial failure at the sensor–host interface along the DFOS bonded length, as well as comparable resulting strain transfer behaviour over time. This consistency highlights the model's robustness in representing bond degradation dynamics across different bond conditions and adhesive chemistries, supporting its potential for broader application

in DFOS configurations using varying adhesive joint systems.

- While the current validation focused on GFRP bars, the model is not substrate-specific and is expected to be applicable to other host materials, though further validation is recommended to confirm its effectiveness across different sensor–substrate interfaces.

Across all samples, including variations in adhesive type and bonding conditions, the numerical implementation consistently captured interfacial degradation and time-dependent inelastic strain transfer through the adhesive interface over time. All input values used in the incremental calculations, including those directly adopted from literature (e.g. $q(t)$) and the newly introduced parameters for simplification ($\lambda_{SC}(t)$ and $\beta_3'(t)$), remained consistently aligned across samples, as verified through curve-fitting of experimental data presented in **Tables 5-5** and **5-6**. This consistency supports the reliability of the theoretical framework and affirms the validity of both the established input set and the simplified parameters introduced for representing evolving bond conditions in surface-bonded DFOS systems. As a first-time implementation of this modeling framework in DFOS applications, the results provide a strong basis for its robustness and indicate potential for extension to a wider range of sensor–host and adhesive configurations.

- Defining the boundary between the damaged and intact zones, and adjusting BCs in $Z_e(x,t)$ according to the current $L_d(t)$ effectively aligned the two segments using $cosh\big(\beta_2 x_{\pm L_d}(t)\big)$. This approach avoided considering the entire initial sensing length, allowing for a smooth transition at the inner created boundary, ensuring a balanced local value of $Z_e(x,t)$.

- The overall responsive effect of the time-dependent decay function, $\lambda_{SC}(t)e^{-q(t)(|L|-|x|)}$, through the scaling factor, $\lambda_{SC}(t)$ and $q(t)$, is illustrated in **Figure 5-17** for a representative sample. Initially, $\lambda_{SC}(t)$ was set to increase the influence of $L_d(t)$ in the formulation of $Z_p(x,t)$ for localized damage, compensating for the side effects of simplifying assumptions. However, as damage progressed, the impact of $\lambda_{SC}(t)$ was progressively reduced, effectively scaling down the

influence of $L_d(t)$ and minimizing the high transfer loss in the mathematical model, to reflect the remaining effective interaction between the adhesive interfaces within the damage zone. The model initially overestimates the effects of $L_d(t)$ by assuming full debonding in areas of localized damage. However, as the damage propagates, the remaining adhesive areas continue to contribute to strain transfer, though at a reduced efficiency. Similarly, $q(t)$ was instrumental to address the diminishing influence of damage as it spreads along the bond. In the early stages, localized damage exerts a significant effect on stress and separation distribution along the damage zone, which is closer to bond edges. However, as the damage propagates along the bondline, its influence through relative displacement between adherends gradually decreases. Overall, the decay function allows the model to accurately reflect the reduction in damage impact over time and position, ensuring that localized damage is neither overestimated nor underestimated.

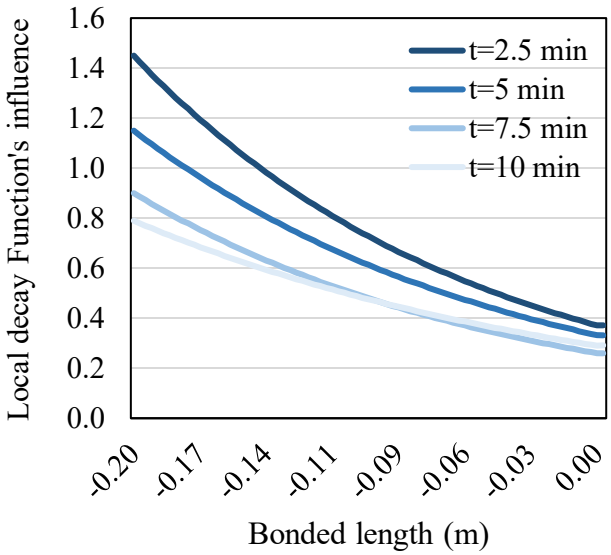

Figure 5-*17*. Overall functionality of the decay function for a representative sample, SC-12-g

- Experimental correlation results indicate that adhesive joints can tolerate localized damage in concentrated regions near the bonding edges without compromising overall strength under typical loading conditions in certain samples, including s/g-PVC-EP and s-PVC-CN SP-S and SC-16-g. Particularly, strain localization at the bond edge was observed to be effectively contained in

s-PVC-EP and s-PVC-CN layouts of sample SP-S at $x = L$ and $x = -L$, respectively, preventing progression along the adhesive bondline despite high-level sustained loading. However, within the other half of the sensing length, the localized damage zone extended over a relatively larger region near the bond edge, with limited progression beyond this concentrated area. This partial spatial degradation indicates that the bondline integrity was preserved within certain regions, with the inelastic shear deformation (or interfacial separation) accumulation mitigated, preventing further damage propagation. This behaviour reflects the adhesive's ability to resist widespread failure under controlled loading, maintaining its performance within localized areas of deformation.

- The pilot test samples, except SC-16-g, experienced the complete loss of the elastic-dominated region, with damage extending well beyond the relatively localized areas. One contributing factor to this behaviour, alongside potential installation-related inconsistencies and variations in bond conditions, is the constrained bonded length of almost 400 mm. This limitation, compared to longer reinforcing bars used in practice, reduces resistance to damage accumulation. As a result, the damage zone is more likely to dominate the bondline and effective sensing length under sustained, excessive loading. In this case, the bondline plays a critical role in the progressive development of damage, particularly when defects or inconsistencies are present along the bond. These imperfections, such as voids or irregularities in the adhesive's path (controlled by the host's surface features) or installation, gradually contribute to localized areas of stress concentration. As sustained loading progresses, these regions of weakness, influenced by variations in manual installation and surface preparation across test samples, gradually expand, transitioning into the damage zone. In samples with less proper surface preparation, like GFRP SC samples, defects such as uneven bonding, air gaps, or weak adhesive zones are more pronounced, leading to faster and more localized damage propagation. The damage does not spread uniformly, but instead follows the path of least resistance, typically extending along areas of higher stress (strain) or lower bond strength. Over time, the adhesive's ability to effectively transfer strain diminishes, leading to

further degradation in the bondline, compromising the sensor's distributed monitoring reliability. These results highlight the critical importance of managing load thresholds, as excessive loads exacerbate damage and compromise the adhesive's capacity to resist further propagation and degradation. This challenge can be addressed through serviceability control limits applied to the host GFRP reinforcing bar, ensuring that the adhesive bond remains within safe operational parameters and preventing premature failure.

- In the pilot samples, those subjected to higher loads relative to their distributed local bond strength exhibited accelerated damage accumulation. The remaining elastic portion along the sensing length, indicative of a region with reliable STE, decreased in the following order: SP-S SC-16-g, SP-12-s, SP-12-g, SP-16-s, SC-12-g, SP-16-g, SC-12-s, and SC-16-s (as also listed in **Chapter 4**), with the spatial extent of damage increasing as the load exceeded the adhesive's local bond strength. The evolution of bond degradation and its final impact at the end of sustained loading varied significantly across the test specimens. This variability supports the potential differences in bond performance, particularly influenced by surface energy, which plays a critical role in determining the bond's integrity, dynamic load-bearing capacity, and resistance to degradation under severe stressors. These variations highlight the sensor path conditions and energy characteristics that influence the durability of the sensor adhesive bond.

- The theoretical predictions for sample SP-16-s, as shown in **Figure 5-15**, reveal a reduction in model reliability in capturing the actual STE distribution at t = 10 minutes, particularly in the region near the inner damage tip. The model tends to slightly underestimate the $Z_p(x,t)$ values in this area, indicating potential limitations in the theoretical representation of strain transfer for specific cases as the damage zone develops. Trial corrections were made to $\lambda_{SC}(10)$ and $q(10)$, but tip led to overestimations in other regions of the sensing length. This suggests that while the model generally can effectively track the trend and overall strain distributions, it may not fully capture the finer details of strain redistribution in areas experiencing damage progression, as the maximum

bias captured here reached approximately -4%. This specific example highlights the potential for further enhancements by implementing more precise segmentation of the adhesive zone, coupled with the application of varying decay functions (factors) to better reflect the complex, nonlinear progression of damage in real-world scenarios.

- DFOS measurement curves across various test conditions have revealed limitations in signal integrity, particularly in regions with steep strain gradients, as consistently observed and discussed in this study. Due to this, the optical system struggled to maintain signal accuracy along the newly formed strain transfer length after the damage zone developed. Additionally, strain data near the bond edge, where steep gradients correspond to higher load and strain levels during elastic strain transfer, were often only captured after damage had formed at each sensing location. This delayed capture and subsequent reduction in measured strain values as strain dissipates, causing a decrease in the gradient and, consequently, an apparent improvement in signal quality after degradation. This effect arises from the redistribution of strain across the bondline, resulting in a strain profile with a reduced gradient within the damage zone. This is reflected by the measured values of $q(t)$, which commonly fell within the range of $4-7\ m^{-1}$ for varying test specimens, significantly lower than $\beta_2 = 40.5\ m^{-1}$. Both values are linked to incremental measurements between two gauge points. During the elastic regime, as the strain transfer length generally remains nearly constant, the increase in the host strain level results in a steeper gradient. However, energy dissipation leads to a reduction in strain, resulting in a significant decrease in the gradient. This dissipation alters the strain profile, and the strain reduction follows an evolving pattern of STE loss. Consequently, this leads to a reduction in the local variations between two sensing points along the damage zone where shear-induced effects are gradually stabilizing, improving the signal as the bondline degrades. However, as the bondline continues to degrade, the sensing system's ability to reliably track the host's experienced strain by DFOS diminishes, limiting their monitoring effectiveness after interfacial damage progression. A recent study by Herbers et al.

(2024) suggests that better signal integrity in strain transfer regions with rapid strain gradients can be achieved by setting the gauge pitch at 0.63 mm, which enhances the system's ability to capture finer details in the strain field. The referenced study demonstrated that signal integrity within the strain transfer zone is notably improved with a gauge pitch (GP) of 0.63 mm, accommodating up to 8000 $\mu\varepsilon$, compared to 2000 $\mu\varepsilon$ with a GP of 2.6 mm. In the present study, the GP was set at 2.6 mm, which contributed to a reduced signal fidelity in capturing the strain variations within these high-gradient regions. To enhance sensitivity in strain transfer length, future research may consider adopting a finer GP, such as 0.63 mm, for improved performance.

5.3.3. Energy Release Rate

This part of the analysis focuses on damage length (zone) rate growth, represented as dL_d/dt, and the associated incremental energy release rate, $\dot{G}_{II}$, for the relevant samples. The energy release rate, $\dot{G}_{II}$, is commonly defined in damage mechanics in terms of the (incremental) stress intensity factor, $\dot{K}_{II}$, which is given by $\dot{K}_{II} = 1.12\bar{\tau}_a^0\sqrt{\pi L_d(t)}$ for edge damage. $\dot{G}_{II}$ is then expressed as $\dot{G}_{II}=\frac{\dot{K}_{II}^{\,2}}{E'} = \frac{\dot{K}_{II}^{\,2}}{E}(1-\nu^2)$, where $E'$is the modified elastic modulus. This formulation provides a foundation for understanding the relation between damage growth and energy dissipation.

The time-dependent relation between the rate of damage zone growth and the incremental stress intensity factor can be expressed as $dL_d/dt = C\ \dot{K}_{II}^{\ m}$, where C and m are empirical exponents that define the overall relation of damage progression to the stress intensity factor. In this study, the damage growth rate, dL_d/dt, was analyzed using the DFOS strain data as outlined for $L_d(t)$ in **Table 5-5**. Further, $L_d(t)$ enabled the approximate calculation of $\dot{K}_{II}$ and $\dot{G}_{II}$ with certain simplifying assumptions made for clarity and practicality.

While the assumptions of input parameters may not yield precise outputs, the calculation of $\dot{G}_{II}$ and $\dot{K}_{II}$ and for the sensor bond interface was performed primarily to enable a comparative analysis

across different samples rather than to determine an exact absolute value. Given that the interface is not a structural adhesive joint, standard fracture mechanics assumptions do not strictly apply. Therefore, while DFOS provided reliable input values for damage length, some parameters used to calculate shear stress were estimated based on simplified assumptions applied uniformly across all samples. While this introduces uncertainty in the absolute values of $\dot{G}_{II}$ and $\dot{K}_{II}$, the analysis focused on relative differences between samples under consistent conditions, making the calculation a practical comparison metric rather than a definitive measure of fracture energy.

Figure 5-18 presents three charts of dL_d/dt, $\log\dot{K}_{II}$, and $\log\dot{G}_{II}$ for different samples. These charts provide a detailed illustration of damage progression across adhesive bondline in various specimens under similar loading conditions. They highlight the energy release rates and the adhesive joint's mechanical response trends, variability, and sensitivity during damage evolution.

1. Damage growth rate (dL_d/dt)

dL_d/dt represents the rate of damage propagation along the adhesive interface, accounting for both spatial spread and temporal evolution. In this study, dL_d/dt was observed primarily in samples under high-level sustained loading, whereas those under cyclic loading showed no measurable bond damage propagation along the DFOS bonded length. This contrast is attributed to differences in load duration and application pattern between the two loading types.

During sustained loading, each step lasted 10 minutes, allowing stress redistribution and damage accumulation along the bondline. This aligns with the adhesion book by Da Silva et al. (2018), who noted that under sustained overloading (commonly referred to as creep loading when applied for longer durations), damage initiates at joint edges and progressively penetrates the bondline, especially in the presence of micro-defects. In the current study, this mechanism resulted in observable damage progression along the bonded interface in the pilot test samples and sample SP-S from Stage II, both of which were subjected to high sustained stresses. Conversely, in the

cyclic loading tests, the load peaks were transient, lasting only a few seconds without sustained hold periods. As such, although localized damage initiated at the bond edges, it remained confined to those regions and did not evolve along the bondline within the short experimental timescale.

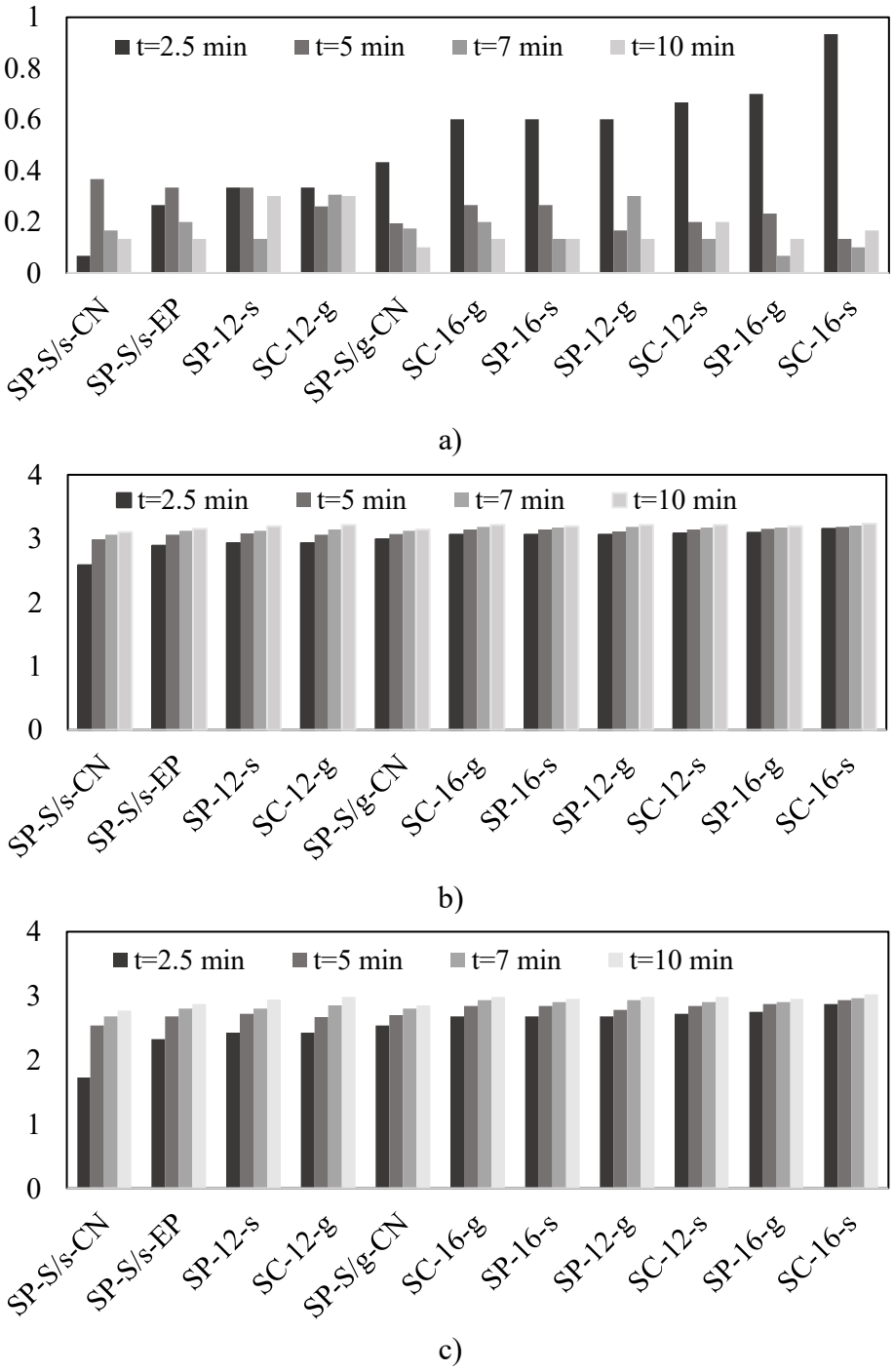

Figure 5-18. Comparative analysis: a) L_d/dt, b) $\log\dot{K}_{II}$, and c) $\log\dot{G}_{II}$

Although the cyclic loading tests simulated certain aspects of real-world dynamic loading, their short duration was insufficient to induce rate-dependent damage progression or measurable damage growth rates (dL_d/dt), which are typically observed under prolonged periods of fatigue. The influence of localized damage in the cyclic test samples (SP-C and MST-C) is evident in the strain distribution curves presented in **Figures 4-16** and **4-17** from the previous chapter, particularly during extreme unloading to 1 *kN*, where DFOS recovered signal integrity within the strain transfer length and revealed compression strain at the bond edges.

Additionally, it is important to recall that the strain levels observed in sample MST-S were below the critical threshold of 12000–13000 $\mu\varepsilon$, where inelastic behaviour typically begins in the adhesive. Therefore, MST-S, like the cyclic test samples, was excluded from the inelastic analysis.

At higher strain levels and steeper strain gradients along the transfer length, signal loss frequently occurred, preventing accurate measurement capture unless the damage zone expanded further. In such cases, the strain gradient becomes detectable again, raising concerns about sensor reliability and highlighting the need for further investigation into damage detection and prevention.

The dL_d/dt chart sorts the test samples according to the bond degradation and STE loss patterns, based on observations under high-level sustained loading (e.g., $\sigma_h \sim 900 + MPa$ and $\varepsilon \approx 0.013$-0.015). It visually captures the progression over time, highlighting varying intensities across all samples. Initially, the damage growth rate increases rapidly, reflecting the high stress concentrations at the bond edges, which facilitate the propagation of localized damage. This is particularly evident in the early stages of the test, where dL_d/dt varies from zero to a specified value by t = 2.5 minutes, indicating the evolution of bond degradation as the damage progressed from a localized region to a more extensive zone near the bond edges.

The rapidly increasing dL_d/dt rate during the initial period reflects the high stress concentrations near the extreme damage tips at the bond interface, where localized damage begins to propagate

along the adhesive interface, extending through regions of greater vulnerability. The localized damage forces the degradation to expand into adjacent flaws along the bonded length, leading to the progressive STE loss along the distributed sensing system. This initial surge in damage growth aligns with localized shear-induced concentrations and interactions at the bond interface, which accelerate damage propagation. After t = 2.5 minutes, dL_d/dt decreased across all specimens, indicating slower damage growth. However, the s-EP/CN layouts on sample SP-S show a shift at t = 5 minutes, where the initially low progression rate continued to rise before eventually declining. After this point, the rate stabilizes, marking the onset of a self-limiting phase as the material begins to stabilize. This behaviour, consistent across all samples, suggests that adhesive bond degradation slows once a critical damage threshold is reached.

The highest initial dL_d/dt values are observed in SC-16-s, SP-16-g, and SC-12-s, meaning these configurations experience the most rapid bond damage at the start. Subsequently, these samples exhibited the highest STE loss at the midpoint, which aligns with the experimental observations as presented in **Section 4.3.1** (**Figures 4-3** and **4-4**). Specifically, these samples are the only ones showing negative strain values at the middle of the bar during unloading. This indicates the most significant STE loss and the highest permanent separation (or interfacial shear displacement) between the DFOS system and the host material. Since the host deflection at this stage is smaller than the magnitude of the introduced interfacial shear displacement, the DFOS read this as negative strain. This is discussed in further detail in the following sections.

In contrast, the lowest initial and stabilized dL_d/dt values are observed in SP-S/s-PVC-CN and EP, and SP-12-s, suggesting that these samples with improved surface installation exhibit superior adhesion and strength and slower initial damage progression. As a result, they exhibit little to no STE loss during severe loading. For samples SC-16-g and SP-S/s-PVC-CN and EP, results reflect damage limited to one half of the bonded length, with the other half remaining unaffected.

In summary, the dL_d/dt values observed in the experiments reflect the interplay between sustained loading, stress concentrations and bond strength effects, localized damage accumulation, and the material's evolving resistance to further degradation. The experimental data support the hypothesis that as damage progresses, its growth rate decreases, and the adhesive stabilizes, which is consistent with both the damage length gradient and the $Z_p(x,t)$ analysis, as presented in the previous section. Overall, these results align with the observations discussed in **Chapter 4**.

2. Stress Intensity Factor and energy release rate ($log\ \dot{K}_{II}$ *&* $\dot{G}_{II}$)

$\dot{G}_{II}$, which represents the stored strain energy available for damage propagation, along with $\dot{K}_{II}$ plays a critical role in understanding bond degradation. The charts of $\log \dot{K}_{II}$ and $\log \dot{G}_{II}$ for the test samples demonstrate a clear increasing trend over time (although at an incrementally reduced rate), with the samples ordered in the chart from lowest to highest in the same sequence as observed for dL_d/dt, reflecting the progression of adhesive damage under the applied sustained loading. This trend indicates a progressive increase in both stress intensity at the damage tip and the energy release rate as damage propagates through the adhesive. The observed charts and trends are based on the analysis methodology employed, which quantifies the evolving bond damage dynamics.

The $\log \dot{K}_{II}$ chart tracks the increasing stress intensity at the edge damage tip, showing a steady rise as damage propagates over time. This indicates that as the adhesive degrades, the stress at the edge damage tip becomes more localized, making it increasingly difficult for bondline to maintain its integrity, which in turn leads to greater energy release. Similarly, the $\log \dot{G}_{II}$ chart illustrates the corresponding increase in energy release rate, indicating a growing dissipation of strain energy as adhesive weakens and damage spreads. The observed trends across all samples highlight the progressive nature of damage: as the damage zone extends, both stress intensity and energy release continue to rise. This escalation in energy dissipation is indicative of the material's weakening adhesive properties, underlining the gradual and cumulative bondline degradation over time.

The threshold energy release rate, G_{th}, controls the damage progression, representing the minimum energy required to initiate damage along the bondline. When $\dot{G}_{II}$ surpasses G_{th}, it triggers the onset of damage. During the early stages of high-level sustained loading, the $\dot{G}_{II}$ values steadily increased, suggesting that the applied load was sufficient to initiate damage. However, the subsequent decrease in the damage growth rate indicated that the energy release rate remained below the critical threshold, G_{cr}, preventing the adhesive from reaching a point of complete failure.

This behaviour indicates a relatively controlled degradation process, where the bond has been compromised but has not yet fully failed. As a result, damage progressed gradually without leading to immediate failure, with the sensor bond continuing to function, albeit with significantly reduced effectiveness, despite severe, prolonged loading. By t = 2.5 minutes, the $\log \dot{K}_{II}$ and $\log \dot{G}_{II}$ values have reached defined levels, indicating the formation of damage zones. While the damage did not escalate rapidly, it continued to evolve at a slower rate and a more gradual progression, with values showing only slight changes by t = 10 minutes. Over time, $\log \dot{G}_{II}$ increases as crack propagation progresses, requiring more energy for further growth.

Overall, lower $\log \dot{K}_{II}$ and $\log \dot{G}_{II}$ values across samples indicate better energy retention and slower degradation of the adhesive bond. In contrast, higher values indicate greater difficulty in maintaining bondline integrity, faster energy dissipation, and more rapid adhesive failure. The comparative charts reinforce the well-established role of surface treatment, sensor installation quality, and adhesion durability in influencing the performance of adhesively bonded DFOS, particularly in long-term, high-stress applications, where the bond strength defines the system, as consistently highlighted throughout the analysis.

5.3.4. Discussion on $Z(x)$ During Loading/Unloading

The experimental results presented in **Chapter 4** reveal a consistent pattern of strain readings within the damage zones following high-level sustained loads. While pilot samples showed further

decline in STE due to fast cyclic loading, most of the test samples exhibited a significant reduction in $Z(x,t)$ by the end of the sustained loading period. This reduction varied in both degree and the spatial extent of the affected bond length across the test samples, especially between the DFOS test layouts of the pilot and Stage II samples. These variations correspond to the relatively stabilized damage state and the final permanent interfacial shear displacement (or separation) at different bond lengths, indicating the spatial extent of permanent loss in STE.

The developed closed-form formulation for strain transfer coefficient along the damage zone, $Z_p(x,t)$, incorporates yield stress distribution and interfacial shear displacement during constant loading. Therefore, this formulation is not directly applicable during the subsequent unloading phase and the remaining applied loading protocol, as it does not account for the fixed residual effects that remain after the removal of loading. These residual effects must be carefully isolated and addressed to ensure a proper assessment of strain transfer behaviour in the post-loading phase. This necessitates an adjustment in the formulation, as the strain transfer mechanism during unloading no longer follows the same response as during loading. Due to the irreversible interfacial effects, the local strain reading in the core optical fibre is influenced by residual interfacial shear displacement, which results in a modified strain transfer condition.

The experimental graphs in **Figure 5-19** illustrate the evolution of the strain transfer coefficient, $Z(x) = \varepsilon_c(x)/(\varepsilon_{c,e}(x=0)/\beta_{1,e})$, during the first unloading phase of pilot samples. These results are representative of the overall distributed monitoring pattern observed throughout the remainder of the test protocol, with curves captured at stress levels near the upper and lower bounds of the unloading range, approximately 55% and 20% of the GFRP host's ultimate strength, respectively.

The overall response trends were largely consistent across the different sensor–host configurations, with some variations attributable to the factors previously discussed. Generally, as the bond continued to degrade under high-level sustained loading, localized slip and reduced anchorage

effectiveness led to increased energy dissipation and irreversible deformations. Moreover, as demonstrated in **Chapter 4**, DFOS strain readings on the pilot test samples declined progressively with each loading cycle following the sustained load steps, indicating ongoing dynamic interactions at the fibre–host interface and a further reduction in measurement accuracy. This degradation accumulated over time, intensifying with repeated cycles and negatively impacting the adhesive joint's performance.

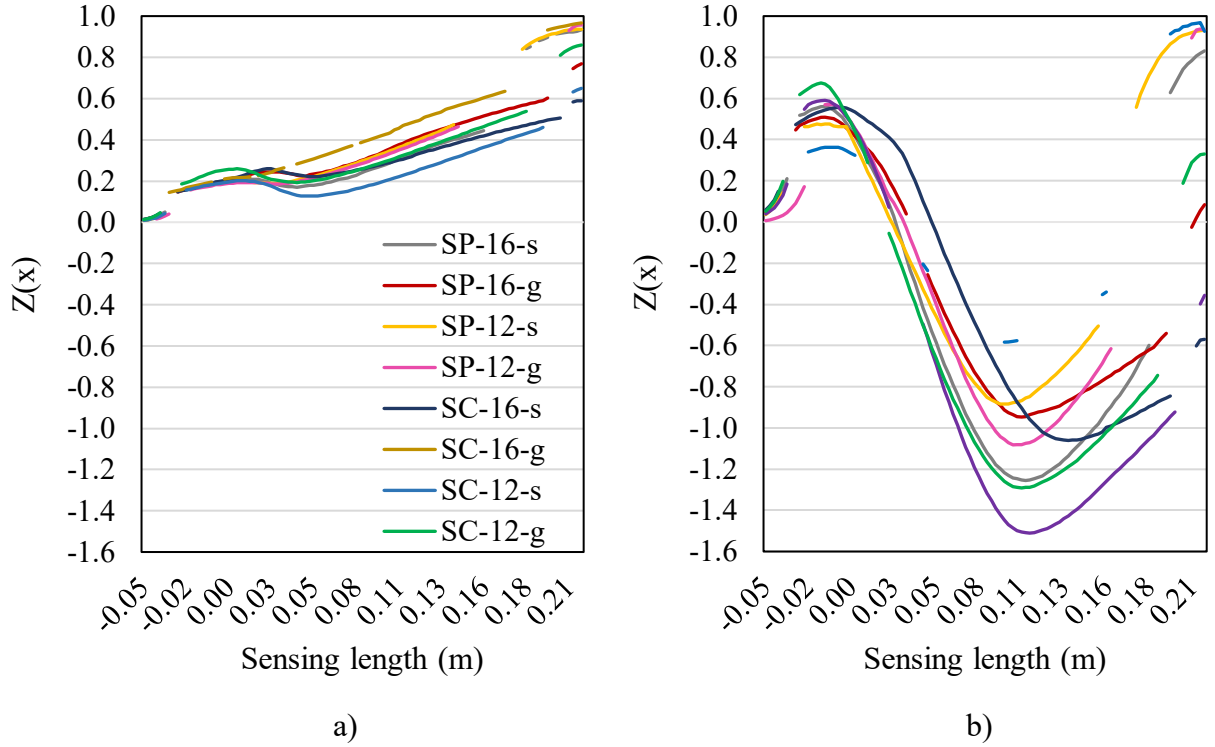

Figure 5-19. The representative $Z(x)$ curves captured during first unloading of pilot samples: a) near upper-level loads and b) near lower-level loads

The influence of localized ε_p becomes evident through the apparent fixed strain readings caused by strain averaging near the bond edge and just past its termination. This behaviour can be attributed to the residual interfacial slip that develops and persists after sustained loading and remains locked after unloading. As previously discussed, the strain transfer mechanism captures shear slip accumulation at the sensor–host interface, particularly near bond edges where stress

concentrations reduce STE to near zero in the elastic regime. Upon unloading, while the host material recovers elastically, the residual shear strain persists, inhibiting a full reversal of strain within the core fibre. The DFOS system, with its fixed 2.6 *mm* gauge length in this study, smooths out localized effects and BCs, smoothing localized strain fluctuations over the gauge length.

This averaging behaviour results in a gradual rather than discrete transition, a phenomenon consistent with the refined elastic regime analysis applied for sample MST, based on the equation derived from the reference study by Falcetelli et al. (2020). Instead of strain being localized at the bonding edge, ε_p appears distributed outward beyond the bond region due to strain averaging by the DFOS system. Consequently, strain readings remain seemingly constant for approximately 40-50 *mm* beyond the actual bond termination. This behaviour reflects the combined effects of residual shear displacement and DFOS gauge-induced strain averaging, rather than representing the true mechanical strain state of the adhesive layer or host material.

Generally, the strain transfer behaviour observed during loading and unloading, along with consistent patterns across test specimens, indicates that adhesive joints in DFOS surface-bonded systems employ energy dissipation mechanisms that maintain bond integrity under stress, ensuring predictable behaviour even after damage. As damage progresses, small defects coalesce, allowing continuous energy dissipation, stress redistribution, and preventing adhesion loss and catastrophic failure. Moreover, adhesive joints typically fail cohesively, allowing strain transfer to persist, though interlaminar strain distribution is disrupted, reducing STE. This degradation impacts STE and the overall performance of the DFOS sensing unit.

Furthermore, the distributed strain transfer behaviour observed during unloading from high-stress levels reveals a consistent trend: the $Z(x)$ shows a progressive increase along the bonded length as shear redistributes after certain threshold strain (applied displacement) levels. This behaviour aligns with theoretical expectations, where shear stresses are redistributed along the fibre-host

interface, leading to a progressive improvement in $Z(x)$ as the system stabilizes away from the bond edges. In this phase, the $Z(x)$ remains positive, displaying a distribution pattern similar to the final $Z_p(x, t = end)$, calculated at the end of the sustained loading phase, with a progressively greater decrease following each cycle of the fast repeated loading/unloading.

However, a critical deviation occurred during near-complete unloading stages. As unloading progressed, $Z(x)$ initially remained positive but gradually transitioned to negative values at specific locations due to residual slip. This transition varied along the bonded length and, in most cases, extends across the entire length for the pilot test samples, following the typical order observed in the sample set. This reversal of strain, opposite to the host structure, is directly related to residual interfacial shear displacement (slip) and anchorage constraints at the sensor terminations. Once residual displacement exceeds a certain threshold, the DFOS strain readings begin to reflect interfacial slip effects rather than true host strain. This signifies a fundamental shift in the strain transfer mechanism, highlighting the importance of accounting for these permanent, residual effects. Upon unloading, different regions of the bonded interface may unload at varying rates. If local stress persists in the DFOS interface due to these differential unloading rates, opposing strain gradients form, leading to negative $Z(x)$ values.

These observations highlight the complex interaction between the DFOS, the adhesive, and the host material during loading and unloading phases, with key implications for accurate strain transfer modeling and SHM. Understanding and quantifying these effects, including residual shear displacement and strain redistribution, can be beneficial for refining the DFOS system to account for both the immediate and long-term behaviour of bonded interfaces in GFRP-RC structures.

In conclusion, while the closed-form formulation for $Z_p(x, t)$ effectively captures strain transfer under constant loading conditions, accounting for both temporal and spatial bond degradation, it does not fully address the complexities introduced during unloading or the residual effects of

damage. The observed behaviour, however, offers valuable insights into the potential for capturing and quantifying strain transfer in damage zones at these follow-up stages. Further modeling efforts can refine the existing framework to better accommodate the dynamic changes in STE, offering an opportunity to more accurately represent the evolving bond damage at sensor–host interface.

5.3.5. Algorithmic Sensor–Host Interaction Assessment

Building upon the analytical and numerical investigations conducted in this study, this section introduces a structured algorithm aimed at evaluating the strain transfer characteristics in DFOS-surface-bonded reinforcing bar applications. The insights gained from the assessment of sensor–host interaction have revealed key parameters influencing dynamic STE, or $Z(x,t)$, particularly under the uniform strain field conditions defined and experimentally investigated.

The findings emphasize the link between bonding integrity and sensor response, with potential for future extension of the analysis to a broader range of arbitrary strain fields and enhance the model's general applicability. While this study focused on understanding these interactions, the proposed framework also lays the groundwork for future research aimed at automating data acquisition, processing, and anomaly classification, whether related to interfacial sensor damage or crack detection, thereby improving the usability of DFOS systems with minimal human intervention.

To develop an automated framework for evaluating both structural behaviour and sensor–host interaction, the system would employ a modular approach. This would involve separate layers for data acquisition, processing, decision-making, and visualization. Real-time strain data from DFOS sensors would be seamlessly streamed, and a multi-stage decision-making process would ensure accurate, automated evaluations of the system's performance. The system would operate on a hierarchical assessment scale, first verifying whether both the structure and sensor reaction are within expected thresholds. The proposed algorithm would follow the stepwise structure outlined below, as qualitatively described and depicted in the flow chart shown in **Figure 5-20**.

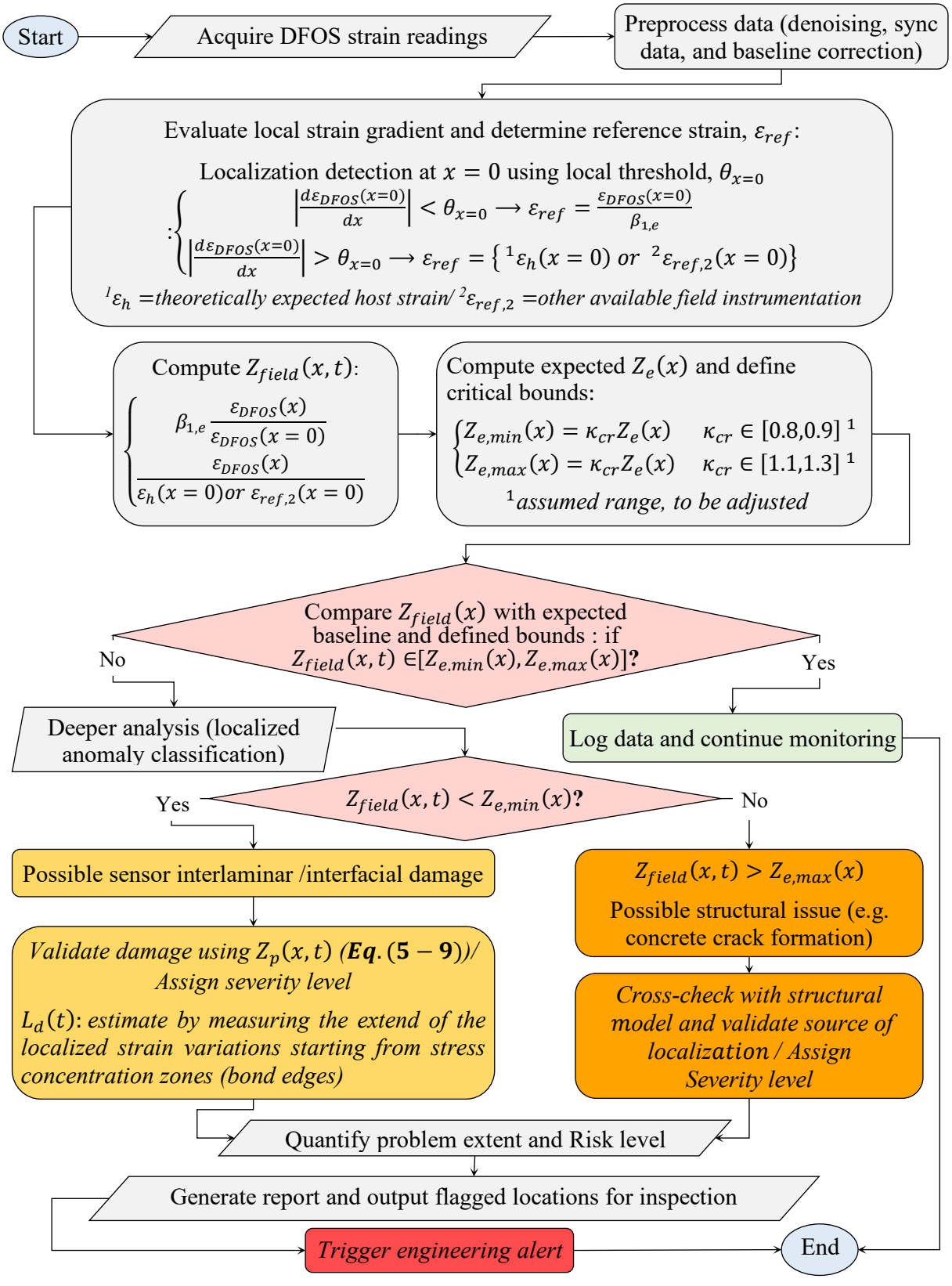

Figure 5-20. Localization Detection and Classification via SRAs

The data acquisition layer continuously collects strain data from DFOS, ensuring uninterrupted transfer and real-time preprocessing for denoising and synchronization before storage. The processing layer then computes STE at discrete sensing points in real time, maintaining consistent sampling distance for accurate evaluation of sensor–host interactions and reliable strain distribution analysis. The strain transfer coefficient along the sensing points is calculated using $Z(x,t) = \beta_{1,e}\, \varepsilon_{DFOS}(x)/\varepsilon_{DFOS}(x=0)$, where the midpoint reading $\varepsilon_{DFOS}(x=0)$ serves as the reference strain if it shows no signs of inelastic localization, with proper calibration of $\beta_{1,e}$ at early stages. Inelastic localization at $x = 0$ is identified by detecting abrupt variations, indicating stress concentrations or cracking. If localization is detected, the expected host strain (ε_h) (either theoretically estimated or correlated with external instrumentation) is used as the reference strain instead. Calculations should be performed within a defined tolerance range to account for measurement noise, intermediate layers, suboptimal installation effects, and material variability.

The decision engine layer then utilizes decision-tree logic to classify anomalies. If the strain data aligns with expected elastic response, the system logs the readings and continues monitoring. However, if deviations exceed predefined analytical thresholds, the system automatically initiates a detailed diagnostic analysis to pinpoint the root cause of the anomaly. This enables the initial classification of the issue's origin, whether related to sensor–host interaction or structural distress, by comparing measured values with an expected baseline, such as $Z_e(x,t)$ formulated in this study, derived from numerical simulations and historical elastic responses. At this stage, the algorithm systematically differentiates whether the anomaly originates from:

1. Structural changes (crack assessment) – Examples include localized cracking near the DFOS-instrumented reinforcing bar, or damage within the reinforcing bar itself, leading to non-uniform strain distribution. By incorporating correlated structural load distribution, if strain readings show progressive localization (spikes) that deviate from expected material elasticity or

correspond with known crack-prone areas, the algorithm flags potential crack formation in the surrounding structure (e.g., concrete) or identifies possible damage along the reinforcement.

2. Strain transfer inefficiency (sensor's interfacial damage assessment) – Indicating potential sensor–host detachment or interfacial bonding degradation, affecting measurement accuracy and sustained drop in $Z(x,t)$, assessed locally. Thus, the system should identify continuous regions, originating from stress concentrations, where strain remains persistently low, indicating anomalies below a critical threshold, $Z(x,t) < Z_{cr}(x) = \kappa_{cr} Z_e(x)$.

In the above formulation, κ_{cr} represents a critical acceptance coefficient, to be calibrated within the project. In such cases, the system prioritizes sensor bond assessment, excluding edge regions where $Z_e(x = \pm L)$ is theoretically zero due to natural BCs. In these areas, localized adhesive shear deformation may cause DFOS to record interfacial plastic strain, ε_p, that persists. In regions a few cable diameters from bond edges, even slight reductions in $Z(x,t)$ may indicate localized debonding or degradation, which was focused and quantified as a key concern in this study.

The system can assign risk levels (low, moderate, critical) based on threshold exceedances to quantify anomaly severity and trigger alerts when limits are surpassed. An interactive dashboard allows engineers to visualize strain trends, flagged anomalies, and severity heatmaps, with options for manual inspection or overriding system decisions. It may also generate spatial maps of $Z(x,t)$ deviations to identify sensor bond damage, supporting maintenance planning. With further development, it could evolve into an autonomous predictive maintenance tool, integrating AI and machine learning for real-time analysis, adaptive thresholds, and improved anomaly detection.

Damage severity assessment during cracking stages can be enhanced by integrating an automated crack quantification process based on detailed strain profiles. By detecting localized strain concentrations and gradients, the algorithm can effectively identify crack zones and estimate their width and intensity. These cracks can then be classified according to relevant serviceability

criteria. For GFRP-reinforced concrete, the Canadian Standards Association (CSA S806-12) specifies a maximum acceptable crack width of 0.5 mm under normal service conditions, with larger widths potentially becoming critical depending on environmental exposure and structural role. Incorporating these thresholds into the automated model allows the system to differentiate between critical and non-critical cracks reliably, facilitating timely engineering alerts and helping ensure compliance with long-term performance standards.

Future research could further validate the proposed closed-form equation for approximating localized $Z(x,t)$, including $Z_e(x)$ or $Z_p(x,t)$ at their respective interface regimes, across a broader range of structural materials, emphasizing sensor–host interactions and long-term monitoring reliability. Additionally, integrating the full algorithm into computational models or simulation frameworks algorithm could be explored for real-time anomaly classification and interfacial interaction assessment. Building on algorithmic methods like that of Zhang et al. (2021b) for decomposing DFOS signals across multiple cracks, an automated system could enable more accurate strain distribution and crack propagation analysis with minimal human input, greatly enhancing DFOS applicability in SHM. While this study does not primarily address crack detection, future developments could extend the current algorithm to support broader structural assessments, including long-term condition monitoring and damage classification. By bridging numerical modeling with practical implementation, this methodology lays a solid foundation for advanced DFOS-based monitoring systems, enabling full automation, better decision-making, and streamlined SHM data processing.

5.4. Summary of Observations

Theoretical and Numerical Validation:

- The chapter quantified experimental observations through theoretical modeling, confirming the reliability of strain transfer mechanics in surface-bonded DFOS within operational limits.

- The developed numerical approach accurately predicts strain distribution and degradation trends, offering a valuable tool for performance assessment.

Bond Degradation and STE:

- Despite maintaining functionality, surface-bonded DFOS systems with bondline damage exhibit progressive losses in STE due to interfacial degradation under prolonged stress.
- Bond damage and strain field constraints (bond edges) reversals lead to energy dissipation, stress redistribution, and localized plastic deformations, further reducing monitoring accuracy.
- Selecting appropriate intermediate layer properties and installation techniques to control sensor bond quality can reduce degradation and improve the long-term reliability of DFOS strain measurements, especially when bond strength serves as a key scaling factor.

Adhesive Thickness and Bonding Properties Optimization:

- The choice of adhesive is critical for balancing bond strength and minimizing interfacial strain loss. Additionally, proper application techniques play a key role in enhancing DFOS sensitivity and durability, especially under prolonged loading.
- Effective shear stress transfer within bonded layers is fundamental for accurate strain sensing, highlighting the importance of advanced bonding techniques and high-quality installation.
- A higher bond strength can effectively localize and contain damage, particularly in endpoints of bonded length, preventing its progression toward the central region by restricting debonding to peripheral areas and maintaining strain transfer integrity.

Impact of Jacket Material on Strain Transfer:

- PI-coated fibres exhibit higher STE and less strain transfer length. Despite their efficiency, they are mechanically delicate, posing potential durability challenges in field applications.

- PVC-coated fibres provide a more gradual strain transfer along the bonded length, with potentially reduced STE in overall.
- The selection of jacket material should carefully balance STE with durability and compatibility with installation techniques. Embedding the fibre within the host material offers better protection, while surface mounting trades off durability for practicality.

The effect of Bonded Length on the DFOS measurement:

- Bonded length can play a crucial role in minimizing strain loss and containing damage within localized regions, preventing it from affecting the entire bonded length.
- A wider bonded length can minimize the portion of low-sensing segment, improving measurement consistency and preventing the influence of inherent, excessive signal degradation in SHM assessment.

Shear Stress Transfer and SHM Applications:

- The model addresses interfacial shear interactions between protective layers, modelled here based on the assumption of a single layer with adhesive bonding interfaces, improving strain distribution predictions under various bond conditions up to progression level.
- The failure criterion aligns well with experimental observations, making it a reliable tool for evaluating long-term DFOS system integrity.
- Proper calibration of DFOS strain measurements in host materials is crucial for accurate SHM, especially in crack quantification and long-term monitoring applications involving DFOS-surface bonded reinforcement.

DFOS in GFRP Reinforced Structures:

- DFOS attachment with GFRP bars introduces greater challenges due to the material's wider elastic strain range and potential interlaminar inelastic behaviour within the strain transfer.

- The assumption of a perfect bond in adhesives must be reconsidered, as GFRP bars' test loading protocols may cause permanent interruptions in strain transfer.
- Proper analytical approaches from microstructural strain transfer mechanics to crack quantification frameworks are essential for reliable SHM.

Monitoring Capabilities:

- DFOS systems can capture nearly the full strain signal during damage progression due to strain energy release, despite initial localized signal integrity loss.
- The mechanical interaction between core fibre and host structures can significantly influence crack detection accuracy and SHM effectiveness.
- Ductile intermediate layers, such as EP and PVC jackets, provide smoother strain distribution curves compared to PI and CN adhesive, as their flexibility allows for gradual strain transfer, potentially reducing strain peaks during crack quantification and lowering accuracy by dampening localized strain variations and underestimating crack width and propagation.

Adhesive Bond Damage Propagation:

- Adhesive joints typically undergo rapid initial damage growth, which gradually slows as stress redistribution engage, reducing localized stresses and stabilizing the degradation process.
- Surface-treated configurations exhibit better adhesion and lower damage propagation rates, making them more resistant to severe, sustained loading.
- Rough surfaces worsen bondline damage, making surface treatment vital in DFOS bonding. While elastic strain transfer is less affected, bond strength largely depends on surface quality.

Implications for Practical DFOS Deployment:

- DFOS systems require careful calibration and optimization to maximize their effectiveness and

reliability in real-world SHM applications.

- Advanced analytical modeling enables improved calibration and scaling of DFOS performance across different structural conditions and material configurations.
- Plastic adhesive interface interactions within DFOS strain transfer mechanics offer significant research opportunities, particularly in predictive modeling for strain distribution following stabilized damage zones and crack monitoring applications.
- Mechanical interactions and installation inconsistencies, particularly associated with manual processes, pose risks to STE, consistency, and reliability in DFOS instrumentation. These challenges must be carefully addressed to improve practical deployment, especially in GFRP-reinforced structures, where precision is critical.

Final Outlook and Future Considerations:

- This part of the study developed numerical formulations and potential algorithms to model strain transfer mechanics in surface-bonded DFOS systems dynamically, addressing key factors like localization, bonding properties, shear stress redistribution, and material interactions. These formulations provide a foundation for further validation, refinement, and implementation, enabling improved accuracy in strain measurement as well as subsequent crack quantification and SHM assessments.
- Future work should prioritize optimizing bonding techniques, calibration strategies, and long-term reliability measures.
- A comprehensive understanding of strain transfer mechanics is key to advancing DFOS performance and ensuring its reliability in diverse engineering applications.

Chapter 6

Summary, Discussion, and Future Work

6.1. General

SHM technologies play a critical role in maintaining civil infrastructure by enabling the early detection of damage indicators. Among these technologies, DFOS stand out for their exceptional sensitivity, high resolution, small size, and ability to provide continuous measurements of strain/stress. While DFOS have been widely used for long-term infrastructure monitoring, their application in concrete structures is limited by the vulnerability of bare optical fibres to harsh conditions. Protective coatings are mostly used to safeguard the optical fibres, but durability challenges persist, as factors like cracking and friction can degrade performance.

A practical solution involves bonding optical sensor cables onto the surface of reinforcing bars, offering multifunctional systems that protect the fibre throughout the service life and ensure accurate, long-term strain measurements while serving as a crucial structural component. This method simplifies sensor installation by enabling direct attachment to the bar surface and efficient instrumentation of entire reinforcing cages using a single continuous sensor cable, up to 20 metres long, monitored via OFDR. However, the use of protective coatings and bonding agents between the optical fibre and host material can introduce measurement inaccuracies due to shear lag effects and interfacial interactions, potentially distorting strain readings.

This study assessed the performance of DFOS-instrumented GFRP reinforcing bars, monitored using the OFDR-based ODiSI integrator, for precise and consistent strain measurement under uniaxial tension. Focusing on electromagnetically neutral, unidirectional high-strength GFRP bars, which inherently protect the bonded DFOS, the research aimed to explore the potential of these systems for long-term in- SHM. The evaluation focused on the reliability of surface-bonded DFOS

for capturing distributed strain data under both laboratory-controlled and application-relevant loading conditions across various short-term experiments. In parallel, the study investigated the mechanics of interfacial interactions within the intermediate layers of the DFOS system, aiming to identify key sources of measurement error, uncertainty, and potential loss of monitoring efficiency in its practical application with GFRP bars.

Through a comprehensive experimental program combined with theoretical and numerical analysis using a closed-form analytical model, this study examined key factors and strain threshold limits that affect the accuracy and stability of DFOS measurements when adhesively bonded to GFRP bars under various stress conditions. The investigated parameters included bar diameter, bar surface treatment characteristics, sensor attachment methods (surface mounting versus groove embedding), DFOS coating and adhesive types, as well as loading type and history. The impact of these factors was assessed by analyzing the quality and stability of distributed strain transfer efficiency (STE). STE represents the proportion of the host strain transmitted to the core optical fibre and reflects measurement bias introduced by the multilayered sensing mechanism. The study aimed to assess the overall monitoring reliability and establish the operational limits for stable distributed measurements across a broad range of static and dynamic strain levels.

The results highlight the significant potential of surface-bonded DFOS for continuous, high-resolution, sub-millimetre strain measurements in GFRP bars, especially within the serviceability limits of GFRP reinforcement. However, stable STE limitations were observed at elevated stress levels, primarily due to localized plastic shear deformations in the adhesive at bond edge discontinuities under excessive loading. Sustained high stresses further induced inelastic shear reponse along the adhesive interface, gradually leading to bondline degradation. This interfacial failure contributed to the underestimation of the host strain by the bonded DFOS. These findings reveal critical efficiency thresholds of the sensing system and offer insights into interfacial engagement at the sensor–host interface, highlighting areas for further optimization.

This thorough preliminary investigation, conducted under uniaxial tension and controlled environmental conditions with a focus on long-term sensor reliability rather than structural damage visualization, supports the adoption of DFOS-bonded GFRP bar systems in civil infrastructure. It addresses measurement uncertainties and lays the foundation for refining these systems to improve the reliability and longevity of SHM applications for GFRP-RC elements.

6.2. Summary of Key Findings

The experimental findings, based on the observed time scale and testing conditions, demonstrated the consistent reliability of DFOS in capturing distributed tensile strain along their bonded length on GFRP bars under varying strain conditions up to 12000 $\mu\varepsilon$. However, supported by theoretical correlations, the findings demonstrated that the accuracy and stability of DFOS strain measurements were governed by a complex interplay of factors influencing interfacial behaviour.

Within the identified operational limit, where strain was transmitted elastically through intermediate layers, monitoring performance variability was observed even among test specimens with similar sensor assemblies. These inconsistencies, reflected in differences in STE, noisy strain profiles, or localized signal disruptions, intensified at higher strain levels, highlighting the sensitivity of DFOS performance to subtle variations in configuration and bonding conditions. The comparative results for different intermediate layer types shwon that DFOS with polyimide (PI) coatings consistently recorded higher strain readings than those with PVC coatings. Similarly, DFOS bonded with cyanoacrylate (CN) resin recorded higher strain readings than those bonded with two-part epoxy (EP). The reason PI- and CN-based DFOS configurations exhibited enhanced STE is that the thinner, stiffer, and stronger interfacial bonding characteristics of their intermediate layers facilitated more efficient strain transmission from the GFRP to the core fibre.

Beyond the mentioned strain limit, comparisons between DFOS strain profiles and consistent extensometer readings, which confirmed the fully elastic behaviour of the host GFRP up to failure,

revealed a high potential for significant measurement inaccuracies in the bonded DFOS. Repeated high-level loading, concentrated on the inherently small cross-sectional area of DFOS bond joints (typically $< 10\ mm^2$), induced localized plastic shear strains within the adhesive interface.

This reduced interfacial stiffness and progressively degraded the bond between the DFOS and the GFRP substrate, with damage severity proportional to the strain energy release rate (SERR). This resulted in a loss of STE and the emergence of progressive strain reading anomalies (SRAs), which permanently compromised the accuracy of distributed measurements. The presence of plastic shear strains within the adhesive was further evidenced by DFOS strain profiles recorded after unloading from severe loading. Compressive strains frequently appeared in damaged regions, despite the absence of externally applied compression, suggesting an anomalous yet consistent pattern of stress redistribution resulting from internal bond degradation.

The extent of measurement degradation varied among test specimens, primarily governed by the loading type and the adhesive joint's capacity to preserve bondline integrity under high stress. These observations highlight the critical influence of strain conditions, surface irregularities, and installation quality on maintaining adhesive confinement and interfacial stability, which are essential for reliable long-term monitoring.

Bond damage formation and progression were influenced by three key parameters, including: 1) the GFRP bar surface characteristics with different microvoid volumes and irregularities, which initiate bond imperfections and impede proper adhesion between the sensor and host surface; 2) the quality of manual installation and the uniformity of sensor adhesion along the DFOS bonded length, influenced by consistent and adequately sustained pressure during adhesive curing, impacting the achieved bond strength through adhesive and cohesive forces; and 3) the duration of the severe loading: unlike cyclic or monotonic loading, only sustained high-level loading compromised adhesive interface stability along the entire or partial DFOS bonded length. When

such stress was not sustained, bond damage remained confined near the ends and had minimal impact on the consistency of distributed strain measurements.

The developed closed-form analytical model simulated strain transfer mechanics in surface-bonded DFOS, encompassing both elastic behaviour and a defined plastic regime of the adhesive joint. It advanced existing models by enabling tracking and quantification of distributed STE along the bonded length during damage progression at the sensor–host interface. Its primary goal was to assess the dynamic durability of DFOS strain measurements during service. The model's reliability was validated through numerical implementation and experimental comparison, offering valuable insights into sensor bondline degradation under sustained stress beyond the critical strength limit.

The elastic component of the analytical model, which accounts for shear lag effects in multilayered sensing mechanisms, provides a powerful tool for real-time structural monitoring. In crack detection applications using bonded DFOS on reinforcement, where precise distributed strain measurements are essential for accurate crack quantification, this theoretical framework can enhance SHM assessment reliability by calibrating strain readings.

In the subsequent analytical phase, the damage progression component of the model introduced localized perturbations to simulate the propagation of shear bands or microcracks within the adhesive interface. This approach progressively divided the DFOS bonded length into damaged and undamaged regions, enabling quantification of both elastic and inelastic STE through the adhesive interface, dependent on the local sensing position. The ability to dynamically detect these damage zones represents a key strength of the developed analytical and numerical model.

While these effects may be less critical within typical GFRP bar serviceability limits, they are essential for understanding the long-term performance and durability of the sensor system. Future work can also expand this approach to account for other potential scenarios of bond damage progression, including harsh environmental conditions and long-term factors such as creep,

fatigue, or thermal stresses. By implementing these dynamic strain transfer models to account for shear localization and bondline degradation, the numerical analysis offers a valuable framework for evaluating DFOS strain data in long-term applications. This enhancement strengthens long-term monitoring strategies by improving the reliability assessment of SHM systems in service. It is particularly valuable as structures age and are subjected to repeated load cycles.

The study successfully achieved its objectives by developing a comprehensive understanding of DFOS-bonded GFRP bars through combined experimental and numerical analyses. Experimental results provided valuable insights into the bonded sensing system's behaviour under varied loading conditions, while numerical simulations extended these findings by predicting performance across different stress regimes. This integrated approach validated the experimental data and reinforced strategies for tracking DFOS reliability in long-term SHM applications.

6.3. Conclusions

In conclusion, the study validated the reliable performance of DFOS GFRP systems for distributed strain monitoring. Key findings further emphasized the importance of optimizing critical parameters and interface mechanics to ensure accurate strain measurements. The results also highlighted limitations arising from physical and geometric factors that impact both precision and durability under high-stress conditions. Based on these observations, the recommended installation technique for surface-bonded DFOS on GFRP bars involves incorporating grooves to embed the DFOS within the GFRP, using a stiff adhesive material. This approach enhances the stability and reliability of strain monitoring, while eliminating noise in strain distribution caused by irregular sensor paths. Consequently, it ensures uniform strain transfer across stiff intermediate interfaces, reducing the risk of misinterpretation in subsequent crack monitoring applications.

- **Overall Implications:**

The study demonstrated the potential of surface-bonded DFOS GFRP bars for consistent strain

monitoring across a range of loading conditions, achieving reliable performance up to a strain threshold of 12000–13000 microstrain ($\mu\varepsilon$). The DFOS system, visualized by OFDR technology, delivered real-time, high-resolution strain measurements while effectively minimizing inaccuracies related to strain transfer within this threshold. The reliable and stable performance of DFOS-instrumented GFRP bars under both static and dynamic stress conditions highlights their suitability for SHM and reinforcement of concrete structures subjected to fluctuating and sustained stresses, including those from traffic, seismic activity, and dead loads.

- **Limitations and Constraints:**

Despite the promising potential of DFOS-instrumented GFRP bars within certain strain limits, several possible challenges in the sensing systems were identified. The test results highlighted the critical role of sensor path configuration and the initial and dynamic quality of the installation in distributed strain monitoring performance. This quality was influenced by factors such as proper adhesive application, consistent bondline uniformity and thickness determined by curing conditions, and effective confinement of the adhesive layer to minimize internal particle movement and maintain uniform stress transfer between the sensor and host under challenging conditions.

Additionally, the long-term efficacy of sensor–host interactions degrades due to worsening bond flaws within the adhesive interface under sustained high strains. Over time, these imperfections dissipate energy and redistribute stresses, eventually stabilizing into a new, predictable state, provided the loading remains within the critical strength threshold and does not approach failure.

Together, these factors significantly affected strain measurement consistency and the gradual development of interfacial failure at the sensor–host interface. Moreover, although the overall signal integrity remained largely effective, signal degradation was frequently observed in regions with steep strain gradients (previously referred to as low-sensing lengths). In some cases, partial complete signal attenuation was noted along the central bonded DFOS length (termed effective

sensing length), which were mainly caused by inadequate physical interactions within the system rather than optical limitations.

Measurement limitations in surface-bonded DFOS on GFRP reinforcing bars are more critical than in concrete surface applications. This is because embedded sensors inside concrete cannot be repaired or replaced without damaging the structure. Both sensor damage and interfacial failure between the DFOS and the GFRP bar can compromise strain transfer and reliable measurements, potentially resulting in permanent signal loss or compromised strain data reliability. These limitations underscore the necessity for bonding techniques suitable for large-scale sensor deployment, in-field verification of installation quality, and, where feasible, the integration of redundant sensing paths to enhance the long-term viability and reliability of the monitoring system.

6.4. Recommendations and Future Work

The findings from this comprehensive investigation provide valuable insights into the design and practical application of surface-bonded DFOS-instrumented GFRP bars. Future research should prioritize addressing the identified performance limitations, optimizing sensor integration techniques to enhance sensor installation consistency and rigidity, and exploring the potential for large-scale production of DFOS-instrumented GFRP reinforcing bars and cages.

Additionally, further studies are required to assess the performance of DFOS-instrumented GFRP bars within concrete structures, validating their effectiveness in both reinforcement and real-time monitoring for practical applications. In this regard, particular focus should be given to testing and specifying adhesive materials that enhance crack detection in the surrounding concrete when used with surface-bonded DFOS GFRP reinforcement.

The analytical model and algorithmic evaluation of sensor–host interactions developed in this study provide valuable insights into strain transfer mechanisms. These findings lay the groundwork

for developing robust strain transfer frameworks for surface-bonded DFOS systems and machine learning algorithms designed to track STE stability alongside SHM assessments. These approaches aim to improve the accuracy and reliability of DFOS data interpretation in real-world applications.

Recognizing and addressing STE stability challenges is critical to advancing the use of DFOS technology in large-scale SHM, particularly for infrastructure subjected to complex, high-magnitude static and dynamic loads, such as those induced by heavy traffic or severe seismic events in GFRP-reinforced concrete bridges.

Moreover, the influence of environmental factors, such as humidity and temperature, on strain measurement accuracy and stability must be thoroughly investigated to ensure reliable DFOS performance in GFRP bars for SHM projects.

While the developed model provided valuable insight into strain transfer and bondline degradation, it relied on certain assumptions that may not fully reflect real-world complexities. In particular, post-unloading responses and subsequent time-dependent effects during service or testing were beyond the scope of the present analysis. The idealized parameters used to represent interface conditions, while effective for initial evaluation, may vary under practical conditions. Future work should aim to refine these assumptions and extend the modeling approach to improve its applicability for long-term monitoring scenarios.

Finally, to ensure the effective deployment of a robust SHM strategy, surface-bonded DFOS systems should be complemented by high-precision reference sensors. Electrical strain gauges, in particular, are recommended for this purpose. These systems should be correlated through prior laboratory testing to enable accurate cross-validation of DFOS data, crucial during early deployment stages such as installation quality assessment. Laboratory efforts should focus on calibrating DFOS data based on the mechanical properties of the fibre's jacket and bonding layer, as defined by the numerical model, to ensure reliable strain representation under field conditions.

In the field, it is recommended that, after surface-bonding the DFOS to the reinforcement and before concrete casting, a minor mechanical load be applied. As part of the installation verification process, this pre-loading serves as an early check, allowing verification of sensor installation and strain transfer behaviour prior to concrete casting. Any irregularities observed under low stress may indicate bond imperfections or installation defects, allowing for timely correction before permanent embedding.

For effective implementation in RC structures, DFOS installation should adhere to a rigorously defined protocol. Based on the findings of this study, it is recommended to embed the optical fibre within a pre-drilled groove along the GFRP reinforcement using CN adhesive, selected for its rapid curing properties and high STE. To improve sensor durability during concrete casting, while preserving the system's ability to monitor cracking, a thin, optimized layer of silicone sealant should be applied. However, this protective layer should only be added after confirming, through field testing, that the underlying CN bond ensures effective strain transfer.

To support maintenance planning and enable in-situ, continuous assessment of distributed measurement reliability, a practical framework is recommended. This framework may draw on the preliminary insights from the analytical and numerical analysis developed in this study. It could serve as a foundation for automating DFOS data interpretation and identifying service-induced errors. In field applications, such a framework has the potential to reduce the need for intensive engineering intervention when analyzing large volumes of DFOS data, while supporting effective tracking of both the sensing system and structural health.

References

Abdel-Jaber, H., and B. Glisic. 2016. “Structural Health Monitoring Methods for the Evaluation of Prestressing Forces and Prerelease Cracks.” Front. Built Environ., 2. https://doi.org/10.3389/fbuil.2016.00020.

Aksel, E., and J. L. Jones. 2010. “Advances in Lead-Free Piezoelectric Materials for Sensors and Actuators.” Sensors, 10 (3): 1935–1954. https://doi.org/10.3390/s100301935.

Alasia, D., M. Gonzalez Herraez, L. Abrardi, S. Martin-Lopez, and L. Thevenaz. 2005. “Detrimental effect of modulation instability on distributed optical fiber sensors using stimulated Brillouin scattering.” 587. Bruges, Belgium.

Alexander, M. G., H.-D. Beushausen, F. Dehn, and P. Moyo (Eds.). 2012. “Analysis of the strain transfer mechanism between a truly distributed optical fiber sensor and the surrounding medium.” Concrete Repair, Rehabilitation and Retrofitting III, 288–289. CRC Press.

AlNajmi, L., and F. Abed. 2020. “Evaluation of FRP Bars under Compression and Their Performance in RC Columns.” Materials, 13 (20): 4541. https://doi.org/10.3390/ma13204541.

Altabey, W. A., Z. Wu, M. Noori, and H. Fathnejat. 2023. “Structural Health Monitoring of Composite Pipelines Utilizing Fiber Optic Sensors and an AI-Based Algorithm, A Comprehensive Numerical Study.” Sensors, 23 (8): 3887. https://doi.org/10.3390/s23083887.

Ansari, F., and Y. Libo. 1998. “Mechanics of Bond and Interface Shear Transfer in Optical Fiber Sensors.” J. Eng. Mech., 124 (4): 385–394. https://doi.org/10.1061/(ASCE)0733-9399(1998)124:4(385).

ASTM Standard, D7205/d7205M (2021). Standard Test Method for Tensile Properties of Fiber Reinforced Polymer Matrix Composite Bars, ASTM D7205-21. ASTM International, West Conshohocken, Philadelphia

Azimi, M., A. Eslamlou, and G. Pekcan. 2020. “Data-Driven Structural Health Monitoring and Damage Detection through Deep Learning: State-of-the-Art Review.” Sensors, 20 (10): 2778. https://doi.org/10.3390/s20102778.

Bado, M., J. Casas, and A. Barrias. 2018. “Performance of Rayleigh-Based Distributed Optical Fiber Sensors Bonded to Reinforcing Bars in Bending.” Sensors, 18 (9): 3125. https://doi.org/10.3390/s18093125.

Bado, M. F., and J. R. Casas. 2021. “A Review of Recent Distributed Optical Fiber Sensors Applications for Civil Engineering Structural Health Monitoring.” Sensors, 21 (5): 1818. https://doi.org/10.3390/s21051818.

Bado, M. F., J. R. Casas, A. Dey, and C. G. Berrocal. 2020. “Distributed Optical Fiber Sensing Bonding Techniques Performance for Embedment inside Reinforced Concrete Structures.” Sensors, 20 (20): 5788. https://doi.org/10.3390/s20205788.

Bao, X., and L. Chen. 2011. “Recent Progress in Brillouin Scattering Based Fiber Sensors.” Sensors, 11 (4): 4152–4187. https://doi.org/10.3390/s110404152.

Bao, X., and L. Chen. 2012. “Recent Progress in Distributed Fiber Optic Sensors.” Sensors, 12 (7): 8601–8639. https://doi.org/10.3390/s120708601.

Barrias, A., J. Casas, and S. Villalba. 2016. “A Review of Distributed Optical Fiber Sensors for Civil Engineering Applications.” Sensors, 16 (5): 748. https://doi.org/10.3390/s16050748.

Barrias, A., J. Casas, and S. Villalba. 2018a. “Embedded Distributed Optical Fiber Sensors in Reinforced Concrete Structures, A Case Study.” Sensors, 18 (4): 980. https://doi.org/10.3390/s18040980.

Barrias, A., G. Rodriguez, J. R. Casas, and S. Villalba. 2018b. “Application of distributed optical fiber sensors for the health monitoring of two real structures in Barcelona.” Structure and Infrastructure Engineering, 14 (7): 967–985. https://doi.org/10.1080/15732479.2018.1438479.

Bassil, A., X. Chapeleau, D. Leduc, and O. Abraham. 2018. “Quantification of cracks in reinforced concrete structures using distributed fibre optic sensors.” 1–9. Manchester, United Kingdom: EWSHM 2018.

Bassil, A., X. Wang, X. Chapeleau, E. Niederleithinger, O. Abraham, and D. Leduc. 2019. “Distributed Fiber Optics Sensing and Coda Wave Interferometry Techniques for Damage Monitoring in Concrete Structures.” Sensors, 19 (2): 356. https://doi.org/10.3390/s19020356.

de Battista, N., N. Cheal, R. Harvey, and C. Kechavarzi. 2017. “Monitoring the axial displacement of a high-rise building under construction using embedded distributed fibre optic sensors.”

Belarbi, A., S. E. Watkins, K. Chandrashekhara, J. Corra, and B. Konz. 2001. “Smart fiber-reinforced polymer rods featuring improved ductility and health monitoring capabilities.” Smart Mater. Struct., 10 (3): 427–431. https://doi.org/10.1088/0964-1726/10/3/301.

Benmokrane, B., E. El-Salakawy, Z. Cherrak, and A. Wiseman. 2004. “Fibre reinforced polymer composite bars for the structural concrete slabs of a Public Works and Government Services Canada parking garage.” Can. J. Civ. Eng., 31 (5): 732–748. https://doi.org/10.1139/l04-049.

Berrocal, C. G., I. Fernandez, M. F. Bado, J. R. Casas, and R. Rempling. 2021a. “Assessment and visualization of performance indicators of reinforced concrete beams by distributed optical fibre sensing.” Structural Health Monitoring, 20 (6): 3309–3326. https://doi.org/10.1177/1475921720984431.

Berrocal, C. G., I. Fernandez, and R. Rempling. 2021b. “Crack monitoring in reinforced concrete beams by distributed optical fiber sensors.” Structure and Infrastructure Engineering, 17 (1): 124–139. https://doi.org/10.1080/15732479.2020.1731558.

Bigoni, D. 2012. Nonlinear Solid Mechanics: Bifurcation Theory and Material Instability. Cambridge University Press.

Billon, A., J.-M. Hénault, M. Quiertant, F. Taillade, A. Khadour, R.-P. Martin, and K. Benzarti. 2015. “Qualification of a distributed optical fiber sensor bonded to the surface of a concrete structure: a methodology to obtain quantitative strain measurements.” Smart Mater. Struct., 24 (11): 115001. https://doi.org/10.1088/0964-1726/24/11/115001.

Brault, A., and N. Hoult. 2019. “Monitoring Reinforced Concrete Serviceability Performance Using Fiber Optic Sensors.” ACI Structural Journal, 116 (1). https://doi.org/10.14359/51710870.

Brault, A., N. A. Hoult, T. Greenough, and I. Trudeau. 2019. “Monitoring of Beams in an RC Building during a Load Test Using Distributed Sensors.” J. Perform. Constr. Facil., 33 (1): 04018096. https://doi.org/10.1061/(ASCE)CF.1943-5509.0001250.

Brownjohn, J. M. W. 2007. “Structural health monitoring of civil infrastructure.” Phil. Trans. R. Soc. A., 365 (1851): 589–622. https://doi.org/10.1098/rsta.2006.1925.

Budzik, M. K., and H. Myhre Jensen. 2014. “Perturbation analysis of crack front in simple cantilever plate peeling experiment.” International Journal of Adhesion and Adhesives, 53: 29–33. https://doi.org/10.1016/j.ijadhadh.2014.01.014.

Burke, P. E. H. 1999. “THE TENSILE DEFORMATION PROCESS OF POLYPROPYLENE AT HIGH PRESSURE.” University of Toronto.

Canning, L., and S. Luke. 2010. “Development of FRP Bridges in the UK, An Overview.” Advances in Structural Engineering, 13 (5): 823–835. https://doi.org/10.1260/1369-4332.13.5.823.

Chapeleau, X., and A. Bassil. 2021. “A General Solution to Determine Strain Profile in the Core of Distributed Fiber Optic Sensors under Any Arbitrary Strain Fields.” Sensors, 21 (16): 5423. https://doi.org/10.3390/s21165423.

Chhoa, C. Y., X. Bao, T. W. Bremner, A. W. Brown, M. D. DeMerchant, A. L. Kalamkarov, and A. V. Georgiades. 2001. “Strain measurement in concrete structure using distributed fiber optic sensing based on Brillouin scattering with single-mode fibers embedded in glass fiber reinforcing vinyl ester rod and bonded to steel reinforcing bars.” S. B. Chase and A. E. Aktan, eds., 466–476. Newport Beach, CA.

Choi, H., S. Choi, and H. Cha. 2008. “Structural Health Monitoring system based on strain gauge enabled wireless sensor nodes.” 2008 5th International Conference on Networked Sensing Systems, 211–214. IKanazawa: IEEE.

Claus, R. O., K. D. Bennett, A. M. Vengsarkar, and K. A. Murphy. 1989. “Embedded optical fiber sensors for materials evaluation.” J Nondestruct Eval, 8 (2): 135–145. https://doi.org/10.1007/BF00565637.

Clauß, F., M. A. Ahrens, and P. Mark. 2021. “A comparative evaluation of strain measurement techniques in reinforced concrete structures–A discussion of assembly, application, and accuracy.” Structural Concrete, 22 (5): 2992–3007. https://doi.org/10.1002/suco.202000706.

Coricciati, A., I. Ingrosso, A. P. Sergi, and A. Largo. 2017. “Application of Smart FRP Devices for the Structural Health Monitoring of Heritage Buildings - A Case Study: The Monastery of Sant’Angelo d’Ocre.” KEM, 747: 448–455. https://doi.org/10.4028/www.scientific.net/KEM.747.448.

Cox, H. L. 1952. “The elasticity and strength of paper and other fibrous materials.” Br. J. Appl. Phys., 3 (3): 72–79. https://doi.org/10.1088/0508-3443/3/3/302.

Curie, J., and P. Curie. 1880. “Development by pressure of polar electricity in hemihedral crystals with inclined faces.” Bull. soc. min. de France, 3: 90–102.

Da Silva, L. F. M., A. Öchsner, and R. D. Adams (Eds.). 2018. Handbook of Adhesion Technology. Cham: Springer International Publishing.

Davis, M. B., N. A. Hoult, S. Bajaj, and E. C. Bentz. 2017. “Distributed Sensing for Shrinkage and Tension Stiffening Measurement.” ACI Structural Journal, 114 (3). https://doi.org/10.14359/51689463.

Ding, Z., C. Wang, K. Liu, J. Jiang, D. Yang, G. Pan, Z. Pu, and T. Liu. 2018. “Distributed Optical Fiber Sensors Based on Optical Frequency Domain Reflectometry: A review.” Sensors, 18 (4): 1072. https://doi.org/10.3390/s18041072.

Dong, M., S. Li, B. Yu, Q. Jiang, H. Zhu, J. Zhao, J. Huang, and S. Tao. 2024. “Experimental investigation on the freeze-thaw durability of a phase change concrete in cold regions.” Cold Regions Science and Technology, 218: 104102. https://doi.org/10.1016/j.coldregions.2023.104102.

Du, W., X. Zheng, B. Shi, M. Sun, H. Wu, W. Ni, Z. Zheng, and M. Niu. 2023. “Strain Transfer Mechanism in Surface-Bonded Distributed Fiber Optic Sensors under Different Strain Fields.” Sensors, 23 (15): 6863. https://doi.org/10.3390/s23156863.

Dumoulin, C., G. Karaiskos, J.-Y. Sener, and A. Deraemaeker. 2014. “Online monitoring of cracking in concrete structures using embedded piezoelectric transducers.” Smart Mater. Struct., 23 (11): 115016. https://doi.org/10.1088/0964-1726/23/11/115016.

Duo, Y., X. Liu, Y. Liu, T. Tafsirojjaman, and M. Sabbrojjaman. 2021. “Environmental impact on the durability of FRP reinforcing bars.” Journal of Building Engineering, 43: 102909. https://doi.org/10.1016/j.jobe.2021.102909.

Falcetelli, F., L. Rossi, R. Di Sante, and G. Bolognini. 2020. “Strain Transfer in Surface-Bonded Optical Fiber Sensors.” Sensors, 20 (11): 3100. https://doi.org/10.3390/s20113100.

Farrar, C. R., and K. Worden. 2007. “An introduction to structural health monitoring.” Phil. Trans. R. Soc. A., 365 (1851): 303–315. https://doi.org/10.1098/rsta.2006.1928.

Fendzi, C., N. Mechbal, M. Rébillat, M. Guskov, and G. Coffignal. 2016. “A general Bayesian framework for ellipse-based and hyperbola-based damage localization in anisotropic composite plates.” Journal of Intelligent Material Systems and Structures, 27 (3): 350–374. https://doi.org/10.1177/1045389X15571383.

Feng, X., J. Zhou, C. Sun, X. Zhang, and F. Ansari. 2013. “Theoretical and Experimental Investigations into Crack Detection with BOTDR-Distributed Fiber Optic Sensors.” J. Eng. Mech., 139 (12): 1797–1807. https://doi.org/10.1061/(ASCE)EM.1943-7889.0000622.

Fernandez, A. F., P. Rodeghiero, B. Brichard, F. Berghmans, A. H. Hartog, P. Hughes, K. Williams, and A. P. Leach. 2005. “Radiation-tolerant Raman distributed temperature monitoring system for large nuclear infrastructures.” IEEE Trans. Nucl. Sci., 52 (6): 2689–2694. https://doi.org/10.1109/TNS.2005.860736.

Froggatt, M., and J. Moore. 1998. “High-spatial-resolution distributed strain measurement in optical fiber with Rayleigh scatter.” Appl. Opt., 37 (10): 1735. https://doi.org/10.1364/AO.37.001735.

Galkovski, T., Y. Lemcherreq, J. Mata-Falcón, and W. Kaufmann. 2021. “Fundamental Studies on the Use of Distributed Fibre Optical Sensing on Concrete and Reinforcing Bars.” Sensors, 21 (22): 7643. https://doi.org/10.3390/s21227643.

Gallucci, L., C. Menna, L. Angrisani, D. Asprone, R. S. L. Moriello, F. Bonavolontà, and F. Fabbrocino. 2017. “An Embedded Wireless Sensor Network with Wireless Power Transmission Capability for the Structural Health Monitoring of Reinforced Concrete Structures.” Sensors, 17 (11): 2566. https://doi.org/10.3390/s17112566.

García Garino, C., M. S. Ribero Vairo, S. Andía Fagés, A. E. Mirasso, and J.-P. Ponthot. 2013. "Numerical simulation of finite strain viscoplastic problems." Journal of Computational and Applied Mathematics, 246: 174–184. https://doi.org/10.1016/j.cam.2012.10.008.

Gouda, O., A. Asadian, and K. Galal. 2023. "Investigation of different parameters affecting the crack width and k coefficient of GFRP-RC beams." Engineering Structures, 297: 116181. https://doi.org/10.1016/j.engstruct.2023.116181.

Gowshikan, A., K. Kariyawasam, X. Xu, C. Kechavarzi, N. De Battista, N. Ferdinando, S. Acikgoz, N. D. Gunawardana, and M. Ranasinghe. 2023. "A Review on the Advances in Distributed Fibre Optic Sensing Technology for Structural Health Monitoring." 12th International Conference on Structural Engineering and Construction Management, Lecture Notes in Civil Engineering, R. Dissanayake, P. Mendis, K. Weerasekera, S. De Silva, S. Fernando, and C. Konthesingha, eds., 145–159. Singapore: Springer Nature Singapore.

Hassani, S., and U. Dackermann. 2023. "A Systematic Review of Advanced Sensor Technologies for Non-Destructive Testing and Structural Health Monitoring." Sensors, 23 (4): 2204. https://doi.org/10.3390/s23042204.

Her, S.-C., and C.-Y. Huang. 2011. "Effect of Coating on the Strain Transfer of Optical Fiber Sensors." Sensors, 11 (7): 6926–6941. https://doi.org/10.3390/s110706926.

Herbers, M., B. Richter, and S. Marx. 2024. "Rayleigh-based crack monitoring with distributed fiber optic sensors: experimental study on the interaction of spatial resolution and sensor type." J Civil Struct Health Monit. https://doi.org/10.1007/s13349-024-00896-5.

Hill, K. O., Y. Fujii, D. C. Johnson, and B. S. Kawasaki. 1978. "Photosensitivity in optical fiber waveguides: Application to reflection filter fabrication." Applied Physics Letters, 32 (10): 647–649. https://doi.org/10.1063/1.89881.

Ihn, J.-B., and F.-K. Chang. 2004. "Detection and monitoring of hidden fatigue crack growth using a built-in piezoelectric sensor/actuator network: II. Validation using riveted joints and repair patches." Smart Mater. Struct., 13 (3): 621–630. https://doi.org/10.1088/0964-1726/13/3/021.

Ilki, A., D. Çavunt, and Y. S. Çavunt (Eds.). 2023. Building for the Future: Durable, Sustainable, Resilient: Proceedings of the fib Symposium 2023 - Volume 1. Lecture Notes in Civil Engineering. Cham: Springer Nature Switzerland.

Ilki, A., M. Ispir, and P. Inci (Eds.). 2022. 10th International Conference on FRP Composites in Civil Engineering: Proceedings of CICE 2020/2021. Lecture Notes in Civil Engineering. Cham: Springer International Publishing.

Inaudi, D., and B. Glisic. 2005. "Application of distributed Fiber Optic Sensory for SHM." 2nd International Conference on Structural Health Monitoring of Intelligent Infrastructure (SHMII-2'2005), 1–7. Shenzhen, China.

InformationGatekeepers. 2019. 2019 Distributed and Single Point Fiber Optic Sensing Systems Forecast.

Jaradat, M., J. L. Duran, D. H. Murcia, L. Buechley, Y.-L. Shen, C. Christodoulou, and M. R. Taha. 2023. "Cognizant Fiber-Reinforced Polymer Composites Incorporating Seamlessly Integrated Sensing and Computing Circuitry." Polymers, 15 (22): 4401. https://doi.org/10.3390/polym15224401.

Ji, X.-L., L.-J. Chen, K. Liang, W. Pan, and R. Kai-Leung Su. 2023. “A review on FRP bars and supplementary cementitious materials for the next generation of sustainable and durable construction materials.” Construction and Building Materials, 383: 131403. https://doi.org/10.1016/j.conbuildmat.2023.131403.

Johar, M., S. F. M. Asasaari, and M. N. Tamin. 2014. “Strain rate-dependent deformation and failure process of adhesive joints.” 36th International Electronics Manufacturing Technology Conference, 1–5. Johor, Malaysia: IEEE.

Johnson, W. S., J. E. Masters, D. W. Wilson, J. Chin, T. Nguyen, and K. Aouadi. 1997. “Effects of Environmental Exposure on Fiber-Reinforced Plastic (FRP) Materials Used in Construction.” J. Compos. Technol. Res., 19 (4): 205. https://doi.org/10.1520/CTR10120J.

Kalamkarov, A. L., S. B. Fitzgerald, and D. O. MacDonald. 1999. “The use of Fabry Perot fiber optic sensors to monitor residual strains during pultrusion of FRP composites.” Composites Part B: Engineering, 30 (2): 167–175. https://doi.org/10.1016/S1359-8368(98)00052-3.

Kalamkarov, A. L., D. O. MacDonald, S. B. Fitzgerald, and A. V. Georgiades. 2000. “Reliability assessment of pultruded FRP reinforcements with embedded ®ber optic sensors.” Composite Structures.

Kalamkarov, A. L., G. C. Saha, A. V. Georgiades, K. Challagulla, and J. P. Newhook. 2004. “Smart FRP Reinforcements for Long-Term Health Monitoring in Infrastructure.” Journal of Thermoplastic Composite Materials, 17 (4): 359–381. https://doi.org/10.1177/0892705704045189.

Karataş, M. A., and H. Gökkaya. 2018. “A review on machinability of carbon fiber reinforced polymer (CFRP) and glass fiber reinforced polymer (GFRP) composite materials.” Defence Technology, 14 (4): 318–326. https://doi.org/10.1016/j.dt.2018.02.001.

Koch, G., J. Varney, N. Thompson, and O. Moghissi. 2016. NACE International Measures of Prevention, Application, and Economics of Corrosion Technologies Study. 216.

Komurlu, E., F. Cihangir, A. Kesimal, and S. Demir. 2016. “Effect of Adhesive Type on the Measurement of Modulus of Elasticity Using Electrical Resistance Strain Gauges.” Arab J Sci Eng, 41 (2): 433–441. https://doi.org/10.1007/s13369-015-1837-0.

Kralovec, C., and M. Schagerl. 2020. “Review of Structural Health Monitoring Methods Regarding a Multi-Sensor Approach for Damage Assessment of Metal and Composite Structures.” Sensors, 20 (3): 826. https://doi.org/10.3390/s20030826.

Krempl, E., and J. M. Gleason. 1996. “Isotropic viscoplasticity theory based on overstress (VBO). The influence of the direction of the dynamic recovery term in the growth law of the equilibrium stress.” International Journal of Plasticity, 12 (6): 719–735. https://doi.org/10.1016/S0749-6419(98)80002-8.

Kristufek, L., A. Zahedi, D. Tawil, L. Sanchez, B. Martin-Perez, and M. Noël. 2022. “Preliminary evaluation of Pier cap from an ASR affected bridge in Central Canada.” MATEC Web Conf., (H. Beushausen, J. Ndawula, M. G. Alexander, F. Dehn, and P. Moyo, eds.), 364: 03005. https://doi.org/10.1051/matecconf/202236403005.

LeBlanc, M., A. Guemes, A. Othonos, S. Y. Huang, M. Ohn, and R. M. Measures. 1996. “Distributed strain measurement based on a fiber Bragg grating and its reflection spectrum analysis.” Opt. Lett., 21 (17): 1405. https://doi.org/10.1364/OL.21.001405.

LeBlanc, M. J. 1999. “Interaction Mechanics of Embedded Single-Ended Optical Fibre Sensors U sing Novel In-situ Measurement Techniques.” University of Toronto.

Li, C. Z., Z. Guo, D. Su, B. Xiao, and V. W. Y. Tam. 2022. “The Application of Advanced Information Technologies in Civil Infrastructure Construction and Maintenance.” Sustainability, 14 (13): 7761. https://doi.org/10.3390/su14137761.

Li, D. 2006. “Strain transferring analysis of fiber Bragg grating sensors.” Opt. Eng, 45 (2): 024402. https://doi.org/10.1117/1.2173659.

Li, E. 2017. “Rayleigh scattering based distributed optical fiber sensing.” AOPC 2017: Fiber Optic Sensing and Optical Communications, L. Wei, W. Zhang, D. Jiang, W. Wang, K. T. Grattan, Y. Liao, and Z.-S. Zhao, eds., 97. Beijing, China: SPIE.

Li, H.-N., G.-D. Zhou, L. Ren, and D.-S. Li. 2009a. “Strain Transfer Coefficient Analyses for Embedded Fiber Bragg Grating Sensors in Different Host Materials.” J. Eng. Mech., 135 (12): 1343–1353. https://doi.org/10.1061/(ASCE)0733-9399(2009)135:12(1343).

Li, Q., G. Li, and G. Wang. 2003. “Effect of the plastic coating on strain measurement of concrete by fiber optic sensor.” Measurement, 34 (3): 215–227. https://doi.org/10.1016/S0263-2241(03)00052-6.

Li, Q., G. Li, G. Wang, F. Ansari, and Q. Liu. 2002. “Elasto-Plastic Bonding of Embedded Optical Fiber Sensors in Concrete.” J. Eng. Mech., 128 (4): 471–478. https://doi.org/10.1061/(ASCE)0733-9399(2002)128:4(471).

Li, W. Y., C. C. Cheng, and Y. L. Lo. 2009b. “Investigation of strain transmission of surface-bonded FBGs used as strain sensors.” Sensors and Actuators A: Physical, 149 (2): 201–207. https://doi.org/10.1016/j.sna.2008.11.011.

Lißner, M., E. Alabort, H. Cui, R. Rito, B. R. K. Blackman, and N. Petrinic. 2019. “Experimental characterisation and numerical modelling of the influence of bondline thickness, loading rate, and deformation mode on the response of ductile adhesive interfaces.” Journal of the Mechanics and Physics of Solids, 130: 349–369. https://doi.org/10.1016/j.jmps.2019.06.011.

Liu, H., S. Zhang, A. A. S. Coulibaly, J. Cheng, and M. J. DeJong. 2021. “Monitoring Reinforced Concrete Cracking Behaviour under Uniaxial Tension Using Distributed Fiber-Optic Sensing Technology.” J. Struct. Eng., 147 (12): 04021212. https://doi.org/10.1061/(ASCE)ST.1943-541X.0003191.

Lopez-Higuera, J. M., L. Rodriguez Cobo, A. Quintela Incera, and A. Cobo. 2011. “Fiber Optic Sensors in Structural Health Monitoring.” J. Lightwave Technol., 29 (4): 587–608. https://doi.org/10.1109/JLT.2011.2106479.

Lu, P., N. Lalam, M. Badar, B. Liu, B. T. Chorpening, M. P. Buric, and P. R. Ohodnicki. 2019. “Distributed optical fiber sensing: Review and perspective.” Applied Physics Reviews, 6 (4): 041302. https://doi.org/10.1063/1.5113955.

Lu, Z., T. Feng, F. Li, and X. S. Yao. 2023. “Optical Frequency-Domain Reflectometry Based Distributed Temperature Sensing Using Rayleigh Backscattering Enhanced Fiber.” Sensors, 23 (12): 5748. https://doi.org/10.3390/s23125748.

Lu, Z., and Q. Xu. 2013. “Cohesive zone modeling for viscoplastic behaviour at finite deformations.” Composites Science and Technology, 74: 173–178. https://doi.org/10.1016/j.compscitech.2012.11.009.

Lynch, J. P. 2006. “A Summary Review of Wireless Sensors and Sensor Networks for Structural Health Monitoring.” The Shock and Vibration Digest, 38 (2): 91–128. https://doi.org/10.1177/0583102406061499.

Malkiel, N., and O. Rabinovitch. 2021. “Stochastic cohesive interface analysis of layer debonding.” International Journal of Solids and Structures, 226–227: 111081. https://doi.org/10.1016/j.ijsolstr.2021.111081.

Markolefas, S. I., and Th. K. Papathanassiou. 2009. “Stress redistributions in adhesively bonded double-lap joints, with elastic–perfectly plastic adhesive behaviour, subjected to axial lap-shear cyclic loading.” International Journal of Adhesion and Adhesives, 29 (7): 737–744. https://doi.org/10.1016/j.ijadhadh.2009.04.001.

Nanni, A., A. De Luca, and H. Jawaheri Zadeh. 2014. Reinforced Concrete with FRP Bars. CRC Press.

Niklès, M., L. Thévenaz, and P. A. Robert. 1996. “Simple distributed fiber sensor based on Brillouin gain spectrum analysis.” Opt. Lett., 21 (10): 758. https://doi.org/10.1364/OL.21.000758.

Ortiz, J. D., S. S. Khedmatgozar Dolati, P. Malla, A. Nanni, and A. Mehrabi. 2023. “FRP-Reinforced/Strengthened Concrete: State-of-the-Art Review on Durability and Mechanical Effects.” Materials, 16 (5): 1990. https://doi.org/10.3390/ma16051990.

Pak, Y. E. 1992. “Longitudinal shear transfer in fiber optic I sensors.” Smart Mater.Struct., 1 (1992): 57–62.

Palmieri, L. 2013. “Distributed Optical Fiber Sensing Based on Rayleigh Scattering.” TOOPTSJ, 7 (1): 104–127. https://doi.org/10.2174/1874328501307010104.

Panigrahi, S. K., and B. Pradhan. 2007. “Three Dimensional Failure Analysis and Damage Propagation Behaviour of Adhesively Bonded Single Lap Joints in Laminated FRP Composites.” Journal of Reinforced Plastics and Composites, 26 (2): 183–201. https://doi.org/10.1177/0731684407070026.

Pellegrino, C., F. Faleschini, M. A. Zanini, J. C. Matos, J. R. Casas, and A. Strauss (Eds.). 2022. Proceedings of the 1st Conference of the European Association on Quality Control of Bridges and Structures: EUROSTRUCT 2021. Lecture Notes in Civil Engineering. Cham: Springer International Publishing.

Pendão, C., and I. Silva. 2022. “Optical Fiber Sensors and Sensing Networks: Overview of the Main Principles and Applications.” Sensors, 22 (19): 7554. https://doi.org/10.3390/s22197554.

Qureshi, J. 2022. “A Review of Fibre Reinforced Polymer Structures.” Fibers, 10 (3): 27. https://doi.org/10.3390/fib10030027.

Rahmatian, A. 2014. Static and Fatigue Behaviour of FRP-Reinforced Concrete Beams and a SHM. Montreal, Quebec: Concordia University.

Rajan, G., and B. G. Prusty (Eds.). 2016. Structural Health Monitoring of Composite Structures Using Fiber Optic Methods. CRC Press.

Rao, K. R., D. N. Kim, and J. J. Hwang. 2010. “Fast Algorithms.” Fast Fourier Transform - Algorithms and Applications, Signals and Communication Technology, 41–110. Dordrecht: Springer Netherlands.

Rodrigues, R., S. Gaboreau, J. Gance, I. Ignatiadis, and S. Betelu. 2021. “Reinforced concrete structures: A review of corrosion mechanisms and advances in electrical methods for corrosion monitoring.” Construction and Building Materials, 269: 121240. https://doi.org/10.1016/j.conbuildmat.2020.121240.

Rodríguez, G., J. R. Casas, and S. Villaba. 2015. “Cracking assessment in concrete structures by distributed optical fiber.” Smart Mater. Struct., 24 (3): 035005. https://doi.org/10.1088/0964-1726/24/3/035005.

Rolland, A., M. Quiertant, A. Khadour, S. Chataigner, K. Benzarti, and P. Argoul. 2018. “Experimental investigations on the bond behaviour between concrete and FRP reinforcing bars.” Construction and Building Materials, 173: 136–148. https://doi.org/10.1016/j.conbuildmat.2018.03.169.

Romano, M. G., M. Guida, F. Marulo, M. Giugliano Auricchio, and S. Russo. 2020. “Characterization of Adhesives Bonding in Aircraft Structures.” Materials, 13 (21): 4816. https://doi.org/10.3390/ma13214816.

Sampaio, R. P. C., and N. M. M. Maia. 2009. “Strategies for an efficient indicator of structural damage.” Mechanical Systems and Signal Processing, 23 (6): 1855–1869. https://doi.org/10.1016/j.ymssp.2008.07.015.

Sbahieh, S., G. Mckay, and S. G. Al-Ghamdi. 2023. “A comparative life cycle assessment of fiber-reinforced polymers as a sustainable reinforcement option in concrete beams.” Front. Built Environ., 9: 1194121. https://doi.org/10.3389/fbuil.2023.1194121.

Seo, S.-Y., J.-H. Park, H.-D. Yun, and K.-S. Kim. 2020. “Installation Technique of Fiber Optic Sensor into FRP Used as NSM Structural Strengthening System.” Sustainability, 12 (20): 8501. https://doi.org/10.3390/su12208501.

Siddika, A., Md. A. A. Mamun, W. Ferdous, and R. Alyousef. 2020. “Performances, challenges and opportunities in strengthening reinforced concrete structures by using FRPs – A state-of-the-art review.” Engineering Failure Analysis, 111: 104480. https://doi.org/10.1016/j.engfailanal.2020.104480.

Simo, J. C. 1988. “A framework for finite strain elastoplasticity based on maximum plastic dissipation and the multiplicative decomposition: Part I. Continuum formulation.” Computer Methods in Applied Mechanics and Engineering, 66 (2): 199–219. https://doi.org/10.1016/0045-7825(88)90076-X.

Sun, F., N. A. Hoult, L. Butler, and M. Zhang. 2024. “Monitoring and Assessment of Buckling in Slender Members with Varying Lateral Restraint and Thermal Loading Using Distributed Sensing.” J. Struct. Eng., 150 (1): 04023190. https://doi.org/10.1061/JSENDH.STENG-12661.

Sun, X., Y. Du, W. Liao, H. Ma, and J. Huang. 2019. “Measuring the heterogeneity of cement paste by truly distributed optical fiber sensors.” Construction and Building Materials, 225: 765–771. https://doi.org/10.1016/j.conbuildmat.2019.07.187.

Taheri, S. 2019. “A review on five key sensors for monitoring of concrete structures.” Construction and Building Materials, 204: 492–509. https://doi.org/10.1016/j.conbuildmat.2019.01.172.

Tan, X., A. Abu-Obeidah, Y. Bao, H. Nassif, and W. Nasreddine. 2021a. “Measurement and visualization of strains and cracks in CFRP post-tensioned fiber reinforced concrete beams using

distributed fiber optic sensors." Automation in Construction, 124: 103604. https://doi.org/10.1016/j.autcon.2021.103604.

Tan, X., Y. Bao, Q. Zhang, H. Nassif, and G. Chen. 2021b. "Strain transfer effect in distributed fiber optic sensors under an arbitrary field." Automation in Construction, 124: 103597. https://doi.org/10.1016/j.autcon.2021.103597.

Tang, Y., and Z. Wu. 2016. "Distributed Long-Gauge Optical Fiber Sensors Based Self-Sensing FRP Bar for Concrete Structure." Sensors, 16 (3): 286. https://doi.org/10.3390/s16030286.

Tang, Y., Z. Wu, C. Yang, G. Wu, L. Zhao, and S. Song. 2010. "Application of smart BFRP bars with distributed fiber optic sensors into concrete structures." M. Tomizuka, ed., 76471I. San Diego, California, USA.

Tavares, D. H., J. S. Giongo, and P. Paultre. 2008. "Behaviour of reinforced concrete beams reinforced with GFRP bars." Rev. IBRACON Estrut. Mater., 1 (3): 285–295. https://doi.org/10.1590/S1983-41952008000300004.

Tomlinson, G. R., and W. A. Bullough. 1998. Smart materials and structures: proceedings of the 4th European Conference on Smart Structures and Materials in conjunction with the 2nd International Conference on Micromechanics, Intelligent Materials and Robotics, Harrogate, UK, 6 - 8 July 1998. Bristol: Institute of Physics Publishing.

Torkan, B. 2011. Development of a protection mechanism for fiber optic sensors in monitoring GFRP reinforced concrete beams. Ottawa: Library and Archives Canada = Bibliothèque et Archives Canada.

Uthaman, A., H. M. Lal, and S. Thomas. 2024. "Introduction of fibre-reinforced polymers−polymer nanocomposites: Applications and durability." Aging and Durability of FRP Composites and Nanocomposites, 1–16. Elsevier.

Vemuganti, S., R. Chennareddy, A. Riad, and M. Taha. 2020. "Pultruded GFRP Reinforcing Bars Using Nanomodified Vinyl Ester." Materials, 13 (24): 5710. https://doi.org/10.3390/ma13245710.

Vollebregt, E. A. H. 2014. "Numerical modeling of measured railway creep versus creep-force curves with CONTACT." Wear, 314 (1–2): 87–95. https://doi.org/10.1016/j.wear.2013.11.030.

Wan, K. T., C. K. Y. Leung, and N. G. Olson. 2008. "Investigation of the strain transfer for surface-attached optical fiber strain sensors." Smart Mater. Struct., 17 (3): 035037. https://doi.org/10.1088/0964-1726/17/3/035037.

Wang, B., J. G. Teng, L. D. Lorenzis, L.-M. Zhou, J. Ou, W. Jin, and K. T. Lau. 2009. "Strain monitoring of RC members strengthened with smart NSM FRP bars." Construction and Building Materials, 23 (4): 1698–1711. https://doi.org/10.1016/j.conbuildmat.2008.07.027.

Wang, C. S., F. Wu, and F.-K. Chang. 2001. "Structural health monitoring from fiber-reinforced composites to steel-reinforced concrete." Smart Mater. Struct., 10 (3): 548–552. https://doi.org/10.1088/0964-1726/10/3/318.

Wang, H., and P. Xiang. 2016. "Strain transfer analysis of optical fiber based sensors embedded in an asphalt pavement structure." Meas. Sci. Technol., 27 (7): 075106. https://doi.org/10.1088/0957-0233/27/7/075106.

Wang, H., P. Xiang, and L. Jiang. 2019. “Strain transfer theory of industrialized optical fiber-based sensors in civil engineering: A review on measurement accuracy, design and calibration.” Sensors and Actuators A: Physical, 285: 414–426. https://doi.org/10.1016/j.sna.2018.11.019.

Waters, D. H., M. Kumosa, and J. Hoffman. 2022. “Evaluating Strain Limits of Embedded FBG Sensors in Pultruded Hybrid Composite Rods.” IEEE Trans. Power Delivery, 37 (6): 5025–5032. https://doi.org/10.1109/TPWRD.2022.3166070.

Webb, G. T., P. J. Vardanega, N. A. Hoult, P. R. A. Fidler, P. J. Bennett, and C. R. Middleton. 2017. “Analysis of Fiber-Optic Strain-Monitoring Data from a Prestressed Concrete Bridge.” J. Bridge Eng., 22 (5): 05017002. https://doi.org/10.1061/(ASCE)BE.1943-5592.0000996.

Yan, M., X. Tan, S. Mahjoubi, and Y. Bao. 2022. “Strain transfer effect on measurements with distributed fiber optic sensors.” Automation in Construction, 139: 104262. https://doi.org/10.1016/j.autcon.2022.104262.

Yang, C. Q., Z. S. Wu, and L. P. Ye. 2006. “Self-Diagnosis of Hybrid CFRP Rods and As-Strengthened Concrete Structures.” Journal of Intelligent Material Systems and Structures, 17 (7): 609–618. https://doi.org/10.1177/1045389X06059954.

Yang, T., H. Wang, and X. Wang. 2021. “Strain Transfer Characteristics of Multi-Layer Optical Fiber Sensors with Temperature-Dependent Properties at Low Temperature.” Sensors, 21 (2): 495. https://doi.org/10.3390/s21020495.

Zeringue, C., I. Dajani, S. Naderi, G. T. Moore, and C. Robin. 2012. “A theoretical study of transient stimulated Brillouin scattering in optical fibers seeded with phase-modulated light.” Opt. Express, 20 (19): 21196. https://doi.org/10.1364/OE.20.021196.

Zhang, J., L. Peng, S. Wen, and S. Huang. 2024a. “A Review on Concrete Structural Properties and Damage Evolution Monitoring Techniques.” Sensors, 24 (2): 620. https://doi.org/10.3390/s24020620.

Zhang, J., Z. Wu, and M. Noori (Eds.). 2021a. Resilience of civil infrastructure systems: developments in testing, sensing, monitoring, and control. Boca Raton, FL: CRC Press.

Zhang, S., H. Liu, J. Cheng, and M. J. DeJong. 2021b. “A mechanical model to interpret distributed fiber optic strain measurement at displacement discontinuities.” Structural Health Monitoring, 20 (5): 2584–2603. https://doi.org/10.1177/1475921720964183.

Zhang, S., H. Liu, S. Govindjee, and M. J. DeJong. 2022. “Strain Transfer Mechanisms and Mechanical Properties of Optical Fiber Cables.” Sensors, 22 (24): 9966. https://doi.org/10.3390/s22249966.

Zhang, X., Z. Hua, C. A. Picklesimer, W. C. Chuirazzi, C. Sun, M. D. McMurtrey, and J. Rufner. 2024b. “Integrating fiber optic sensors into metallic components for sensing in harsh environments.” Optics & Laser Technology, 170: 110188. https://doi.org/10.1016/j.optlastec.2023.110188.

Zhang, X., H. Zhu, X. Jiang, and W. Broere. 2024c. “Distributed fiber optic sensors for tunnel monitoring: A state-of-the-art review.” Journal of Rock Mechanics and Geotechnical Engineering, S1674775524001045. https://doi.org/10.1016/j.jrmge.2024.01.008.

Zhou, J., C. Kang, M. Peng, M. Stümpel, and S. Marx. 2023. “Investigations on bond performances of GFRP/stainless steel reinforcements using distributed fiber optical sensors (DFOSs).” Journal of Building Engineering, 75: 106881. https://doi.org/10.1016/j.jobe.2023.106881.

Zhou, Z., J. He, K. Yan, and J. Ou. 2007. “Large scale distribution monitoring of FRP-OF based on BOTDR technique for infrastructures.” The 14th International Symposium on: Smart Structures and Materials & Non-destructive Evaluation and Health Monitoring, K. J. Peters, ed., 653006:1–12. San Diego, California: Proc. of SPIE.

Zhou, Z., J. P. Ou, and B. Wang. 2003. “Smart FRP-OFGB bars and their application in reinforced concrete beams.” A A Balkema Publishers, 861–866. Leiden, The Netherlands.

Zingoni, A. (Ed.). 2016. Insights and Innovations in Structural Engineering, Mechanics and Computation. CRC Press.

Zotti, A., S. Zuppolini, M. Zarrelli, and A. Borriello. 2016. “Fracture Toughening Mechanisms in Epoxy Adhesives.” Adhesives - Applications and Properties, A. Rudawska, ed. InTech.

Appendix A

Detailed Pilot Test Results

- Initial Monotonic Loading (strain data of each sample in almost 10 *kN* load increments)

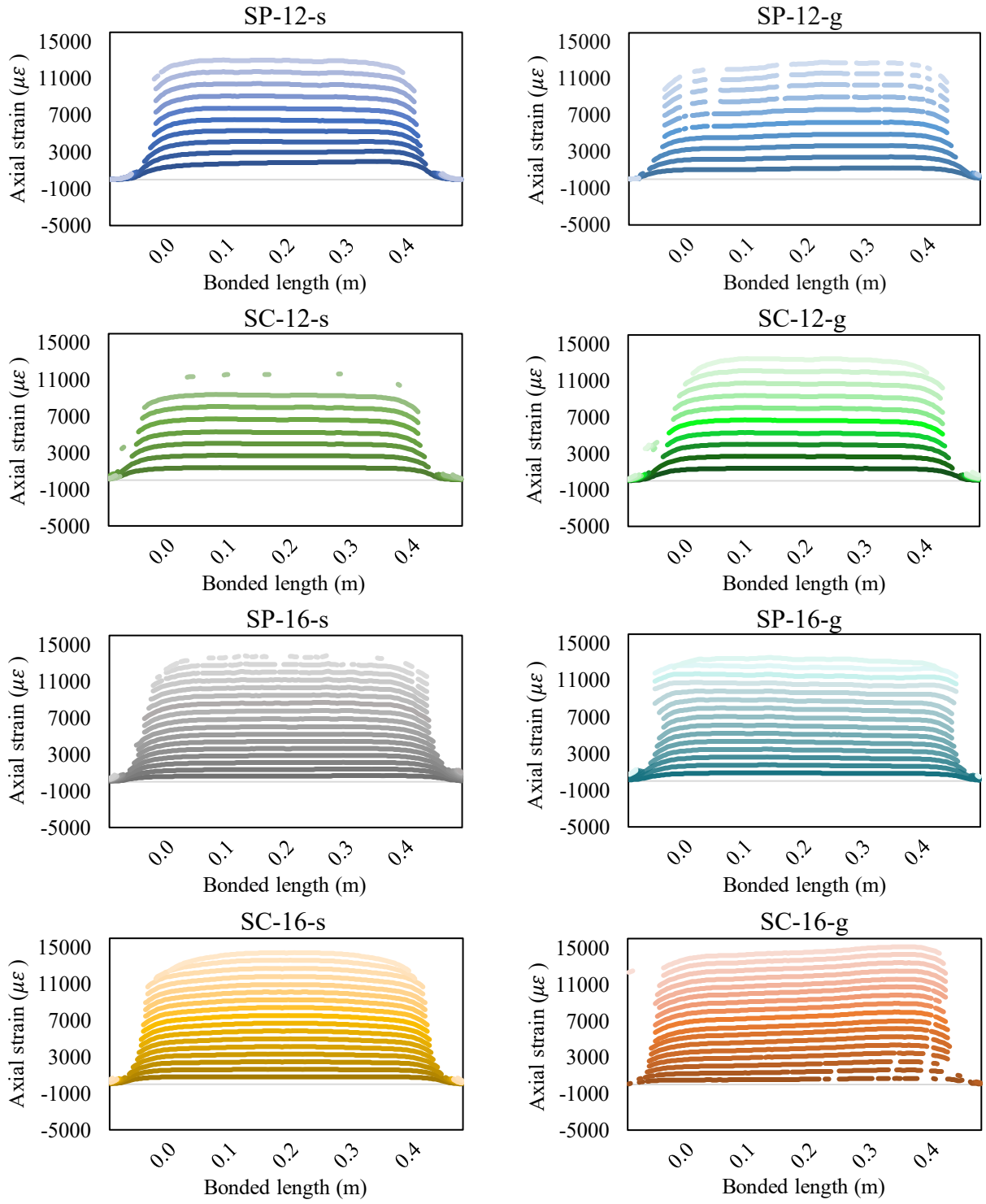

Figure A-1. DFOS strain distributions captured during initial monotonic loading of pilot samples

- High-level Sustained Loading Period

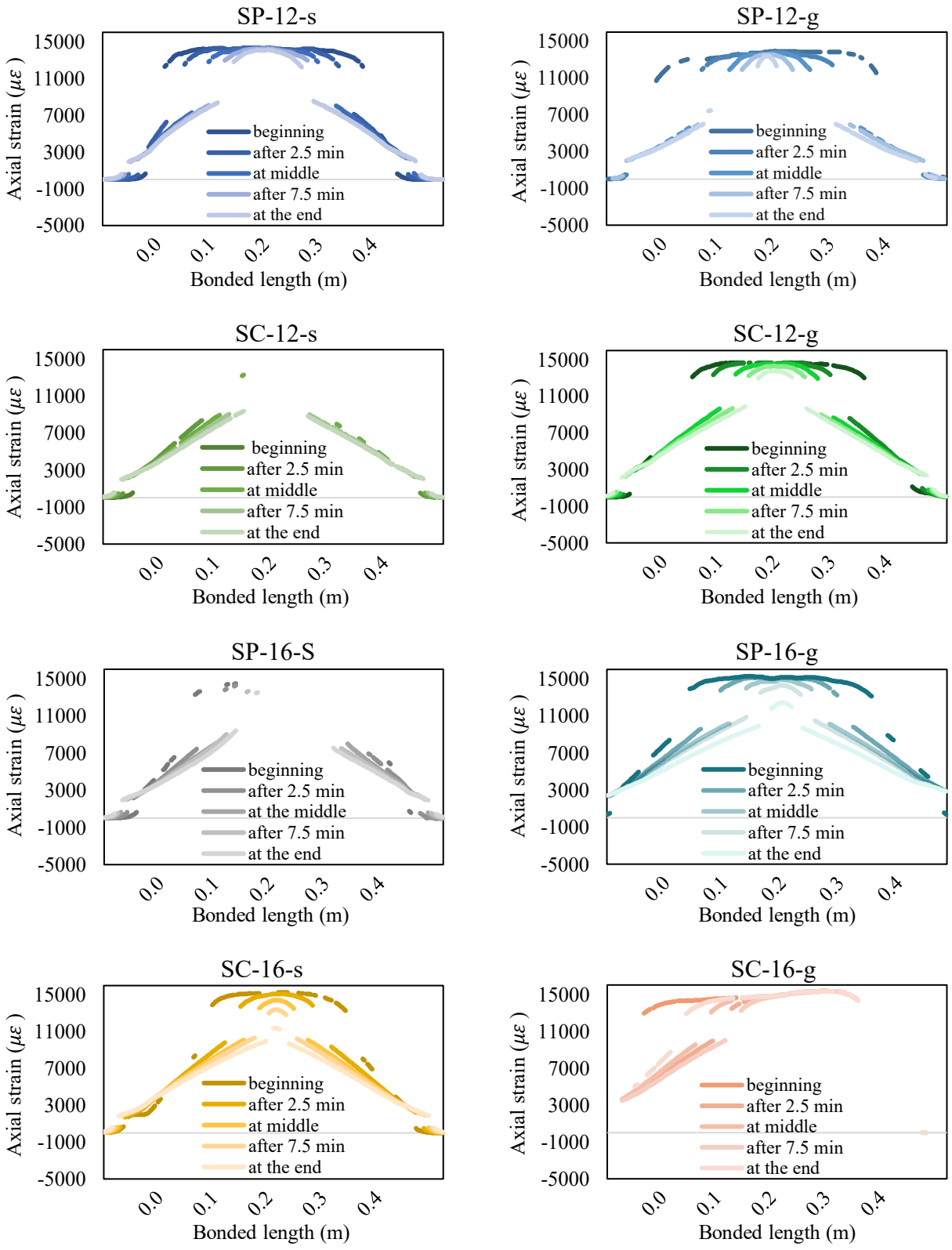

Figure A-2. DFOS strain distributions during sustained load period of pilot samples

- First Unloading After Sustained Load Stop

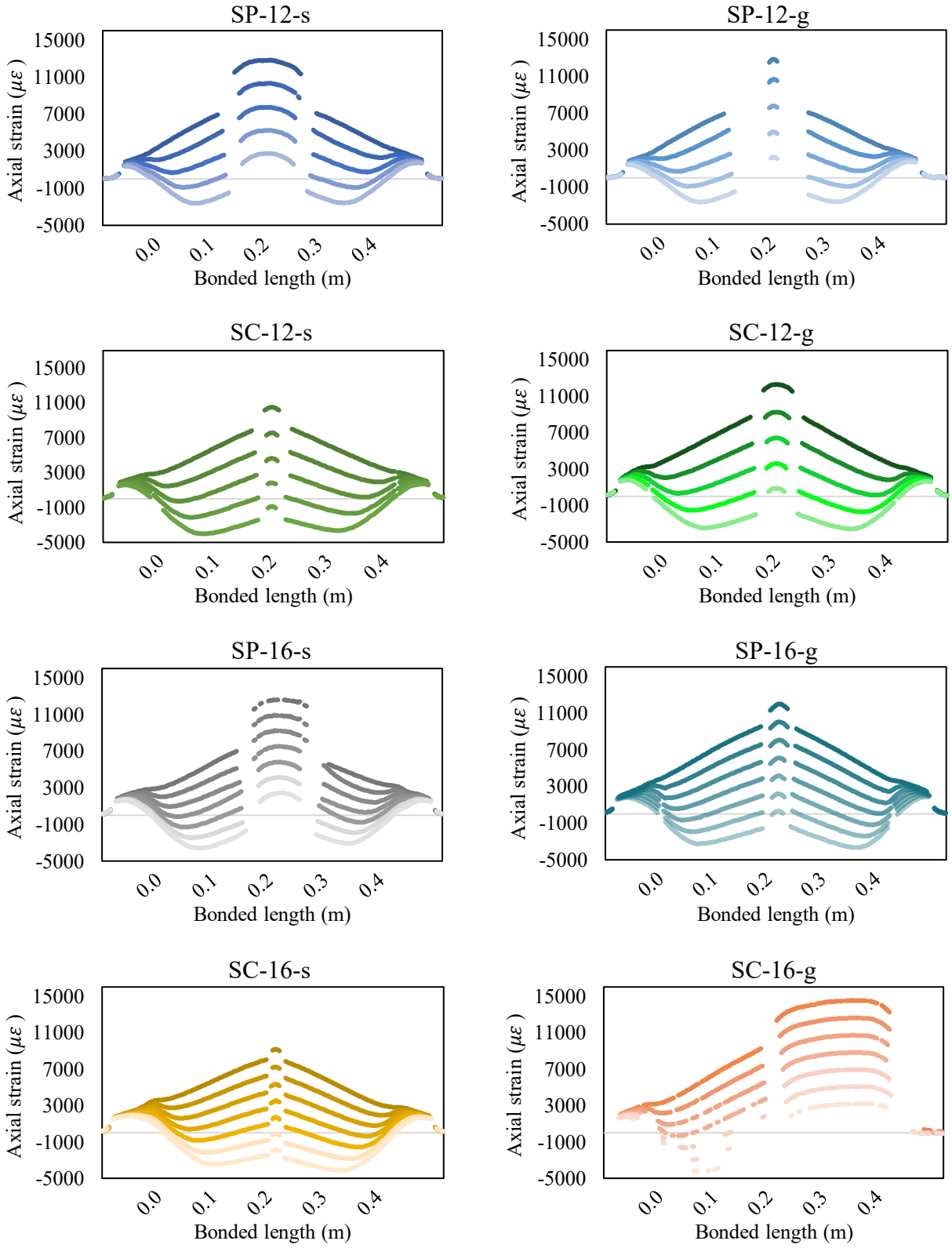

Figure A-3. DFOS strain distributions during first unloading of pilot samples

- Peaks and Troughs of Cyclic Loading Ranges

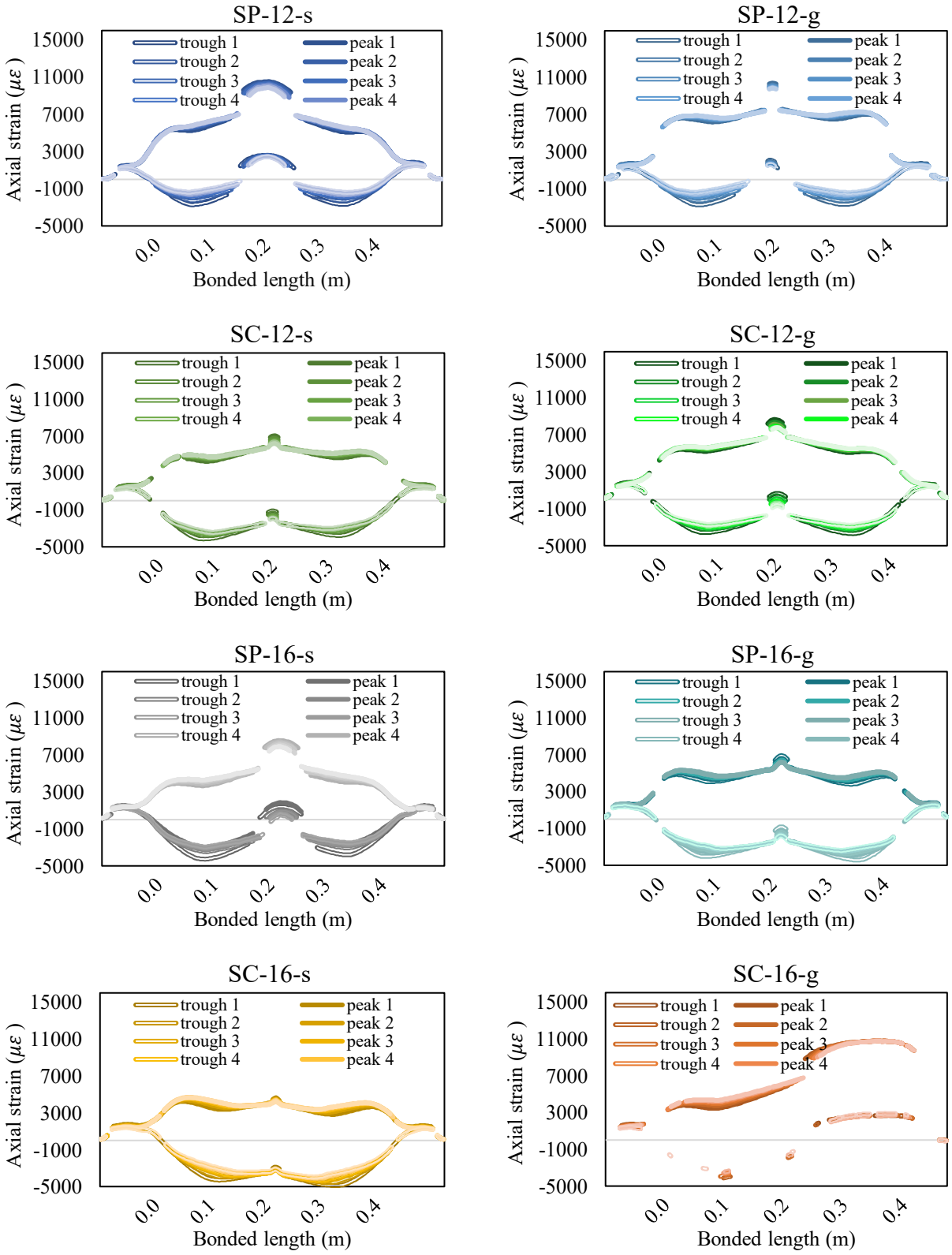

Figure A-4. DFOS strain distributions at cyclic loading peaks and troughs of pilot samples

- Last Loading to Failure

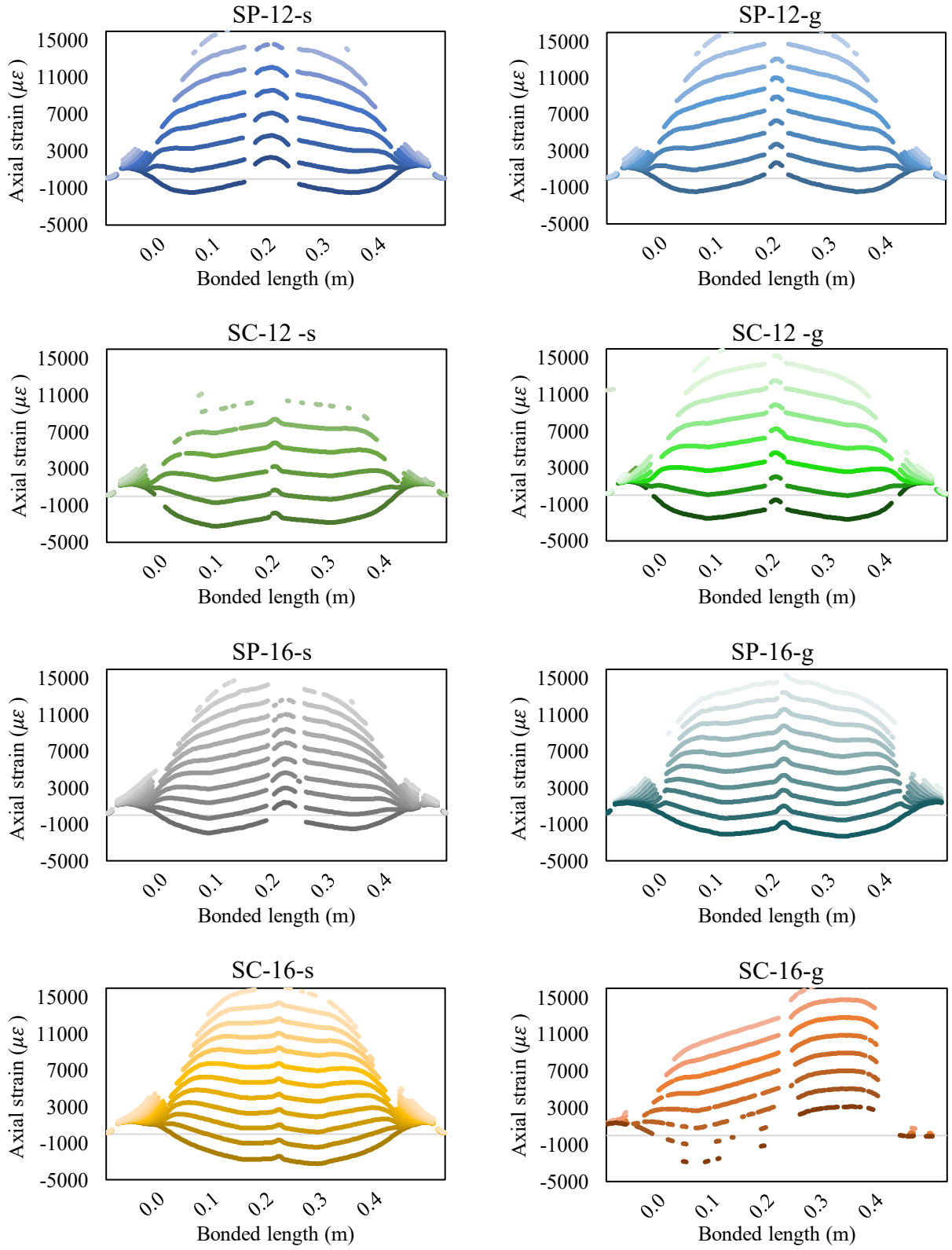

Figure A-5. DFOS strain distributions during last loading to failure of pilot samples